Technische Universität München

TUM School of Natural Sciences

Active-site Imprinted M-N-C Electrocatalysts: Tailor-made Synthesis and Tuned Activity

Davide Menga

Vollständiger Abdruck der von der TUM School of Natural Sciences der Technischen Universität München zur Erlangung des akademischen Grades eines

Doktors der Naturwissenschaften (Dr. rer. nat.)

genehmigten Dissertation.

Vorsitz:	Prof. Dr. Sebastian Günther
Prüfer*innen der Dissertation:	1. Prof. Dr. Hubert A. Gasteiger
	2. Prof. Dr. Tom Nilges
	3. Prof. Dr. Ulrike I. Kramm

Diese Dissertation wurde am 09.11.2022 bei der Technischen Universität München eingereicht und durch die TUM School of Natural Sciences am 18.11.2022 angenommen.

Abstract

Metal- and nitrogen- co-doped carbons (M-N-Cs) are currently the best alternative among noble-metal-free catalysts set to replace critical raw materials in several fundamentally important electrochemical reactions.

The topic of this thesis is the tailor-made synthesis, deep understanding and further development of M-N-Cs, with a particular focus on Fe-N-Cs.

In the first part, a new synthetic method towards the preparation of Fe-N-Cs is developed. This involves the imprinting of the desired N_4 coordination sites by Zn ions, followed by a transmetalation reaction with Fe. By carefully tuning the synthetic conditions, a material with defined morphology, exlusively containing tetrapyrrolic Fe-N_4 sites is obtained.

In the second part, this synthesis procedure is successfully transferred to different systems. The obtained catalysts are investigated in terms of intrinsic activity descriptors such as active-site density and turnover frequency in both acidic and alkaline electrolyte, revealing specific structure-activity relations.

In the final part, with the aid of advanced spectroscopic techniques, the stability of these catalysts is investigated, both in terms of powder storage and during operation in a proton exchange membrane fuel cell device.

Kurzfassung

Metall- und stickstoffkodotierte Kohlenstoffe (M-N-Cs) sind derzeit die beste Alternative unter den edelmetallfreien Katalysatoren, die kritische Rohstoffe in mehreren grundlegend wichtigen elektrochemischen Reaktionen ersetzen sollen.

Das Thema dieser Arbeit ist die maßgeschneiderte Synthese, das tiefe Verständnis und die Weiterentwicklung von M-N-Cs, mit besonderem Fokus auf Fe-N-Cs.

Im ersten Teil wird eine neue Synthesemethode zur Herstellung von Fe-N-Cs entwickelt. Dabei werden die gewünschten N_4-Koordinationsstellen durch Zn-Ionen templatiert, gefolgt von einer Transmetallierungsreaktion mit Fe. Durch sorgfältige Abstimmung der Synthesebedingungen wird ein Material mit definierter Morphologie erhalten, das ausschließlich tetrapyrrolische Fe-N_4-Zentren enthält.

Im zweiten Teil wird dieses Syntheseverfahren erfolgreich auf verschiedene Systeme übertragen. Die erhaltenen Katalysatoren werden im Hinblick auf intrinsische Aktivitätsdeskriptoren wie Dichte der aktiven Zentren und Turnover-Frequenz sowohl im sauren als auch im alkalischen Elektrolyten untersucht, wodurch spezifische Struktur-Aktivitäts-Beziehungen aufgezeigt werden.

Im letzten Teil wird mit Hilfe modernen spektroskopischer Techniken die Stabilität dieser Katalysatoren sowohl in Bezug auf die Pulverlagerung als auch während des Betriebs in einer Protonenaustauschmembran-Brennstoffzellenvorrichtung untersucht.

Contents

List of Abbreviations

Abbreviation	Description
BEV	Battery Electric Vehicle
FCEV	Fuel Cell Electric Vehicle
PEMFC	Proton Exchange Membrane Fuel Cell
CCM	Catalyst Coated Membrane
MEA	Membrane Electrode Assembly
GDL	Gas Diffusion Layer
HOR	Hydrogen Oxidation Reaction
ORR	Oxygen Reduction Reaction
PGM-free	Platinum Group Metal free
CO2RR	Carbon dioxide Reduction Reaction
OER	Oxygen Evolution Reaction
HER	Hydrogen Evolution Reaction
M-N-C	Metal and Nitrogen co-doped Carbon
SAC	Single Atom Catalyst
Fe-N-C	Iron and Nitrogen co-doped Carbon
XAS	X-ray Absorption Spectroscopy
HRTEM	High Resolution Transmission Electron Microscopy
RDS	Rate Determining Step
NDC	Nitrogen Doped Carbon
ROS	Reactive Oxygen Species
TOF	Turnover Frequency
SD	Active-site Density
CO	Carbon Monoxide
NO	Nitric Oxide
ZIF	Zeolitic Imidazolate Framework
IL-TEM	Identical-Location Transmission Electron Microscopy
EFC-ICP-MS	Electrochemical Flow Cell coupled to Inductively Coupled Plasma Mass Spectrometry

R(R)DE	Rotating (Ring) Disk Electrode
DFT	Density Functional Theory
XPS	X-ray Photoelectron Spectroscopy
EXAFS	Extended X-ray Absorption Fine Structure
Emim-dca	1-Ethyl-3-methylimidazolium dicyanamide
TS	Tafel Slope
DOS	Density of States
E_f	Energy of the Fermi level
TGA-MS	Mass Spectrometry coupled Thermogravimetric Analysis
PTFE	Polytetrafluoroethylene

1 Introduction

We are currently living in critical times regarding our CO_2 emissions and carbon footprint and drastic changes in our way to produce energy and materials are required in order to tackle global warming.[1] In order to produce energy in a cleaner fashion, electrochemical devices represent a central technology.[2] They have demonstrated practical industrial applications in many energy-related sectors, such as the conversion of electricity to produce chemicals and vice versa. The conversion of electricity into chemicals becomes especially important when the aforementioned electricity comes from renewable resources such as solar or wind energy and with the perspective of using the produced chemicals not only for their direct use but also as energy carrier. Let us take H_2 as a practical example. Even though the round-trip conversion from power to gas and back might seem less attractive when compared to the storage of electricity directly within batteries, certain applications can benefit more from fuel cells. This can be the case, for example, of the automotive sector. Nowadays, about 16 % of the global greenhouse gas emissions come from the transport sector.[3] Next to battery-based electric vehicles (BEV), fuel cell- based ones (FCEV) are a key technology in order to electrify the transportation system and lower the CO_2 emissions related to it.[4] FCEVs have demonstrated longer driving range and shorter refuelling time when compared to BEVs.[5] Moreover, in order to obtain longer driving ranges, vehicles need to store more energy. For BEVs this is possible by implementing a higher mass of battery, which can considerably increase the weight of the vehicle, whereas FCEVs only need a larger tank, keeping the associated increase in mass low due to the low molecular weight of H_2. This becomes especially attractive when looking at heavy-duty vehicles such as trucks.

Proton exchange membrane fuel cells

There are different types of fuel cells. Depending on type of fuel and operating temperature, they find application in different branches of the energy sector, from stationary to portable usage. Among them, proton exchange membrane fuel cells (PEMFCs) are particularly interesting especially for automotive applications. PEMFCs employ H_2 as fuel and operate at temperatures ~ 80 °C. As shown in Figure 1.1, the hearth of the PEMFCs is the catalyst coated membrane (CCM) or membrane electrode assembly (MEA) which consist of the PEM sandwiched between anode and cathode. The MEA is placed between two gas diffusion layers (GDLs) which provide a homogeneous gas distribution from the flow fields to the anode and cathode and ensure the removal of produced water. At the anode side, the hydrogen oxidation reaction (HOR) takes place and H_2 is split into protons which then travel through the PEM to the cathode side. At the cathode side, the oxygen reduction reaction (ORR) occurs and O_2 is reduced to water, after recombining with protons coming from the anode side. In order to provide sufficient current, both reactions require a catalyst to increase the reaction rate, and Pt-based catalysts are especially active. Due to the fast kinetics of the HOR compared to the ORR, the amount of Pt needed at the anode side is minute, whereas at the cathode side a considerable amount of Pt is required.[6-7]

Figure 1.1: Schematic illustration of the main components of a 5 cm^2 single cell PEMFC. Curtesy of Dr. Björn M. Stühmeier.

1.1 Fe-N-C electrocatalysts

Nowadays, low temperature PEMFCs rely on expensive critical raw materials, e.g. Pt, especially at the cathode side, where the ORR takes place and considerable Pt amounts are required in order to accelerate its sluggish kinetics.[6-7] According to the cost analysis of PEMFC systems for lightweight duty vehicles, the majority of the fuel cell stack cost comes largely from the Pt-based catalyst, especially when further increasing the manufacturing volume.[8] In the perspective of mass commercialization, relying on expensive metals is not a viable option, due to their scarcity and cost. Moreover, even though they possess good activity and stability for practical applications, the price volatility arising from their trading in the stock market is a risk factor that needs to be accounted for. For this reason, a tremendous research effort is currently being made in order to find suitable alternatives.

Platinum-group-metal free (PGM-free) electrocatalysts are being studied not only for the ORR in PEMFCs but for other electrochemical-relevant reactions, including but not limited to CO_2 reduction reaction (CO2RR),[9-12] oxygen evolution reaction (OER),[13-14] hydrogen evolution and oxidation reaction (HER and HOR, respectively).[15-18]

In the family of PGM-free electrocatalyst, a sub-group which is largely investigated is metal- and nitrogen- co-doped carbons (M-N-Cs). The interest of the scientific community for this class of materials arises from the variety of chemical precursors and synthetic methods that can be employed to obtain them as well as from the several chemical and electrochemical reaction that these materials are able to catalyse, proving good activity and stability.[19-20] Moreover, since different metals give rise to different reactivities, the combination of materials and reactions which is possible to investigate is basically unlimited. Atomically dispersed M-N-Cs belong to the family of single atom catalysts (SACs), which have attracted the interest of researchers in heterogeneous/electro catalysis due to their maximization of the atomic efficiency of the metal component.[21-22]

The interest for M-N-Cs started in 1964 when Jasinski discovered that cobalt dibenzotetraazazanulene was able to catalyse the ORR in alkaline medium[23] and later on when Jahnke et al. reported that the activity could be further improved when such molecular precursor was pyrolyzed.[24] Since then, many researchers

tried to bridge the knowledge we have from molecular catalysis to M-N-Cs, in order to explain the different reactivities observed.

M-N-Cs are generally produced via a pyrolytic process at high temperature in order to incorporate the M and N into the carbon scaffold. Due to the ability of carbon to reduce different metals at high temperature (carbothermal reduction), it is challenging to produce atomically dispersed M-N-Cs with high metal loading free from side phases. Even though it might be interesting for some applications to produce composite materials containing more phases, for other applications (e.g., the ORR in PEMFCs) these side phases are generally less active and can even be harmful for the electrochemical device. For this reason, harsh and time-consuming steps are employed to remove the inactive side phases and the active-site density obtainable is limited. This is especially true for Fe-N-C electrocatalysts for the ORR. These catalysts have proven comparable activity in respect to Pt-based materials and are so far the best candidates to replace them in PEMFCs.[25-26]

Nowadays there is a general consensus that the nature of the active sites is atomically dispersed Fe-N_x moieties (x = 2-5, usually 4), recalling the active site observed in molecular macrocycles and enzymes.[27] This is the result of many years of collective scientific effort both on the synthesis and on the spectroscopic side. The nature of the active site in Fe-N-Cs has remained elusive for many years due to limitations arising from their synthesis. Conventional synthetic methods involve mixing and pyrolysis of Fe, N and C precursors. When reaching the temperature of their pyrolytic formation, Fe-N_x sites decompose and the density of active sites that can be achieved is limited. This phenomenon, commonly described as the dilemma of Fe-N-Cs, is due to the carbothermal reduction: the more Fe is employed to increase the active site density, the more carbothermal reduction will be triggered, with formation of Fe(0) side phases at the cost of the active sites. For this reason, synthetic methods have focused on the kinetic stabilization (i.e. immobilization) of Fe atoms in order to avoid agglomeration of the latter into inorganic side phases.

Asset and Atanassov showed the possible Fe species that can be obtained during a conventional synthesis of Fe-N-C materials (Figure 1.2).[28] With this picture in mind, it is clear why the desirable composition of this class of catalysts was debated for decades and why the nature of the active site has been so elusive, since each

different Fe species will contribute differently to any spectroscopic signal. Nevertheless, advances in synthetic methods and spectroscopical investigations have led researchers to the nature of the active Fe-N_4 site.[27] This has been possible especially due to advanced characterization techniques, among which high resolution transmission electron microscopy (HRTEM), Mössbauer spectroscopy and X-ray absorption spectroscopy (XAS) stand out.

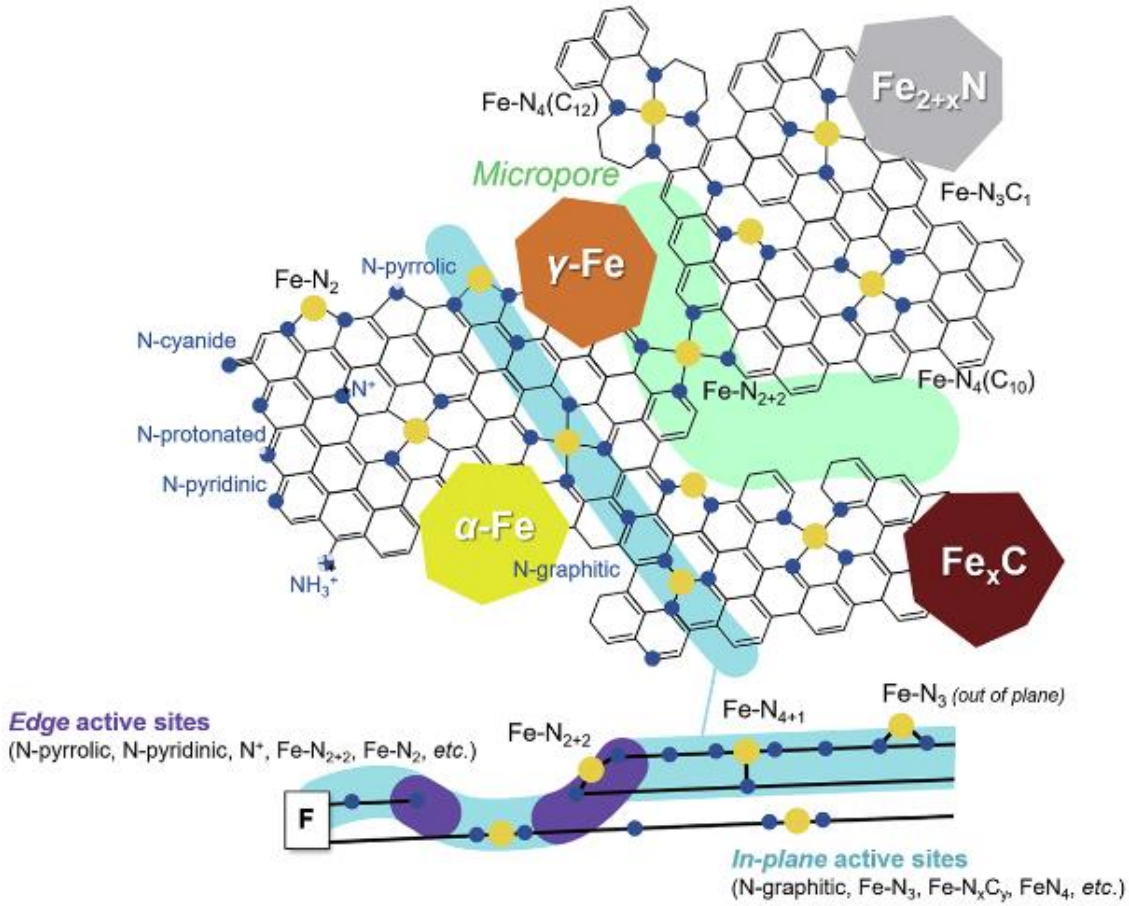

Figure 1.2: Overview of the possible different species present in a Fe-N-C material. Adapted from Ref [28].

Techniques able to identify the active-site environment on an atomic level are extremely valuable. Mössbauer spectroscopy has proven fundamental in the development of Fe-N-C catalysts due to its ability to discern different Fe phases as well as different Fe coordination.[29-33] On the other hand, the low amount of Fe present (usually < 3 wt.%) makes the data acquisition hard (unless the sample is enriched with expensive isotopic labelled ^{57}Fe) and techniques with high sensitivity such as XAS become very valuable. Being bulk techniques, it has been only in combination with advanced synthetic methods able to prevent the presence of side phases in the material that the structure of the active site could be disentangled.

The general understanding gathered from different spectroscopic techniques, aided by theoretical calculations and in combination with in-situ and operando work,[30, 34-36] is that in the catalyst powder the active site consists of Fe-N_4 moieties with or without an additional axial O_2/OH ligand (Fe-N_2, Fe-N_3 and Fe-N_5 have also been reported but are less common). These two different Fe states, namely +III and +II, give rise to the two distinct quadrupole doublets usually observed in Mössbauer spectroscopy, usually labelled as D1 and D2. In terms of type of N binding the Fe atoms (i.e., pyridinic or pyrrolic) and number of C atoms around the Fe-N_4 structure, the exact coordination is still under debate. Planar tetrapyridinic Fe-N_4 sites have been visualized in atomic resolution[37] and a tetrapyridinic macrocycle has been successfully employed as a model structure for Fe-N-Cs.[38] On the other hand, tetrapyrrolic sites have also been reported.[27, 39] Some research groups have attributed the D1 to a tetrapyrrolic Fe(III)N_4C_{12} binding an additional oxy ligand, and D2 to a tetrapyridinic Fe(II)N_4C_{10}[30, 36, 40]. Moreover, D1 has been attributed to the most active and less stable site, whereas D2 corresponds to the site with less activity and more stability.[30] It goes without saying that these two different sites could co-exist in Fe-N-C catalysts. Regardless of the surrounding structure of the Fe-N_4 sites, it is accepted that during operation the Fe is present as Fe(III) at high potential and coordinates an OH axial ligand. When the potential is decreased and the Fe is reduced from +III to +II, the axial OH ligand will desorb, leaving the coordination site available for the ORR.[35]

Even though catalysts with remarkable activity have been synthetised and the understanding of this class of materials have been significantly pushed in the last

decade, the intrinsic limitation of their synthetic method has left the performance of Fe-N-Cs for the ORR stagnant for many years and a quest for new synthetic methods has started.

1.2 ORR mechanism on Fe-N-Cs

Even though the ORR mechanism is well understood on Pt-based catalysts both in acidic and alkaline electrolyte, it remains still not well characterized on Fe-N-C electrocatalysts. In general, the ORR could proceed through an inner- or outer-sphere mechanism.

In acidic electrolyte, the inner-sphere route is generally called into play to explain the reduction of O_2 to H_2O_2 or H_2O, with the oxidative addition of O_2 to the active site (generally accompanied by a concerted proton transfer) proposed as the rate determining step (RDS) for low polarizations.[41-43] One of the main reactivity descriptors is the O_2 binding energy to the metal site, which correlates to the redox potential of the M-N_4 chelate.[42] The central importance of the metal site has been further proven via poisoning experiments, where it has been shown that a large drop in performance is observed when the metal centre is poisoned, pointing out to an inner-sphere mechanism where the M-N_4 (specifically, Fe-N_4) site plays a central role.[44-45] Moreover, if we consider the N-doped carbon scaffold as an "infinite large" ligand, the connection to molecular catalysis is straightforward and correlation between the activity and the electron donor properties of the carbon scaffold have been drawn.[46]

When the pH is varied, differences in ORR mechanism are observed.[47] This can be linked to the differences in the catalyst surface when it is in contact to an alkaline environment compared to an acidic one.[47-48]

In a very alkaline electrolyte (pH > 10.5), the OH^- adsorption on the electrode surface makes the inner Helmholtz plane populated by hydroxyl species and a double layer effect dominant.[47, 49] Moreover, in alkaline electrolyte, the overpotential for the first electron transfer to O_2 molecules to form superoxide radical anions ($O_2^{\bullet-}$) is significantly reduced compared to acidic electrolyte,[50] hence implying that a strong chemisorption to the electron surface is not required.[49] This facilitates the long-range electron transfer in the outer Helmholtz plane, i.e. an outer-sphere electron transfer. Reports in the scientific literature have proposed that in alkaline environment both inner- and outer-sphere mechanism can occur, both independently or in parallel.[43, 46-47, 49] Usually, when an outer-sphere mechanism occurs, it promotes the 2 e^- reduction of O_2 to H_2O_2 (which, due to its

pK_a of 11.69 for the first ionization, would be predominantly HO_2^- at pH > 12[49]). Further reduction to H_2O (or, better, OH^- in alkaline electrolyte) for a total of 4 e^- can happen if the reaction intermediates adsorb to the catalyst surface, hence via an inner-sphere mechanism.[49, 51] The RDS is generally attributed to the first electron transfer to O_2[52] or the first proton transfer to $*O_2^-$ to form *OOH (* indicates that the intermediate is adsorbed on the active site)[41, 53] and kinetic isotope effect studies suggest the occurrence of two parallel pathways, one of which has a proton independent RDS.[43] Finally, Fe poisoning experiments suggest that the active site under acidic and alkaline conditions are intrinsically different, indicating a non-metal-centred active site in alkaline electrolyte, i.e., that Fe might not be directly involved in the ORR mechanism.[45]

All these findings, combined with the high activity of metal free N-doped carbon materials (NDC) in alkaline electrolyte,[54] point to the fact that the N-doped carbon scaffold might play a role way more important in alkaline compared to acidic electrolyte, where it "merely" controls the electron density around the Fe-N_4 sites. For this reason, C and N atoms have also been proposed as adsorption sites for the ORR in alkaline electrolyte via an inner sphere mechanism.

The elucidation of the ORR mechanism on Fe-N-C surfaces is of great importance for the scientific community. Only with a clear picture of the elementary reaction steps and intermediates it is possible to pinpoint the key factors governing the catalyst kinetics. This, together with advancements in synthetic methods set to produce exclusively specific sites, would push the field towards more active and stable catalysts.

1.3 Stability issues of Fe-N-C electrocatalysts

Fe-N-C electrocatalysts have now proved beginning of life performance comparable to the one of Pt-based materials, both in acidic [40, 55-57] and in alkaline[58-59] electrolyte, making them meet the activity requirements for applications.[25] However, their stability during operation is still far from what is necessary for practical system-level usage.[60] The stability displayed by PEMFCs operating with a typical Pt/C cathode catalyst is extremely challenging to reach for most Fe-N-C materials, which have shown significant drops in performance in the initial few hours with the majority of the activity completely lost after ~100 hours of operation.[61-63] Even though some niche applications have been reported, such as a battery pack from Ballard Power System (which employs a Fe-N-C catalyst from Nisshimbo[64]) and, in a recent breakthrough, a Fe-N-C catalyst could show > 300 hours of steady-state operation,[40] these are still small "stability-drops" in an otherwise ocean of instability. In order to target specific stability issues, understanding their degradation mechanisms both on the atomic level and at the macroscale becomes critically important.[65-71]

Nowadays, mainly two mechanisms are identified as detrimental for the stability of Fe-N-C catalysts. These are (i) demetallation[72-73] and (ii) carbon oxidation (chemical and/or electrochemical).[74-75] Other mechanisms, such as micropores flooding and anion adsorption, have been proposed in earlier times but they have been either disproved/repostulated or they are still lacking convincing evidence.[72, 76-77] Besides acting independently from each other, these different mechanisms can occur at the same time. This, together with the synthetic challenge of producing active catalysts free from harmful side phases, is hampering a clear understanding of the degradation process and how to avoid it.

Demetallation has been widely reported in the literature.[72-74, 78] This process suggests that the atomically dispersed Fe inside the N_4 active-site centre loses the coordination with nitrogen atoms (and consequentially with the carbon scaffold), resulting in loss of ORR activity. It has been reported that, after demetallation, Fe atoms could stay coordinated to the ionomer phase[55, 79] and/or precipitate as iron oxide.[30, 80-81] Even though the exact mechanism is not yet understood, with the aid of theoretical calculations, some groups reported N_4-coordinated $Fe(OH)_2$ as a key

intermediate in the demetallation process,[78, 82] whereas others suggested that first the N atoms of the Fe-N_4 sites need to be protonated and only then the O_2-coordinated Fe desorbs from the catalyst.[40] Overall, it is widely accepted that the presence of O_2 (i.e., the ORR itself and not the acidic environment or the applied potential) plays a crucial role in the demetallation process both in acidic[80] and in alkaline electrolyte.[83] Demetallation can also be the consequence of the corrosion of the carbon support, which is triggered by carbon oxidation.[74, 84-85]

Carbon oxidation can occur via a chemical or an electrochemical route. Due to kinetic limitations, the electrochemical carbon oxidation (i.e., carbon corrosion) is usually observed when the potential surpasses ~ 1.3 V and strongly relates to the graphitization degree of the carbon.[74, 84-85] On the other hand, chemical carbon oxidation is caused by reactive oxygen species (ROS) produced during the ORR. It has been shown that these radicals are the main responsible for the carbon oxidation only in acidic electrolyte, since their formation from H_2O_2 is pH dependent.[75, 86] Like for the analogous molecular species,[87] ROS attack could result into carbon corrosion or into the production of oxygen-containing functional groups on the catalyst surface. This carbon functionalization results into lower turnover frequency (TOF) due to a change in the electron donating properties of the carbon scaffold to the Fe-N_4 sites with consequent change in O_2 binding energy.[75]

Lately, several groups have tried to link the observed trend in stability to the different sites that might be present in the catalyst.[30, 40] It has been proposed that the site responsible for the quadrupole doublet D1 in Mössbauer spectroscopy, attributed to a surface exposed tetrapyrrolic Fe(III)N_4C_{12} moiety, is very active but rapidly degrades, leading to Fe demetallation and agglomeration into iron oxide.[30] The site responsible for D2, attributed to a tetrapyridinic Fe(II)N_4C_{10} configuration buried underneath few carbon layers, is on the other hand stable but less active.[30] Even though the assignment of D1 to a tetrapyrrolic site and D2 to a tetrapyridinic one still remains an open question, the stability of an Fe-N-C catalyst could be drastically improved by the deposition of a thin N-doped carbon layer on its surface, with concomitant transformation of a certain percentage of D1 into D2.[40]

Rationally comparing the stability of catalysts with different morphology and number/type of active sites is complicated. Therefore, the degradation rate should

be analysed in terms of change in intrinsic activity values such as TOF and active-side density (SD). For Fe-N-Cs, the assessment of these parameters has been elusive for many years and several methods are currently under investigation.

1.4 Methods for the determination of intrinsic activity metrics

The activity of a catalyst is governed by several factors. Comparing structurally different catalysts is not always meaningful since their activity is overlayed with morphological features.[88] For this reason, it is important to quantify intrinsic activity values which exclude morphological effects, namely active-site density (SD) and TOF.

In the Fe-N-C community, the determination of these parameters has been out of reach for many years and only lately new approaches are being proposed.[89] There are several reasons for this. First of all, the nature of the active site has been debated for long time. This is due to the synthetic limitations of these materials, which generally show the presence of inactive Fe(0) side phases. After scientific advances have cleared the nature of the active site by synthesizing materials free from inactive side phases,[27] the community has started to look for ways to probe it. Due to the similarity between the active Fe-N_4 site and molecular macrocycles, the use of probe molecules that would interact with the metal centre in macrocycles seemed straightforward but it has been hard to implement. Even for catalysts containing exclusively the desired active phase, it has been a herculean task to find probe molecules and methods able to bind specifically the active site. Nowadays two main methods are widely accepted and used by the community. These are (i) nitrite stripping techniques and (ii) CO cryo chemisorption.

The nitrite stripping method has been firstly introduced in 2016[44] and since then it has widely spread.[55-57, 90] It is based on the poisoning of Fe sites by nitrite anions (resulting in NO adsorption) followed by electrochemical stripping of NO into ammonia. Measuring the stripping charge of this five-electrons reaction allows for the SD quantification. This method has the great advance of being an in-situ technique and, since the stripping process happens at potentials below 0.2 V_{RHE}, it is possible to measure ORR activity without removing the probe molecule. Afterwards, the TOF is calculated using equation (1.1):

$$TOF\ (s^{-1}) = \frac{\Delta i_k\ (A\ g^{-1})}{F\ (A\ s\ mol^{-1}) \times SD\ (mol\ g^{-1})} \qquad Equation\ (1.1)$$

where Δi_{kin} is the difference in kinetic current between the unpoisoned and the poisoned state at a certain potential, SD is the site density determined from the NO stripping charge and F is the Faraday constant. One pitfall related to this method is the disproportionation of nitrous acid (formed in acidic conditions) into NO and NO_2. Since these species interfere with the stripping, the method is very sensitive to the concentration of nitrite used and the pH at which the measurement is conducted. This limits the applicability of the nitrite stripping method to pH values ~ 5.7, which is far from relevant pH values for most fuel cell research. Moreover, it was found that the stripping process occurs on iron oxide particles as well, hence the method is restricted to phase pure Fe-N-Cs and to the pristine activity, since iron oxide could form upon degradation.[30, 80] Finally, only a fraction of the active sites is probed and the method is based on the assumption that only a single NO adsorbs on each site. Another assumption is that the reduction of NO is selective towards the 5-electron reduction to ammonia, but a 3-electron reduction to hydroxylamine could also occur.[44, 56, 91] Recently, in order to overcome some of the limitations of the exposure to aqueous nitrite, it has been successfully reported that the electrochemical stripping could be performed on a catalyst poisoned ex-situ with a gaseous NO treatment.[56, 92]

The CO cryo chemisorption has been first introduced in 2015[93] but it took until 2019 to achieve the reliable and accurate evaluation of SD values.[94] This method is based on the ability of $Fe\text{-}N_4$ sites to bind CO molecules at -80 °C followed by a temperature-programmed desorption. The results obtained via this method are extremely sensitive to the pre-treatment of the sample. In order to yield reproducible SD values, temperatures as high as 600 °C are required in order to fully clean the catalyst surface from adsorbates but this could also alter the chemical properties of the catalyst. Another issue is the possibility of the active sites to bind more than one CO molecule and, similarly to O_2 binding in heme-proteins, the change in subsequent CO uptake due to initial poisoning of some active-sites. Moreover, being an ex-situ technique, it is not possible to show that the probed sites are ORR active. Interestingly, this method always overestimates the SD when compared to the nitrite stripping and this effect has been attributed to the fact that CO cryo chemisorption probes sites that are only accessible to the gas phase but not to the liquid electrolyte. In order to overcome their intrinsic limitations, these two

methods are generally used in combination, and this enabled the deconvolution of specific ORR reactivities.[55, 90]

Recently, new methods based on probe molecules have been proposed. Similarly to the nitrite stripping method, cyanide anion poisoning has been used to probe the number of active sites.[95] Although this method could be applied to a variety of M-N-C as well as Pt nanoparticle in a broad pH range (1-13) it has the drawback of employing a toxic molecule, requiring special safety measurements. NO has also been used has probe molecule in chemisorption experiments, similarly to the CO cryo chemisorption.[92] Comparing the results of NO chemisorption experiments and in-situ nitrate stripping allowed for considerations regarding the location of the active sites.

In order to surpass the constraints of employing probe molecules, in 2022 an in-situ method based on the electrochemical response of the catalyst measured via Fourier transform alternating current voltammetry has been introduced.[96] This method, based on the electrochemical reversibility of the active sites, is able to discern Faradaic from non-Faradaic processes and can be used to study electron transfer reactions without the contribution of other electrochemical processes that may occur in parallel. Due to the high capacity currents usually displayed by high surface area carbons, this method is particularly fit to study Fe-N-C electrocatalysts. Moreover, since the method only requires a potentiostat, it has the great advantage to be used in-situ in PEMFCs and it offers the possibility of probing SD during stability measurements.

1.5 Active-site imprinting

Whether it is to better study reaction kinetics and intrinsic activity metrics, to draw structure-performance relations or simply to increase the activity and stability, it is always desirable to have a catalyst free from inactive side phases containing ideally only one type of active site. For Fe-N-Cs, this is particularly hard to achieve. The Fe-N_4 active site decomposes at the pyrolytic temperature required to form the electrically conductive N-doped carbon matrix and the synthesis of Fe-N-Cs usually requires several steps comprising pyrolysis, leaching of soluble side-phases and additional thermal processes.[48, 93] Reducing the mobility of Fe atoms throughout the pyrolysis, for example pyrolyzing Fe-containing zeolitic imidazolate frameworks (ZIFs), is a successful approach but the atomically dispersed Fe content is still limited.[27, 57, 97-98] This kinetic stabilization has to overcome the thermodynamic drive of Fe cations toward the carbothermal reduction (with formation of metallic Fe), which will depend on their chemical environment, concentration and gas atmosphere employed in the pyrolytic step.[99] Being a catalyst for graphitization, metallic Fe is able to dissolve carbon and reprecipitate it. This removes the control over the catalyst morphology, which is essentially destroyed (unless using hard templates, which then need to be removed[100-103]), and over the amount of heteroatoms doping the carbon matrix, since they are lost during the recrystallization event. Last but not least, the inorganic side phases formed (e.g., metallic iron, iron nitride and iron carbide) require extensive and time-consuming acid washing in order to be leached out, since they do not contribute to the catalyst activity and can be harmful during operations (at least in PEMFCs). The intrinsic limitations of Fe-N-Cs synthesis, commonly known as the dilemma of Fe-N-Cs, called for a new method decoupling the formation of the carbon scaffold from the formation of the active site, which should ideally be performed at low temperature.

In 2018, it was shown that Fe-N-C electrocatalysts can be obtained via a low temperature ion-exchange reaction from Mg-N-C containing Mg-N_4 sites.[104] Based on the stability of metal oxides, compared to Fe cations, the reduction of Mg^{2+} is thermodynamically not favoured at temperatures typically chosen for the pyrolytic synthesis.[99] For this reason, during pyrolysis, a high density of Mg-N_4 sites can be obtained within the carbon matrix, without forming side phases. Similarly to the

way transmetalation reactions are carried out in molecular chemistry, a low temperature wet-chemical ion-exchange reaction (i.e., a Mg-to-Fe transmetalation) was performed, employing a methanol-based solution of $FeCl_2$. Since the transmetalation is carried out at ~ 80 °C, the carbothermal reaction of Fe can be avoided. The Fe-N-Cs obtained via this newly developed synthetic method, called active-site imprinting, are equivalent in active-site coordination and activity to those obtained via the synthetic methods involving direct pyrolysis of Fe-containing precursors. For the first time, it was shown that high temperatures are not required in order to form the desired Fe-N_4 sites, actively decoupling the pyrolytic synthesis of the carbon scaffold from the active-site formation. It was the first step towards finally solve the dilemma. Upon optimization, this method holds the potential to surpass the limitations of previous synthetic procedures due to the higher active-site density that can be achieved. Moreover, several metals could be used as imprinters to obtained different N_x-type coordination otherwise impossible to achieve when directly employing Fe (which is then retained upon transmetalation) and metals other than Fe can be used in the ion-exchange reaction, yielding several different M-N-Cs.

This thesis work is collocated in the context of the active-site imprinting method but focusing on Zn as active-site imprinter. Following the synthetic work presented in this thesis,[105-106] new Fe-N-C catalysts have been developed via the Zn-to-Fe transmetalation reaction of ZIF-based Zn-N-Cs. So far, these works represent the Fe-N-Cs with the highest SD, utilization and activity reported in the literature.[55-56]

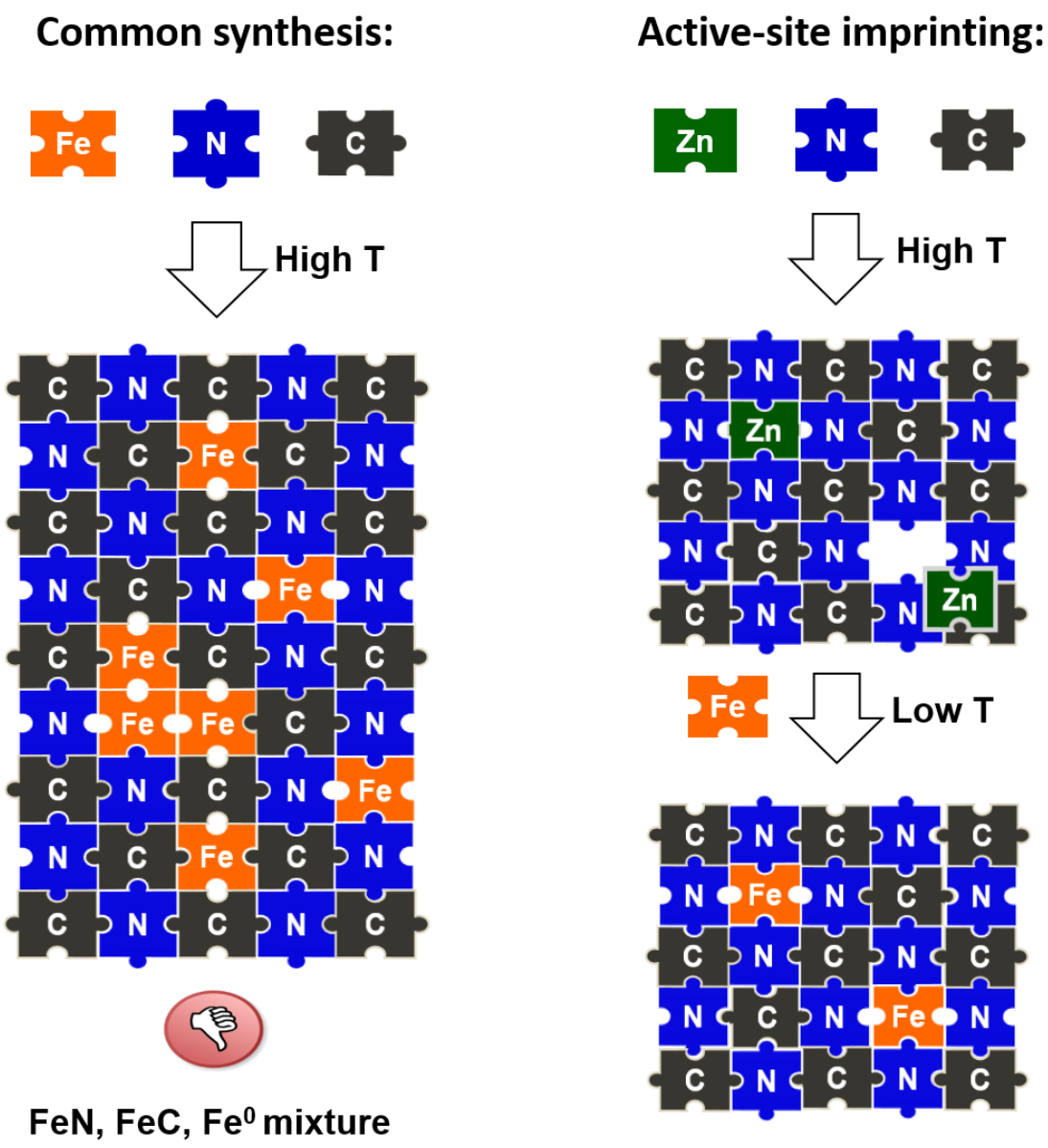

Figure 1.3: Cartoon illustrating the metastability of Fe-N_4 sites during their pyrolytic formation (left) and the synthetic approach of the Zn-based active-site imprinting and transmetalation towards Fe-N-Cs (right).

1.6 Thesis outline

The aim of this thesis work is to develop the active-site imprinting method using for the first time Zn as imprinting metal. The choice of using Zn derives from the numerous and established processes which involve the use of $ZnCl_2$ in the carbon industry (i.e., chemical activation),[107-108] which gives the chance to scale-up the proposed synthetic methods. Moreover, ZIF-based carbons have been extensively used in the catalysis community,[27, 109-111] and the discoveries of this thesis work could be easily applied to those and other Zn-based N-doped carbon materials.

In the first part of this thesis work, a series of tailor-made carbon materials is synthetised employing a salt-templating strategy.[112-113] This synthetic method allows for high yields and controlled morphology and, at the same time, using $ZnCl_2$-based salt mixtures, for the formation of the desired Zn-N_4 moieties. Compared to hard templating strategies, the salt templating avoids the use of hazardous chemicals for the removal of the template and, since the salt mixture could be recovered and reused, it presents a more sustainable pathway for the synthesis.[114] Moreover, when Fe cations are employed during the synthesis, the conditions need to be extremely controlled to avoid their carbothermal reduction, whereas the higher thermodynamic stability of Zn^{2+} gives more freedom during the pyrolysis, with the chance to shift the synthetic focus more on the carbon morphology. The Zn-to-Fe ion-exchange reaction is studied in details employing different Fe precursors and cutting-edge techniques such as identical location atomic resolution transmission electron microscopy imaging (IL-TEM) and in situ electrochemical flow cell coupled to inductively coupled plasma mass spectrometry measurements (EFC–ICP-MS). Advanced spectroscopic techniques, such as XAS and Mössbauer spectroscopy, are employed to investigate the nature of the M-N_4 coordination, which preserves its structure upon Zn-to-Fe transmetalation. The final Fe-N-C catalyst obtained presents a well-defined tetrapyrrolic Fe-N_4 single site and it is shown that the active-site formation is conservative towards the catalyst morphology.

In the second part of this thesis work, the aforementioned synthesis is successfully transferred to different precursors, showing the versatility of the active-site imprinting method employing Zn as N_4-imprinter. Moreover, the single-site nature

of the obtained catalysts and the possibility to exchange the central M atom (employing different metals as well as protons, i.e. in a metal extraction reaction) keeping the morphology unchanged, creates the ideal platform to systematically investigate specific properties of the catalyst. This allows for the facile quantification of SD and TOF of ORR active tetrapyrrolic M-N_4 sites as well as pyrrolic N sites both in acidic and alkaline electrolyte and for the elucidation of the ORR reaction mechanism.

In the third and final part of this thesis work, the stability of the well-defined tetrapyrrolic Fe-N_4 single site is investigated both as storage stability (i.e., stability over time of the powder material upon air exposure) as well as stability under realistic PEMFC conditions (i.e., electrochemical stability of the material upon operation). The understanding of the degradation of the active sites during their shelf life is extremely important in order to prevent it and assure the long-time storage required for big scale production and application. Moreover, if this degradation is not taken into account, contradicting results can arise when characterizing materials over a long period of time. After tracking the change in activity as well as morphological and active-site modifications over a period of time of ~ one year, a recovery procedure is successfully employed. Finally, in-situ XAS is used to monitor the degradation of the active sites in an O_2-fed cathode of a PEMFC at 80 °C and two different mechanisms are identified depending on the oxidation state of the Fe. New fundamental understandings are therefore brought to the scientific community.

2 Experimental Methods

Details on the experimental procedures specific to each topic can be found in the respective publications in chapter 3. This section will give additional information about the experimental details with emphasis on details that could not be discussed in the respective publications. This is to ensure the quality and reproducibility, especially regarding the synthesis of the novel catalyst materials.

2.1 Preparation of novel catalyst materials

Preparation of Zn-N-C materials

- *Salt-templating-based samples*: In this section, the synthetic strategies employing the salt templating approach is presented. In a typical synthesis, a certain amount of the carbon and nitrogen precursor (e.g. phthalonitrile or emim-dca) is mixed with the corresponding $ZnCl_2$-based salt mixture (e.g. $ZnCl_2$/LiCl or $ZnCl_2$/NaCl) inside an Ar-filled glovebox. It is important to thoroughly mix the components in an agate mortar. The mixture is then transferred inside a non-porous alumina crucible and covered with a quartz lid to diminish evaporation of the salt. The mixture is then transferred inside a tube furnace minimizing its exposure to air and subjected to the respective heat treatment to a certain temperature and heat rate, always employing Ar 5.0 as gas. The sample is then let to naturally cool at room temperature and collected. After crushing it in an agate mortar, it is washed in 0.1 M HCl for several hours, filtered, washed with deionized water until neutral pH is reached and dried at 80 °C overnight.

- *Carbon-support based samples*: The carbon-support based synthesis resembles the one based on salt templating in regards of handling of the chemicals, heat treatment and post-synthetic work up. The main difference

is that instead of a carbon and nitrogen precursor mixed with a salt mixture, in this synthesis a carbon support is used (e.g. Ketjenblack®). In order to build the Zn-N_4 sites, $ZnCl_2$ is employed as Zn source and an ionic liquid (e.g. emim-dca) is employed as N source. The amount of ionic liquid used to impregnate the carbon support is based on the pore volume of the latter.

Low temperature transmetalation

In reference [105], we demonstrated that during the low temperature transmetalation a higher Fe content, and hence a higher activity, could be achieved when using a $FeCl_3$/LiCl eutectic mixture instead of $FeCl_2$ dissolved in MeOH. Moreover, it is noted that the Fe oxidation state and coordination environment in the Fe-N-C materials is independent from the transmetalation method employed. For this reason, only the low temperature transmetalation employing $FeCl_3$/LiCl eutectic is described here, which is the procedure utilized for all the materials reported in this thesis, except for the ones in ref [105] where both procedures have been employed. Details about the low temperature transmetalation can be found elsewhere.[104]

In a typical transmetalation procedure, the Zn-N-C material is firstly degassed in a Büchi oven at 250 °C under vacuum for at least 10 hours and afterwards introduced into an Ar-filled glovebox. The $FeCl_3$/LiCl eutectic mixture is also stored inside the Ar-filled glovebox and premixed in advance ($FeCl_3$ to LiCl ratio is 4.13 in mass). The amount of eutectic mixture employed for the transmetalation procedure depends on the sample amount and total pore volume. If the salt mixture is not able to completely fill the pores and is confined inside the sample, a proper stirring will not be possible. For this reason, it is suggested to use the salt mixture in excess, so that the sample would be able to be stirred into the liquid salt mixture.

After introducing the sample and the Zn-N-C material into a closed flask, the heating can be done outside the glovebox. Due to the low vapor pressure of the eutectic mixture, it is not necessary to have an outlet for the overpressure, even though a connection to a Schlenk-line filled with inert gas is recommended. The mixture is then heated up to 170 °C to ensure proper melting of the salts (T_m = 150 °C) and stirred for 5 hours. It is noted that for the sample reported in ref [105] and [106], no difference in performance has been observed when varying the transmetalation time between 1 and 24 hours and for temperatures up to 200 °C.

When the transmetalation reaction is concluded, the sample is let to cool down at room temperature and water is added to the mixture in order to remove the salts. After filtration, the sample is stirred in 0.1 M HCl for at least 24 hours. At this stage, it is possible to control the amount of the Fe in the sample performing the washing with 1 M HCl at 85 °C. This procedure is not able to completely dissolve the Fe(III) oxide observed after low temperature transmetalation, but the total Fe content is generally lower. An optimum Fe to N ratio in the sample is important during the following high temperature transmetalation in order to coordinate the Fe to the N_4 pockets and avoid formation of metallic Fe(0). Finally, the sample is filtered, washed with H_2O until neutral pH is reached and dried at 80 °C overnight.

High temperature transmetalation

For the high temperature transmetalation, a certain amount of Fe-N-C was placed in an alumina crucible. This procedure could be scaled up from few mg of sample to the gram scale without any influence on the final performance. The crucible was then pushed inside a tube furnace pre-heated at the desired temperature under Ar atmosphere. In order to completely decompose the Fe(III) oxide phase, a minimum temperature of 700 °C was required. No differences were observed when performing the high temperature transmetalation between 700 and 1000 °C. TGA-MS results showed that when performing the high temperature transmetalation at 1000 °C, it was possible that some FeN_4 sites can be destroyed. If the N content of the sample is high enough this is not a problem but temperature and time become crucial in case the Fe to N ratio is not optimal and some Fe(0) could form. For this reason, a temperature of 800 °C is advised. After 20 minutes the furnace was turned off and opened to quickly cool down the sample to room temperature. No further treatment was applied to the sample.

Metal extraction

For the M-to-H^+ ion exchange (i.e., M extraction), the M-N-C was placed inside a closed Carius tube and stirred for a certain amount of time in 2.4 M HCl at a certain temperature. The amount of time and the temperature employed will have a big impact on the total amount of M removed, but would also depend on the type of M. For a complete removal of Zn, temperatures up to 160 °C have been employed for at least 24 h, repeating the procedure 2 times. For partial Fe extraction, the

temperature employed was 100 °C for 6 days. After filtering and thoroughly washing with deionized water until neutral pH was achieved, the final sample was obtained.

2.2 Electrochemical techniques

Rotating (Ring) Disk Electrode measurements

R(R)DE measurements were carried out in a three-electrode glass cell when employing acidic electrolyte and in a Teflon® cell when employing alkaline electrolyte to avoid glass dissolution. Prior to their first use, the cells were soaked in a mixture of sulfuric acid and hydrogen peroxide solution overnight in order to clean off all the possible organic residues and boiled several times in deionized ultrapure water (Milli-Q Integral 5, 18.2 MΩ cm). The cells were stored in a closed container under deionized ultrapure water and boiled at least two times prior to each use. 0.1 M $HClO_4$ was prepared from a 60% solution (Guaranteed Reagent, Kanto Chemical) and deionized ultrapure water (Milli-Q Integral 5, 18.2 MΩ cm) and 0.1 M NaOH was prepared from monohydrate NaOH pellets (99.996 %, Alfa Aesar) and deionized ultrapure water. An Autolab PGSTAT302N (Metrohm) potentiostat was employed for the measurements. For acidic measurements, a freshly calibrated RHE was used as the reference electrode and an Au wire as the counter electrode. For alkaline measurements, saturated Ag/AgCl was employed as reference electrode and a Pt wire as counter. The solution resistance was determined by electrochemical impedance spectroscopy and the reported potentials were corrected accordingly. The ORR polarization curves were corrected for capacitive contributions by subtracting the curves recorded in Ar-saturated electrolyte from the ones recorded in O_2-saturated electrolyte. The catalyst inks were prepared dispersing a certain amount of catalyst powder in either *N*,*N*-dimethylformamide or a mixture of isopropanol and water, followed by sonication for 30 minutes. Afterward, an aliquot of Nafion® suspension was added and the ink was sonicated for 10 more minutes. Subsequently, the amount of ink required to reach the desired loading was drop-cast onto a well-polished glassy carbon electrode (diameter = 5 mm, obtained from Pine Research Instrumentation) and dried under an infrared lamp for at least 60 minutes. For more details the reader is invited to refer to the specific publications.

Proton Exchange Membrane Fuel Cell measurements

All the PEMFC measurements were conducted in a 5 cm^2 single cell. Measurements in section 3.1.2 were conducted on an automated fuel cell test stations (G60,

Greenlight Innovations, Canada) whereas measurements in section 3.3.2 were conducted in a portable, semi-automated fuel cell test station (Fuel Cell Technologies, USA) with a special cell hardware designed to allow XAS measurements.[115]

MEAs were produced by the decal transfer method. Catalyst inks were prepared by dispersing the catalyst powder in a mixture of water, 1-propanol, and ionomer solution. The ink was coated onto PTFE substrates (50 µm) by applying a bar-coating technique. The anode electrodes were prepared analogously, but using a 20 wt% Pt/C catalyst (TKK) with a final Pt loading of 0.1 mg/cm^2 and an I/C ratio of 0.65 g/g. Through a hot-pressing-based decal procedure (130-160^{o}C with applied pressure 2.2 kN for 12 min), the catalyst layers (both anode and cathode) were directly transferred onto the membrane and subsequently the PTFE substrates were peeled off, yielding the final MEAs. For more details the reader is invited to refer to the specific publications.

In-situ Electrochemical Flow Cell coupled to Inductively Coupled Plasma Mass Spectrometry

The EFC-ICP-MS were conducted in collaboration with Léonard Moriau and Martin Šala at the National Institute of Chemistry in Ljubljana. The details of the coupling of the EFC with ICP-MS can be found in details in other publications.[116-117] Briefly, the electrochemical flow cell is coupled with an ICP-MS instrument (Agilent 7900, Agilent Technologies, Santa Clara, CA). Upstream the EFC, a diagonal 4-way flow valve is used to switch between different solutions. It is important to keep a constant flow of the solutions and for this reason syringe pumps (WPI sp100i and Harvard apparatus 11 plus) were used to pump the appropriate solution at a constant flow of 400 µL min^{-1}. The working and counter electrodes are both made of glassy carbon in order to avoid contaminations, while the reference electrode is an Ag/AgCl electrode (BASi), which is calibrated prior to the flow experiments in a separate cell versus a Pt electrode in H_2-saturated 0.1 M $HClO_4$. It is very important to adjust the orientation of working and counter electrode so that the inlet of the electrolyte flow is at the counter and the outlet is at the working electrode to avoid any redeposition. The electrochemical control is established with a potentiostat (CompactStat.e, Ivium technology). In order to keep the catalyst layer well attached

to the working electrode, after drop casting the well-dispersed suspension of the catalyst and evaporation of the solvent, a Teflon® suspension was drop cast on the catalyst layer.

2.3 Further methods

N_2-sorption porosimetry

N_2-sorption measurements were carried out using a Quantachrome Autosorb iQ2 instrument. Prior to the measurements, the samples were outgassed at 250 °C under vacuum for at least 10 hours. Specific surface areas were determined according to Brunauer–Emmett–Teller (BET) theory using the Micropore BET Assistant supplied by Quantachrome ASiQwin software. Pore size distributions were calculated from the absorption branch of the isotherm with the quenched-solid density functional theory (QSDFT) method, selecting the appropriate pore shapes depending on the different materials.

Mössbauer spectroscopy

The Mössbauer spectroscopy measurements were conducted in cooperation with Prof. Friedrich E. Wagner from the Physics Department at TUM. Spectra were recorded with a sinusoidal velocity waveform at room temperature and at 4.2 K on powder samples enclosed in lucite holders. When exposure to air wanted to be excluded, the sample was stored in an Ar-filled vial and the holder was filled under N_2 gas. For the low-temperature measurements, both the absorber and the ^{57}Co in rhodium source were cooled in a liquid helium bath cryostat. Isomer shifts were measured with respect to the source having the same temperature as the absorber. In order to refer the shifts to α-Fe at room temperature, 0.115 mm s^{-1} was added to the shifts measured at room temperature and 0.245 mm s^{-1} to those measured at 4.2 K. The spectra were fitted with Lorentzian lines grouped into electric quadrupole doublets and sextets arising from magnetic hyperfine splitting.

X-ray absorption spectroscopy

XAS data were recorded at different sources. The data in section 3.1.1 were collected at the soft X-ray analytics facility WERA of the Institut für Festkörperphysik at the Karlsruhe synchrotron ANKA, Germany, with the help of Dr. Stefan Schuppler and Dr. Peter Nagel. Data in section 3.1.2 were measured in cooperation with Prof. Iztok Arčon at the XAFS beamline of the ELETTRA synchrotron radiation facility in Trieste, Italy. For the measurements presented in section 3.2, data were collected in cooperation with Dr. Ana Guilherme Buzanich at

the BAMline located at BESSY-II (Berlin, Germany), operated by the Helmholtz-Zentrum Berlin für Materialien und Energie. The in-situ XAS measurements presented in section 3.3.2 have been conducted in cooperation with Dr. Olivier Proux at the European Synchrotron Radiation Facility (Grenoble, France) on the beamline FAME (BM30). For more details the reader is invited to refer to the specific publications.

Thermogravimetric analysis coupled with mass spectrometry

TGA-MS was performed on a Mettler Toledo TGA/DSC 1 instrument connected to a Pfeiffer Vacuum Thermostar mass spectrometer in Ar atmosphere. The employed heating rate was 10 K min^{-1}. Two isothermal steps (150 °C and 250 °C for 20 and 45 minutes, respectively) were performed in order to ensure the complete outgas of the samples prior to heating at higher temperature.

Electron microscopy

SEM images shown in section 3.1.1 were taken using a field-emission FE-SEM Zeiss Ultra Plus microscope, whereas samples in section 3.2.1 were characterized using a JEOL JSM-IT200 equipped with a EDX detector. TEM analyses were carried out in cooperation with Dr. Francisco Ruiz-Zepeda at the National Institute of Chemistry (Ljubljana, Slovenia) in an atomic resolution aberration corrected scanning transmission electron microscope JEOL ARM 200CF. The imaging was performed with a beam current of ~14 pA and at an accelerating voltage of 80 kV. Sample preparation was carried out by diluting the sample powder in ethanol and drop-casting the solution on lacey carbon support Au grids. For the IL-TEM experiment, the sample was firstly imaged and afterwards the grid was attached to an RDE electrode with extreme care. The electrode was stirred in a solution of $FeCl_2$ in 0.1 M $HClO_4$ for several hours and afterwards washed with fresh 0.1 M $HClO_4$ again for several hours. After washing with water and drying, the grid was placed again in the TEM microscope and the same portions of the catalysts were imaged again.

X-ray photoelectron spectroscopy

XPS measurements were carried out with a Kratos Axis Supra spectrometer (Kratos, UK) with monochromatized Al K_α radiation (1486.6 eV). Samples were either prepared by dispersing the powder in an isopropanol and water mixture

followed by drop-casting on Cu tape or via pressing the catalyst powder directly into pellets. Spectra were corrected with respect to C 1s peak at 284.7 eV. Data analysis was performed with ESCAA software.

Density Functional Theory calculations

DFT calculations were performed in cooperation with Jian Liang Low and Prof. Beate Paulus from the Freie Universität Berlin. Jian Liang Low provided the calculations shown throughout this thesis. For more details the reader is invited to refer to the specific publications.

3 Results

This section contains the journal articles comprising this PhD thesis and the manuscripts which are currently under review or will be submitted soon. Firstly, a new synthetic method based on the active-site imprinting is presented in section 3.1. This synthetic method allows for high yields, controlled morphology and high metal loadings. After intensively studying the Zn-to-Fe ion-exchange reaction and following the active-site imprinting approach, the publication presented in section 3.1.2 surpasses the limitations encountered in the previous research and well-defined tetrapyrrolic Fe-N_4 single sites are obtained, surpassing the so-called dilemma of Fe-N-C catalysts and gaining a general understanding on the formation mechanism of Fe-N-Cs. The aforementioned synthesis is then successfully transferred to different precursors, showing the versatility of the active-site imprinting method employing Zn as N_4-imprinter, and the results are presented in section 3.2. In section 3.2.1, the single-site nature of the obtained catalysts and the possibility to exchange the central M atom with protons (i.e., metal extraction) is exploit to quantify intrinsic activity parameters, such as TOF and SD, in a facile fashion in acidic electrolyte. In section 3.2.2, this method is extended to alkaline electrolyte and by comparing the activity of isomorphic M-N-Cs with different type and loading of the metal centre, new insights into the ORR reaction mechanism are deduced. Moreover, for the first time, the TOF for the ORR of pyrrolic N atoms is calculated. Lastly, the stability of the well-defined tetrapyrrolic Fe-N_4 single site is investigated in section 3.3. In section 3.3.1 the storage stability (i.e., its shelf life) of the catalyst is targeted. Mössbauer spectroscopy is used to monitor the evolution of the quadrupole doublets D1 and D2 (and hence of the active site) from the moment of their formation to ~ one year of air exposure. In section 3.3.2 the stability under

realistic PEMFC conditions (i.e., electrochemical stability of the material upon operation) is studied via in-situ XAS experiments.

3.1 Development of new catalyst concepts

In this section, novel catalyst concepts based on the active-site imprinting will be presented. The overlying target is to address the synthetic limitations of Fe-N-C materials discussed in section 1.1. The first publication presents a novel way of synthetizing Fe-N-Cs using Zn^{2+} during pyrolysis to imprint the desired N_4 sites which enables the subsequent Zn-to-Fe ion exchange and thus the formation of Fe-N_4 sites at low temperature. Then, this unique synthetic strategy is improved to obtain a catalyst containing exclusively tetrapyrrolic Fe-N_4 sites in record-high amount.

3.1.1 Active-Site Imprinting: Preparation of Fe–N–C Catalysts from Zinc Ion–Templated Ionothermal Nitrogen-Doped Carbons

The article "Active-Site Imprinting: Preparation of Fe–N–C Catalysts from Zinc Ion–Templated Ionothermal Nitrogen-Doped Carbons", was submitted in July 2019 and published in the peer-reviewed journal *Advanced Energy Materials* in September 2019. The permanent web-link to the article is https://onlinelibrary.wiley.com/doi/full/10.1002/aenm.201902412.

In this publication, a new method for the synthesis of Fe-N-C electrocatalysts with high metal loadings is presented. The desired Fe-N_4 sites are metastable at the high temperatures that are usually employed for their synthesis and high metal loadings (~ 3 wt. %) are usually out of reach. By employing Zn^{2+} ions in a pyrolytic template ion reaction, it is shown that the Zn-N-Cs materials comprising Zn-N_4 as well as metal free N_4 sites can be obtained with a controlled morphology. These materials can be used for the coordination at low temperature of Fe^{2+} and Fe^{3+} ions to form atomically dispersed Fe-N-Cs with loadings as high as 3.12 wt.%, effectively decoupling the pyrolytic step needed to form the nitrogen-doped carbon scaffold from the formation of the active site. Mössbauer spectroscopy is employed to show that the Fe oxidation state in the final catalysts is independent from the oxidation state of the Fe precursor employed in the transmetalation process, but is rather controlled by the carbon scaffold, which acts as a solid-state ligand. Moreover, in

situ EFC–ICP-MS measurements are employed to directly prove the concept of the active-site imprinting method, showing that a metalation reaction does not take place on a nitrogen doped carbon with a random distribution of N atoms but it is possible only when an imprinting metal (in this case Zn^{2+}) is employed to form the desired N_4 pocket. The Zn-to-Fe ion exchange is also visualized via IL-TEM imaging. Finally, the ORR activity and stability of the catalysts synthetized with this newly developed method is screened in acidic electrolyte employing an RDE setup.

Author contributions

D.M. and T.-P.F. planned and designed the experiments. D.M. synthesized and characterized the catalyst and performed the RDE experiments. F.R.-Z. performed the TEM imaging. D.M., L.M. and M.S. worked on the EFC-ICP-MS measurements. F.E.W. performed and analyzed the Mössbauer spectroscopy measurements. B.K. measured and analyzed the XPS data. D.M. and M.B. performed the SEM imaging. U.P., N.H. and M.G. contributed to the manuscript. D.M. and T.-P.F. wrote the manuscript. All authors discussed the results and commented on the manuscript.

ADVANCED ENERGY MATERIALS
www.advenergymat.de

Active-Site Imprinting: Preparation of Fe–N–C Catalysts from Zinc Ion–Templated Ionothermal Nitrogen-Doped Carbons

*Davide Menga, Francisco Ruiz-Zepeda, Léonard Moriau, Martin Šala, Friedrich Wagner, Burak Koyutürk, Marjan Bele, Urša Petek, Nejc Hodnik, Miran Gaberšček, and Tim-Patrick Fellinger**

Atomically dispersed Fe–N–C catalysts are considered the most promising precious-metal-free alternative to state-of-the-art Pt-based oxygen reduction electrocatalysts for proton-exchange membrane fuel cells. The exceptional progress in the field of research in the last ≈30 years is currently limited by the moderate active site density that can be obtained. Behind this stands the dilemma of metastability of the desired FeN_4 sites at the high temperatures that are believed to be a requirement for their formation. It is herein shown that Zn^{2+} ions can be utilized in the novel concept of active-site imprinting based on a pyrolytic template ion reaction throughout the formation of nitrogen-doped carbons. As obtained atomically dispersed Zn–N–Cs comprising ZnN_4 sites as well as metal-free N_4 sites can be utilized for the coordination of Fe^{2+} and Fe^{3+} ions to form atomically dispersed Fe–N–C with Fe loadings as high as 3.12 wt%. The Fe–N–Cs are active electocatalysts for the oxygen reduction reaction in acidic media with an onset potential of E_0 = 0.85 V versus RHE in 0.1 M $HClO_4$. Identical location atomic resolution transmission electron microscopy imaging, as well as in situ electrochemical flow cell coupled to inductively coupled plasma mass spectrometry measurements, is employed to directly prove the concept of the active-site imprinting approach.

1. Introduction

Our planet is currently facing many environmental issues such as abuse of resources and vast emissions of climate-active gases. In order to move toward a more green society, electrochemical systems are promising alternatives for coal-based devices, especially in the automotive field, where sales of light electric vehicles (battery electric vehicles and plug-in hybrid electric vehicles) are politically pushed and increasing exponentially.[1] Vehicles based on proton-exchange-membrane fuel cells (PEMFCs) have the potential to surpass the limitations of battery-based ones, especially, regarding the driving range. Unfortunately, the mass commercialization of this technology is hampered by the limited availability and high cost of Pt, which is required to speed up the anodic and cathodic reactions happening in a PEMFC.[2,3] Since ≈4 times more Pt is required on the cathode than at the anode side, the development of cathode materials containing low Pt amount is a promising way to reduce costs. Unfortunately, low-Pt cathode materials suffer from other limitations, such as losses due to mass transport;[4] also, when the Pt content is reduced below 100 μg cm^{-2}, the cost of other components rises.[3] For these reasons, completely replacing the Pt at the cathode side is a reasonable and promising way to go.

In the last 10 years, platinum-group-metal-free (PGM-free) catalysts for the oxygen reduction reaction (ORR) have drawn the attention of many research groups all over the world. Since it has been shown that bioinspired metal-nitrogen-doped-carbon (M–N–C, M = Fe, Co) catalysts could meet the requirements for

D. Menga, B. Koyutürk, Dr. T.-P. Fellinger
Chair of Technical Electrochemistry
Department of Chemistry and Catalysis Research Center
Technische Universität München
Lichtenbergstraße 4, 85748 Garching, Germany
E-mail: Tim.Fellinger@tum.de
Dr. F. Ruiz-Zepeda, Dr. M. Bele, Dr. U. Petek, Prof. M. Gaberšček
Department of Materials Chemistry
National Institute of Chemistry
Hajdrihova 19, 1000 Ljubljana, Slovenia
The ORCID identification number(s) for the author(s) of this article can be found under https://doi.org/10.1002/aenm.201902412.
L. Moriau, Prof. N. Hodnik
Department of Catalysis and Chemical Reaction Engineering
National Institute of Chemistry
Hajdrihova 19, 1000 Ljubljana, Slovenia
Dr. M. Šala
Department of Analytical Chemistry
National Institute of Chemistry
Hajdrihova 19, 1000 Ljubljana, Slovenia
Prof. F. Wagner
Department of Physics
Technische Universität München
James-Franck-Str. 1, 85748 Garching, Germany

DOI: 10.1002/aenm.201902412

real application in PEMFCs,[5–7] the number of publications on this topic has grown considerably and even commercialization of a PGM-free cathode-based fuel cell was recently reported.[8]

State-of-the-art synthetic protocols involve the mixing of Fe, N, and C precursors followed by pyrolysis. Despite the impressively optimized catalyst preparation, leading to very active catalysts, the procedure is intrinsically limited, since the desired atomically dispersed FeN_4 sites are metastable in the temperature range of their thermochemical formation. This dilemma limits the concentration of FeN_4 active sites, since higher iron precursor concentrations trigger the condensation of iron atoms that are produced by carbothermal reduction. Accompanied by support degradation,[9] eventually nanoparticles of elemental iron, iron carbide, and iron nitride are formed, which have been shown to be poorly ORR active compared to FeN_4 moieties (**Scheme 1**A).[10,11] For this reason, multiple processing steps are required to prepare phase pure catalysts containing FeN_4 sites only. Although the challenge of scalability is not always taken in account, some recent approaches to limit the ion mobility show very promising results; however, since all pyrolytic approaches are based on kinetic stabilization only, the active site density is usually pretty low, with Fe contents typically not exceeding 3 wt%.[12–14]

In more than 30 years of research, no successful preparation of ORR-active Fe–N–Cs was reported based on the coordination of iron to metal-free nitrogen-doped carbons (NDCs). Obviously, the likelihood of randomly occurring N_4 coordination sites is very low, so that Fe ions will, normally, only be loosely bound to the NDC surface (Scheme 1B). Recently, our group was able to decouple the synthesis of the carbon scaffold, acting as a solid-state ligand, from the formation of the active sites using a newly developed strategy involving Mg^{2+} as an imprinting metal ion throughout carbonization, analogous to the template ion reaction used in the preparation of macrocycles.[15] The preparation of highly porous Mg–N–C was followed by a low-temperature wet-chemical coordination step to form square-planar FeN_4 sites by either metalation (Equation (1)), transmetalation (Equation (2)), or both.[16] By which reaction the active sites are generated remains an open question to the scientific community.

$$Fe^{2+} + \text{“}N_4\text{”} \rightarrow \text{“}Fe^{II}N_4\text{”} \quad (1)$$

$$Fe^{2+} + \text{“}Mg^{II}N_4\text{”} \rightarrow \text{“}Fe^{II}N_4\text{”} + Mg^{2+} \quad (2)$$

At temperatures typically chosen for the pyrolytic synthesis, the reduction of Mg^{2+} is thermodynamically not favored; hence, this method has a great potential to increase the active sites' density by avoiding thermally induced side reactions.

The inspiration for the research on Fe–N–C materials lies in the oxygen-binding property of the FeN_4 motif in the naturally abundant heme molecule. Already in 1938, Cook described the activity of iron phthalocyanine (FePc), a synthetic analog

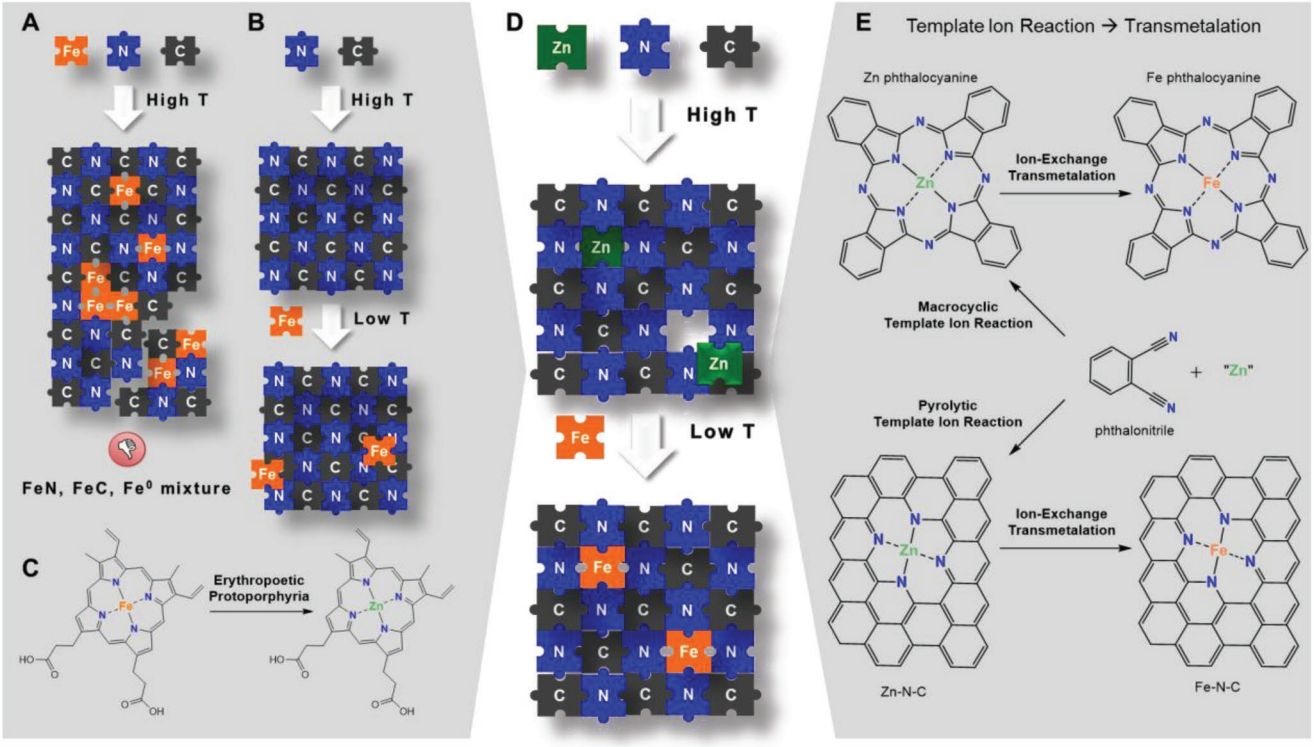

Scheme 1. Cartoon illustrating A) the dilemma of metastability of FeN_4 sites at pyrolytic conditions, and B) the unlikelihood to form FeN_4 sites by Fe ion coordination to metal-free NDCs. C) The natural abundance of Zn coordinated N_4 macrocycles (protoporphyrin) is exemplified by the physiological condition of the erythropoetic protoporphyria disease. D) The synthetic approach of active-site imprinting using Zn as imprinting metal and transmetalation toward Fe–N–Cs. E) The conceptual analogy between the synthesis of Fe phthalocyanine via template-ion-assisted formation of Zn phthalocyanine followed by transmetalation and the herein presented synthetic solid-state chemistry approach.

of heme, toward the catalytic decomposition of H_2O_2 and later in the 1960s, Jasinski was able to show that different metal phthalocyanines were able to electrochemically catalyze the ORR in a fuel cell cathode.[17,18] A famous biomolecule that has the isostructural porphyrin motif of heme is chlorophyll, with the difference that the central metal ion, in this case, is Mg^{2+}. Coordination of Mg^{2+} leads to the color shift from red to green, ultimately allowing for efficient light harvesting in photosynthesis.[19] In this regard, the aforementioned potential for Mg^{2+} to direct the formation of MgN_4 does not come with a surprise.

Interestingly, modifications of both, heme and FePc, with Fe^{2+} being substituted by Zn^{2+} also exist, which suggests the possibility of realizing ZnN_4 sites embedded into carbon supports, which are isostructural to FeN_4 in Fe–N–Cs. An example of these modifications is found in case of iron deficiency or for people suffering from the "erythropoetic protoporphyria" disease, where throughout biosynthesis, the Fe^{2+} is inefficiently incorporated into protoporphyrin, the precursor to the heme molecule.[20] Instead of heme, some Zn^{2+}-coordinated protoporphyrins are formed (Scheme 1C). Furthermore, zinc phthalocyanine (ZnPc) is a commercially available product used as catalyst, photosensitizer, etc.

After the success of our previous work based on Mg and the proof-of-principle for the general method of active-site imprinting, there are two reasons to move on with Zn-based carbons: 1) unlike for Mg, many literature studies are available on the preparation of porous carbon materials in the presence of Zn (especially involving $ZnCl_2$). This includes our own efforts e.g. reference 30, 34 and 40 in context with the Antonietti group et al. 2) The non-PGM/ Fe–N–C community has recently increased involving Zn^{2+}-containing zeolitic imidazolium framework (ZIF)-based carbons with very interesting results.[21] It has to be mentioned that a few recent publications also reported on atomically dispersed Zn–N–C catalysts, which seems to be an upcoming topic.[22–24] Moreover, there are other potential advantages of using Zn, as further discussed.

Suitable mass-transport porosity is very important for the performance of catalysts in general, and especially for ORR electrocatalysts, which require the formation of three-phase boundaries. Often, advantageous morphologies are obtained with the hard template strategy, where an inorganic template acts as scaffold for the replication of the mesostructured morphology and removed after pyrolysis.[25–28] On the other hand, the drawback of this method is that corrosive chemicals are needed in order to remove the template, whereas hydrothermal and salt template/ionothermal syntheses have the advantages of avoiding this potential hazard.[29,30] In this regard, the selection of established synthetic methods involving zinc, leading to numerous NDCs with many different pore systems, is advantageous. Porous carbon preparation procedures involving Mg ions, in contrast, are rather rare.[31–33] Like for ZIF-8-derived carbons, for $ZnCl_2$-derived NDCs, relatively high residual amounts of Zn are reported, depending, of course, on the synthesis temperature.[21,30] A partial removal of these residual amounts is possible by washing with concentrated acids, which points to strong coordination of Zn^{2+} to the NDC support as in the case of complexes with chelating ligands.[34]

Herein, we report an adapted ionothermal carbonization recipe that targets the maximization of intermediate formation of macrocyclic ZnN_4 sites throughout carbonization, with the assumption that this will result in a high concentration of imprinted N_4 and ZnN_4 sites in the final porous Zn–N–C (Scheme 1D). The coordinated Zn^{2+} ions within the obtained Zn–N–Cs are selectively exchanged with Fe^{2+} or Fe^{3+} to gain further understanding of the general properties of Fe–N–Cs and preferable preparation strategies. Fe–N–C catalysts with high Fe contents are prepared and investigated regarding their general structure as well as their ORR activity. The active site formation mechanism is further investigated using modern cutting-edge techniques. Identical location aberration-corrected scanning transmission electron microscopy (IL-ARSTEM) is used for the investigation of identical Fe–N–C voxels before and after the exchange of Zn^{2+} with Fe^{3+}. The ion-exchange event is further studied using an in situ electrochemical flow cell (EFC) coupled to an inductively coupled plasma mass spectrometer (ICP-MS).

2. Results and Discussion

2.1. Imprinting NDCs by Zn^{2+} Templating (Zn–N–C)

The ionothermal carbonization involves 1,2-dicyanobenzene (phthalonitrile) as a carbon and nitrogen precursor (Scheme 1E). This compound is the precursor that is used for the organic synthesis of phthalocyanine macrocycles,[35] and an isomer of the precursor used in the original work on soft ionothermal carbonization at 600 °C by Kuhn et al.[36] Different LiCl–$ZnCl_2$ salt mixtures are used as combined solvent, porogen, and imprinting agent. The reaction mixture is prepared under dry conditions and then carbonized in Ar atmosphere. For convenience, samples are named *X*Li_*Y*(M), where *X* represents the molar ratio of LiCl in the salt mixture, *Y* stands for the carbonization temperature, and M represents Zn^{2+} or $Fe^{2+/3+}$, indicating the coordinated metal ions.

Carbon materials with very high surface areas were obtained after aqueous acidic work-up in order to remove the salt and relatively loosely bound, i.e., physisorbed and probably N-coordinated or N_2-coordinated Zn^{2+} with very high carbon yields in the range of ≈60%. Nitrogen sorption porosimetry was used to investigate the pore structure of the Zn–N–Cs. For all samples, a large nitrogen uptake at low relative pressure due to the presence of microporosity is observed (Figure S1, Supporting Information). In agreement with previous studies on ionothermal carbonizations, the porosity of *X*Li_*Y* can be controlled by changing solvent properties via the LiCl amount in the salt mixture, and an increase in mesoporosity is herein observed with increasing LiCl fractions (Figure S1 and Table S1, Supporting Information).[30,37] This leads also to tuned surface area, with samples synthesized with lower LiCl amount showing higher surface area, as high as 2069 $m^2\ g^{-1}$. The temperature of carbonization only moderately influences the final porosity, with increasing temperatures (between 800 and 1000 °C) leading to slightly increasing abundance of pores smaller than ≈26 nm in diameter at the costs of the abundance of larger pores (26–50 nm); the surface area is also very similar

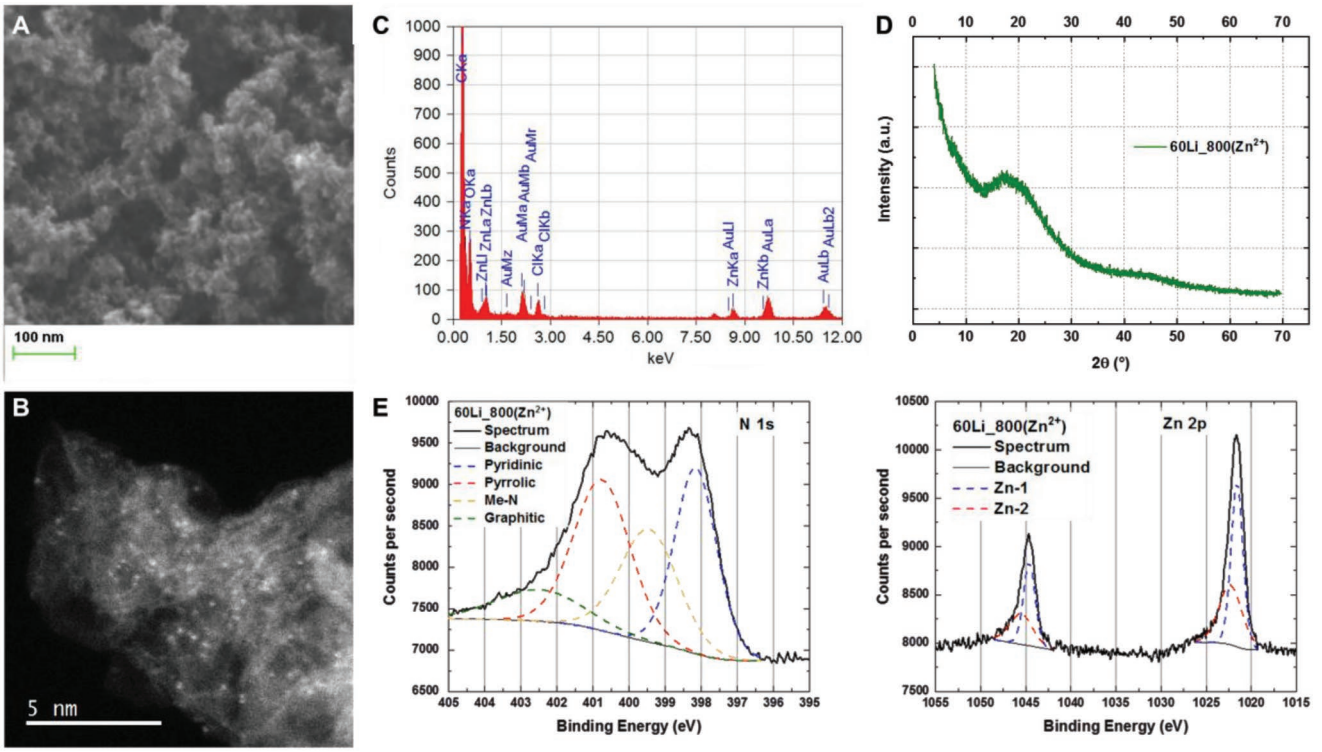

Figure 1. Morphological and chemical characterization of 60Li_800(Zn^{2+}) with different techniques. A) SEM image shows the morphology on the meso- and macroscale. B) ADF STEM image shows atomically dispersed metal atoms. C) STEM–EDX spectrum shows the presence of C, N, Zn, O, and Cl; Au signal arises from the TEM grid. D) PXRD spectrum shows the characteristic pattern for highly disordered carbons and no crystalline phase is detected. E) XPS of N 1s (left) and Zn 2p (right) with experimental data (black line) and peak fitting (dashed colored lines).

in the range of 1430–1475 $m^2\ g^{-1}$ (Figure S2 and Table S1, Supporting Information). Scanning electron microscopy (SEM) was used to investigate the morphology on the meso- and macroscale (pores larger than 50 nm), which is inaccessible to N_2 sorption porosimetry (**Figure 1**A). The optimized Zn–N–C sample 60Li_800(Zn^{2+}) shows a hierarchical pore system, considered advantageous for mass transport, with an aerogel-type structure. Scanning transmission electron microscopy (STEM) imaging reveals an amorphous carbon structure with quasi-spherical mesopores, apparently originating from molten salt droplets acting as templates throughout synthesis as well as high amount of atomically dispersed metal atoms (Figure 1B; Figure S3, Supporting Information). Energy-dispersive X-ray spectra (EDX) show the presence of C, N, Zn, and Cl according to the precursor composition and pointing to relatively high amounts of strongly coordinated Zn^{2+} (Figure 1C). No crystalline inorganic phases were detected by powder X-ray diffractometry (PXRD) with the spectrum showing the characteristic pattern for amorphous, highly disordered carbons with very broad reflections at 17.7° and ≈43° 2Θ, respectively (Figure 1D). The high scattering intensity at low angles originating from ultra-microporosity and the broad shoulder with a clear shift to low angles (compared to 26.7° 2Θ for graphite) is herein indicative of a carbon material mostly composed of a few layers of carbon sheets. In combination with the very high specific surface area, it can be assumed that all Zn^{2+} complexes are surface complexes and, therefore, in principle accessible to an ion-exchange reaction. X-ray photoelectron spectroscopy (XPS) was used for elemental analysis and for the determination of N and Zn sites within 60Li_800(Zn^{2+}) (Figure 1E). The material turned out to have a relatively high N content of 5.66 wt%, with a residual content of coordinated Zn of 1.33 wt%. The majority of N sites represent pyridinic and pyrrolic sites, which may point to the large abundance of terminal sites caused by dative Zn—N bonds. This is further confirmed in the Zn 2p spectrum of the sample which is consistent with the one of ZnPc (Figure S4, Supporting Information) and does not show contributions from Zn—O bonds[38] or nitride-like bonds.[39] Interestingly, even for samples synthesized at higher temperature, namely 60Li_900(Zn^{2+}) and 60Li_1000(Zn^{2+}), the Zn 2p spectrum does not change, except for the decreasing Zn content obtained with increasing synthesis temperature, pointing out that the formation and retaining of ZnN_4 sites are possible (at least) up to 1000 °C. In all synthesized samples, a smaller contribution arising from Zn—Cl bonds is also present.[40] Due to the low penetration depth of XPS analysis, the Zn content was further investigated using ICP-MS giving much larger values of 2.95% Zn and the very high N content (by CHNS combustion analysis) of 13.61% N. Due to the high surface area of these carbons, the amount of adsorbed water is conspicuous (usually in the range of 20%). For this reason, it is important to refer to the elemental composition to the real mass of the samples, which was obtained after degassing the samples under vacuum at 250 °C for at least 12 h.

To further investigate the nature of the Zn—N bonds, samples synthesized between 700 and 1000 °C have been investigate with

near-edge X-ray absorption fine structure (NEXAFS). Figure S5 (Supporting Information) shows a comparison between these samples and two references, namely ZnO and ZnPc. Looking at the peak positions and at the shape of the Zn $L_{2,3}$ edge, it can be stated that no ZnO phase is present and the coordination of Zn in the Zn–N–C materials well resembles the one in ZnPc. Moreover, since no clear difference is present, the composition of the sites seems not to significantly change between 700 and 1000 °C, confirming the XPS results. At this stage, since all the techniques employed strongly point in that direction, the formation of imprinted ZnN_4 sites seems reasonable.

60Li_800(Zn^{2+}) was then separately subjected to Fe^{3+} coordination and Fe^{2+} coordination, respectively. Fe^{2+} was coordinated to 60Li_800(Zn^{2+}) according to our previous procedure, with the difference of using higher Fe^{2+} concentrations.[16] Fe^{3+} was coordinated using a novel molten salt approach. The coordination was carried out in a $FeCl_3$/LiCl mixture at 170 °C (T_m = 150 °C). The advantage of choosing a molten iron salt is that the depletion of Fe^{3+} ions throughout infiltration and coordination of the porous material can be nearly excluded, so each pore should be reached with Fe species. Fe^{3+} ions are also smaller compared to Fe^{2+} ions, possibly leading to the occupation of smaller coordination sites resulting in a higher concentration of N_4 sites. After washing again with diluted HCl in order to remove the remaining salt and loosely bound Fe ions, the samples were collected by filtration, dried at 80 °C overnight, and analyzed for coordination-induced changes.

2.2. Fe Coordination to Imprinted NDC (Fe–N–C)

Nitrogen sorption analysis after Fe coordination typically results in no qualitative changes in porosity, i.e., isotherms and pore size distributions remain qualitatively the same. This observation indicates that the carbon scaffold stays unchanged. However, reduced quantitative values resulting from a downshift of the isotherms are observed, pointing to an increased specific weight of the sample after transmetalation employing the $FeCl_3$/LiCl mixture. The coordination with $FeCl_2$ in MeOH, on the other side, leads to an upshift of the isotherm, pointing to a decrease in the specific weight of the sample. This difference is also reflected in the elemental analysis of the two samples, with 60Li_800(Fe^{3+}) having Fe and Zn amounts of 3.12 and 0.56 wt% and 60Li_800(Fe^{2+}) of 0.55 and 2.27 wt%, respectively, after correction for the water content (Table S2, Supporting Information). The ICP-MS results show a decrease in Zn content, very pronounced especially in the case of 60Li_800(Fe^{3+}), suggesting the replacement of Zn^{2+} by Fe ions. 60Li_800(Fe^{2+}) and 60Li_800(Fe^{3+}) show specific surface areas (SSAs) of 1707 and 1147 $m^2\ g^{-1}$, and total pore volumes (TPVs) of 2.43 and 1.07 $cm^3\ g^{-1}$, respectively (Table S1, Supporting Information). SEM and STEM imaging after Fe coordination reveal no apparent changes in the carbon morphology due to Fe coordination, suggesting the successful coordination of atomically dispersed Fe only (**Figure 2**A,B; Figure S6, Supporting Information). STEM–EDX analysis clearly proves the presence of Fe, confirming the

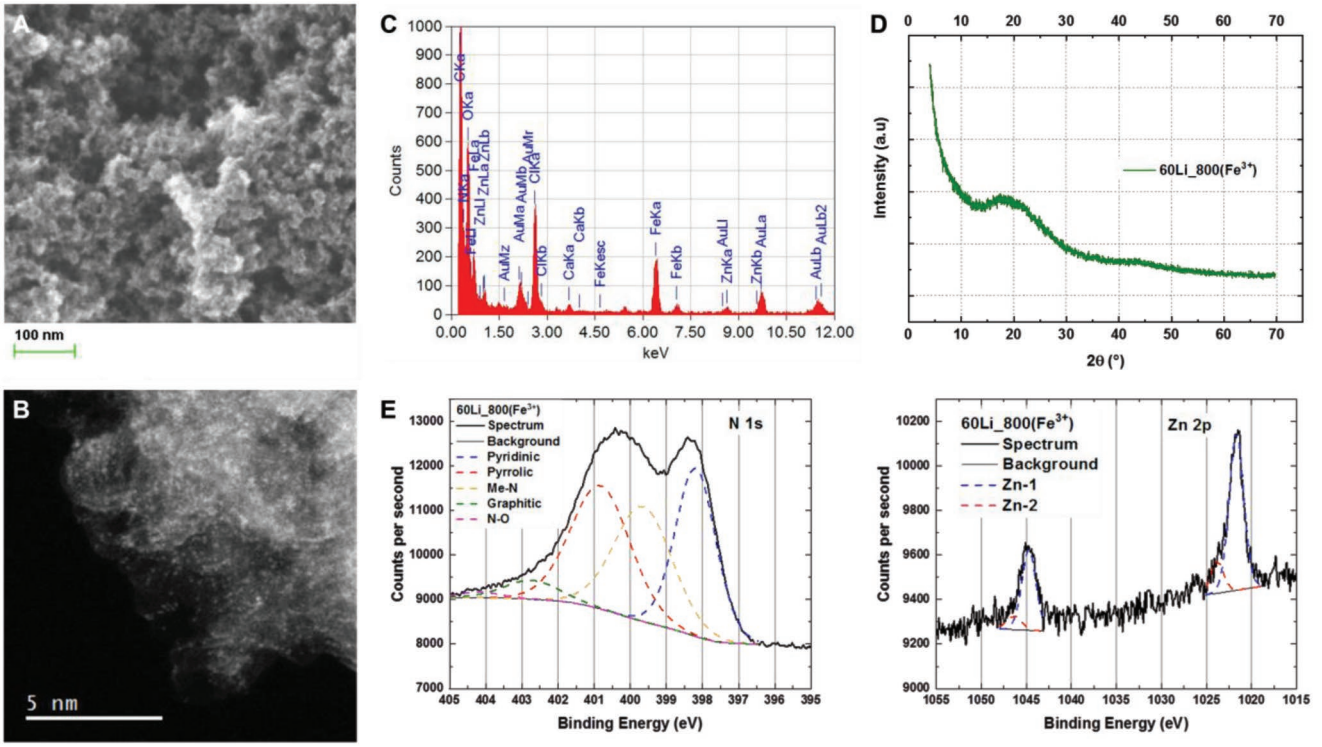

Figure 2. Morphological and chemical characterization of 60Li_800(Fe^{3+}) with different techniques. A) SEM image does not show any change on the meso- and macroscale due to transmetalation. B) ADF STEM image shows higher density of atomically dispersed metal atoms. C) STEM–EDX spectrum shows the same composition of the sample before transmetalation with the addition of Fe peaks; Au signal arises from the TEM grid. D) PXRD spectrum shows the characteristic pattern for highly disordered carbons and no crystalline phase is detected, as for the sample before transmetalation. E) XPS of N 1s (left) and Zn 2p (right) with experimental data (black line) and peak fitting (dashed colored lines).

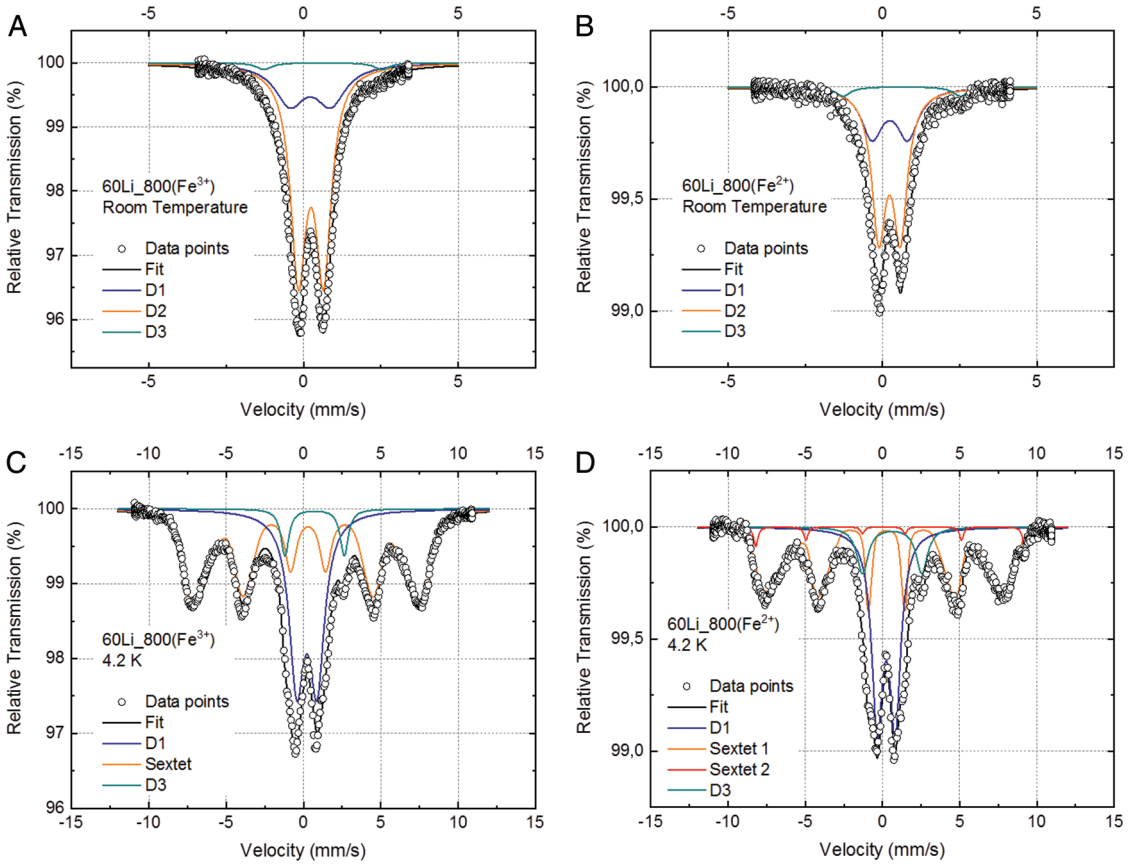

Figure 3. Mössbauer spectra recorded at room temperature between −5 and 5 mm s^{-1} (a,b) and 4.2 K between −15 and 15 mm s^{-1} (c,d) of 60Li800(Fe^{3+}) (a,c) and 60Li800(Fe^{2+}) (b,d).

successful introduction of Fe in an atomically dispersed form (Figure 2C). PXRD additionally confirms the absence of crystalline inorganic phases, as expected after the acidic work-up, which followed the coordination step (Figure 2D). XPS survey show residual amounts of zinc (2.25 wt% Zn for 60Li_800(Fe^{2+}) and 0.39 wt% Zn for 60Li_800(Fe^{3+})) and allow for the quantification of the iron content to 0.57 wt% Fe for 60Li_800(Fe^{2+}) and 0.54 wt% Fe for 60Li_800(Fe^{3+}) (Figure 2E; Figure S7, Supporting Information). Since all other techniques employed point to much higher concentrations of atomically dispersed Fe, XPS analysis is likely underestimating the concentrations due to its surface sensitivity.

For the investigation of the nature of the obtained Fe complexes (degree of covalent bonding, spin state, etc.), the Fe^{2+} and Fe^{3+} coordinated samples 60Li_800(Fe^{2+}) and 60Li_800(Fe^{3+}) were independently investigated by Mössbauer spectroscopy. In this context, it is worth mentioning that with the pyrolytic state-of-the-art preparation of Fe–N–Cs, a deliberate selection of the oxidation state of Fe is not possible due to carbothermal reduction. Pyrolysis-derived Fe–N–Cs seem to be mostly consisting of Fe^{2+} species and, therefore, Fe^{3+} species are often not considered for the interpretation of the spectra.[41] A sextet, originating from super-paramagnetically coupled species, is however assigned to Fe^{3+} species and its d^5 electron configuration. We recorded Mössbauer spectra of 60Li_800(Fe^{3+}) and 60Li_800(Fe^{2+}) at room temperature (RT) and 4.2 K, respectively (**Figure 3**).

Looking at the room-temperature spectra, it can be stated that no sextets or singlets are observed. Accordingly, no non-nanometric iron side phases (i.e., metallic iron or iron carbide) that would be super-paramagnetic at room temperature are present after the acidic work-up. This is in contrast to many pyrolytic Fe–N–C syntheses, in which particles of such phases may be covered by graphitic shells and therefore protected from acidic removal.[9] Liquid helium temperature measurements were performed to distinguish between the desired active FeN_4 sites and nanoscopic iron species, which exhibit quadrupole doublets at RT either because they are not magnetically ordered or super-paramagnetic but exhibit a magnetic hyperfine splitting at 4.2 K, where their super-paramagnetism is blocked.[42]

At 4.2 K, indeed, what we called D2 disappears and apparently splits into a sextet (two for 60Li_800(Fe^{2+})). At this temperature, although, two doublets (named D1 and D3) give still a strong signal, namely 37.1% and 5.7% of the total spectrum for 60Li_800(Fe^{3+}) and 39.2% and 9.9% for 60Li_800(Fe^{2+}). Surprisingly, regardless of the transmetalation procedure (Fe^{2+} vs Fe^{3+}), these two samples have very similar Mössbauer spectra. As already indicated by ICP-MS measurements, 60Li_800(Fe^{3+}) shows ≈4 times higher Fe content compared to 60Li_800(Fe^{2+}) (Table S2, Supporting Information), pointing to the effectiveness of the novel molten salt approach used for the transmetalation, especially since the resulting structure

of Fe sites is apparently equal. Compared to conventional Fe–N–Cs, it is interesting to observe the large abundance of the magnetically coupled Fe^{3+}species in the 4.2 K spectra. This is notable since the coordination with Fe^{2+} also leads to the large abundance of magnetic Fe^{3+} ions. This observation may be explained by both the contact to oxygen in the ambient atmosphere and the treatment with the oxidative acid. The larger extent of oxidation of Fe^{2+} to Fe^{3+} species compared to conventional Fe–N–C is not surprising because here the entire number of complexes is surface complexes, and therefore fully accessible to oxygen of the atmosphere. Even more intriguing is, however, the fact that these species resist the acid work-up. The Mössbauer parameters for each component are given in Table S3 (Supporting Information). The two quadrupole doublets that remain at 4.2 K are well known in the Fe–N–C community and are typically assigned to different spin configurations of the FeN_4 sites.[43] D1 can be assigned to strongly covalent Fe^{2+} as in Fe porphyrin. According to its Mössbauer parameters, it can, however, also be assigned to Fe^{3+}. Comparison of samples 60Li_800(Fe^{2+}) and 60Li_800(Fe^{3+}) reveals very similar parameters for the D1 doublets, suggesting the possibility that regardless of the initial oxidation state of the iron, the same species are formed. D3 can certainly be assigned to high-spin Fe^{2+}, perhaps with a moderately covalent character. Considering that for 60Li_800(Fe^{3+}) no Fe^{2+} would be expected, this result is somewhat surprising and requires further investigation. The sextet in the 4.2 K spectra is assigned to nanometric oxidic clusters, in which the Fe atoms are close to each other in a magnetically ordered arrangement; such clusters are also visible in the transmission electron microscopy (TEM) picture of 60Li_800(Fe^{3+}) (Figure S8, Supporting Information). The high abundance of such species may be explained by the high abundance of micropores in the original NDC scaffold.

In order to further elucidate these data, additional samples were analyzed. 60Li_800(Zn–Fe) was prepared in the same fashion as 60Li_800(Zn^{2+}) but containing 2.2 wt% Fe of $FeCl_3$ (with respect to the precursor) in the mixture prior to heat treatment, resembling the classic route to synthesize Fe–N–C catalysts.[44] The aforementioned sample was further subject to transmetalation with the novel ionothermal approach, leading to the catalyst 60Li_800(Fe–Fe^{3+}). Due to the low Fe content, the Mössbauer spectrum of 60Li_800(Zn–Fe) is too noisy to draw any conclusion. On the other hand, 60Li_800(Fe–Fe^{3+}) shows a clear spectrum, very similar compared to 60Li_800(Fe^{2+}) and 60Li_800(Fe^{3+}) both at room temperature and 4.2 K (Figure S9, Supporting Information).

After this comparison, it is possible to draw the following conclusions: 1) the novel molten salt approach using a $FeCl_3$/LiCl mixture is capable of loading more Fe onto the samples compared to the wet-chemical coordination step using $FeCl_2$ in MeOH. 2) The final configuration of Fe in the catalyst seems not to depend on the Fe source used during the transmetalation, but rather can be determined by the fact that the active sites have been imprinted by Zn^{2+}. 3) It seems that once the Fe ions fill all the available pockets, they start to form some magnetic ordered structure. This indicates the possibility that Mössbauer spectroscopy could be used to track the status of the transmetalation process.

The electrocatalytic activity toward the ORR was tested in the PEMFC-relevant acidic conditions using a standard three-electrode rotating (ring) disk electrode (R(R)DE) setup with O_2-saturated 0.1 M $HClO_4$ as the electrolyte and a freshly calibrated and separated RHE reference electrode. Comparison of the activities at 1600 rpm of the equally loaded samples (290 µg cm^{-2} without taking into consideration the water content), 60Li_800(Zn^{2+}), 60Li_800(Fe^{2+}), and 60Li_800(Fe^{3+}), shows a strong positive shift of ≈323 mV for 60Li_800(Fe^{2+}) and ≈383 mV for 60Li_800(Fe^{3+}) toward higher ORR activity compared to 60Li_800(Zn^{2+}) (**Figure 4**A). The onsets of the electrocatalytic reaction are found at relatively low overpotentials at ≈0.85 V for 60Li_800(Fe^{3+}). The moderate slopes in the mixed kinetic diffusion-controlled regime, related to Tafel slopes of ≈108 mV dec^{-1} for 60Li_800(Fe^{2+}) and ≈83 mV dec^{-1} for 60Li_800(Fe^{3+}), lead to a moderate half-wave potential $E_{1/2}$ of 0.66 V for 60Li_800(Fe^{2+}) and a more promising $E_{1/2}$ of 0.72 V for 60Li_800(Fe^{3+}). An increase in the loading could herein be utilized to shift the $E_{1/2}$ values positively, but considering the high Fe concentrations and the high amount of micropores, in which active sites are supposed to be hosted,[45–47] even more positive values would be expected. Based on our previous study on ionothermal carbons as ORR catalysts in alkaline electrolyte, we assign the relatively low slopes to a limited catalyst utilization originating from high abundance of so-called bottleneck pores. Further optimization of the nanopore systems seems reasonable, but is beyond the scope of the present work. The limiting current of both catalysts approaches the theoretical limiting current density of 5.6 mA cm^{-2} at 1600 rpm pointing at a complete reduction of O_2 to H_2O in a four-electron reduction at this catalyst loading. Comparing the same loading of 290 µg cm^{-2} for both catalysts, RRDE measurements reveal a more selective reduction of O_2 for 60Li_800(Fe^{3+}) with a maximum peroxide yield of 7% at ≈0.55 V compared to 17% for 60Li_800(Fe^{2+}) (Figure S10, Supporting Information). Koutecký–Levich analysis reveals a kinetic current density, j_{kin}, of 15.5 mA cm^{-2} (at 0.6 V) for 60Li_800(Fe^{2+}) and 10.4 mA cm^{-2} (at 0.7 V) for 60Li_800(Fe^{3+}), respectively (Figure S11, Supporting Information).

For Fe–N–C catalysts the main degradation mechanisms that are usually discussed are iron-ion dissolution, electrochemical carbon corrosion, protonation of N-groups, and surface oxidation induced by H_2O_2. To investigate the degradation of our catalysts in this regard, we carried out an accelerated stress test of the most active catalyst 60Li_800(Fe^{3+}), using voltammetric cycling (between 0.4 and 0.8 V for up to 500 cycles at a scan rate of 50 mV s^{-1}) in both O_2- and Ar-saturated electrolytes (Figure 4A and Figure 4B, respectively). Interestingly, there is no degradation (quantified by the shift of the half-wave potential) observed in the Ar case, whereas in O_2-saturated electrolyte, we observed a high degradation rate in the first few hundred cycles, eventually leveling out toward the 500th cycle. The reduction of the half-wave potential after 500 cycles amounts to ≈45 mV, indicating relatively high sensitivity toward oxidation. Recent literatures suggest the role of peroxide species in reducing the activity of Fe–N–C catalysts throughout operation.[48,49] Our results confirm these reports and suggest that additional active sites/materials catalyzing the disproportionation of peroxide species might be important for the mitigation of the oxidation in future catalysts.

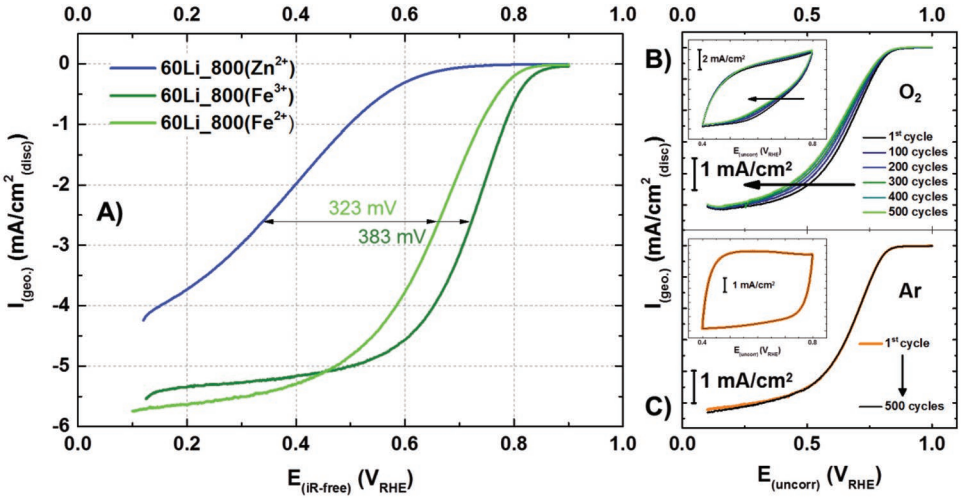

Figure 4. A) ORR curves of 60Li_800(Zn^{2+}), 60Li_800(Fe^{3+}), and 60Li_800(Fe^{2+}) recorded with an RDE setup at room temperature in 0.1 M $HClO_4$ at 1600 rpm, 5 mV s^{-1} (anodic scans). B,C) Accelerated stress test of 60Li_800(Fe^{3+}) recorded with an RDE setup at room temperature in 0.1 M $HClO_4$. B) O_2-saturated and C) Ar-saturated. The ORR curves were measured at the beginning of the test and after the 100th, 200th, 300th, 400th, and 500th cycles at 1600 rpm, 5 mV s^{-1} (anodic scans). The inset shows the cycling of the catalyst between 0.4 and 0.8 V (w/o *iR* correction) at 400 rpm, 50 mV s^{-1}. All curves were corrected for capacity contributions.

The activity of the sample obtained from the pyrolysis experiment with the addition of $FeCl_3$ in the $ZnCl_2$/LiCl mixture, namely 60Li_800(Zn–Fe), and the activity of the same sample after transmetalation, 60Li_800(Fe–Fe^{3+}), already presented in the Mössbauer part, have also been investigated. Figure S12 (Supporting Information) shows an exemplary comparison between these two samples and 60Li_800(Fe^{3+}). Looking at this comparison, two facts are worth mentioning: 1) our novel approach based on active-site imprinting followed by metalation/transmetalation is capable of producing catalysts with the same activity as in the case of pyrolytic synthesis, but with the chance of surpassing the limitation due to metastability of the FeN_4 sites at high temperatures; 2) 60Li_800(Fe–Fe^{3+}) does not show any improvement compared to 60Li_800(Zn–Fe), meaning that the added iron is not contributing to the activity, either because it is forming small oxidic clusters (see Mössbauer part) or because it is occupying N_x sites, which are not active toward the ORR. Although intriguing, unveiling this observation is beyond the scope of this manuscript, and more detailed characterizations will be performed in the future.

However, when comparing 60Li_800(Zn^{2+}), 60Li_800(Fe^{2+}), and 60Li_800(Fe^{3+}), it cannot be disregarded that the positive shift of the ORR is extraordinarily large, which is very important considering the mild procedure of the active-site formation. The results imply a very large potential of the imprinting metalation method for the rational design of future M–N–C catalysts. In the concluding part of this work, the focus will be on the fundamental question of the formation mechanism of the FeN_4 sites at low temperature.

2.3. Mechanistic Study

Although the increase in activity is remarkable, this remains only an indirect proof for the transmetalation of imprinted active sites. In order to unambiguously demonstrate this process, 60Li_800(Zn^{2+}) was placed on a gold grid for identical location TEM (IL-TEM),[50] and the transmetalation was carried out using a solution of $FeCl_2$ in 0.1 M $HClO_4$, sequentially washing with fresh 0.1 M $HClO_4$. **Figure 5** shows annular-dark-field (ADF) STEM images of the same area of a carbon particle before (upper row) and after (middle row) transmetalation with the respective EDX spectra. Before transmetalation, only atomically dispersed Zn atoms are present and no Fe is detected. On the other hand, after transmetalation, the density of atomically dispersed metal atoms is clearly higher with the EDX spectrum showing the presence of Fe.

Lately, many interesting techniques have been adopted to characterize Fe–N–C catalysts. Besides IL-TEM, ICP-MS coupled to an EFC system has proved to be a powerful tool.[11] In this study, we applied the aforementioned technique to follow the transmetalation in situ. The main idea was to record the activity of 60Li_800(Zn^{2+}), while exchanging Zn with Fe. However, the EFC setup is not optimized for recording ORR activity, and the obtained values cannot be directly compared to the ones obtained with an RDE setup due to different hydrodynamics; moreover, the Fe content in the carrying solution had to be low due to limitations related to the saturation of the signal in the MS; for these reasons, it was not possible to observe a shift in the activity as big as in the RDE when comparing 60Li_800(Zn^{2+}) with 60Li_800(Fe^{2+}). At this point, we decided to use the EFC–ICP-MS in a different fashion.

To confirm complexation of Fe atoms, 60Li_800(Zn^{2+}) was cycled between −0.5 and 1.6 V after flowing an ≈10 ppb solution of $FeCl_2$ in 0.1 M $HClO_4$ on the sample. It has already been reported that at high potentials the oxidation of the carbon material directly leads to destruction of the carbon surface with a consequential release of the components of the just formed active sites.[11] For comparison, the same set of experiments, including complexation and degradation, has been carried out on an NDC reproduced from the literature.[51] In this material, no imprinting metal is present and hence no N_4-type anchoring

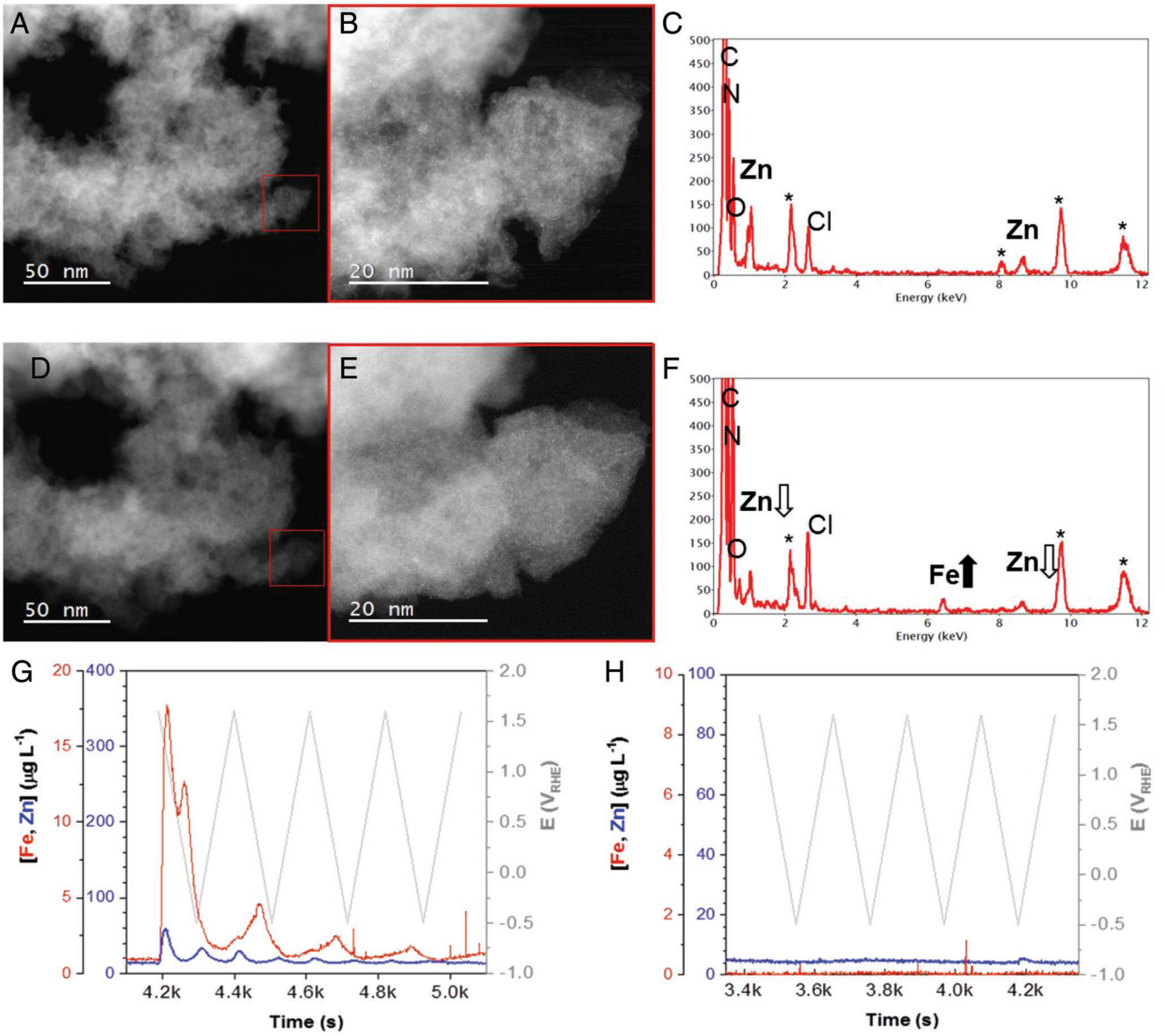

Figure 5. ADF STEM images and corresponding EDX spectra of the same catalyst's area before (a–c) and after (d–f) transmetalation. The full arrow is indicating the rise of the Fe signal (Kα) and the empty arrows are indicating the decrease of the Zn signals (Lα and Kα); the star is the Au signal from the grid. G, h) ICP-MS signals over 14 min of time recorded during the cycling from –0.5 to 1.6 V with 20 mV s^{-1} of 60Li_800(Zn^{2+}) (g) and the reference N-doped carbon (NDC) (h).

sites for Fe are to be expected. Although the coordination of Fe to terminal N sites cannot be excluded, for this material, loosely bound Fe species that are considered less active and stable are the most likely case.

The MS spectra for the two samples are shown in Figure 5 (lower row). For 60Li_800(Zn^{2+}), as expected, several Fe (as well as Zn) peaks are observed during cycling, confirming that the transmetalation (or metalation) has taken place, whereas, for the NDC with a random distribution of N atoms, no peaks are observed.

In conclusion, we reported a new synthetic route for Fe–N–C catalysts starting from Zn–N–C materials in which Zn^{2+} ions act as active-site imprinter, followed by low-temperature Fe coordination. The Zn–N–Cs possess very high surface area and tuned properties obtained by simply using a LiCl–$ZnCl_2$ salt mixture as the reaction medium; also, the high yields and the easiness of sample processing make this synthesis promising for large-scale production. We showed that a novel molten salt transmetalation approach is capable of loading more Fe compared to our previously reported method involving $FeCl_2$ in MeOH. Besides, we demonstrated that Fe coordination is independent of the Fe source employed for the transmetalation event (Fe^{2+} vs Fe^{3+}). In addition to the indirect proof of the activity gain in RDE, we visualized the transmetalation process with cutting-edge techniques such as IL-TEM and EFC–ICP-MS.

This work further proves the effectiveness of our active-site imprinting strategy already reported using Mg^{2+} as an active-site imprinter, which makes it possible to decouple the formation of the carbon scaffold from the one of the active site,

possibly surpassing the limitation of current synthetic methods, which rely on kinetic stabilization of Fe atoms at high temperatures. Also, the use of different imprinting metals could lead to different Fe configurations with enhanced activity, something that is not straightforward with current synthesis procedures.

We believe that our work will open new frontiers in both the synthesis and the understanding of Fe–N–C catalysts and M–N–C materials in general.

3. Experimental Section

Materials and Methods: 1,2-dicyanobenzene, LiCl, $ZnCl_2$, $FeCl_2$, $FeCl_3$, and methanol were purchased from Sigma Aldrich. All chemicals were used without further purification.

In a typical synthesis, 1,2-dicyanobenzene (0.7 g) was thoroughly mixed with the respective LiCl–$ZnCl_2$ mixture (7 g) prior to the heat treatment. The resulting mixtures were placed in an alumina crucible covered with a quartz lid and heated to the desired temperature with a heating rate of 10 K min^{-1} in a tube furnace. After holding the temperature for 1 h, the samples were let in the tube to cool down to room temperature. All steps were conducted with a constant Ar flow. The obtained materials were ground and washed with 0.1 M HCl for several hours. Finally, the samples were dried at 80 °C overnight.

Coordination of iron was carried out in two different fashions. 60Li_800(Fe^{2+}) was prepared from 60Li_800(Zn^{2+}) employing the metal-coordination procedure from ref. [16]. 60Li_800(Fe^{3+}) was obtained after mixing ≈0.1 g of 60Li_800(Zn^{2+}) with ≈3 g of LiCl–$FeCl_3$ eutectic mixture in a Schlenk tube, heating up to 170 °C for 22 h in Ar atmosphere, and washing with 0.1 M HCl for several hours and drying.

Characterization: N_2 sorption measurements were carried out using Quantachrome Autosorb iQ2. The samples were outgassed at 250 °C under vacuum overnight prior to the measurements. The data were collected between 10^{-5} and 1 P/P_0. Specific surface areas were determined according to Brunauer–Emmett–Teller (BET) theory using Micropore BET Assistant supplied by Quantachrome ASiQwin software. The total pore volume was calculated at ≈0.99 P/P_0. Pore size distributions were calculated with the quenched-solid density functional theory (QSDFT) method (slit/cylindrical/spherical pores). For the morphological examinations, the samples were characterized using a field-emission FE-SEM Zeiss Ultra Plus microscope.

STEM imaging was performed with a beam current of ≈14.5 pA and at an accelerating voltage of 80 kV in an atomic resolution aberration-corrected scanning transmission electron microscope ARM 200CF. Sample preparation was carried out by diluting the sample powder in ethanol and drop-casting the solution on lacey carbon support Au grids.

XRD data were recorded with a StadiP diffractometer with Cu Kα radiation (λ = 1.54060, 50 kV, 30 mA, germanium (111)).

XPS measurements were conducted using a Kratos Axis Supra spectrometer with monochromatized Al Kα radiation. Samples were prepared by dispersing the powder in an isopropanol and water mixture followed by drop-casting on Cu tape. Each spectrum was acquired with 0.1 eV step size and corrected with respect to C 1s peak at 284.7 eV. Data analysis was performed with ESCAA software.

NEXAFS spectra were collected at the soft X-ray analytics facility WERA of the Institut für Festkörperphysik at the Karlsruhe synchrotron ANKA, Germany. Partial fluorescence-yield detection was used. The photon energy was calibrated to better than 30 meV by simultaneously measuring a NiO reference sample at the Ni L_3 edge.

Mössbauer spectra were recorded with a sinusoidal velocity waveform at room temperature and at 4.2 K on powder samples enclosed in lucite holders. For the low-temperature measurements, both the absorber and the ^{57}Co in rhodium source were cooled in a liquid helium bath cryostat. MOS90 software (version 2.2) was used for the fitting of the spectra. Isomer shifts were measured with respect to the source having the same temperature as the absorber. In order to refer the shifts to α-Fe at room temperature, 0.115 mm s^{-1} was added to the shifts measured at room temperature and 0.245 mm s^{-1} to those measured at 4.2 K.

The coupling of EFC with ICP-MS was already introduced in previous publications.[52,53] Briefly, a replica of BASi electrochemical flow cell (Cross-Flow Cell Kit MW-5052) made of polyetheretherketone (PEEK) was coupled with an Agilent quadrupole ICP-MS instrument (Agilent 7900, Agilent Technologies, Santa Clara, CA), equipped with MicroMist glass concentric nebulizer and Peltier-cooled, Scott type spray chamber. Upstream the EFC, a diagonal four-way flow valve (Idex, V-100D, from PEEK) was used to switch from 0.1 M $HClO_4$ (Merck, Suprapur) and the 10 ppb $FeCl_2$ in $HClO_4$ solution. Two syringe pumps (WPI sp100i and Harvard apparatus 11 plus) were used to pump the appropriate solution at a constant flow of 400 µL min^{-1}. The working and counter electrodes were made of glassy carbon, while the reference electrode was a Ag/AgCl electrode (BASi). The potential of the reference related to RHE was determined prior to flow experiments in a separate cell versus a Pt electrode in 0.1 M $HClO_4$, saturated with H_2. The orientation of the working electrode and the counter electrode was adjusted, so the inlet of the electrolyte flow was at the counter electrode and the outlet was at the working electrode to avoid any redeposition. Electrochemical control was established with a potentiostat (CompactStat.e, Ivium technology). The catalyst thin films were prepared by drop-casting 5 µL of a 1 mg mL^{-1} well-dispersed suspension of the catalyst. After evaporation of the solvent, 2 µL of a 9 mg mL^{-1} Teflon suspension was drop-cast on the catalyst layer. Zn and Fe amounts in the synthesized materials were quantified by the same ICP-MS.

Electrochemical measurements were carried out in a three-electrode glass cell using Ar- and O_2-saturated 0.1 M $HClO_4$ prepared from a 60% solution (Guaranteed Reagent, Kanto Chemical) and deionized ultrapure water (Milli-Q Integral 5, 18.2 MΩ cm). An Autolab PGSTAT302N (Metrohm) potentiostat was employed for the measurements. A freshly calibrated RHE was used as the reference electrode and an Au wire as the counter electrode. The solution resistance was determined by electrochemical impedance spectroscopy and the reported potentials (except for those of the accelerated stress tests) were corrected accordingly. The reported polarization curves for ORR were corrected for capacitive currents by subtracting the curves recorded in Ar-saturated electrolyte from the ones recorded in O_2-saturated electrolyte. The catalyst inks were prepared by dispersing 5 mg of catalyst powder in 840 µL of *N*,*N*-dimethylformamide (≥99.8, Fisher Scientific), followed by sonication for 30 min. Afterward, an aliquot of 50 µL of 5 wt% Nafion suspension (Sigma-Aldrich) was added and the ink was sonicated for 10 min more. Subsequently, 10 µL of ink was drop-cast onto a well-polished glassy carbon electrode (Ø = 5 mm, obtained from Pine Research Instrumentation) and dried under an infrared heater for 60 min. The resulting catalyst loading was 290 µg cm^{-2}. The accelerated stress tests were conducted by cycling between 0.4 and 0.8 V at 400 rpm and with a scan rate of 50 mV s^{-1}.

Supporting Information

Supporting Information is available from the Wiley Online Library or from the author.

Acknowledgements

The authors would first of all like to acknowledge Prof. Hubert Gasteiger for hosting the group and for providing a supportive atmosphere. Furthermore, the whole TEC team is acknowledged for the friendly and constructive atmosphere. The German Federal Ministry of Economic Affairs and Energy (BMWi) is acknowledged for funding within the Verbundproject innoKA (Project No.: 03ET6096A) and Dr. Gilleßen from PTJ for constructive supervision of the project. The Karlsruhe Nano Micro Facility (KNMF) and KARA are acknowledged for the provision of beamtime and Dr. Stefan Schuppler and Dr. Peter Nagel for the precious help provided with the NEXAFS experiments.

Conflict of Interest

The authors declare no conflict of interest.

Keywords

active-site imprinting, Fe–N–C, PGM-free ORR electrocatalysts, template ion reaction, Zn–N–C

Received: July 24, 2019
Revised: September 1, 2019
Published online:

[1] Roland Irle, Global EV Sales for 2018, http://www.ev-volumes.com/country/total-world-plug-in-vehicle-volumes.
[2] F. Jaouen, D. Jones, N. Coutard, V. Artero, P. Strasser, A. Kucernak, *Johnson Matthey Technol. Rev.* **2018**, *62*, 231.
[3] A. Kongkanand, M. F. Mathias, *J. Phys. Chem. Lett.* **2016**, *7*, 1127.
[4] A. Orfanidi, P. Madkikar, H. A. El-Sayed, G. S. Harzer, T. Kratky, H. A. Gasteiger, *J. Electrochem. Soc.* **2017**, *164*, F418.
[5] M. Lefèvre, E. Proietti, F. Jaouen, J.-P. Dodelet, *Science* **2009**, *324*, 71.
[6] R. Bashyam, P. Zelenay, *Nature* **2006**, *443*, 63.
[7] H. A. Gasteiger, S. S. Kocha, B. Sompalli, F. T. Wagner, *Appl. Catal., B* **2005**, *56*, 9.
[8] Ballard Power Systems, News Releases 2017 (Archive), http://ballard.com.
[9] S. Glatzel, Z. Schnepp, C. Giordano, *Angew. Chem., Int. Ed.* **2013**, *52*, 2355.
[10] J.-P. Dodelet, R. Chenitz, L. Yang, M. Lefèvre, *ChemCatChem* **2014**, *6*, 1866.
[11] C. H. Choi, C. Baldizzone, J.-P. Grote, A. K. Schuppert, F. Jaouen, K. J. J. Mayrhofer, *Angew. Chem., Int. Ed.* **2015**, *54*, 12753.
[12] X. Wan, X. Liu, Y. Li, R. Yu, L. Zheng, W. Yan, H. Wang, M. Xu, J. Shui, *Nat. Catal.* **2019**, *2*, 259.
[13] Q. Liu, X. Liu, L. Zheng, J. Shui, *Angew. Chem., Int. Ed.* **2018**, *57*, 1204.
[14] X. Wan, W. Chen, J. Yang, M. Liu, X. Liu, J. Shui, *ChemElectroChem* **2019**, *6*, 304.
[15] *Phthalocyanines:Properties and Applications* (Eds: C. C. Leznoff, A. B. P. Lever), Vol. *1–4*, Wiley VCH, Weinheim **1989**.
[16] A. Mehmood, J. Pampel, G. Ali, H. Y. Ha, F. Ruiz-Zepeda, T.-P. Fellinger, *Adv. Energy Mater.* **2018**, *8*, 1701771.
[17] A. Cook, *J. Chem. Soc.* **1938**, 1761.
[18] R. Jasinski, *Nature* **1964**, *201*, 1212.
[19] R. E. Blankenship, *Molecular Mechanisms of Photosynthesis*, John Wiley & Sons, New York, NY **2014**.
[20] R. F. Labbé, H. J. Vreman, D. K. Stevenson, *Clin. Chem.* **1999**, *45*, 2060.
[21] V. Armel, S. Hindocha, F. Salles, S. Bennett, D. Jones, F. Jaouen, *J. Am. Chem. Soc.* **2017**, *139*, 453.
[22] F. Yang, P. Song, X. Liu, B. Mei, W. Xing, Z. Jiang, L. Gu, W. Xu, *Angew. Chem., Int. Ed.* **2018**, *57*, 12303.
[23] Z. Chen, K. Mou, S. Yao, L. Liu, *ChemSusChem* **2018**, *11*, 2944.
[24] J. Li, S. Chen, N. Yang, M. Deng, S. Ibraheem, J. Deng, J. Li, L. Li, Z. Wei, *Angew. Chem., Int. Ed.* **2019**, *58*, 7035.
[25] R. Gokhale, Y. Chen, A. Serov, K. Artyushkova, P. Atanassov, *Electrochim. Acta* **2017**, *224*, 49.
[26] R. Janarthanan, A. Serov, S. K. Pilli, D. A. Gamarra, P. Atanassov, M. R. Hibbs, A. M. Herring, *Electrochim. Acta* **2015**, *175*, 202.
[27] D. Sebastián, V. Baglio, A. S. Aricò, A. Serov, P. Atanassov, *Appl. Catal., B* **2016**, *182*, 297.
[28] A. Serov, K. Artyushkova, P. Atanassov, *Adv. Energy Mater.* **2014**, *4*, 1301735.
[29] R. Gokhale, L.-K. Tsui, K. Roach, Y. Chen, M. M. Hossen, K. Artyushkova, F. Garzon, P. Atanassov, *ChemElectroChem* **2018**, *5*, 1848.
[30] N. Fechler, T.-P. Fellinger, M. Antonietti, *Adv. Mater.* **2013**, *25*, 75.
[31] D. Eisenberg, P. Prinsen, N. J. Geels, W. Stroek, N. Yan, B. Hua, J.-L. Luo, G. Rothenberg, *RSC Adv.* **2016**, *6*, 80398.
[32] Z. Guan, H. Liu, B. Xu, X. Hao, Z. Wang, L. Chen, *J. Mater. Chem. A* **2015**, *3*, 7849.
[33] B. Xu, H. Duan, M. Chu, G. Cao, Y. Yang, *J. Mater. Chem. A* **2013**, *1*, 4565.
[34] Z. Chen, S. Pronkin, T.-P. Fellinger, K. Kailasam, G. Vile, D. Albani, F. Krumeich, R. Leary, J. Barnard, J. M. Thomas, J. Perez-Ramirez, M. Antonietti, D. Dontsova, *ACS Nano* **2016**, *10*, 3166.
[35] T. Haruhiko, S. Shojiro, S. Shinsaku, *Chem. Lett.* **1983**, *12*, 313.
[36] P. Kuhn, A. Forget, D. Su, A. Thomas, M. Antonietti, *J. Am. Chem. Soc.* **2008**, *130*, 13333.
[37] J. Pampel, T.-P. Fellinger, *Adv. Energy Mater.* **2016**, *6*, 1502389.
[38] R. Al-Gaashani, S. Radiman, A. R. Daud, N. Tabet, Y. Al-Douri, *Ceram. Int.* **2013**, *39*, 2283.
[39] M. B. Haider, *Nanoscale Res. Lett.* **2017**, *12*, 5.
[40] A. Schmidt, S. N. Kumar, A. Shchukarev, K. Eränen, J.-P. Mikkola, D. Murzin, T. Salmi, *Appl. Catal., A* **2013**, *468*, 120.
[41] U. I. Kramm, *Structural Arrangement of Iron in Pyrolysed Iron-Porphyrin Electrocatalysts—an Fe-57 Mößbauer Spectroscopic Survey*, Technische Universität Berlin, Berlin **2009**.
[42] M. T. Sougrati, V. Goellner, A. K. Schuppert, L. Stievano, F. Jaouen, *Catal. Today* **2016**, *262*, 110.
[43] U. I. Kramm, J. Herranz, N. Larouche, T. M. Arruda, M. Lefevre, F. Jaouen, P. Bogdanoff, S. Fiechter, I. Abs-Wurmbach, S. Mukerjee, J.-P. Dodelet, *Phys. Chem. Chem. Phys.* **2012**, *14*, 11673.
[44] K. Elumeeva, J. Ren, M. Antonietti, T.-P. Fellinger, *ChemElectroChem* **2015**, *2*, 584.
[45] F. Jaouen, M. Lefèvre, J.-P. Dodelet, M. Cai, *J. Phys. Chem. B* **2006**, *110*, 5553.
[46] F. Jaouen, J. Herranz, M. Lefèvre, J.-P. Dodelet, U. I. Kramm, I. Herrmann, P. Bogdanoff, J. Maruyama, T. Nagaoka, A. Garsuch, J. R. Dahn, T. Olson, S. Pylypenko, P. Atanassov, E. A. Ustinov, *ACS Appl. Mater. Interfaces* **2009**, *1*, 1623.
[47] W. Wang, M. Tang, Z. Zheng, S. Chen, *Adv. Energy Mater.* **2019**, *9*, 1901718.
[48] C. H. Choi, H.-K. Lim, M. W. Chung, G. Chon, N. Ranjbar Sahraie, A. Altin, M.-T. Sougrati, L. Stievano, H. S. Oh, E. S. Park, F. Luo, P. Strasser, G. Dražić, K. J. J. Mayrhofer, H. Kim, F. Jaouen, *Energy Environ. Sci.* **2018**, *11*, 3176.
[49] V. Goellner, V. Armel, A. Zitolo, E. Fonda, F. Jaouen, *J. Electrochem. Soc.* **2015**, *162*, H403.
[50] N. Hodnik, S. Cherevko, *Curr. Opin. Electrochem.* **2019**, *15*, 73.
[51] M. Sevilla, G. A. Ferrero, N. Diez, A. B. Fuertes, *Carbon* **2018**, *131*, 193.
[52] P. Jovanovič, A. Pavlišič, V. S. Šelih, M. Šala, N. Hodnik, M. Bele, S. Hočevar, M. Gaberšček, *ChemCatChem* **2014**, *6*, 449.
[53] A. Pavlišič, P. Jovanovič, V. S. Šelih, M. Šala, N. Hodnik, S. Hočevar, M. Gaberšček, *Chem. Commun.* **2014**, *50*, 3732.

ADVANCED ENERGY MATERIALS

Supporting Information

for *Adv. Energy Mater.,* DOI: 10.1002/aenm.201902412

Active-Site Imprinting: Preparation of Fe–N–C Catalysts from Zinc Ion–Templated Ionothermal Nitrogen-Doped Carbons

*Davide Menga, Francisco Ruiz-Zepeda, Léonard Moriau, Martin Šala, Friedrich Wagner, Burak Koyutürk, Marjan Bele, Urša Petek, Nejc Hodnik, Miran Gaberšček, and Tim-Patrick Fellinger**

Supporting Information

Active Site Imprinting: Preparation of Fe-N-C Catalysts from Zinc Ion Templated Ionothermal Nitrogen Doped Carbons

*Davide Menga, Francisco Ruiz-Zepeda, Léonard Moriau, Martin Šala, Friedrich Wagner, Burak Koyutürk, Marjan Bele, Urša Petek, Nejc Hodnik, Miran Gaberšček and Tim-Patrick Fellinger**

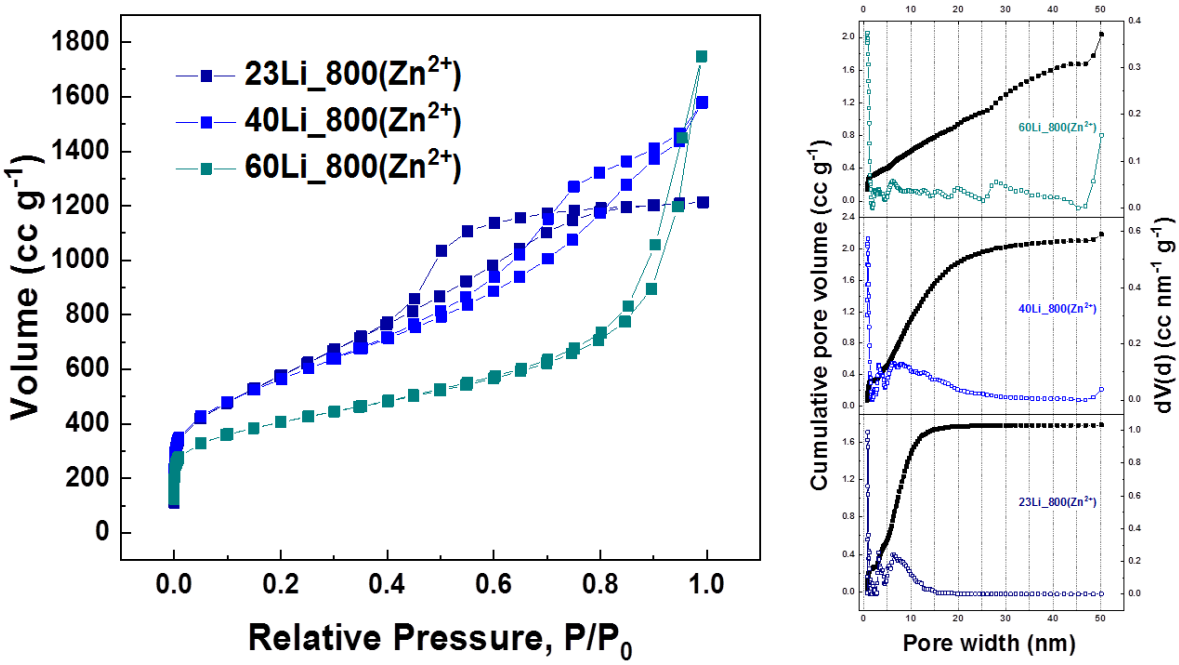

Figure S1. Characterization of Zn-N-Cs with N_2 sorption porosimetry. Isotherms of samples synthesized with different LiCl molar ratios (23%, 40% and 60%) (left) and their corresponding pore size distributions calculated using a QSDFT model for carbon with slit/cylindrical/spherical pores and cumulative pore volumes (right).

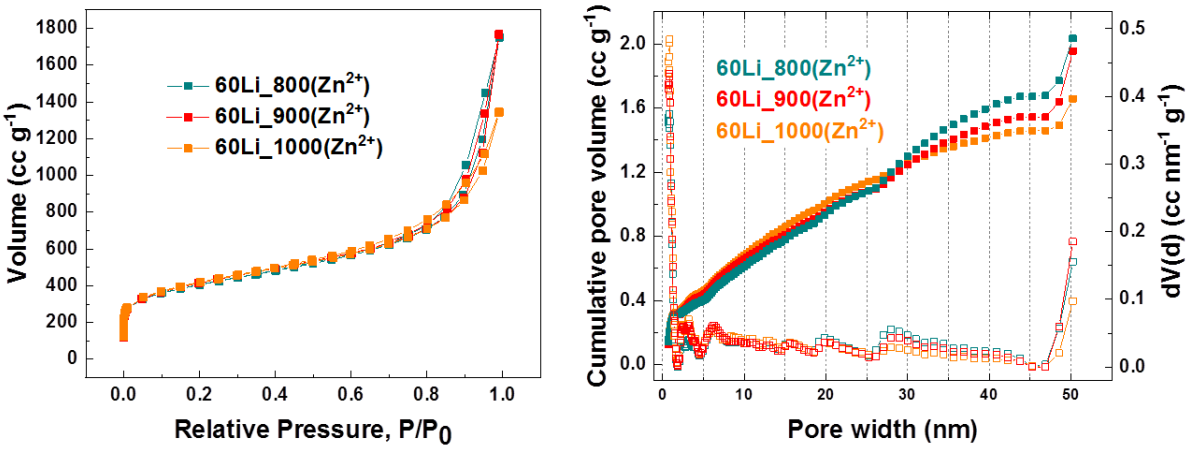

Figure S2. Characterization of Zn-N-Cs with N_2 sorption technique. Isotherms of samples synthesized with 60% molar ratio of LiCl at different temperatures (800 °C, 900 °C and 1000 °C) (left) and their corresponding pore size distributions calculated using a QSDFT model for carbon with slit/cylindrical/spherical pores and cumulative pore volumes (right).

Table S1. Surface areas and pore volumes of samples synthesized with different LiCl amount, different temperatures and containing different metals. Data were obtained from N_2-sorption measurements. QSDFT model for slit shaped, spherical and cylindrical pores was employed. N/C ratio was calculated from the values obtained from combustion analysis.

Sample	SA_{BET} [m^2/g]	SA_{QSDFT} [m^2/g]	Pore Volume [cm^3/g]			N/C ratio
			TPV	$V_{micro, QSDFT}$	$V_{meso, QSDFT}$	
23Li_800(Zn^{2+})	2069	1794	1.88	0.26	1.52	0.10
40Li_800(Zn^{2+})	1977	1844	2.45	0.32	1.80	0.12
60Li_800(Zn^{2+})	1433	1477	2.71	0.32	1.45	0.14
60Li_900(Zn^{2+})	1465	1455	2.73	0.31	1.33	0.08
60Li_1000(Zn^{2+})	1473	1472	2.08	0.33	1.16	0.05
60Li_800(Fe^{3+})	1147	1254	1.07	0.35	0.32	0.13
60Li_800(Fe^{2+})	1707	1749	2.43	0.38	1.54	0.14

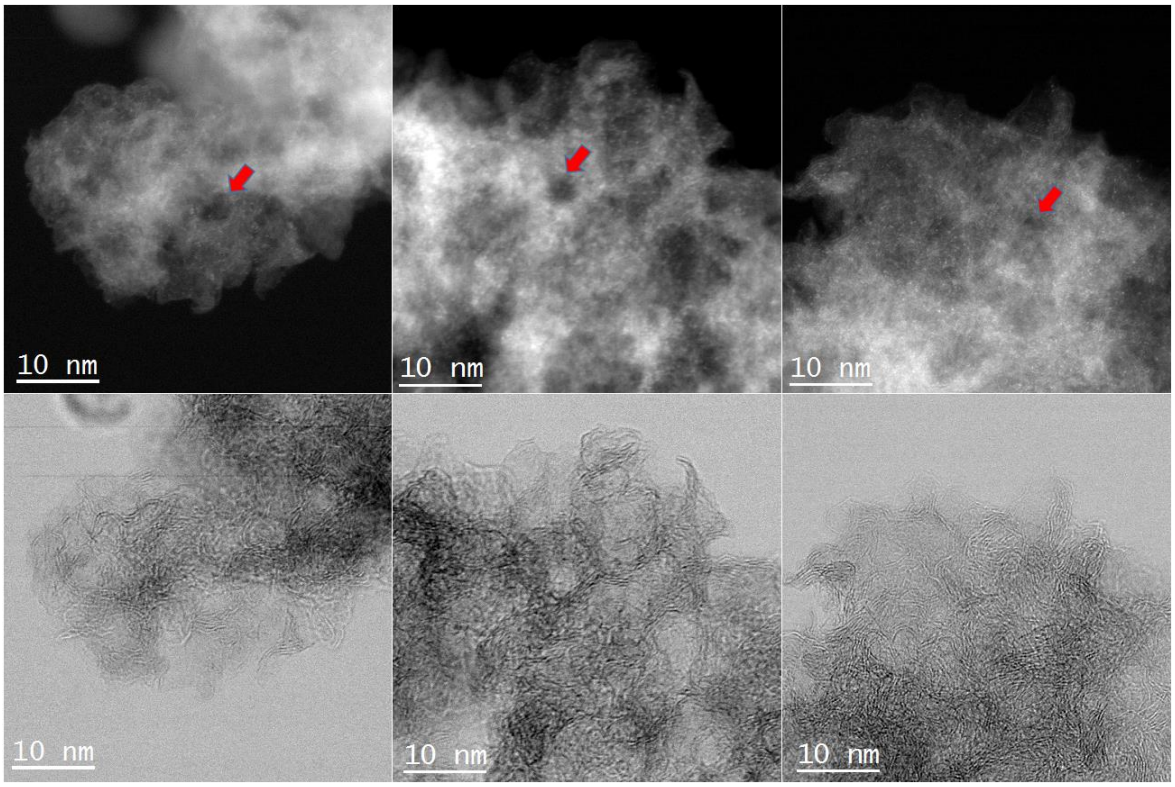

Figure S3. STEM ADF and BF images of 60Li_800(Zn^{2+}) showing the porous (red arrows pointing to some of the multiple pores) and disordered graphitic structure of the sample, as well as the high amount of atomically dispersed metal atoms.

Table S2. Nitrogen, zinc and iron content for the most relevant samples obtained from different techniques. All values are corrected for the water content in the samples except the ones from XPS.

Sample	N content (wt%)		Zn content (wt%)		Fe content (wt%)		
	CHNS	XPS	XPS	ICP-MS	Mössbauer	XPS	ICP-MS
60Li_800(Zn^{2+})	13.61	5.66	1.33	2.95	-	0	0
60Li_800(Fe^{2+})	11.10	7.80	2.25	2.27	1.40	0.57	0.55
60Li_800(Fe^{3+})	10.35	7.92	0.39	0.56	5.43	0.54	3.12
60Li_800(Zn-Fe)	9.25	8.59	1.62	2.36	0.32	0	0.13
60Li_800(Fe-Fe^{3+})	11.73	9.19	0.28	0.37	3.40	0.64	1.94

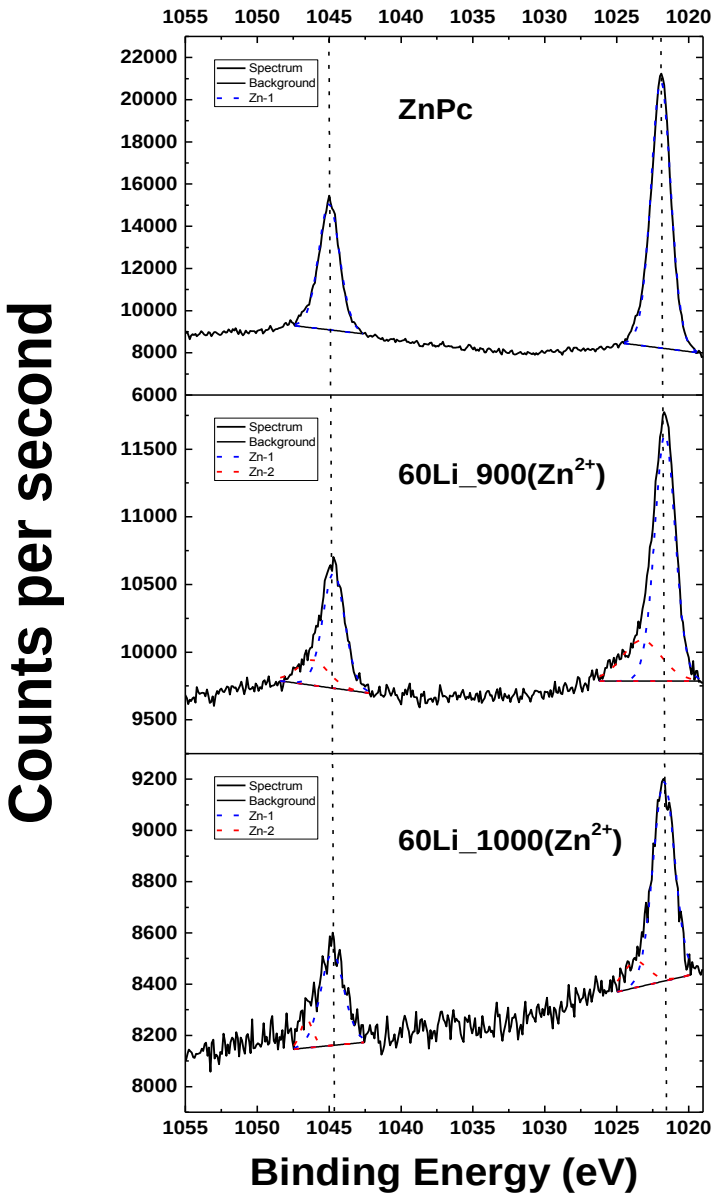

Figure S4. XPS of Zn 2p with experimental data (black line) and peak fitting (dashed colored lines) for ZnPc (upper), 60Li_900(Zn^{2+}) (middle) and 60Li_1000(Zn^{2+}). The blue dotted line (Zn-1) represent Zn-N coordination whereas the red dotted line (Zn-2) is consistent with Zn-Cl bonds.

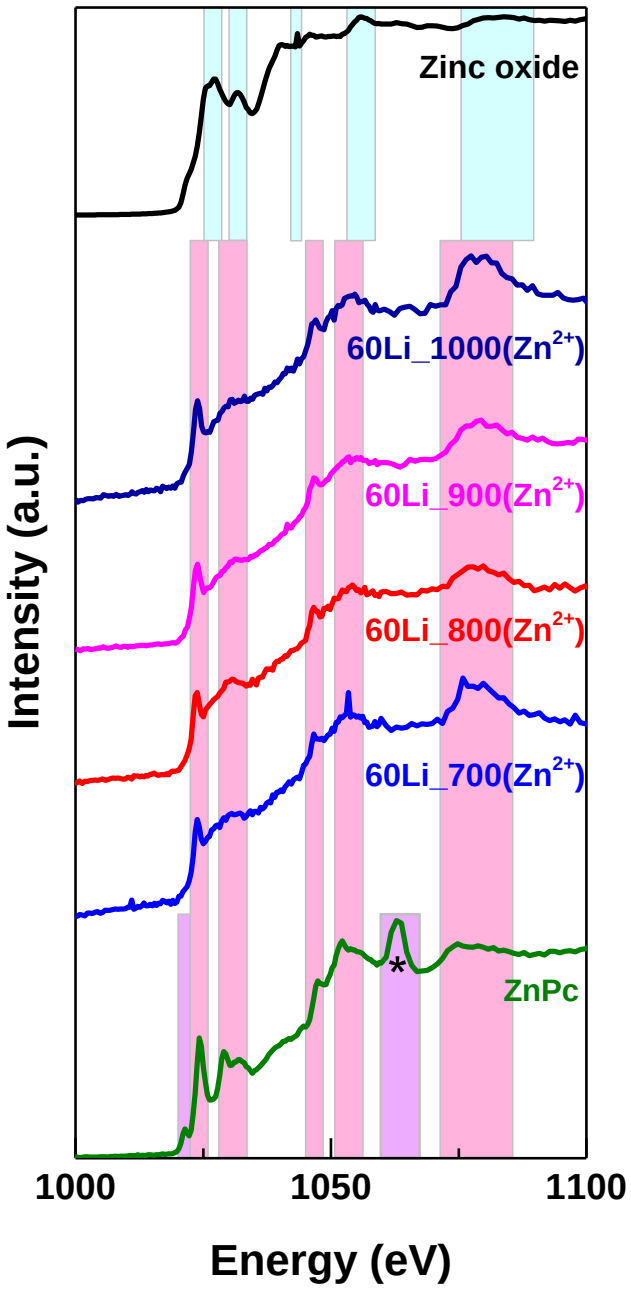

Figure S5. Room temperature NEXAFS spectra at the Zn $L_{2,3}$ edge recorded in fluorescence mode for reference compounds and samples synthesized at different temperatures. The star represents possibly a Bragg peak.

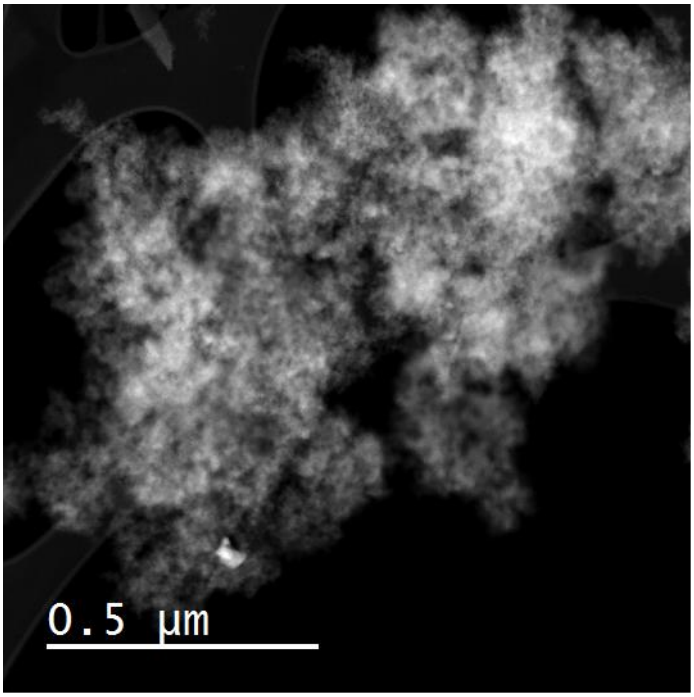

Figure S6. STEM ADF image of 60Li_800(Fe^{3+}) showing the carbon structure of the sample after the transmetalation event.

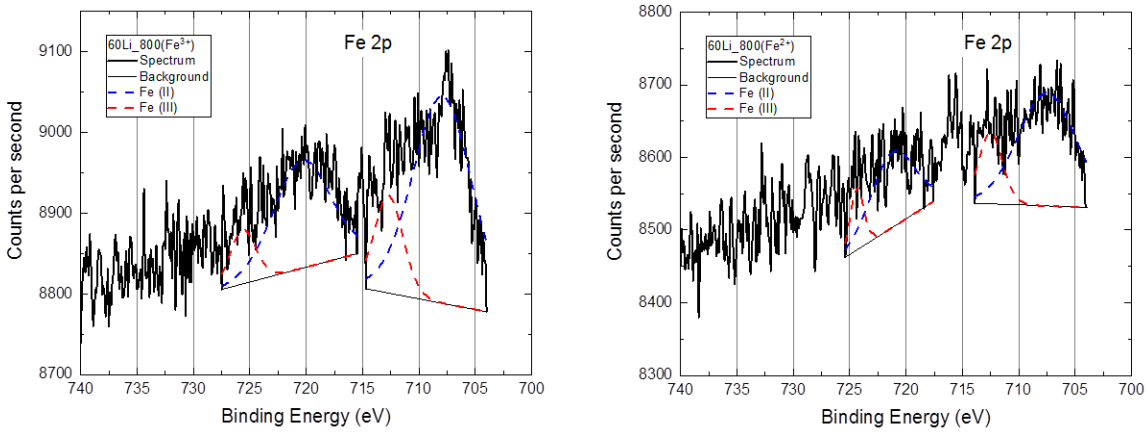

Figure S7. XPS Fe 2p signals for 60Li_800(Fe^{3+}) (left) and 60Li_800(Fe^{2+}) (right).

Table S3. Mössbauer parameters of each component: isomer shift (IS, mm/s), quadrupole splitting (QS, mm/s), relative area (RA, %) and magnetic field (H, Tesla).

Sample	D1 (IS; QS; %)		D2 (IS; QS; %)		D3 (IS; QS; %)		Sextet 1 (IS; H; %)		Sextet 2 (IS; H; %)	
	RT	4.2 K	RT	4.2 K	RT	4.2 K	RT	4.2 K	RT	4.2 K
60Li_800_TM Fe3+	0.22; 1.32; 26.4	0.22; 1.32; 37.1	0.24; 0.82; 71.3	-	0.62; 3.81; 2.3	0.71; 3.84; 5.7	-	0.25; 44; 57.2	-	-
60Li_800_TM Fe2+	0.24; 1.16; 33.1	0.24; 1.16; 39.2	0.23; 0.70; 62.4	-	0.62; 3.81; 4.5	0.63; 3.84; 9.9	-	0.23; 45.5; 47.9	-	0.29; 54; 3
60Li_800(Fe-Fe3+)	0.27; 1.03; 51.8	0.28; 1.03; 36.8	0.24; 0.72; 45.7	-	0.62; 3.81; 2.5	0.65; 3.92; 9.6	-	0.24; 44.5; 49.8	-	0.31; 54.6; 3.8

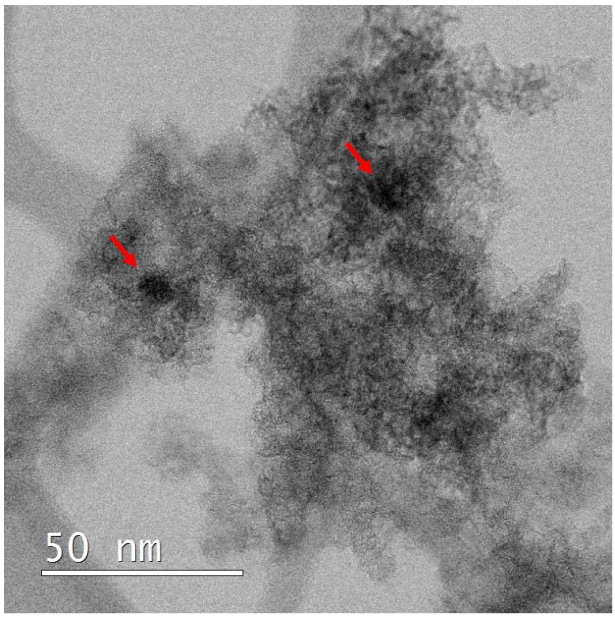

Figure S8. STEM BF image of 60Li_800(Fe^{3+}). Red arrows are pointing at the Fe particles.

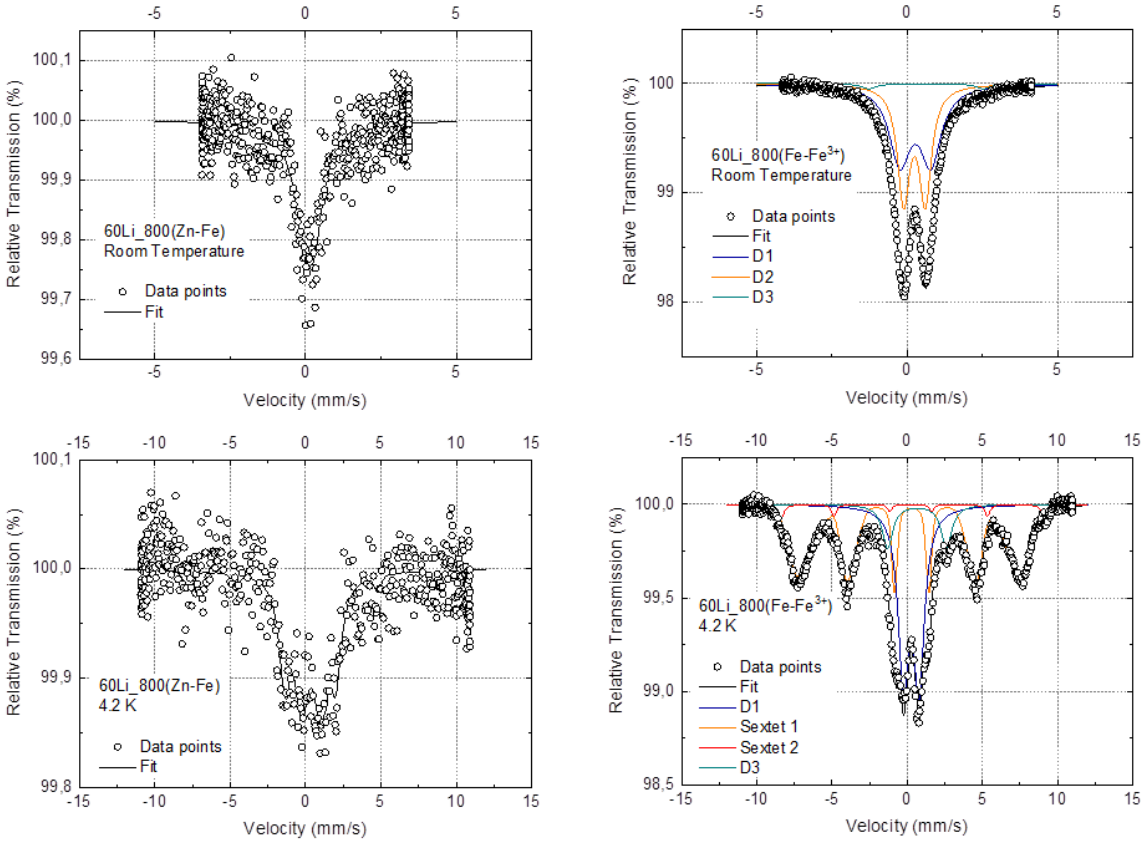

Figure S9. Mössbauer spectra recorded at room temperature (upper) and 4.2 K (lower) of 60Li800(Zn-Fe) (left) and 60Li800(Fe-Fe^{3+}) (right).

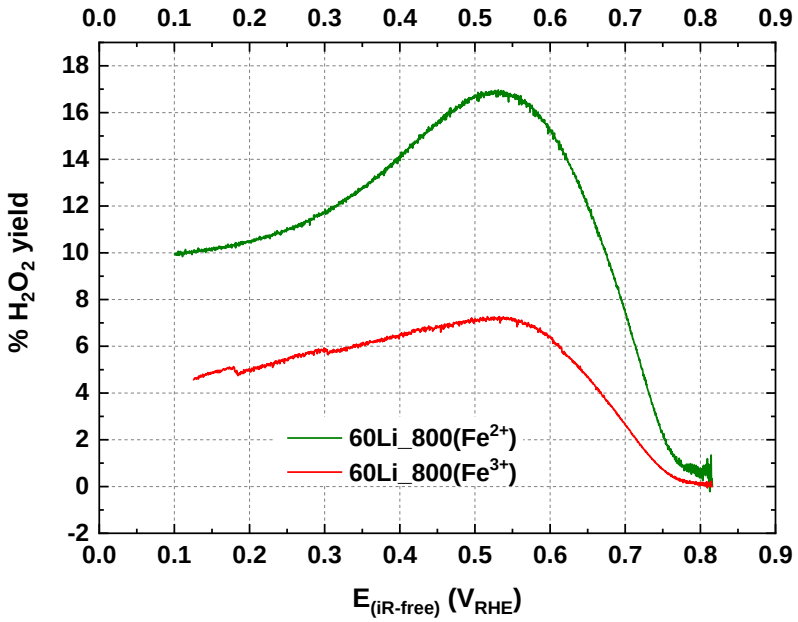

Figure S10. 60Li_800(Fe^{3+}) and 60Li_800(Fe^{2+}) H_2O_2 yield over the measured potential window. Measurements were conducted in an RRDE setup consisting of a glassy carbon disc and a Pt ring kept at a constant potential of 1.2 V. The experiment was performed at room temperature in a O_2-saturated 0.1 M $HClO_4$ at 1600 rpm, 5 mV s^{-1} (anodic scans) and with a loading of 290 µg cm^{-2}.

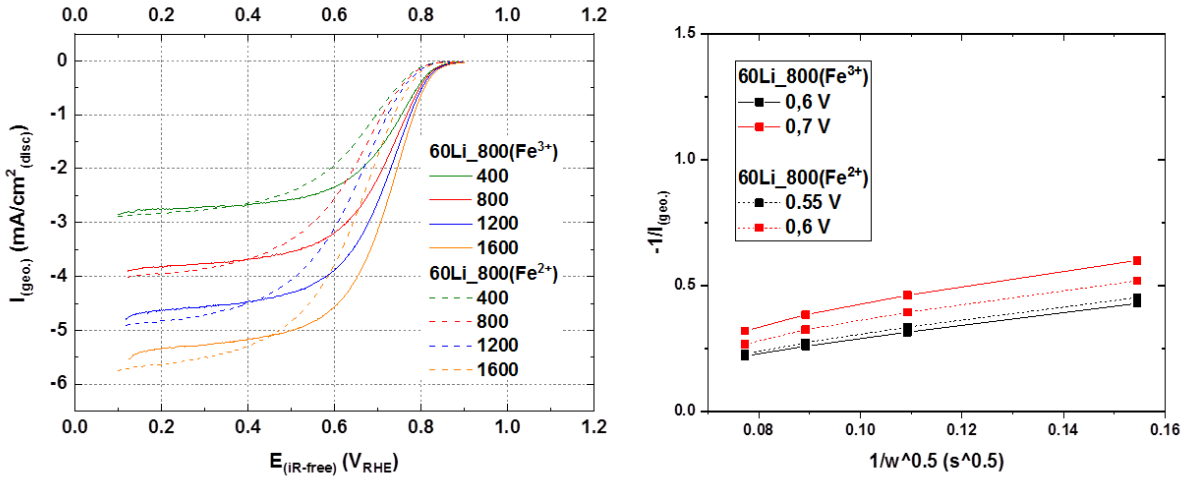

Figure S11. Capacitance corrected ORR curves for 60Li_800(Fe^{3+}) and 60Li_800(Fe^{2+}) at different rotation rates (left) and corresponding Koutecký-Levich analysis (right). Measurements were conducted in an RDE setup at room temperature in 0.1 M $HClO_4$ at 400, 800, 1200 and 1600 rpm and with a loading of 290 µg cm^{-2}.

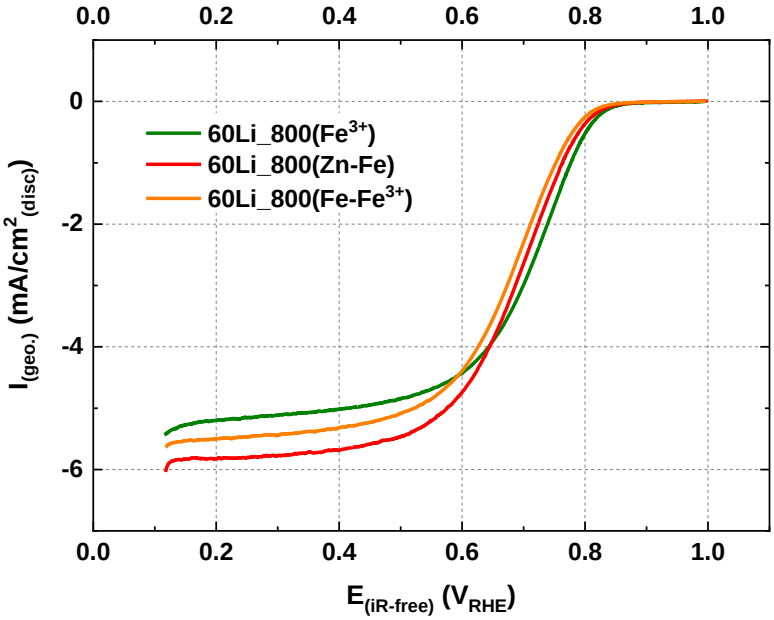

Figure S12. ORR curves of 60Li_800(Fe^{3+}), and 60Li_800(Zn-Fe) and 60Li_800(Zn-Fe^{3+}) recorded with an RDE setup at room temperature in 0.1 M $HClO_4$ at 1600 rpm, 5 mV s^{-1} (anodic scans). All curves were corrected for capacitance contributions.

3.1.2 Resolving the Dilemma of Fe–N–C Catalysts by the Selective Synthesis of Tetrapyrrolic Active Sites via an Imprinting Strategy

Here, the article "Resolving the Dilemma of Fe–N–C Catalysts by the Selective Synthesis of Tetrapyrrolic Active Sites via an Imprinting Strategy" is presented, which was submitted to the peer-reviewed *Journal of the American Chemical Society* in May 2021 and published in October 2021 as an editor choice article. The permanent web-link to the article is https://pubs.acs.org/doi/full/10.1021/jacs.1c04884.

In this work, aided by density functional theory (DFT) calculations, fundamental principles for the synthesis of M-N-C materials are proposed: (i) tetrapyrrolic M-N_4 sites are formed within defective carbon scaffolds throughout heating of metal, nitrogen and carbon precursors. (ii) pyrolytic reactions happening at ~ 750 °C generate the critical conductivity required for electrocatalysis. (iii) if catalytic graphitization takes place, pyridinic M-N_4 sites are formed. Metallic Fe is a good graphitization catalyst and for this reason mostly pyridinic Fe-N_4 sites are found in the literature[37-38] and tetrapyrrolic sites are obtained only with low loadings.[27] In contrast to Fe, Zn is less prone to carbothermal reduction and should allow for higher concentration of tetrapyrrolic sites. The proposed principles are employed to selectively synthetized tetrapyrrolic Zn-N_4 sites, which are confirmed by extraction experiments (i.e., M-to-H^+ ion exchange) in combination with XPS as well as EXAFS measurements. The tetrapyrrolic Zn-N-C material is utilized in the previously reported low temperature Zn-to-Fe ion exchange reaction. Due to different thermodynamic stability, this method allows for the formation of only certain Fe-N_4 sites and nanoscopic Fe(III) oxide is also formed upon exposure to air. To surpass this limit, a thermal treatment is employed to decompose the oxidic phase and coordinate Fe ions through a high temperature transmetalation reaction. The combination of low- and high- temperature Zn-to-Fe transmetalation allows for the selective synthesis of phase-pure tetrapyrrolic Fe-N-C catalysts with Fe loading higher than 3 wt.%, as confirmed by EXAFS and Mössbauer spectroscopy. The synthetized material shows state-of-the-art activity and stability both in RDE and single-cell PEMFC measurements.

Author contributions

D.M. and T.-P.F. planned and designed the experiments. D.M. synthesized and characterized the catalyst and performed the RDE experiments. J.L.L. and B.P. provided the DFT calculations. Y.-S.L. performed the single-cell PEMFC measurements. I.A. performed and analyzed the XAS measurements. B.K. measured and analyzed the XPS data. F.E.W. performed and analyzed the Mössbauer spectroscopy measurements. F.R.-Z. performed the TEM imaging. M.G. contributed to the manuscript. D.M. and T.-P.F. wrote the manuscript. All authors discussed the results and commented on the manuscript.

JACS
JOURNAL OF THE AMERICAN CHEMICAL SOCIETY

pubs.acs.org/JACS

Article

Resolving the Dilemma of Fe−N−C Catalysts by the Selective Synthesis of Tetrapyrrolic Active Sites via an Imprinting Strategy

Davide Menga, Jian Liang Low, Yan-Sheng Li, Iztok Arčon, Burak Koyutürk, Friedrich Wagner, Francisco Ruiz-Zepeda, Miran Gaberšček, Beate Paulus, and Tim-Patrick Fellinger*

Cite This: J. Am. Chem. Soc. 2021, 143, 18010−18019

ABSTRACT: Combining the abundance and inexpensiveness of their constituent elements with their atomic dispersion, atomically dispersed Fe−N−C catalysts represent the most promising alternative to precious-metal-based materials in proton exchange membrane (PEM) fuel cells. Due to the high temperatures involved in their synthesis and the sensitivity of Fe ions toward carbothermal reduction, current synthetic methods are intrinsically limited in type and amount of the desired, catalytically active Fe−N_4 sites, and high active site densities have been out of reach (dilemma of Fe−N−C catalysts). We herein identify a paradigm change in the synthesis of Fe−N−C catalysts arising from the developments of other M−N−C single-atom catalysts. Supported by DFT calculations we propose fundamental principles for the synthesis of M−N−C materials. We further exploit the proposed principles in a novel synthetic strategy to surpass the dilemma of Fe−N−C catalysts. The selective formation of tetrapyrrolic Zn−N_4 sites in a tailor-made Zn−N−C material is utilized as an active-site imprint for the preparation of a corresponding Fe−N−C catalyst. By successive low- and high-temperature ion exchange reactions, we obtain a phase-pure Fe−N−C catalyst, with a high loading of atomically dispersed Fe (>3 wt %). Moreover, the catalyst is entirely composed of tetrapyrrolic Fe−N_4 sites. The density of tetrapyrrolic Fe−N_4 sites is more than six times as high as for previously reported tetrapyrrolic single-site Fe−N−C fuel cell catalysts.

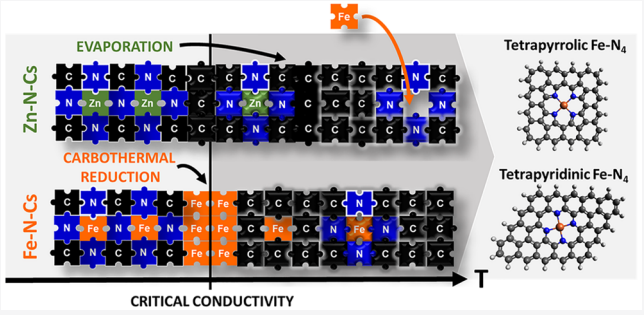

INTRODUCTION

In order to move from the burning of fossil fuels to clean and sustainable energy conversion and storage, electrochemical systems represent a central future technology, and reactions such as CO_2- and O_2-reduction reaction (CO2RR and ORR, respectively) as well as the O_2 evolution reaction (OER) play a pivotal role.[1] To be sustainable and yet economically advantageous, the materials employed to catalyze electrochemical reactions should be preferably composed of abundant and inexpensive elements.[2] Maximizing the atomic efficiency of metals, single-atom catalysts (SACs) have attracted the interest of many scientists in the field of catalysis, both heterogeneous and electrochemical.[3,4] Undoubtedly, the most promising class of such electrocatalysts, regarding activity and range of applications, is the family of metal and nitrogen co-doped carbons (M−N−Cs). In particular, Fe−N−C catalysts are among the best candidates to replace Pt-based materials for fuel cell applications due to their promising ORR activity.[5,6] While the desirable composition of Fe−N−C catalysts was debated for decades, in recent times the community vastly agrees that atomically dispersed square-planar Fe−N_4 sites, embedded into the conductive and supporting nitrogen-doped carbon (NDC) scaffold, are the desirable catalytically active motif. Therefore, Fe−N−C SACs are currently the subject of numerous research activities, fueled by the need for electrification of the transport sector.

Although the activity of Fe−N−C catalysts was impressively optimized in the past ∼30 years, further substantial improvements were hampered by limitations in the preparation of the catalysts. The formation of Fe−N−C SACs having concentrations above 0.5 wt % of Fe results in the formation of inorganic side phases such as metallic Fe, iron carbides, or iron nitrides.[7,8] The atomically dispersed Fe−N_4 active sites decompose at the temperature of their pyrolytic formation. This phenomenon is commonly described as the dilemma of Fe−N−C catalysts. There have been tremendous efforts in the last years to optimize the synthetic conditions in order to improve the activity by increasing the active site density for Fe−N−C catalysts.[9] Multistep syntheses are employed, comprising pyrolysis, leaching of soluble side-phases, and additional thermal processing steps.[10,11] The employment of

Received: May 18, 2021
Published: October 24, 2021

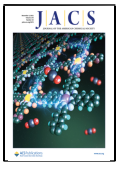

https://doi.org/10.1021/jacs.1c04884
J. Am. Chem. Soc. 2021, 143, 18010−18019

metal−organic framework precursors led to a significant increase in activity.[12] Reducing the mobility of Fe atoms throughout the pyrolytic synthesis can also reduce side-phase formation, leading to higher Fe loadings. The success of the mostly quite advanced synthetic protocols proves the possibility for further performance gain, although generally Fe contents still do not exceed 3 wt %.[12−14] Furthermore, there has been a long-standing debate and uncertainty about the surrounding structure of the Fe−N_4 sites. It is commonly believed that the active site exists mainly in a pyridinic Fe−N_4 environment. Such an environment has indeed been visualized in atomic resolution,[15] and, recently, for the first time a tetrapyridinic macrocycle (Cl-coordinated or O-bridged) has been employed as a model for Fe−N−Cs.[16] On the other end, Zitolo and Jaouen et al. developed a single-site Fe−N−C catalyst with minute amounts of Fe and proved the active sites therein to be of square-planar pyrrolic nature.[8] Supported by DFT calculations, pyrrolic M−N_4 sites with different metals in M−N−Cs are supposed to have superior activity compared to pyridinic ones in many catalytic applications.[17−19] Nonetheless, a comprehensive understanding on the formation of Fe−N−Cs, resulting in a rational synthesis of specific active sites, is still lacking. The uncontrolled nature of pyrolysis and the endless number of possible precursor systems obscure a clear view on the chemistry of Fe−N−Cs.

Herein, we identify a paradigm change for the synthesis of Fe−N−Cs arising from recent developments of other M−N−C single-atom catalysts. Supported by DFT calculations we propose ground-breaking principles for the synthesis of Fe−N−C catalysts, and M−N−C materials in general. On the basis of an abstract view on the formation pathway of different active sites, we came up with a synthesis strategy toward atomically dispersed, iron-rich Fe−N−C SACs hosting tetrapyrrolic Fe−N_4 complexes as single active sites and solve the long-standing dilemma of Fe−N−C catalysts.

RESULTS AND DISCUSSION

Today, there is evidence for pyrrolic and pyridinic (better tetrapyrrolic and tetrapyridinic) Fe−N_4 sites as active sites in Fe−N−C SACs. Density functional theory (DFT) calculations on isomeric model structures with the chemical formula of $[FeN_4]C_{52}H_{20}$ reveal that the square-planar tetrapyridinic motifs (Figure 1a) are thermodynamically more stable compared to the square-planar tetrapyrrolic motif (Figure 1b and c). The total energy difference of 3.02 eV for the pyrrolic-D_{4h} structure and 3.05 eV for the pyrrolic-C_{4h} structure (Table 1) arises by the necessity for defects within the carbon honeycomb structure in order to embrace the tetrapyrrolic site,

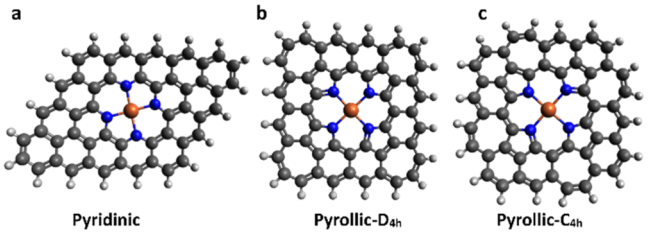

Figure 1. Chemical structure of planar tetrapyridinic (a) and two planar tetrapyrrolic (with two different symmetries, D_{4h} (b) and C_{4h} (c)) $[FeN_4]C_{52}H_{20}$ isomers. The seven-membered-ring defects are necessary to introduce the tetrapyrrolic motif into the planar graphene lattice.

Table 1. Comparison of Calculated M Binding Energy and Calculated Conformational Stability for Different $MN_4C_{52}H_{20}$ Clusters (M = Zn, Fe)[a]

stability	empty	Zn	Fe	Zn binding energy	Fe binding energy
pyridinic	0 (ref)	0 (ref)	0 (ref)	−4.2 eV	−7.9 eV
pyrrolic-D_{4h}	4.79 eV	2.97 eV	3.04 eV	−6.1 eV	−9.7 eV
pyrrolic-C_{4h}	3.45 eV	2.29 eV	3.01 eV	−5.4 eV	−8.3 eV

[a]Stability values are presented with reference to the energy of the pyridinic structure.

while the tetrapyridinic site perfectly fits into the graphene lattice, entirely made of C6 units. The tetrapyrrolic motif only fits the honeycomb lattice if the misalignment caused by five-membered pyrrolic rings is compensated by seven-membered-ring defects as in the case of Stone−Wales defects.

The thermodynamically more stable tetrapyridinic Fe−N_4 structure is interestingly incompatible with findings in organic coordination chemistry, in which pyridinic complexes of Fe^{2+} usually have an octahedral structure, e.g., in $[Fe(bipy)_3]X_2$ or $[Fe(terpy)_2]X_2$ (X = monovalent anion). Only recently was one tetrapyridinic macrocycle presented as an Fe−N_4 model, although the square-planar geometry seems to only arises in the case of an axial Cl ligand or for oxygen-bridged dimers.[16,20] The tetrapyrrolic M−N_4 structure, in contrast, is ubiquitously present in organic coordination chemistry[21,22] and in natural compounds, with the most prominent heme molecules for the case of Fe−N_4 motifs in mammal's blood. Hence, although the tetrapyridinic form is thermodynamically favored, the kinetically preferred tetrapyrollic FeN_4 is the abundant form. The realization of the graphene lattice entirely made of C6 units via preparative wet-chemical bottom-up synthesis is a highly complex discipline, typically involving many synthetic steps and requiring extraordinary synthetic control.[23]

How are tetrapyridinic Fe−N_4 sites formed? To facilitate discrimination from the tetrapyrrolic motif, the tetrapyridinic motif is simply called "pyridinic" in the following. The pyridinic Fe−N_4 site is thermodynamically favorable; however, the rearrangement of the carbon backbone into the honeycomb structure requires temperatures above 1300 °C, as known from graphitization. M−N−Cs are typically prepared between 750 and 1050 °C, where the critical conductivity of electrocatalysts is obtained along with electrocatalytic activity. Hence, the formation of pyridinic M−N_4 sites is actually surprising in common M−N−C syntheses.

Some metals, including iron, are catalysts for graphitization though.[24] At elevated temperature, metallic iron is able to dissolve carbon (formation of iron carbide) and reprecipitate it, allowing for dissociative reaction mechanisms, such as the formation of pyridinic Fe−N_4 sites, as well as further enhancement in conductivity. At the same time, the carbon structure is essentially recrystallized, going along with the destruction of the catalyst morphology, the loss of heteroatoms, and the formation of harmful inorganic side phases (metallic iron, iron carbide, and iron nitride). This process is very common for Fe−N−C syntheses, where metallic iron is formed via carbothermal reduction at elevated temperatures.

With this in mind, we can propose general principles for all conventional M−N−C preparations, which are bottom-up, comprising the heating of the metal, carbon, and nitrogen

https://doi.org/10.1021/jacs.1c04884
J. Am. Chem. Soc. 2021, 143, 18010−18019

Scheme 1. Representation of the Synthetic Route Adopted to Obtain NDC-Fe-HT Containing Exclusively Atomically Dispersed Fe from the Starting Zn−N−C Material Employing Low- and High-Temperature Ion Exchange Reactions

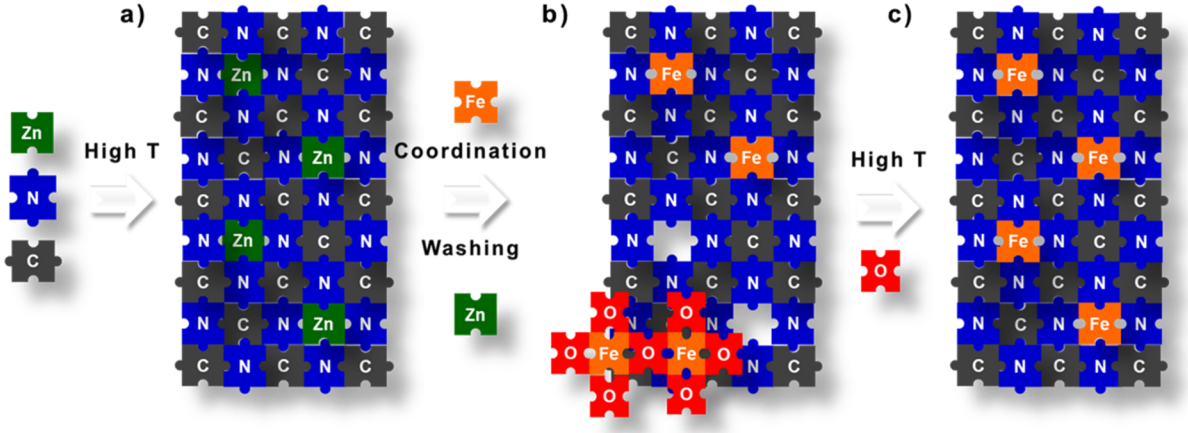

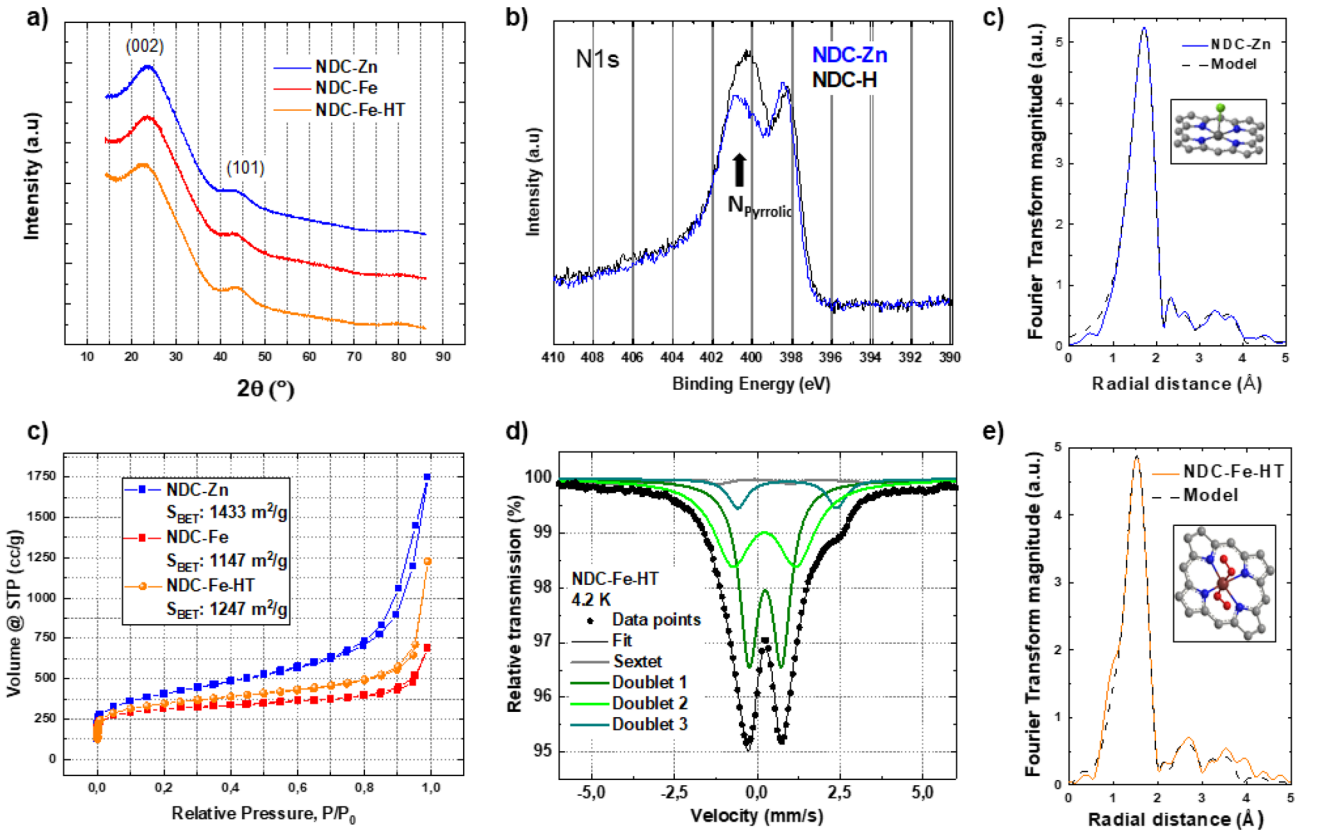

Figure 2. XRD of the NDC-M is characteristic for highly disordered carbons (a). XPS of the N 1s showing the increase of pyrrolic nitrogen after replacing Zn^{2+} with H^+ (b). Fourier transform magnitude of k^3-weighted Zn EXAFS spectra of an NDC-Zn sample, calculated in the k range of 3.0−12 $Å^{-1}$ and R range of 1−4 Å. Experiment (solid blue line); best fit EXAFS model (dashed black line). The structure used as model for the EXAFS analysis is displayed in the inset: the Zn atom (dark gray sphere) is bound axially with one Cl atom (green sphere) and in plane to four nitrogen atoms (blue spheres) in the porphyrin complex, where carbon atoms are presented as light gray spheres (c). Isotherms of the NDC-M obtained from N_2 sorption measurement (d). Mössbauer spectra of NDC-Fe-HT recorded at 4.2 K with the corresponding fitting (e). Fourier transform magnitude of k^3-weighted Fe K-edge EXAFS spectra of an NDC-Fe-HT sample, calculated in the k range of 3.0−11.5 $Å^{-1}$ and R range of 1−3.8 Å. Experiment (solid orange line); best fit EXAFS model (dashed black line). The structure used as a model for the EXAFS analysis is displayed in the inset: the Fe atom (brown sphere) is bound axially with two O_2 molecules (red spheres) and in plane to four nitrogen atoms (blue spheres) in the porphyrin complex, where carbon atoms are presented as gray spheres (f).

precursors in an inert atmosphere to temperatures between ∼750 and ∼1300 °C.

1. Throughout heating, tetrapyrrolic $M-N_4$ sites are formed within defective carbon scaffolds.
2. Pyrolytic reactions generate the critical conductivity for electrocatalysts at ∼750 °C.
3. Pyridinic $M-N_4$ sites are formed in the case of catalytic graphitization.

https://doi.org/10.1021/jacs.1c04884
J. Am. Chem. Soc. 2021, 143, 18010−18019

According to this description of the formation of Fe−N−Cs, the dilemma of limited Fe−N_4 site concentration is only valid for pyridinic Fe−N_4 sites, since only their formation is connected to the pyrolytic decomposition of the Fe−N−C structure arising from carbothermal reduction. Indeed, Fe−N_4 sites were shown to be formed already slightly above 400 °C, where it is extremely unlikely that pyridinic Fe−N_4 sites will form.[25]

The stability of $Fe^{2+/3+}$ toward carbothermal reduction depends on their chemical environment, their concentration, and the chosen gas atmosphere.[26] If the carbothermal reduction is avoided until a sufficiently conductive Fe−N−C is obtained, only tetrapyrrolic Fe−N_4 sites should be present. This is consistent with the finding of a tetrapyrrolic model Fe−N−C by Zitolo and Jaouen et al., which was obtained with Fe concentrations as low as 0.5 wt %.[8]

In contrast to Fe, less precious metals, such as Zn, are also less sensitive toward carbothermal reduction.[26,27] Therefore, the selective synthesis of tetrapyrrolic M−N_4 sites should allow for higher concentrations. In fact, M−N_4 complexes for M−N−Cs with metals other than Fe were recently also subjected to intense research.[28,29] For example Zn−N−Cs were previously reported, and Zn is also present in the popular Fe−N−C preparation protocols involving specific metal−organic frameworks.[30,31]

We carried out DFT calculations on the Zn-coordinated isomers of the above presented tetrapyrrolic and pyridinic Fe−N_4 structures. Like in the case of the iron-based structures, the pyridinic structures have higher thermodynamic stability.

Curiously, the difference in energy is lower for Zn compared to Fe, indicating a higher stability of the kinetically favored tetrapyrrolic Zn−N_4 toward transformation to pyridinic sites. Due to back-bonding effects of the Fe d-orbitals, the Zn−N binding energy is however smaller compared to the Fe−N binding energy (Table 1). We recently discovered that Fe−N_4 active sites can be prepared by ion exchange from other M−N−C materials.[32,33] A relatively high concentration of atomically dispersed Fe−N_4 sites, corresponding to an Fe loading of 1.34 wt %, was obtained from Zn−N−Cs. This can be explained by our DFT calculations showing that the Zn−N bond is weaker than the Fe−N bond. The exchange of $Fe^{2+/3+}$ with Zn^{2+} ions consequently results in the more stable Fe−N−C SACs. However, after aqueous workup, insoluble Fe(III) oxide remained as an inorganic side phase, impeding proper determination of the resulting Fe−N_4 active site structure. Therefore, herein we attempt successive ion exchange reactions, at low temperature and at high temperature, targeting Fe−N−Cs with very high total Fe contents. The summarized synthetic strategy is illustrated in Scheme 1.

Preparation of Fe−N−C SACs. The catalysts are named as NDC-M, where M indicates the metal ions coordinated to the NDC solid-state ligand (here either Zn^{2+} or $Fe^{2+/3+}$) or NDC-M-HT when the high-temperature ion exchange treatment is performed. NDC-Zn was prepared by pyrolysis of a mixture of 1,2-dicyanobenzene and a binary $ZnCl_2$/LiCl (60 mol % LiCl) mixture in an Ar atmosphere at 800 °C for 1 h, followed by washing with 0.1 M hydrochloric acid and aqueous workup.[33] NDC-Zn was converted into NDC-Fe via a low-temperature ion exchange reaction at 170 °C (slightly above T_m) by stirring in an excess eutectic $FeCl_3$/LiCl salt melt for 5 h, with a workup as described before. NDC-Fe-HT was obtained subjecting NDC-Fe to a flash pyrolysis at 1000 °C in an Ar atmosphere for 20 min.

Materials Characterization. NDC-Zn is a hierarchically porous carbon material with a high specific surface area of 1433 m^2/g. X-ray powder diffraction (XRD) data are characteristic for amorphous carbons, which are highly defective in their structure (Figure 2a). The possibility to form a high concentration of defects is a consequence of the precursor choice. In our case, the surface stabilization provided by the $ZnCl_2$-based molten salt route provides structural versatility.[27,34]

Although a fraction of Zn^{2+} coordinated to N_4 sites might be removed by washing (ion exchange with protons), a residual Zn content of 2.95 wt % and a total N content of 13.61 wt % are prospective for a high concentration of N_4 coordination sites for the formation of Fe−N_4 sites (Table S3). Zn K-edge EXAFS analysis of an NDC-Zn sample was used to determine the local Zn structure in the pristine NDC-Zn (Figure 2c).

Structural parameters of the local Zn neighborhood (type and average number of neighbor atoms; the radii and the Debye−Waller factor of neighbor shells) are quantitatively resolved from the EXAFS spectra by comparing the measured EXAFS signal with the model signal, constructed *ab initio* using the FEFF6 program code,[35] based on Zn-porphyrin as a model structure, where Zn is bound to four pyrrolic nitrogen atoms and surrounded by respective carbon atoms with one additional Cl atom placed at an axial position (model parameters are given in Table S1).

An almost perfect fit is found (best fit parameters are given in Table S1), which shows that the Zn cations in NDC-Zn are indeed embedded into the carbon matrix in a macrocyclic tetrapyrrolic motif with the four pyrrolic N neighbors detected at 2.05 Å, similar to the Zn-porphyrin structure. The axial Cl atom is reasonably explained by the synthesis using $ZnCl_2$ or from the washing with HCl.

To further prove the pyrrolic nature of the Zn-imprinted N_4 cavities, NDC-Zn has been treated in strong, but not oxidizing 2.4 M aqueous HCl at 150 °C, in a closed vessel to replace Zn^{2+} ions with protons. XPS comparison of the pristine NDC-Zn and the obtained NDC-H sample shows a drastic drop in Zn content, while the N 1s spectra reveal that the N−Zn signal fully turns into pyrrolic N when Zn^{2+} ions are replaced by H^+ (Figure 2b, Figure S1 and Table S2), whereas the content of the other nitrogen species (i.e., graphitic, oxidized, and pyridinic) remains constant.

The finding of a single-site Zn−N−C being entirely composed of tetrapyrrolic Zn−N_4 embedded in the amorphous carbon structure allows for first conclusions on the proposed general principles of M−N−C syntheses. In fact, Zn ions undergo carbothermal reduction at higher temperature compared to Fe ions.[26] However, metallic Zn does not catalyze graphitization and already evaporates in the relevant temperature range (T_b = 907 °C). Hence the dissociative reorganization of the carbon structure in the present synthesis is obviously limited to the development of conductivity. The formation of pyridinic Zn−N_4 sites or transformation of tetrapyrrolic Zn−N_4 sites via dissociation of multiple bonds is expected to require much higher temperatures. The finding agrees well with our herein proposed M−N−C formation mechanism.

After the first ion exchange reaction, Zn^{2+} ions are partly removed and replaced by $Fe^{2+/3+}$ ions, which additionally occupy previously empty (i.e., protonated) tetrapyrrolic cavities. Due to the low temperature employed, it is reasonable to assume that the nitrogen content remains stable. The

https://doi.org/10.1021/jacs.1c04884
J. Am. Chem. Soc. 2021, 143, 18010−18019

decrease in wt % N is therefore an indication for the increased density of the material. This is also reflected in the N_2-sorption isotherm of NDC-Fe, which presents a downshift compared to NDC-Zn and consequently lower surface area and cumulative pore volume, but with an unchanged pore size distribution (Figure S2). This indicates that once the NDC solid-state ligand has been formed, its properties are retained throughout the ion exchange. The increased density of NDC-Fe is explained by the coordination of $Fe^{2+/3+}$ to protonated N_4 cavities as well as by the formation of iron oxide. XRD, like in case of NDC-Zn, reveals no indication of graphitization at the low temperature of 170 °C (Figure 2a). In order to study the kinetics of the substitution reaction at the N_4 site, we conducted a DFT study on the adsorption of an Fe atom on the various ZnN_4 motifs ($Fe@ZnN_4$) and *vice versa* ($Zn@FeN_4$) as well as the transition state between these states (Figure S4). For all tetrapyrrolic and pyridinic motifs, $Fe@ZnN_4$ exhibits a unique geometry with Fe anchored to two of the N atoms instead of the Zn center, resulting in a relatively strong adsorption. In contrast, Zn prefers a direct coordination to the Fe center in $Zn@FeN_4$ and exhibits weaker binding. The activation barriers between the two intermediates are relatively low (0.4−0.9 eV), suggesting that the ion exchange is kinetically feasible. Residual amounts of Zn after the ion exchange reaction may be explained by incomplete ion exchange caused by steric hindrance, e.g., accessibility from only one site of the active site. Furthermore, the adsorption of Zn to the $Fe-N_4$ sites is stable and explains the importance of the acidic workup.

The atomically dispersed nature of the iron species after ion exchange can nicely be observed by aberration-corrected annular-dark-field scanning transmission electron microscopy (ADF-STEM) shown in Figure S5. No crystalline phases are observed; however due to the folded nature of the carbon, the atomic Fe species may appear in some cases as clusters, if the carbon layers are overlapping. Low-temperature Mössbauer spectra more accurately reveal the Fe species present in the Fe−N−C catalyst than room-temperature spectra, since nanosized Fe(III) oxide can only be distinguished from the $Fe-N_4$ site doublets by the magnetic hyperfine splitting they exhibit at low temperatures.[36] We recorded the Mössbauer spectrum at 4.2 K for NDC-Fe (Figure S6) and find two doublets, characteristic for atomically dispersed Fe, as well as a sextet, indicative of nanosized oxidic Fe(III), which is tentatively assigned to ferrihydrite, a poorly crystalline hydrous ferric oxyhydroxide ($Fe_{10}O_{14}(OH)_2$).[37] Based on these results, the $Fe-N_4$ sites correspond to ∼1.34 wt % of the total Fe, indicating that the ion exchange at lower temperature is kinetically hampered.[38] Despite the presence of the oxidic iron, the structure of the $Fe-N_4$ formed should still be entirely of tetrapyrrolic nature.

It has been recently shown that nanosized oxidic iron can decompose and release Fe atoms, which can coordinate to NC defects in ZIF-based carbons.[39] Accordingly, a thermal treatment may similarly decompose the ferrihydrite and activate the oxidic iron for a successive ion exchange reaction to form more $Fe-N_4$ sites. Indeed, based on investigation of the thermal treatment of NDC-Fe at 1000 °C in Ar in TGA-MS experiments (described in the SI), the following mechanism for the coordination of Fe to empty (protonated) N_4 cavities is proposed:

Step 1: Dehydration of ferrihydrite:

$$Fe_{10}O_{14}(OH)_2 \rightarrow Fe_{10}O_{15} + H_2O$$

Step 2: Carbothermal reduction:

$$2\ Fe_{10}O_{15} + 5\ C \rightarrow 20\ FeO + 5\ CO_2$$

Step 3: Coordination of iron:

$$FeO + H_2{-}N_4 \rightarrow Fe{-}N_4 + H_2O$$

In fact, the decomposition of the inorganic particles is indicated by a lower gravimetric density of NDC-Fe-HT compared to NDC-Fe, which is reflected in the N_2-soprtion isotherms and subsequent increase of surface area to 1247 m^2/g. Moreover, in the pore size distribution plot, a 61% increase in porosity can be assigned to pores larger than 5 nm (Figure S2). This further points to ferrihydrite decomposition and the related disclosure of previously blocked porosity as well as the reactive activation of the carbon scaffold (step 2). Both phenomena are desirable to further improve the mass transport and the accessibility of active sites. Overall, the final NDC-Fe-HT catalyst shows hierarchical porosity, including microporosity, high external surface area, mesoporosity (with negligible hysteresis), and macroporosity, which is advantageous for catalytic applications in general. We have previously reported the impact of the pore design on the ORR performance for morphologically related nitrogen-doped carbons.[40]

Intriguingly, the XRD pattern of NDC-Fe-HT still shows no sign of graphitization, with a characteristic diffractogram for amorphous carbon, essentially unchanged compared to NDC-Zn (Figure 2a). This is the case despite the high pyrolytic temperature and the presence of a large quantity of Fe. Mössbauer spectroscopy (Figure 2e) reveals that the ferrihydrite phase of NDC-Fe (sextet signal) is almost quantitatively removed after the second heat treatment, while a second doublet (often referred to as D2), characteristic for atomically dispersed $Fe-N_4$ sites, arose. Indeed, 90% of the iron previously present as an oxidic side phase is converted into atomically dispersed $Fe-N_4$ sites in the high-temperature ion exchange (step 3), while no other side phases are formed. The synthetic strategy of N_4-site imprinting by means of Zn^{2+} ions and successive low- and high-temperature ion exchange successfully results in Fe−N−C SACs with a very high Fe loading of 3.46 wt % (according to ICP-MS, Table S3). The Mössbauer spectrum comprises three doublets, D1, D2, and D3, with relative intensities of 44% (D1), 42% (D2), and 8% (D3), which are characteristic of atomically dispersed $Fe-N_4$ sites. The doublets do not allow the assignment of pyrrolic or pyridinic $Fe-N_4$ sites.[16,41,42] However, the absence of side phases such as metallic iron, iron carbide, or iron nitride confirms that no graphitization has occurred, despite the high temperature of 1000 °C and the high total Fe content. Obviously, the stability of pyrrolic Fe−N bonds (at least in the tetrapyrrolic $Fe-N_4$ sites originating from Zn^{2+} imprinting) is high enough to overcome temperatures of 1000 °C, at least for some time, without undergoing carbothermal reduction, although the quantity and quality of the nitrogen doping is still affected by the heating (Table S3, Figure S3). Also, the mobile Fe species formed by the thermolysis of the ferrihydrite (step 2) do not lead to the formation of condensed metallic iron and hence no initiation of catalytic graphitization. This may be explained by fast trapping in preformed N_4 cavities.

Fe K-edge XANES spectroscopy was employed to determine the average Fe valence state in NDC-Fe-HT, deduced from the energy position of the Fe K-edge. The energy position of the absorption edge is correlated with the valence state of the

https://doi.org/10.1021/jacs.1c04884
J. Am. Chem. Soc. 2021, 143, 18010−18019

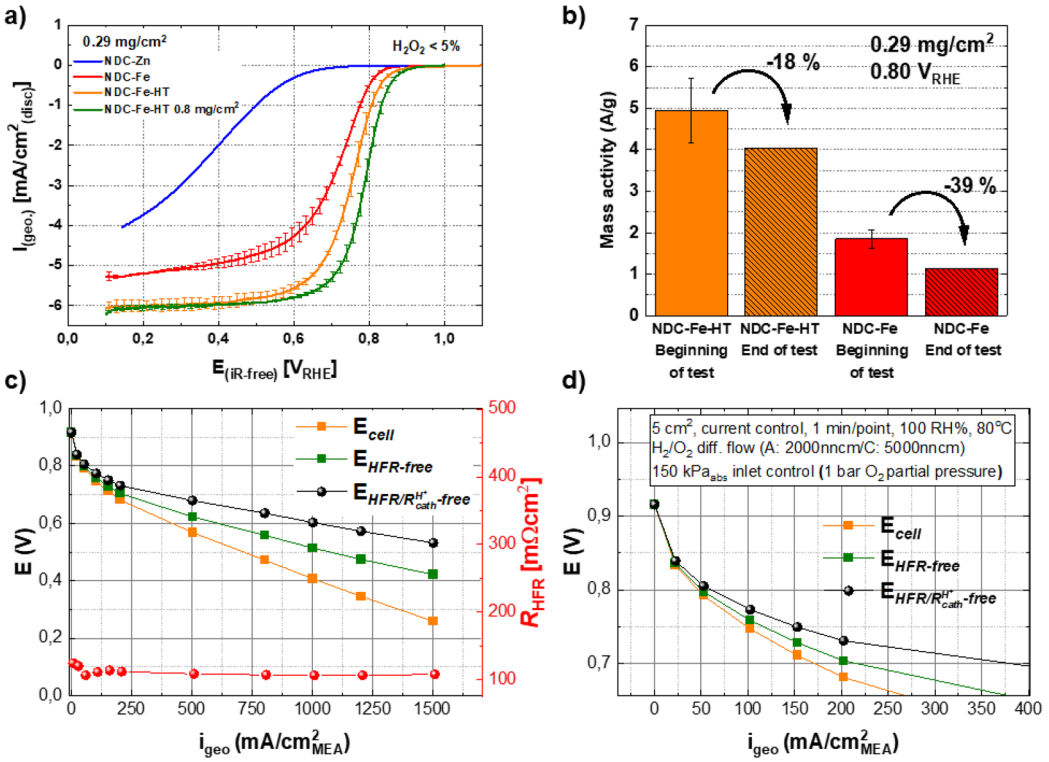

Figure 3. ORR curves of the three NDC-M recorded with an RDE setup at room temperature in O_2-saturated 0.1 M $HClO_4$ at 1600 rpm, 5 mV/s (anodic scans). All curves were corrected for capacitance contributions (a). Kinetic mass activity at 0.8 V calculated from RDE measurement of NDC-Fe (red) and NDC-Fe-HT (orange) before (full color) and after (line pattern) the stability test (b). Polarization curve of NDC-Fe-HT with a catalyst loading of 2 mg/cm^2 recorded in current-control mode (1 min-hold/point) at 80 °C, 150 kPa_{abs} inlet-controlled pressure, 100% RH for both reactants, and constant flows of 2000 nccm of H_2 on the anode and 5000 nccm of O_2 on the cathode. Anode and cathode were operated in counter flow mode. Measured cell voltage curve (orange), cell voltage corrected by the HFR (green), and corrected by the HFR and the effective proton conduction resistance (black) (c). Zoom-in of the low current density region of the polarization curve of NDC-Fe-HT (d).

absorbing atom in the sample. With increasing oxidation state the absorption edge is shifted to higher energies for about 4.5 eV per valence from Fe^{2+} to Fe^{3+}.[43−45] Comparing the XANES spectrum of NDC-Fe-HT with spectra of reference Fe compounds we found that the energy position of the Fe K-edge in NDC-Fe-HT is between the edge position of Fe^{3+} compounds and the edge position of $Fe^{2.67+}$ compound Fe_3O_4 (Figure S7), indicating that iron in the sample is predominantly in a trivalent state with about 20% of Fe^{2+} in the mixture. Fe K-edge EXAFS analysis was used to directly probe the local structure around Fe cations in an NDC-Fe-HT sample in the same way as for NDC-Zn. The results based on the tetrapyrrolic Fe-porphyrin molecule as model structure (Figure 2f) show that the Fe cations in NDC-Fe-HT are embedded into the carbon matrix in a macrocyclic, tetrapyrrolic motif, almost perfectly resembling the Fe-porphyrin structure (even the more distant coordination shell of carbon atoms is characteristic for Fe-porphyrin). In addition, each Fe cation is bound to oxygen on both axial positions (oxygen molecules according to the Fe−O distance), suggesting that the atomically dispersed Fe atoms, embedded into the high-surface-area, nongraphitized carbon scaffold, are accessible to the gas phase. This is not surprising, since formation of $Fe-N_4$ sites already required the accessibility to Fe ions/atoms. N_4-imprinted Zn−N−C SACs are indeed resulting in entirely tetrapyrrolic and entirely dispersed Fe−N−C SACs, with 3.46 wt % iron content, which is almost seven times as high as that for previously proven tetrapyrrolic single-site Fe−N−C SACs.[8]

Electrocatalytic Activity toward the ORR. The electrocatalytic activity of the catalysts was preliminarily evaluated using rotating disc electrode (RDE) testing in O_2-saturated 0.1 M $HClO_4$ (Figure 3a). NDC-Zn is not particularly active toward the ORR, showing a high overpotential and slow kinetics. However, the voltammetry results show sufficient conductivity due to the pyrolytic synthesis at 800 °C. The related blue curve in Figure 3a can be considered as background activity of the nitrogen-doped carbon scaffold.

After low-temperature ion exchange from Zn to Fe, the catalyst (NDC-Fe) becomes active toward the ORR by the formation of active sites showing a half-wave potential, $E_{1/2}$, already above 0.7 vs RHE. This implies a low ORR activity of $Zn-N_4$ sites in acid. After high-temperature treatment the catalyst gains even more activity, which is attributed to the increased active site density and accessibility derived from the decomposition of the iron oxide. The increased active site density is apparent from the upshift of the onset potential by ∼50 mV. The improved mass transport characteristics within the complex pore system are reflected in the increased slope in the mixed transport- and kinetically limited region.[40] With a high loading of 800 $\mu g/cm^2$, the catalyst exhibits an $E_{1/2}$ of about 0.8 V and an onset above 0.9 V. Since the half-wave potential is loading dependent and higher loadings come with a high film thickness and increased capacitive current, the mass activity is reported as a more reliable activity descriptor.[46] An intermediate loading of 290 $\mu g/cm^2$ is selected for all the experiments shown in continuation. NDC-Fe-HT shows a mass activity of 0.91 ± 0.16 A/g at 0.85 V and 4.95 ± 0.77 A/g

https://doi.org/10.1021/jacs.1c04884
J. Am. Chem. Soc. 2021, 143, 18010−18019

at 0.80 V, with a Tafel slope of 66 mV/dec (Figure S8), representing state-of-the-art performance for Fe−N−C electrocatalysts (Table S4). However, when compared with a reference catalyst prepared like NDC-Fe-HT but with the Fe source already present during the carbonization step (i.e., conventional synthetic method), the catalyst prepared via an active site imprinting strategy shows much higher activity, i.e., more than 20 times higher mass activity at 0.8 V and more than 100 mV in $E_{1/2}$. Comparative RDE tests corroborate that the activity gain is strictly connected to a high-temperature ion exchange, i.e., to the ferrihydrite decomposition within active site imprinted NDC-Zn (Figure S9).

The stability of NDC-Fe and NDC-Fe-HT was evaluated by cycling in O_2-saturated 0.1 M $HClO_4$ between 0.4 and 0.8 V with a relatively slow scan rate of 50 mV/s. The increased active site density after the second ion exchange shows a positive impact not only on the activity but also on the stability of the catalyst, with NDC-Fe-HT showing only 18% loss in mass activity at 0.8 V vs 39% loss for NDC-Fe after 500 cycles at 50 mV/s (Figure 3b). This corresponds to downshifts in half-wave potentials $E_{1/2}$ of 20 mV for NDC-Fe-HT and 40 mV for NDC-Fe. This effect may be understood with the additional activity of Fe−N_4 sites toward the reduction of peroxide, which is a harmful reaction intermediate of the ORR, especially in an acidic electrolyte.[47] NDC-Fe-HT, indeed, shows a very high selectivity toward a 4e$^-$ reduction. Rotating ring disc electrode (RRDE) experiments with different catalyst loading were employed to quantify the H_2O_2 production. For the Fe−N−C catalyst, a substantial increase in the fraction of H_2O_2 produced is usually observed when the catalyst loading is decreased.[48] NDC-Fe-HT shows only ∼3% H_2O_2 even with a low catalyst loading of 0.095 mg/cm^2, which is about seven times less compared to the commercial Fe−N−C benchmark catalyst (Pajarito Powder) measured with similar loading (Figure S10). The high selectivity, which approaches the ones observed for Pt/C catalysts, may intuitively be explained with the single-site nature of the catalyst. If tetrapyrrolic sites are more selective compared to pyridinic Fe−N_4 sites remains speculative until Fe−N−Cs with similar morphology are developed with entirely pyridinic Fe−N_4 sites.[49] Our results indicate that this may be hardly possible with bottom-up synthesis approaches. Additional stability measurements with a faster scan rate (250 mV/s) confirm the high stability of NDC-Fe-HT, only losing 31 mV in half-wave potential $E_{1/2}$ after 10k cycles in O_2-saturated 0.1 M $HClO_4$, (Figure S11a). At the same time the selectivity toward a 4e$^-$ reduction is fully retained (Figure S11b). Upon cycling, no degradation is observed in an Ar-saturated electrolyte, respectively (Figure S11a).

Single-cell (5 cm^2) proton exchange membrane fuel cell (PEMFC) testing of NDC-Fe-HT with a loading of 2 mg/cm^2 was performed in H_2/O_2 under the DOE proposed conditions to determine the ORR activity and in H_2/air to examine the stability in conditions relevant to commercial application.[50] The single-site tetrapyrrolic Fe−N−C SAC shows state-of-the-art ORR activity in H_2/O_2 (Figure 3c and d and Table S5), with a high mass activity of 2.3 A/g already at 0.9 V HFR-free cell voltage, where only the onset of activity is observed in the RDE activity test.

Compared to thin catalyst layers in the range of 10 μm for Pt/C catalysts, the thicker Fe−N−C catalyst layers (∼50 μm for NDC-Fe-HT) go along with larger high-frequency resistances (HFRs) and related voltage losses (Figure 3, E_{cell}). Even though the packing factor f for NDC-Fe-HT is smaller than for the commercial Fe−N−C standard ($f_{NDC\text{-}Fe\text{-}HT}$ ≈ 22−25 μm mg^{-1} cm^{-2} vs $f_{Pajarito}$ ≈ 30 μm mg^{-1} cm^{-2}), further reduction may be a promising target for future catalyst development.

Furthermore, the stability of Fe−N−C catalysts is a key issue for the practical PEMFC application and has been addressed in recent research.[51] Similar to the testing protocol proposed by Banham et al. for the first commercial PGM-free based PEMFC system,[52] the durability of NDC-Fe-HT was investigated in single-cell tests in H_2/air at 80 °C and 100% RH by applying constant current at 140 mA/cm^2 and cell voltage at 0.6 V under this condition. A similar result to the report on the commercial system was obtained,[52] with a fast degradation step observed in the initial ∼10 min of testing, before the cell voltage reaches a relatively stable, slowly decreasing trend. After 12 h of operation, the cell voltage only decreased by ∼12%, suggesting a very promising stability of atomically dispersed Fe−N−C SACs based on tetrapyrrolic Fe−N_4 sites (Figure S11c).

CONCLUSION

Herein we utilized a Zn−N−C synthesis as a pyrolytic Zn^{2+} template ion reaction to imprint a high concentration of tetrapyrrolic N_4 coordination sites into a conductive carbon. Consecutive Zn to Fe ion exchange reactions result in a very high concentration of tetrapyrrolic Fe−N_4 sites, the motif of the heme molecule, that originally inspired the development of M−N-C catalysts.[53] The Fe−N_4 site density, with an Fe loading of 3.46 wt % or 0.72 at. %, of the very selective and stable catalyst surpasses the typical limit for Fe−N−Cs, and higher values seem to be a matter of optimization only.

General principles of M−N−C syntheses are revealed and explain the structural complexity of Fe−N−C/Co−N−C materials, their challenging assignment of active sites, and the previously complicated structure−performance relation. The formation of kinetically preferred tetrapyrrolic Fe−N−C electrocatalysts is interfered by the carbothermal reduction of Fe before critical conductivity is reached. The carbothermal reduction catalyzes the formation of the thermodynamically more stable pyridinic sites, however also leading to morphological destruction (the dilemma). Kinetically preferred tetrapyrrolic Zn−N−Cs can be heated above 900 °C, reaching critical conductivity. Consecutive ion exchange leads to selective formation of tetrapyrrolic Fe−N−Cs, even in high concentrations.

The herein obtained iron loading outmatches the maximum loading of current tetrapyrrolic single-site Fe−N−Cs by more than six times. The possibility to direct the synthesis toward specific active site geometries further unlocks the tool of increasing the specific activity of M−N−C catalysts in general and Fe−N−C SACs in particular. This iron-rich and entirely tetrapyrrolic Fe−N−C SAC, not yet optimized regarding mass transport and electrode design, already reaches state-of-the-art Fe−N−C performance in RDE and single-cell PEMFC tests, additionally showing very promising durability throughout fuel cell operation.

ASSOCIATED CONTENT

Supporting Information

The Supporting Information is available free of charge at https://pubs.acs.org/doi/10.1021/jacs.1c04884.

https://doi.org/10.1021/jacs.1c04884
J. Am. Chem. Soc. 2021, 143, 18010−18019

Experimental section; materials characterization; DFT tables; activity comparison with literature; and TGA-MS analysis (PDF)

AUTHOR INFORMATION

Corresponding Author

Tim-Patrick Fellinger − *Chair of Technical Electrochemistry, Department of Chemistry and Catalysis Research Center, Technische Universität München (TUM), 85748 Garching, Germany; Bundesanstalt für Materialforschung und -prüfung (BAM), 12203 Berlin, Germany;* orcid.org/0000-0001-6332-2347; Email: tim-patrick.fellinger@bam.de

Authors

Davide Menga − *Chair of Technical Electrochemistry, Department of Chemistry and Catalysis Research Center, Technische Universität München (TUM), 85748 Garching, Germany*

Jian Liang Low − *Chair for Theoretical Chemistry, Institut für Chemie und Biochemie, Freie Universität Berlin, 14195 Berlin, Germany*

Yan-Sheng Li − *Chair of Technical Electrochemistry, Department of Chemistry and Catalysis Research Center, Technische Universität München (TUM), 85748 Garching, Germany*

Iztok Arčon − *Laboratory of Quantum Optics, University of Nova Gorica, SI-5001 Nova Gorica, Slovenia; Department of Low and Medium Energy Physics, Jožef Stefan Institute, SI-1001 Ljubljana, Slovenia*

Burak Koyutürk − *Chair of Technical Electrochemistry, Department of Chemistry and Catalysis Research Center, Technische Universität München (TUM), 85748 Garching, Germany*

Friedrich Wagner − *Department of Physics, Technische Universität München (TUM), 85748 Garching, Germany*

Francisco Ruiz-Zepeda − *Department of Materials Chemistry, National Institute of Chemistry, SI-1000 Ljubljana, Slovenia*

Miran Gaberšček − *Department of Materials Chemistry, National Institute of Chemistry, SI-1000 Ljubljana, Slovenia*

Beate Paulus − *Chair for Theoretical Chemistry, Institut für Chemie und Biochemie, Freie Universität Berlin, 14195 Berlin, Germany*

Complete contact information is available at: https://pubs.acs.org/10.1021/jacs.1c04884

Author Contributions

All authors have given approval to the final version of the manuscript.

Notes

The authors declare no competing financial interest.

ACKNOWLEDGMENTS

The German Federal Ministry of Economic Affairs and Energy (BMWi) is acknowledged for funding within the Verbundproject innoKA (Project No. 03ET6096A) and Dr. Gilleßen from PTJ for constructive supervision of the project. Prof. Hubert Gasteiger is acknowledged for hosting the group and for providing an educative and supportive atmosphere. Part of this research was supported by the Slovenian Research Agency (P1-0112) and by the project CALIPSOplus under the Grant Agreement 730872 from the EU Framework Programme for Research and Innovation HORIZON 2020. Access to the synchrotron radiation facilities of ELETTRA (beamline XAFS, project 20185092) is acknowledged. We would like to thank Giuliana Aquilanti, Luca Olivi, and Simone Pollastri of ELETTRA, for support and expert advice on beamline operation.

REFERENCES

(1) Qiao, S.; Liu, J.; Kawi, S. Editorial: Electrocatalysis - From Batteries to Clean Energy Conversion. *ChemCatChem* **2019**, *11* (24), 5835−5837.

(2) Anastas, P.; Eghbali, N. Green Chemistry: Principles and Practice. *Chem. Soc. Rev.* **2010**, *39* (1), 301−312.

(3) Wang, A.; Li, J.; Zhang, T. Heterogeneous single-atom catalysis. *Nature Reviews Chemistry* **2018**, *2* (6), 65−81.

(4) Cheng, N.; Zhang, L.; Doyle-Davis, K.; Sun, X. Single-Atom Catalysts: From Design to Application. *Electrochemical Energy Reviews* **2019**, *2* (4), 539−573.

(5) Gasteiger, H. A.; Kocha, S. S.; Sompalli, B.; Wagner, F. T. Activity benchmarks and requirements for Pt, Pt-alloy, and non-Pt oxygen reduction catalysts for PEMFCs. *Appl. Catal., B* **2005**, *56* (1−2), 9−35.

(6) Lefèvre, M.; Proietti, E.; Jaouen, F.; Dodelet, J.-P. Iron-Based Catalysts with Improved Oxygen Reduction Activity in Polymer Electrolyte Fuel Cells. *Science* **2009**, *324* (5923), 71−74.

(7) Kramm, U. I.; Herrmann-Geppert, I.; Fiechter, S.; Zehl, G.; Zizak, I.; Dorbandt, I.; Schmeißer, D.; Bogdanoff, P. Effect of iron-carbide formation on the number of active sites in Fe-N-C catalysts for the oxygen reduction reaction in acidic media. *J. Mater. Chem. A* **2014**, *2* (8), 2663−2670.

(8) Zitolo, A.; Goellner, V.; Armel, V.; Sougrati, M.-T.; Mineva, T.; Stievano, L.; Fonda, E.; Jaouen, F. Identification of catalytic sites for oxygen reduction in iron- and nitrogen-doped graphene materials. *Nat. Mater.* **2015**, *14* (9), 937−942.

(9) Huang, X.; Shen, T.; Zhang, T.; Qiu, H.; Gu, X.; Ali, Z.; Hou, Y. Efficient Oxygen Reduction Catalysts of Porous Carbon Nanostructures Decorated with Transition Metal Species. *Adv. Energy Mater.* **2020**, *10*, 1900375.

(10) Artyushkova, K.; Rojas-Carbonell, S.; Santoro, C.; Weiler, E.; Serov, A.; Awais, R.; Gokhale, R. R.; Atanassov, P. Correlations between Synthesis and Performance of Fe-Based PGM-Free Catalysts in Acidic and Alkaline Media: Evolution of Surface Chemistry and Morphology. *ACS Applied Energy Materials* **2019**, *2* (8), 5406−5418.

(11) Sahraie, N. R.; Kramm, U. I.; Steinberg, J.; Zhang, Y.; Thomas, A.; Reier, T.; Paraknowitsch, J.-P.; Strasser, P. Quantifying the density and utilization of active sites in non-precious metal oxygen electroreduction catalysts. *Nat. Commun.* **2015**, *6*, 8618.

(12) Wan, X.; Liu, X.; Li, Y.; Yu, R.; Zheng, L.; Yan, W.; Wang, H.; Xu, M.; Shui, J. Fe-N-C electrocatalyst with dense active sites and efficient mass transport for high-performance proton exchange membrane fuel cells. *Nature Catalysis* **2019**, *2* (3), 259−268.

(13) Liu, Q.; Liu, X.; Zheng, L.; Shui, J. The Solid-Phase Synthesis of an Fe-N-C Electrocatalyst for High-Power Proton-Exchange Membrane Fuel Cells. *Angew. Chem., Int. Ed.* **2018**, *57* (5), 1204−1208.

(14) Wan, X.; Chen, W.; Yang, J.; Liu, M.; Liu, X.; Shui, J. Synthesis and Active Site Identification of Fe-N-C Single-Atom Catalysts for the Oxygen Reduction Reaction. *ChemElectroChem* **2019**, *6* (2), 304−315.

(15) Chung, H. T.; Cullen, D. A.; Higgins, D.; Sneed, B. T.; Holby, E. F.; More, K. L.; Zelenay, P. Direct atomic-level insight into the active sites of a high-performance PGM-free ORR catalyst. *Science (Washington, DC, U. S.)* **2017**, *357* (6350), 479−484.

(16) Marshall-Roth, T.; Libretto, N. J.; Wrobel, A. T.; Anderton, K. J.; Pegis, M. L.; Ricke, N. D.; Voorhis, T. V.; Miller, J. T.; Surendranath, Y. A pyridinic Fe-N4 macrocycle models the active sites in Fe/N-doped carbon electrocatalysts. *Nat. Commun.* **2020**, *11* (1), No. 5283.

(17) Zhang, N.; Zhou, T.; Chen, M.; Feng, H.; Yuan, R.; Zhong, C. A.; Yan, W.; Tian, Y.; Wu, X.; Chu, W.; Wu, C.; Xie, Y. High-purity pyrrole-type FeN4 sites as a superior oxygen reduction electrocatalyst. *Energy Environ. Sci.* **2020**, *13* (1), 111−118.
(18) Zhang, J.; Zheng, C.; Zhang, M.; Qiu, Y.; Xu, Q.; Cheong, W.-C.; Chen, W.; Zheng, L.; Gu, L.; Hu, Z.; Wang, D.; Li, Y. Controlling N-doping type in carbon to boost single-atom site Cu catalyzed transfer hydrogenation of quinoline. *Nano Res.* **2020**, *13* (11), 3082−3087.
(19) Zhao, K.; Nie, X.; Wang, H.; Chen, S.; Quan, X.; Yu, H.; Choi, W.; Zhang, G.; Kim, B.; Chen, J. G. Selective electroreduction of CO_2 to acetone by single copper atoms anchored on N-doped porous carbon. *Nat. Commun.* **2020**, *11* (1), No. 2455.
(20) Ogawa, S.; Yamaguchi, T.; Gotoh, N. Preparation of a conjugated tautomer of 1,14:7,8-diethenotetrapyrido-[2,1,6-de:2',1',6'-gh:2,1,6-kl:2,1,6na][1,3,5,8,10,12]hexa-azacyclotetradecine and its metal derivatives. *J. Chem. Soc., Perkin Trans. 1* **1974**, No. 0, 976−978.
(21) Peng, P.; Shi, L.; Huo, F.; Mi, C.; Wu, X.; Zhang, S.; Xiang, Z. A pyrolysis-free path toward superiorly catalytic nitrogen-coordinated single atom. *Science Advances* **2019**, *5* (8), No. eaaw2322.
(22) Peng, P.; Shi, L.; Huo, F.; Zhang, S.; Mi, C.; Cheng, Y.; Xiang, Z. In Situ Charge Exfoliated Soluble Covalent Organic Framework Directly Used for Zn-Air Flow Battery. *ACS Nano* **2019**, *13* (1), 878−884.
(23) Narita, A.; Wang, X.-Y.; Feng, X.; Müllen, K. New advances in nanographene chemistry. *Chem. Soc. Rev.* **2015**, *44* (18), 6616−6643.
(24) Glatzel, S.; Schnepp, Z.; Giordano, C. From Paper to Structured Carbon Electrodes by Inkjet Printing. *Angew. Chem., Int. Ed.* **2013**, *52* (8), 2355−2358.
(25) Li, J.; Zhang, H.; Samarakoon, W.; Shan, W.; Cullen, D. A.; Karakalos, S.; Chen, M.; Gu, D.; More, K. L.; Wang, G.; Feng, Z.; Wang, Z.; Wu, G. Thermally Driven Structure and Performance Evolution of Atomically Dispersed FeN4 Sites for Oxygen Reduction. *Angew. Chem., Int. Ed.* **2019**, *58* (52), 18971−18980.
(26) Ellingham, H. J. T. Transactions and Communications. *J. Soc. Chem. Ind., London* **1944**, *63* (5), 125−160.
(27) Graglia, M.; Pampel, J.; Hantke, T.; Fellinger, T.-P.; Esposito, D. Nitro Lignin-Derived Nitrogen-Doped Carbon as an Efficient and Sustainable Electrocatalyst for Oxygen Reduction. *ACS Nano* **2016**, *10* (4), 4364−4371.
(28) Luo, F.; Roy, A.; Silvioli, L.; Cullen, D. A.; Zitolo, A.; Sougrati, M. T.; Oguz, I. C.; Mineva, T.; Teschner, D.; Wagner, S.; Wen, J.; Dionigi, F.; Kramm, U. I.; Rossmeisl, J.; Jaouen, F.; Strasser, P. P-block single-metal-site tin/nitrogen-doped carbon fuel cell cathode catalyst for oxygen reduction reaction. *Nat. Mater.* **2020**, *19* (11), 1215−1223.
(29) Xie, X.; He, C.; Li, B.; He, Y.; Cullen, D. A.; Wegener, E. C.; Kropf, A. J.; Martinez, U.; Cheng, Y.; Engelhard, M. H.; Bowden, M. E.; Song, M.; Lemmon, T.; Li, X. S.; Nie, Z.; Liu, J.; Myers, D. J.; Zelenay, P.; Wang, G.; Wu, G.; Ramani, V.; Shao, Y. Performance enhancement and degradation mechanism identification of a single-atom Co-N-C catalyst for proton exchange membrane fuel cells. *Nature Catalysis* **2020**, *3* (12), 1044−1054.
(30) Wang, Q.; Ina, T.; Chen, W.-T.; Shang, L.; Sun, F.; Wei, S.; Sun-Waterhouse, D.; Telfer, S. G.; Zhang, T.; Waterhouse, G. I. N. Evolution of Zn(II) single atom catalyst sites during the pyrolysis-induced transformation of ZIF-8 to N-doped carbons. *Sci. Bull.* **2020**, *65*, 1743.
(31) Proietti, E.; Jaouen, F.; Lefèvre, M.; Larouche, N.; Tian, J.; Herranz, J.; Dodelet, J.-P. Iron-based cathode catalyst with enhanced power density in polymer electrolyte membrane fuel cells. *Nat. Commun.* **2011**, *2* (1), 416.
(32) Mehmood, A.; Pampel, J.; Ali, G.; Ha, H. Y.; Ruiz-Zepeda, F.; Fellinger, T.-P. Facile Metal Coordination of Active Site Imprinted Nitrogen Doped Carbons for the Conservative Preparation of Non-Noble Metal Oxygen Reduction Electrocatalysts. *Adv. Energy Mater.* **2018**, *8* (9), No. 1701771.
(33) Menga, D.; Ruiz-Zepeda, F.; Moriau, L.; Šala, M.; Wagner, F.; Koyutürk, B.; Bele, M.; Petek, U.; Hodnik, N.; Gaberšček, M.; Fellinger, T.-P. Active-Site Imprinting: Preparation of Fe-N-C Catalysts from Zinc Ion-Templated Ionothermal Nitrogen-Doped Carbons. *Adv. Energy Mater.* **2019**, *9* (43), 1902412.
(34) Chang, Y.; Antonietti, M.; Fellinger, T.-P. Synthesis of Nanostructured Carbon through Ionothermal Carbonization of Common Organic Solvents and Solutions. *Angew. Chem., Int. Ed.* **2015**, *54* (18), 5507−5512.
(35) Rehr, J. J.; Albers, R. C.; Zabinsky, S. I. High-order multiple-scattering calculations of x-ray-absorption fine structure. *Phys. Rev. Lett.* **1992**, *69* (23), 3397−3400.
(36) Sougrati, M. T.; Goellner, V.; Schuppert, A. K.; Stievano, L.; Jaouen, F. Probing active sites in iron-based catalysts for oxygen electro-reduction: A temperature-dependent 57Fe Mössbauer spectroscopy study. *Catal. Today* **2016**, *262*, 110−120.
(37) Bishop, J. L.; Pieters, C.; Burns, R. G. Reflectance and Mössbauer spectroscopy of ferrihydrite-montmorillonite assemblages as Mars soil analog materials. *Geochim. Cosmochim. Acta* **1993**, *57* (19), 4583−4595.
(38) Baker, H.; Hambright, P.; Wagner, L.; Ross, L. Metal ion interactions with porphyrins. I. Exchange and substitution reactions. *Inorg. Chem.* **1973**, *12* (9), 2200−2202.
(39) Li, J.; Jiao, L.; Wegener, E.; Richard, L. L.; Liu, E.; Zitolo, A.; Sougrati, M. T.; Mukerjee, S.; Zhao, Z.; Huang, Y.; Yang, F.; Zhong, S.; Xu, H.; Kropf, A. J.; Jaouen, F.; Myers, D. J.; Jia, Q. Evolution Pathway from Iron Compounds to Fe1(II)-N4 Sites through Gas-Phase Iron during Pyrolysis. *J. Am. Chem. Soc.* **2020**, *142* (3), 1417−1423.
(40) Pampel, J.; Fellinger, T.-P. Opening of Bottleneck Pores for the Improvementof Nitrogen Doped Carbon Electrocatalysts. *Adv. Energy Mater.* **2016**, *6* (8), No. 1502389.
(41) Wagner, S.; Auerbach, H.; Tait, C. E.; Martinaiou, I.; Kumar, S. C. N.; Kübel, C.; Sergeev, I.; Wille, H.-C.; Behrends, J.; Wolny, J. A.; Schünemann, V.; Kramm, U. I. Elucidating the Structural Composition of an Fe-N-C Catalyst by Nuclear- and Electron-Resonance Techniques. *Angew. Chem., Int. Ed.* **2019**, *58* (31), 10486−10492.
(42) Mineva, T.; Matanovic, I.; Atanassov, P.; Sougrati, M.-T.; Stievano, L.; Clémancey, M.; Kochem, A.; Latour, J.-M.; Jaouen, F. Understanding Active Sites in Pyrolyzed Fe-N-C Catalysts for Fuel Cell Cathodes by Bridging Density Functional Theory Calculations and 57Fe Mössbauer Spectroscopy. *ACS Catal.* **2019**, *9* (10), 9359−9371.
(43) Arčon, I.; Piccolo, O.; Paganelli, S.; Baldi, F. *BioMetals* **2012**, *25* (5), 875−881.
(44) Arčon, I.; Kolar, J.; Kodre, A.; Hanžel, D.; Strlič, M. XANES analysis of Fe valence in iron gall inks. *X-Ray Spectrom.* **2007**, *36* (3), 199−205.
(45) Kuezma, M.; Dominko, R.; Hanžel, D.; Kodre, A.; Arčon, I.; Meden, A.; Gaberšček, M. Detailed In Situ Investigation of the Electrochemical Processes in Li_2FeTiO_4 Cathodes. *J. Electrochem. Soc.* **2009**, *156* (10), A809.
(46) Beltrán, D. E.; Litster, S. Half-Wave Potential or Mass Activity? Characterizing Platinum Group Metal-Free Fuel Cell Catalysts by Rotating Disk Electrodes. *ACS Energy Letters* **2019**, *4* (5), 1158−1161.
(47) Bae, G.; Chung, M. W.; Ji, S. G.; Jaouen, F.; Choi, C. H. pH Effect on the H2O2-Induced Deactivation of Fe-N-C Catalysts. *ACS Catal.* **2020**, *10* (15), 8485−8495.
(48) Bonakdarpour, A.; Lefevre, M.; Yang, R.; Jaouen, F.; Dahn, T.; Dodelet, J.-P.; Dahn, J. R. Impact of Loading in RRDE Experiments on Fe-N-C Catalysts: Two- or Four-Electron Oxygen Reduction? *Electrochem. Solid-State Lett.* **2008**, *11* (6), B105−B108.
(49) Paulus, U. A.; Schmidt, T. J.; Gasteiger, H. A.; Behm, R. J. Oxygen reduction on a high-surface area Pt/Vulcan carbon catalyst: a thin-film rotating ring-disk electrode study. *J. Electroanal. Chem.* **2001**, *495* (2), 134−145.

https://doi.org/10.1021/jacs.1c04884
J. Am. Chem. Soc. 2021, 143, 18010−18019

(50) US Department of Energy. *Multi-Year Research, Development, and Demonstration Plan*; Fuel Cell Technologies Office. Multi-Year Research, D., and Demonstration Plan, 2017.
(51) Shao, Y.; Dodelet, J.-P.; Wu, G.; Zelenay, P. PGM-Free Cathode Catalysts for PEM Fuel Cells: A Mini-Review on Stability Challenges. *Adv. Mater.* **2019**, *31* (31), 1807615.
(52) Banham, D.; Kishimoto, T.; Zhou, Y.; Sato, T.; Bai, K.; Ozaki, J.-i.; Imashiro, Y.; Ye, S. Critical advancements in achieving high power and stable nonprecious metal catalyst-based MEAs for real-world proton exchange membrane fuel cell applications. *Sci. Adv.* **2018**, *4* (3), eaar7180.
(53) Cook, A. Catalytic properties of the phthalocyanines. Part I. Catalase properties. *J. Chem. Soc.* **1938**, *0*, 1761−1769.

https://doi.org/10.1021/jacs.1c04884
J. Am. Chem. Soc. 2021, 143, 18010−18019

Supporting Information

Resolving the Dilemma of Fe-N-C Catalysts by the Selective Synthesis of Tetrapyrrolic Active Sites via Imprinting Strategy

Davide Menga, Jian Liang Low, Yan-Sheng Li, Iztok Arčon, Burak Koyutürk, Friedrich Wagner, Francisco Ruiz-Zepeda, Miran Gaberšček, Beate Paulus and Tim-Patrick Fellinger[*]

Experimental Section

Synthesis of NDC-Zn and conventional Fe-N-C:

In a typical synthesis, 0.7 g of 1,2-dicyanobenzene was mixed with 7 g of a 60 mol% LiCl/$ZnCl_2$ mixture in a Ar-filled glovebox. The resulting powder was placed in an alumina crucible and heated with a heating rate of 10 K/min to 800 °C in a tube furnace with a constant Ar flow. After 1 h at 800 °C, the sample was let to cool down to room temperature. The obtain material was ground, washed with 0.1 M HCl for several hours and dried. The synthesis of the conventional Fe-N-C is analogous but with the addition of 16 mg of $FeCl_3$ to the mixture.

Synthesis of NDC-Fe:

NDC-Zn was employed as starting material in the ion exchange reaction from Zn to Fe. Typically, NDC-Zn was degassed in a Büchi oven at 250 °C under vacuum and afterwards mixed with a eutectic mixture of LiCl/$FeCl_3$ in a Schlenk tube in a Ar-filled glovebox. The closed tube was heated up to 175 °C to melt the salt mixture and the sample was stirred for 5 h to ensure complete ion exchange. Once at room temperature, the sample was washed with H_2O to remove the salt mixture and afterwards washed with 0.1 M HCl for several hours and dried.

Synthesis of NDC-Fe-HT:

For the high temperature treatment, 1 g of NDC-Fe was placed in an alumina crucible and pushed inside a tube furnace pre-heated at 1000 °C under Ar atmosphere. After 20 minutes the furnace was turned off and opened to quickly cool down the sample to room temperature.

Characterization:

Mössbauer spectra were recorded with a standard transmission spectrometer using a sinusoidal velocity waveform. The measurements at 4.2 K were performed with both the source of 57Co in rhodium and the absorber in the liquid He bath of a cryostat. The spectra were fitted with suitable Lorentzian lines grouped into electric quadrupole doublets and sextets arising from magnetic hyperfine splitting. MOSFIT software package version 2.2 (FAST-COMTEC GmbH) was used for the fitting of the spectra. Isomer shifts measured in this way are relative to the source at 4.2 K. In order to refer them to α-Fe at ambient temperature, 0.245 mm s^{-1} was added to the measured shifts.

XRD data were recorded with a StadiP diffractometer with Cu Kα radiation (λ = 1.54060, 50 kV, 30 mA, germanium (111)).

Fe and Zn K-edge absorption spectra of NDC-Fe-HT and NDC-Zn sample, respectively, were measured at room temperature in transmission detection mode at the XAFS beamline of the ELETTRA synchrotron radiation facility in Trieste, Italy. A Si (111) double crystal monochromator was used with 0.8 eV resolution at 8 keV. Higher-order harmonics were effectively eliminated by detuning the monochromator crystals to 60% of the rocking curve maximum. The intensity of the monochromatic X-ray beam was measured by three consecutive 30 cm long ionization detectors respectively filled with the following gas mixtures: 580 mbar N2 and 1420 mbar He; 1000 mbar N2, 90 mbar Ar and 910 mbar He; 350 mbar Ar, 1000 mbar N2 and 650 mbar He. In the XANES region equidistant energy steps of 0.25 eV were used, while for the EXAFS region equidistant k steps of 0.03 $Å^{-1}$ were adopted with an integration time of 1 s/step. The exact energy calibration was established with simultaneous absorption measurement on a 5-micron thick Fe or Zn metal foil placed between the second and the third ionization chamber. Absolute energy reproducibility of the measured spectra was ±0.03 eV. The analysis of XANES and EXAFS spectra was performed with the IFEFFIT program package.[1]

TGA-MS was performed on a Mettler Toledo TGA/DSC 1 instrument connected to a Pfeiffer Vacuum Thermostar mass spectrometer in Ar atmosphere with a heating rate of 10 K/min and two

isothermal steps at 150 °C and 250 °C for 20 and 45 minutes respectively to ensure the complete outgas of the samples.

N_2 sorption measurements were performed using a Quantachrome Autosorb iQ2 after outgassing the samples overnight at 250 °C under vacuum. Specific surface areas were determined using Micropore BET Assistant supplied by Quantachrome ASiQwin software. Pore size distributions were calculated with the quenched-solid density functional theory (QSDFT) method (slit/cylindrical pores) with an error ~ 0.2 %.

XPS measurements were performed using a Kratos Axis Supra spectrometer with monochromatized Al Kα radiation. Spectra were acquired with 0.1 eV step size and corrected with respect to C 1s peak at 284.7 eV. Data analysis was performed with ESCAA software.

Aberration corrected scanning transmission electron microscopy (AC-STEM) was performed in a JEOL ARM 200CF microscope imaging with a probe current of ~14 pA and operated at 80 kV.

RDE tests:

Electrochemical measurements were performed in a three-electrode glass cell using 0.1 M $HClO_4$ as electrolyte, diluted with deionized ultrapure water (Milli-Q Integral 5, 18.2 MΩ cm) from a 60% solution (Guaranteed Reagent, Kanto Chemical). Autolab PGSTAT302N (Metrohm) potentiostat was employed for the measurements. Au wire was used as the counter electrode and a freshly calibrated RHE was used as the reference electrode. The solution resistance was determined by electrochemical impedance spectroscopy. The reported polarization curves for ORR were corrected for capacitive currents by subtracting from the curves recorded in O_2-saturated electrolyte the ones recorded in Ar-saturated electrolyte. The catalyst inks were prepared by dispersing 5 mg of catalyst powder in 840 μL of N,N-dimethylformamide (≥99.8, Fisher Scientific) and 50 μL of 5 wt% Nafion suspension (Sigma-Aldrich), followed by sonication for 30 min. 10 μL of ink was drop-cast onto a well-polished glassy carbon electrode (Ø = 5 mm, obtained from Pine Research Instrumentation) and dried under an infrared heater for 60 min. The resulting catalyst loading was 290 μg/cm^2. The accelerated stress

tests were conducted by cycling between 0.4 and 0.8 V at 400 rpm and with a scan rate of 50 mV/s for the short test and 250 mV/s for the long one.

RRDE technique was employed to quantify the H_2O_2 production with different catalyst loading. The platinum ring was held at 1.2 V_{RHE} and a value of -0.255 was used for the collection efficiency.[2]

MEA preparation and PEMFC tests:

Catalyst inks were prepared by dispersing the catalyst powder in a mixture of water, 1-propanol, and ionomer solution, with an I/C ratio of 0.67 g/g, ca. 40 wt% ionomer loading in the catalyst layer. The ink with PGM-free catalyst was coated onto PTFE substrates (50 µm) by applying a bar-coating technique, targeting a final catalyst loading of 2 mg/cm^2 with 5 cm^2 active area of catalyst layer. The anode electrodes were prepared analogously, but using a 20 wt% Pt/C catalyst (TKK) with a final Pt loading of 0.1 mg/cm^2 and an I/C ratio of 0.65 g/g. Through a hot-pressing-based decal procedure (130-160^{o}C with applied pressure 2.2 kN for 12 min), the catalyst layers (both anode and cathode) were directly transferred onto the membrane and subsequently the PTFE substrates are peeled off, yielding the final catalyst coated membranes (CCMs) or membrane electrode assemblies (MEAs). The membrane used was Nafion® 212 with 50 µm thickness, and the gas diffusion layers (GDLs) used was Freundenberg H14C10 with an uncompressed thickness of ≈150 µm and assembled into the single-cell at a compressive strain of 13%. H_2/O_2 polarization curve was recorded under differential-flow conditions (*i.e.*, with H_2/O_2 feed flows of 2000/5000 nccm) at 80^{o}C and 100% relative humidity (RH). The fuel cell inlet pressure was set to 150 kPa_{abs}, which corresponds to H_2 and O_2 partial pressures of approximately 1 bar at given operating condition. The polarization curve was recorded in the current-control mode, holding at each current for 1 minute and averaging the corresponding voltage over the last 30 seconds. The stability testing was performed by applying constant current for 12 hours (140 mA/cm^2, corresponding to uncorrected cell voltage of 0.6 V) at 100% RH, 80^{o}C, and 150 kPa_{abs} H_2/Air by inlet control.

For determining the ORR kinetics in typical PEMFC, the cell voltage was corrected by using equation 1[3]

$$E_{i\mathrm{R-free}} = E_{\mathrm{cell}} + i \cdot R_{\mathrm{HFR}} + i \cdot R^{\mathrm{eff}}_{\mathrm{H+,cath}}$$

Where R_{HFR} represents the high frequency resistance, which is the contribution of electrical contact resistance across the flow field and GDLs as well as the proton conduction resistance of the membrane. $R^{\mathrm{eff}}_{\mathrm{H+,cath}}$ represents the effective proton sheet resistance across the thickness of the cathode catalyst layer, $R_{\mathrm{H+,cath}}$, (in unit of $\mathrm{m\Omega \cdot cm^2}$) which can be calculated by equation 2

$$R^{\mathrm{eff}}_{\mathrm{H+,cath}} = \frac{R_{\mathrm{H+,cath}}}{3 + \zeta}$$

Where $R_{\mathrm{H+,cath}}$ is further determined from AC impedance spectra recorded with H_2/N_2 feeds (anode/cathode) at 0.2 V, using a peak-to-peak perturbation of 3.5 mV between 500 kHz and 0.2 Hz (20 points per decade). For the determination of $R_{\mathrm{H+,cath}}$ was applied the same approach as reported in ref [4], assuming negligible electronic resistance compared to proton resistance of catalyst layer. ζ represent the correction factor, which is a function of kinetic resistance and can be expressed a function of Tafel slope.[3] The Tafel slope was assumed 140 mV/dec which corresponds to one electron process at 80 °C.[5] The approach of equation 2 enables to determine ORR activity in absence of O_2 diffusion resistances for any given values of current density.

DFT:

Ab-initio calculations were performed using density functional theory (DFT) as implemented in TURBOMOLE.[6] All calculations were performed on finite-sized graphene clusters with H-termination on boundary carbons to reduce boundary effects.[7] After initial geometry optimization using the TPSS-D3(BJ) functional and def2-SVP basis set, a single point calculation was performed with the PBE-D3(BJ) functional and def2-TZVP basis set.[8-12]

The SCF convergence criteria were 10^{-6} E_h in the total energy and 10^{-3} E_h in the orbital energies. The geometry optimization condition was 10^{-3} a.u. in the maximum norm of the Cartesian gradient. All calculations were performed with various pre-assigned multiplicities among which the system with the lowest total energy was determined to be the ground state.

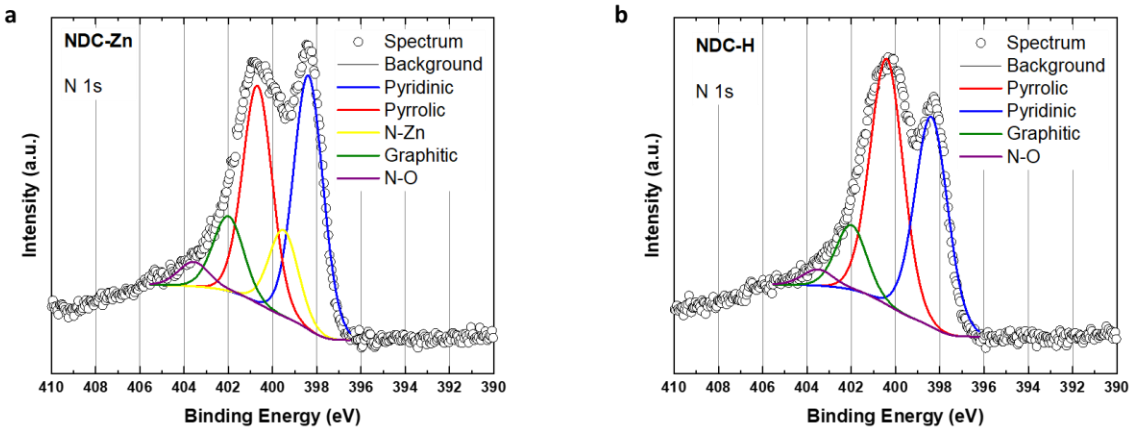

Figure S1: XPS of the N 1s of NDC-Zn (a) and NDC-H (b) with the corresponding peak fitting.

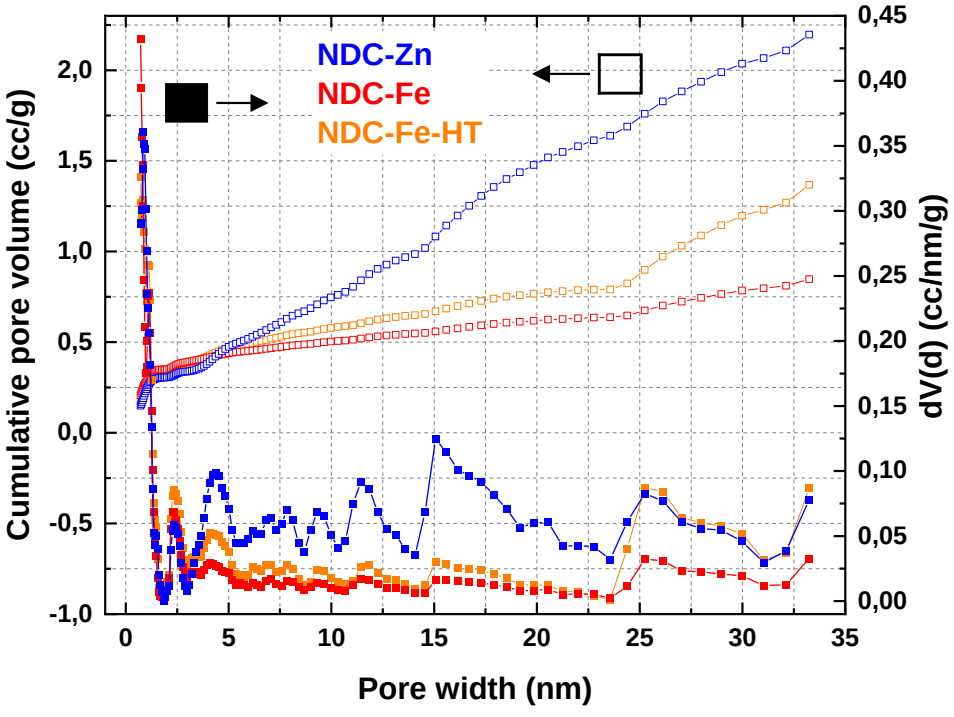

Figure S2: Pore size distributions and cumulative pore volumes calculated from N_2-sorption measurment of NDC-M. QSDFT model for carbon with slit/cylindrical pores was employed. For all three samples the error was ~ 0.2 %.

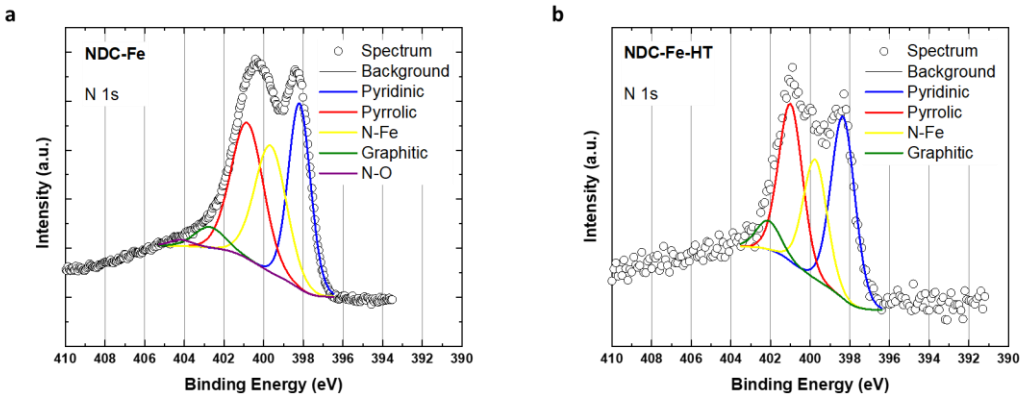

Figure S3: XPS of the N 1s of NDC-Fe (a) and NDC-Fe-HT (b) with the corresponding peak fitting.

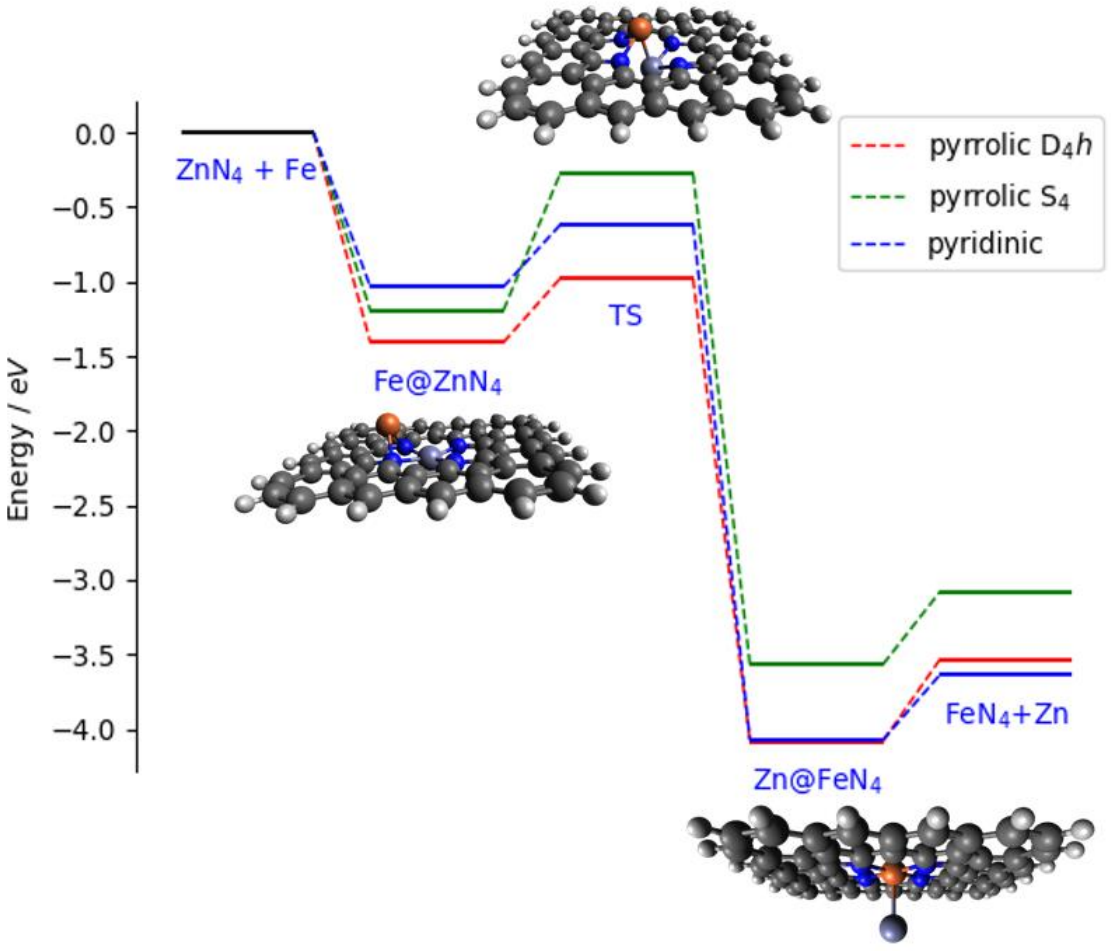

Figure S4. Energy diagram for the Zn-to-Fe exchange reac-tion including the transition states (TS) calculated using the PBE functional. Adsorption geometries for the Pyrrolic-D_{4h} motifs are shown.

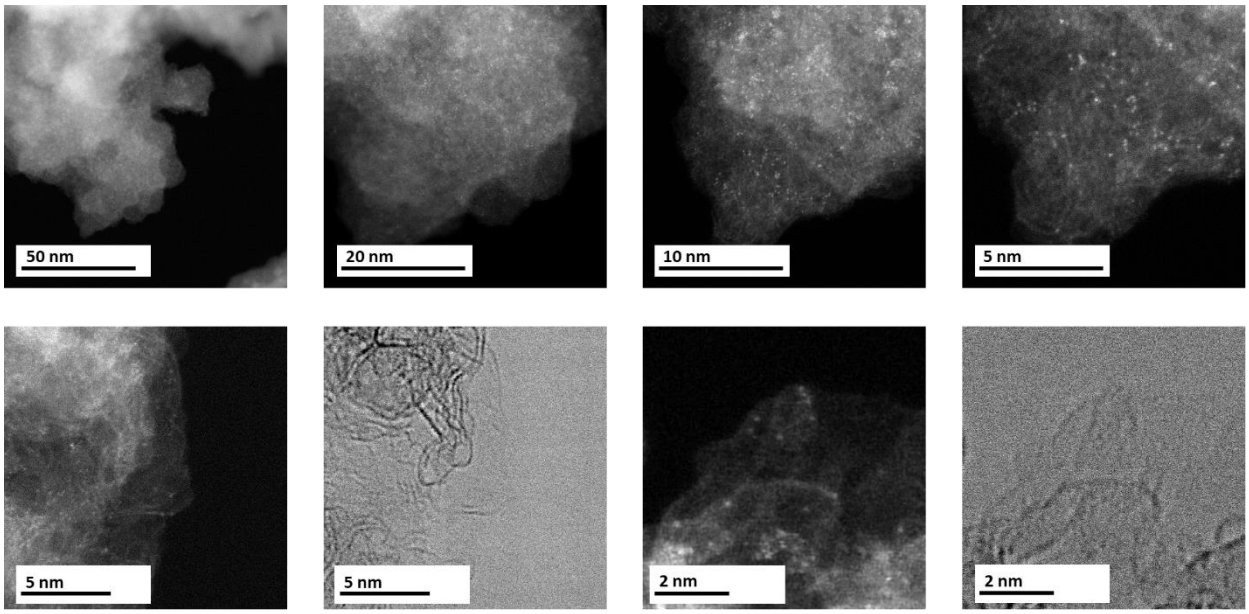

Figure S5: Annular-dark-field and bright-field scanning transmission electron microscopy (ADF- and BF-STEM) and images of NDC-Fe (top) and NDC-Fe-HT (bottom) showing the atomically dispersed Fe atoms.

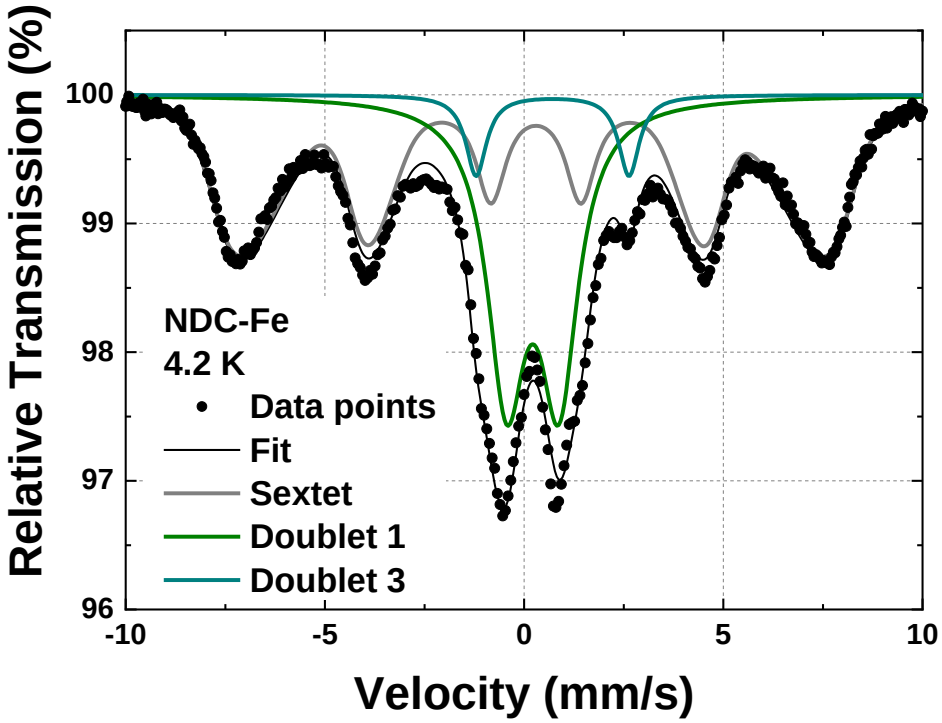

Figure S6: Mössbauer spectra of NDC-Fe recorded at 4.2 K with the corresponding fitting.

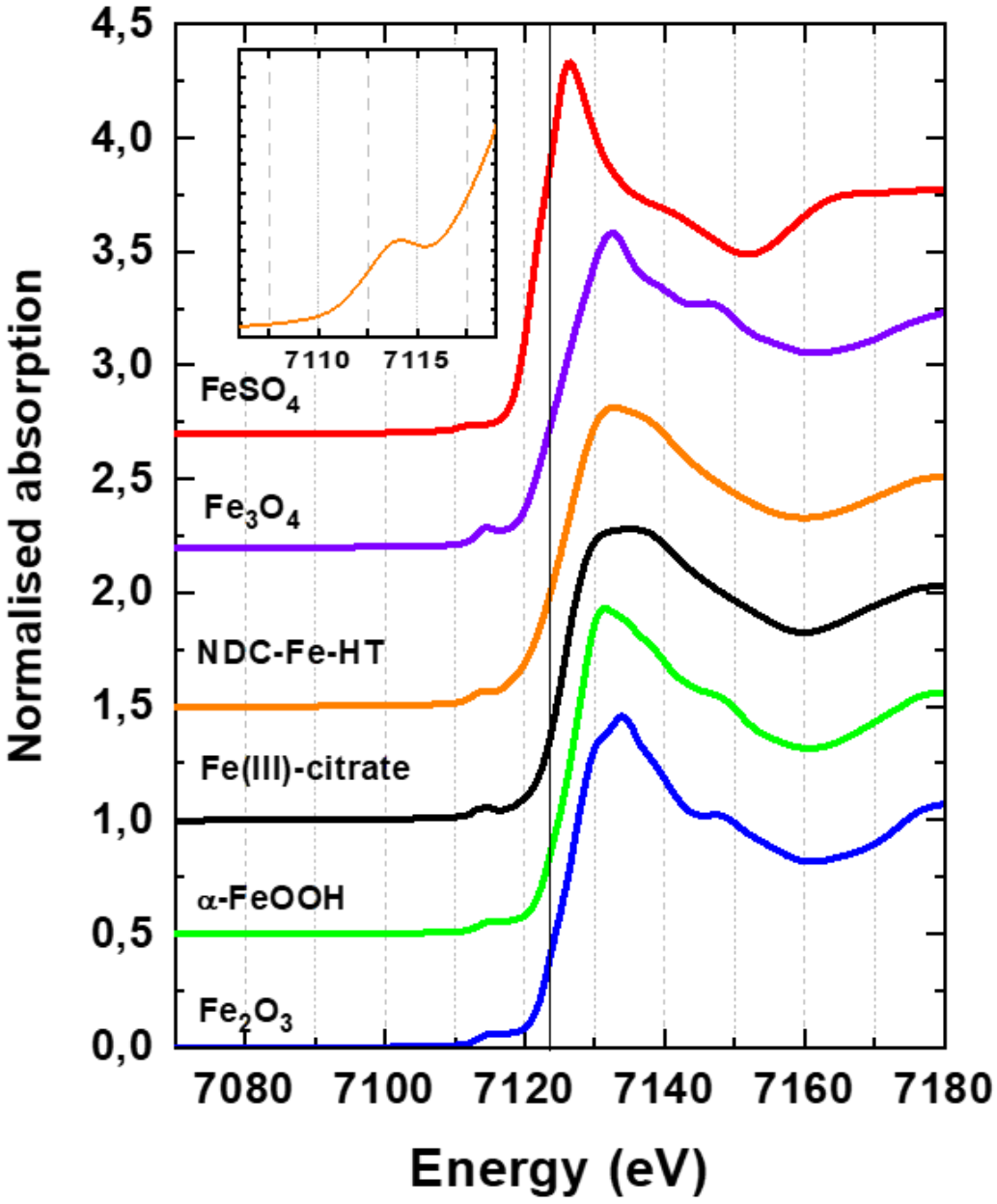

Figure S7: Fe K-edge XANES spectra of NDC-Fe-HT and reference iron compounds with different iron valence states between Fe^{2+} and Fe^{3+} ($FeSO_4 \cdot 7\ H_2O$, Fe_3O_4, Fe(III)-citrate, α-FeOOH and Fe_2O_3). The inset shows the pre-edge peak of NDC-Fe-HT, typical for M-N_4 structures with square-planar coordination.

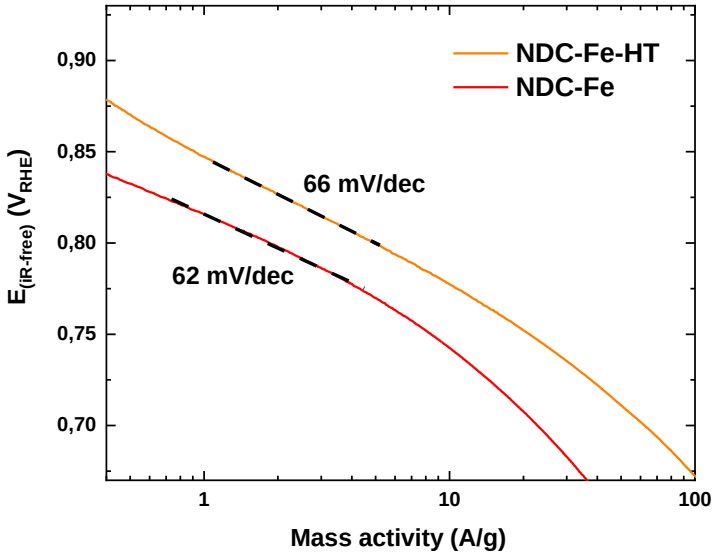

Figure S8: Tafel plot of NDC-Fe (red) and NDC-Fe-HT (orange). Dotted lines represent the Tafel slope.

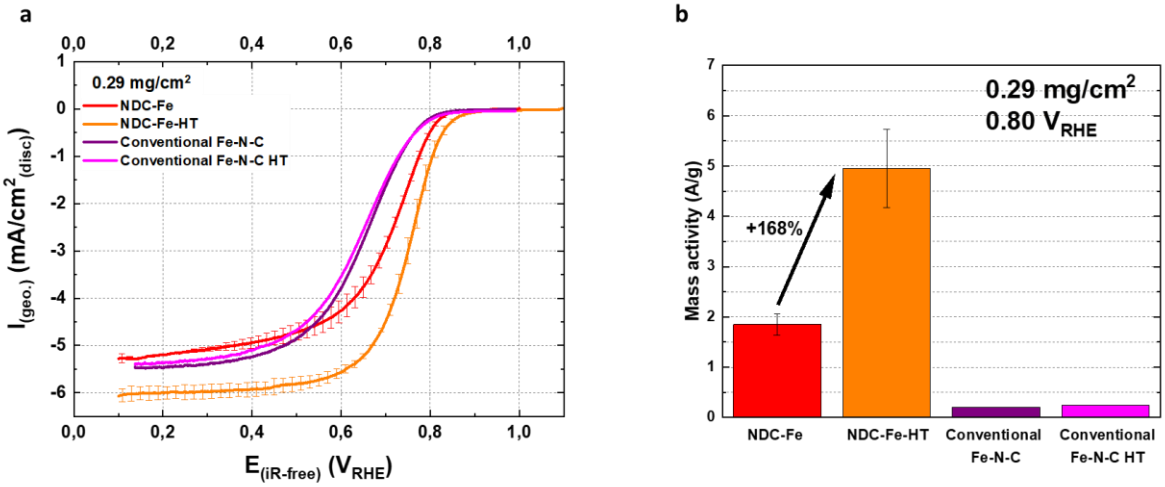

Figure S9: ORR curves of NDC-Fe, NDC-Fe-HT in comparison with a conventional Fe-N-C with and without high temperature treatment recorded with an RDE setup at room temperature in O_2-saturated 0.1 M HClO4 at 1600 rpm, 5 mV/s (anodic scans) (a) and their corresponding kinetic mass activity at 0.8 V (b). All curves were corrected for capacitance contributions.

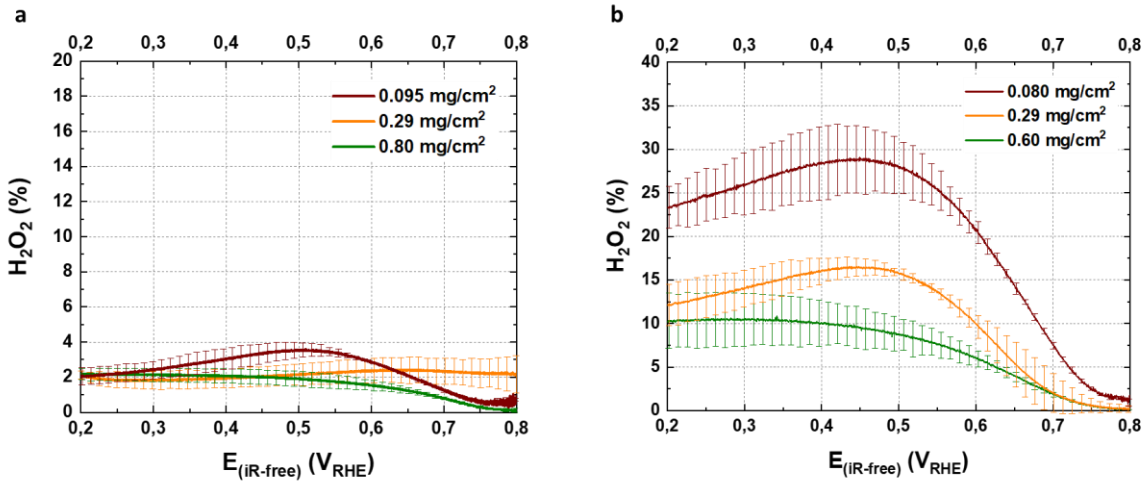

Figure S10: H_2O_2 yield obtained via RRDE experiments for NDC-Fe-HT (a) and a commercially available Fe-N-C catalyst (Pajarito Powder) (b). Measurements were performed at room temperature in O_2-saturated 0.1 M $HClO_4$ at 1600 rpm, 5 mV/s (anodic scans).

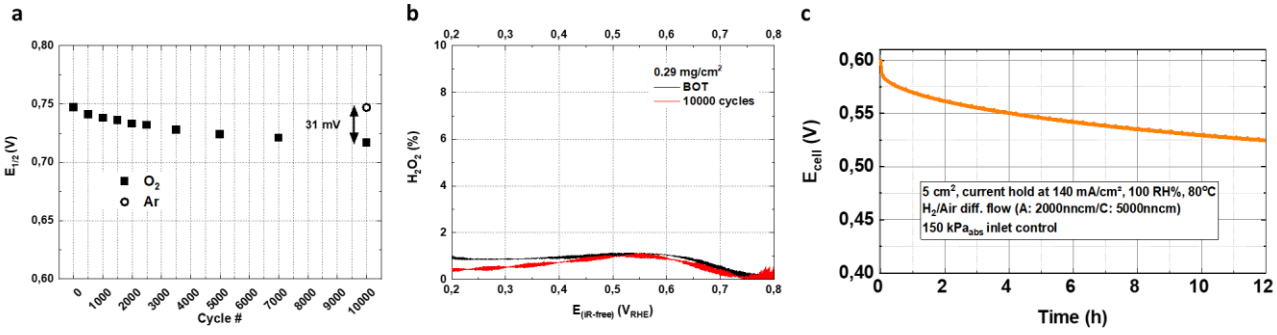

Figure S11: Change in half-wave potential over accelerated stress test (AST) cycle number for NDC-Fe-HT in O_2- or Ar-saturated electrolyte. Activity measurements were performed at room temperature in O_2-saturated 0.1 M $HClO_4$ at 1600 rpm, 5 mV/s (anodic scans) (a). H_2O_2 yield obtained via RRDE experiments for NDC-Fe-HT before and after AST (b). Measured cell voltage curve of NDC-Fe-HT with a catalyst loading of 2 mg/cm^2 recorded with a 140 mA/cm^2 current hold at 80 °C, 150 kPa_{abs} inlet-controlled pressure, 100% RH for both reactants, and constant flows of 2000 nccm of H_2 on the anode and 5000 nccm of air on the cathode. Anode and cathode were operated in counter flow mode (c).

Zn neighbour	*N*	*R* (Å)	σ^2 (Å^2)	*R*-factor
N	4	2.05(1)	0.008(1)	0.00009
Cl	1	2.28(1)	0.006(2)	
C	6	2.99(3)	0.030(5)	
C	4	3.38(3)	0.013(2)	
C	8	4.44(3)	0.014(3)	

Table S1: Parameters of the nearest coordination shells around Zn atoms in the NDC-Zn sample: average number of neighbor atoms (*N*), distance (*R*), and Debye-Waller factor (σ^2). Uncertainty of the last digit is given in parentheses. A best fit is obtained with the amplitude reduction factor S_0^2 = 0.76 and the shift of the energy origin $\Delta E_o = 4 \pm 2$ eV. The goodness-of-fit parameter, *R*-factor, is given in the last column.

The atomic species of neighbours are identified in the fit by their specific scattering factor and phase shift. We constructed the FEFF model for Zn K-edge EXAFS analysis, based on Zn-porphyrin as model structure, where Zn is bound to four pyrrolic nitrogen atoms atoms at 2.05 Å, and surrounded by respective carbon atoms (8 C at 3.07 Å, 4 C at 3.46 Å and 8 C at 4.29 Å), with one additional Cl atom placed at axial position.at the distance of 2.30 Å. Two variable parameters for each shell of neighbours are introduced in each EXAFS model: the distance (*R*) and the Debye-Waller factor (σ^2). The shell coordination numbers (*N*) are kept fixed. A common shift of energy origin ΔE_o in each scattering path is allowed to vary. The amplitude-reduction factor S_0^2 is kept fixed. The EXAFS modelling is performed in the reciprocal k-space, with a k range of 3 Å^{-1} to 12 Å^{-1} and the R range of 1.0 Å to 3.8 Å.

XPS N 1s	NDC-Zn	NDC-H
Total N (wt.%)	8.17	7.95
Npyrrolic/Ntotal (%)	32.93	46.29
Npyridinic/Ntotal (%)	38.43	39.61
N-Zn/Ntotal (%)	13.10	0
Ngraphitic/Ntotal (%)	11.75	11.32
N-O/Ntotal (%)	3.79	2.78

Table S2: Total N content and relative amount of different N species in NDC-Zn and NDC-H (i.e. before and after Zn^{2+} extraction). The amount of $N_{pyrrolic}$ after Zn^{2+} extraction matches the sum of $N_{pyrrolic}$ and N-Zn in the pristine sample, indicating the pyrrolic nature of the Zn-coordinating N atoms.

	Fe wt. %			Zn wt. %		N wt. %	
	XPS	**ICP-MS**	**Mössbauer**	**XPS**	**ICP-MS**	**CHNS**	**XPS**
NDC-Zn	0	0	-	1.26	2.95	13.61	8.17
NDC-Fe	0.54	3.12	4.63	0.39	0.56	10.35	7.92
NDC-Fe-HT	2.31	3.46	3.53	0	-	6.81	5.84

Table S3: Iron, zinc and nitrogen content for NDC-M obtained from different techniques. All values are corrected for the water content in the samples except the ones from XPS.

	i_{mass} at 0.85 VRHE (A/g)	i_{mass} at 0.80 VRHE (A/g)	Ref.
NDC-Fe	0.25 ± 0.02	1.85 ± 0.21	This work
NDC-Fe-HT	0.91 ± 0.16	4.95 ± 0.77	This work
PAJ	0.50	2.33	13
CNRS	0.60	2.00	13
ICL	0.25	1.20	13
UNM	0.50	2.40	13
FeCl2-/NC-1000	1.5	6.6	14
TPI@Z8(SiO2)-650-C	4.04	36.7	15
(CM+PANI)-Fe-C	0.56	5	16
FeNx/GM	1.17	6.37	17
HP-FeN4	0.92	7	18
FeNC-S-MSUFC-2	-	0.53	19
FeSA-N-C	0.92	10.71	20
SA-Fe-N-1.5-800	1.08	7.5	21

Table S4: Literature comparison of mass activity of Fe-N-C catalysts obtained in RDE experiment in acidic electrolyte. When not directly reported by the authors, the values have been extracted from the plots.

	i_{geo} at 0.9 $V_{HFR\text{-}free}$ (mA/cm^2)	i_{geo} at 0.8 $V_{HFR\text{-}free}$ (mA/cm^2)	Loading (mg/cm^2)	i_{mass} at 0.9 $V_{HFR\text{-}free}$ (A/g)	i_{mass} at 0.8 $V_{HFR\text{-}free}$ (A/g)	Ref.
NDC-Fe-HT	4.5	56	2	2.3	28	This work
$FeCl_2$-/NC-1000	1.5	105	4	0.38	26.3	14
TPI@Z8(SiO_2)-650-C	22	300	2.7	8.1	111	15
FeNx/GM	13*	184*	4	3.3	46	17
HP-FeN4	30.4*	169*	4	7.6	42.3	18
PFeTTPP-700	3	158	4	0.75	39.5	22
LANL 2019	34.4**	485**	6.8	5.06	71.3	23

* Not HFR-free

**Data from the first polarization curve

Table S5 Literature comparison of mass activity obtained from H_2-O_2 PEMFC measurements under DOE reference conditions. When not directly reported by the authors, the values have been extracted from the plots.

Sample	D1 (IS; QS; %)	D2 (IS; QS; %)	D3 (IS; QS; %)	Sextet (IS; H; %)
NDC-Fe	0.22; 1.32; 37.1	-	0.71; 3.84; 5.7	0.25; 44; 57.2
NDC-Fe-HT	0.24; 0.98; 44.4	0.22; 1.92; 41.6	0.90; 2.99; 7.6	-0.08; 40; 6.4

Table S6: Isomer shift (IS), quadrupole splitting (QS), magnetic field (H) and percentage (%) values extracted from the Mössbauer measurement of NDC-Fe and NDC-Fe-HT.

Fe neighbour	*N*	*R* (Å)	σ^2 (Å^2)	*R*-factor
O	2.3(5)	1.94(4)	0.008(1)	
N	4	2.05(2)	0.008(1)	
C	8	3.05(2)	0.018(4)	0.006
C	4	3.41(5)	0.013(4)	
C	8	4.29(5)	0.026(7)	

Table S7: Parameters of the nearest coordination shells around Fe atoms in the NDC-Fe-HT sample: average number of neighbor atoms (*N*), distance (*R*), and Debye-Waller factor (σ^2). Uncertainty of the last digit is given in parentheses. A best fit is obtained with the amplitude reduction factor S_0^2 = 0.80 and the shift of the energy origin ΔE_o = -4 ± 2 eV. The goodness-of-fit parameter, *R*-factor, is given in the last column.

The atomic species of neighbours are identified in the fit by their specific scattering factor and phase shift. We constructed the FEFF model for Fe K-edge EXAFS analysis, based on the Fe-porphyrin structure, with two additional oxygen molecules in axial positions Two variable parameters for each shell of neighbours are introduced in each EXAFS model: the distance (*R*) and the Debye-Waller factor (σ^2). The shell coordination numbers (*N*) are kept fixed. A common shift of energy origin ΔE_o in each scattering path is allowed to vary. The amplitude-reduction factor S_0^2 is kept fixed. The EXAFS modelling is performed in the reciprocal k-space, with a k range of 3 Å^{-1} to 12 Å^{-1} and the R range of 1.0 Å to 3.8 Å.

	Empty (½ diagonal N-N)	**Zn**	**Fe**
Pyridine	1.92 Å	1.97 Å	1.90 Å
Pyrollic-D_{4h}-2	1.99 Å	2.02 Å	1.96 Å
Pyrollic- C_{4h}-2	2.09 Å	2.08 Å	2.02 Å

Table S8: Average M-N bond length for M = Zn, Fe compared to half-diagonal N-N distance in the metal-free structure. Geometry optimization was performed in the TPSS functional and def2-SVP basis set.

	Fe-N	Fe-C1	Fe-C2	Fe-C3		Zn-N	Zn-C1	Zn-C2	Zn-C3
Pyrollic-1	2.00	3.05	3.43	4.28		2.06	3.08	3.45	4.32
Pyrollic-D4h-2	1.96	3.01	3.45	4.24		2.02	3.05	3.47	4.28
Pyrollic-C4h-2	2.02	3.03, 3.12	3.53	4.25, 4.33		2.08	3.06, 3.15	3.54	4.28, 4.37
Pyrollic-D4h-3	1.96	3.01	3.45	4.24		2.02	3.05	3.46	4.28
Pyrollic-C4h-2	2.00	3.00, 3.10	3.50	4.20. 4.32		2.05	3.02, 3.13	3.51	4.23. 4.36

Table S9: Comparison of average M-X distances in Å for different pyrrolic clusters (M = Fe, Zn; X = N, C) obtained with DFT geometry optimization with the TPSS functional and def2-SVP basis set.

Fe-N distance	Fe-C distances	Zn-N distance	Zn-C distances
1.90	2.72, 2.98, 3.35, 4.10, 4.28	1.98	2.74, 3.01, 3.37, 4.10, 4.29

Table S10: Comparison of calculated M-X distances in Å for the pyridinic $MN_4C_{52}H_{20}$ clusters (M = Fe, Zn; X = N, C)

NDC-Zn	N wt. %
800	13.61
900	6.66
1000	4.67

Table S11: Nitrogen content obtained from CHNS analysis of NDC-Zn prepared at different temperature.

XPS N 1s	NDC-Fe	NDC-Fe-HT
Total N (wt.%)	7.92	5.84
Npyrrolic/Ntotal (%)	33.21	32.39
Npyridinic/Ntotal (%)	30.81	37.34
N-Fe/Ntotal (%)	30.30	24.49
Ngraphitic/Ntotal (%)	4.67	5.88
N-O/Ntotal (%)	1.01	-

TGA-MS analysis:

TGA-MS was employed to gain a better understanding of the second ion exchange and the relative stability of Zn-N_4 *vs.* Fe-N_4 sites. In the experiment, the selected high surface area samples were degassed twice, first at 150 °C and then at 250 °C in Ar atmosphere. Afterwards, the temperature was raised to 1000 °C, also in Ar atmosphere, with a heating rate of 10 K/minute. The ferrihydrite and the formed Fe-N_4 sites are the only differences between the pristine NDC-Zn and the ion exchanged NDC-Fe. Functional groups on the surface, arising from the aqueous work-up, are expected to be similar for both materials. For both samples, a weight loss of ≈ 15 % attributed to H_2O and air is observed in the first degassing step, as expected for high surface area carbon (**Figure S10**). When comparing the weight loss at temperatures above 250 °C (**Figure S11**), NDC-Fe clearly shows a steeper loss, which is also initiated at lower temperature compared to NDC-Zn. In the MS analysis of NDC-Fe a clear event can be noted at temperature close to 400 °C involving CO_2 and H_2O (**Figure S12**). Since it does not happen in NDC-Zn, we can connect this to the ferrihydrite decomposition. Consequently, the coordination of Fe to empty (protonated) N_4 cavities, in the presence of oxygen, could act in accordance with the following mechanism:

1) Dehydration of ferrihydrite: $Fe_{10}O_{14}(OH)_2 \rightarrow Fe_{10}O_{15} + H_2O$
2) Carbothermal reduction: $2\ Fe_{10}O_{15} + 5\ C \rightarrow 20\ FeO + 5\ CO_2$
3) Coordination of iron: $FeO + H_2\text{-}N_4 \rightarrow Fe\text{-}N_4 + H_2O$

At temperatures around preliminary synthesis temperature of 800 °C, pyrolytic reorganization is observed for both NDC-Fe and NDC-Zn, visible by evolution of CO_2, H_2O and NO (**Figure S13**). When comparing the N_2 signal in the two samples (**Figure S14**) it is worth noticing that for NDC-Fe two different events are visible, one centered at ≈815 °C and another at ≈950 °C, whereas for NDC-Zn only one event centered at ≈985 °C is visible, indicating that the N_2 loss is initiated at ~170 °C lower temperature for NDC-Fe compared to NDC-Zn. This N_2 loss may be attributed to the decomposition of the Fe-N_4 sites. For NDC-Zn the evolution of NO is an obvious difference compared to the NDC-Fe sample. NO may be involved in the decomposition of Zn-N_4 sites.

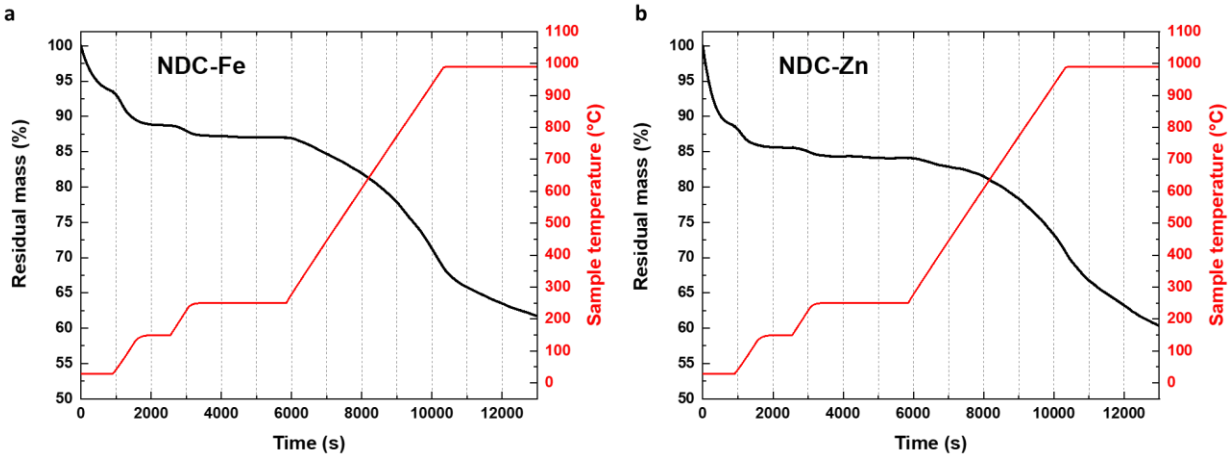

Figure S12: TGA curves for NDC-Fe (a) and NDC-Zn (b). Sample mass in percentage is shown in black and sample temperature in red.

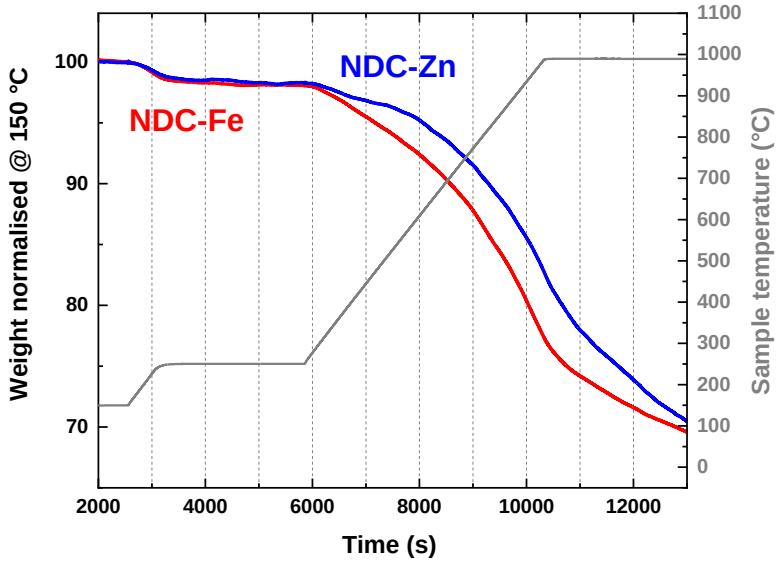

Figure S13: TGA curves for NDC-Fe (red) and NDC-Zn (blue). Sample mass has been normalised to the value after the first degassing step at 150 °C. Sample temperature is displayed in grey.

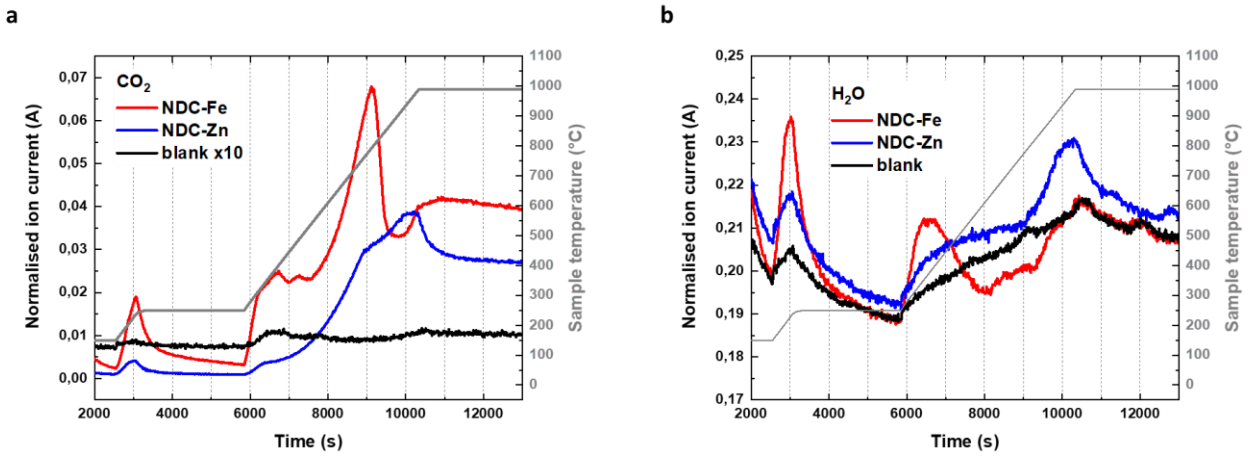

Figure S14: CO_2 (a) and H_2O (b) MS signal for NDC-Fe (red), NDC-Zn (blue) and the blank measurement where no sample is present (black). Sample temperature is displayed in grey.

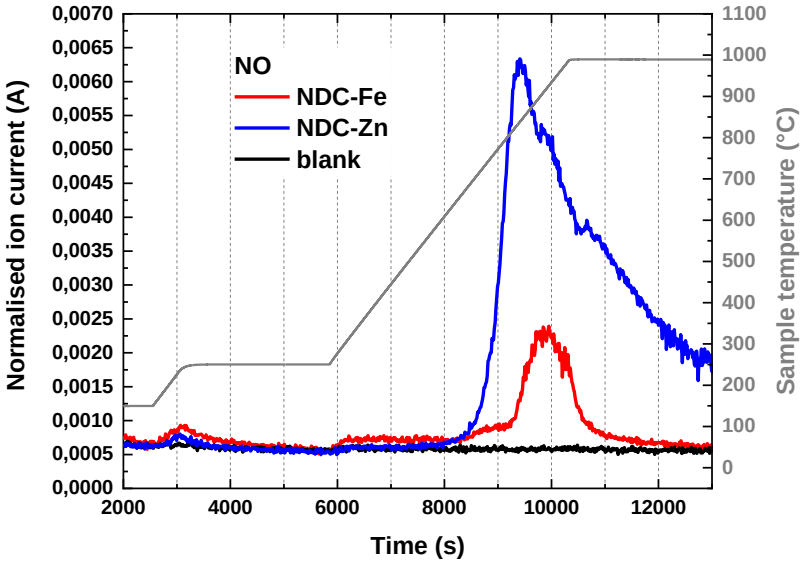

Figure S15: Nitric oxide MS signal for NDC-Fe (red), NDC-Zn (blue) and the blank measurement where no sample is present (black). Sample temperature is displayed in grey.

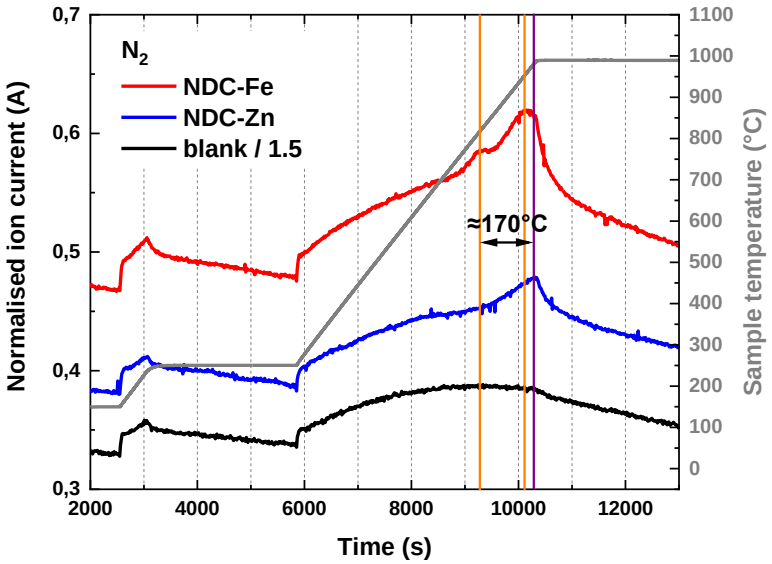

Figure S16: N_2 MS signal for NDC-Fe (red), NDC-Zn (blue) and the blank measurement where no sample is present (black). Sample temperature is displayed in grey. The orange vertical lines are centered with the NDC-Fe related peaks and the purple vertical line is centered with the NDC-Zn related peak.

References:

1. Ravel, B.; Newville, M., ATHENA, ARTEMIS, HEPHAESTUS: data analysis for X-ray absorption spectroscopy using IFEFFIT. *J Synchrotron Radiat* **2005,** *12* (Pt 4), 537-41.
2. Madkikar, P.; Menga, D.; Harzer, G. S.; Mittermeier, T.; Siebel, A.; Wagner, F. E.; Merz, M.; Schuppler, S.; Nagel, P.; Muñoz-García, A. B.; Pavone, M.; Gasteiger, H. A.; Piana, M., Nanometric Fe-Substituted ZrO2on Carbon Black as PGM-Free ORR Catalyst for PEMFCs. *Journal of The Electrochemical Society* **2019,** *166* (7), F3032-F3043.
3. Neyerlin, K. C.; Gu, W.; Jorne, J.; Clark, A.; Gasteiger, H. A., Cathode Catalyst Utilization for the ORR in a PEMFC. *Journal of The Electrochemical Society* **2007,** *154* (2), B279.
4. Liu, Y.; Murphy, M.; Baker, D.; Gu, W.; Ji, C.; Jorne, J.; Gasteiger, H. A., Determination of Electrode Sheet Resistance in Cathode Catalyst Layer by AC Impedance. *ECS Transactions* **2007,** *11* (1), 473-484.
5. Osmieri, L.; Ahluwalia, R. K.; Wang, X.; Chung, H. T.; Yin, X.; Kropf, A. J.; Park, J.; Cullen, D. A.; More, K. L.; Zelenay, P.; Myers, D. J.; Neyerlin, K. C., Elucidation of Fe-N-C electrocatalyst active site functionality via in-situ X-ray absorption and operando determination of oxygen reduction reaction kinetics in a PEFC. *Applied Catalysis B: Environmental* **2019,** *257*, 117929.
6. Ahlrichs, R.; Bär, M.; Häser, M.; Horn, H.; Kölmel, C., Electronic structure calculations on workstation computers: The program system turbomole. *Chemical Physics Letters* **1989,** *162* (3), 165-169.
7. Khosravi, A.; Vessally, E.; Oftadeh, M.; Behjatmanesh-Ardakani, R., Ammonia capture by MN4 (M = Fe and Ni) clusters embedded in graphene. *Journal of Coordination Chemistry* **2018,** *71* (21), 3476-3486.
8. Weigend, F.; Ahlrichs, R., Balanced basis sets of split valence, triple zeta valence and quadruple zeta valence quality for H to Rn: Design and assessment of accuracy. *Physical Chemistry Chemical Physics* **2005,** *7* (18), 3297.
9. Tao, J.; Perdew, J. P.; Staroverov, V. N.; Scuseria, G. E., Climbing the Density Functional Ladder: Nonempirical Meta–Generalized Gradient Approximation Designed for Molecules and Solids. *Physical Review Letters* **2003,** *91* (14).
10. Perdew, J. P.; Burke, K.; Ernzerhof, M., Generalized Gradient Approximation Made Simple. *Physical Review Letters* **1996,** *77* (18), 3865-3868.
11. Grimme, S.; Antony, J.; Ehrlich, S.; Krieg, H., A consistent and accurate ab initio parametrization of density functional dispersion correction (DFT-D) for the 94 elements H-Pu. *The Journal of Chemical Physics* **2010,** *132* (15), 154104.
12. Grimme, S.; Ehrlich, S.; Goerigk, L., Effect of the damping function in dispersion corrected density functional theory. *Journal of Computational Chemistry* **2011,** *32* (7), 1456-1465.
13. Primbs, M.; Sun, Y.; Roy, A.; Malko, D.; Mehmood, A.; Sougrati, M.-T.; Blanchard, P.-Y.; Granozzi, G.; Kosmala, T.; Daniel, G.; Atanassov, P.; Sharman, J.; Durante, C.; Kucernak, A.; Jones, D.; Jaouen, F.; Strasser, P., Establishing reactivity descriptors for platinum group metal (PGM)-free Fe–N–C catalysts for PEM fuel cells. *Energy & Environmental Science* **2020**.
14. Li, J.; Jiao, L.; Wegener, E.; Richard, L. L.; Liu, E.; Zitolo, A.; Sougrati, M. T.; Mukerjee, S.; Zhao, Z.; Huang, Y.; Yang, F.; Zhong, S.; Xu, H.; Kropf, A. J.; Jaouen, F.; Myers, D. J.; Jia, Q., Evolution Pathway from Iron Compounds to Fe1(II)–N4 Sites through Gas-Phase Iron during Pyrolysis. *Journal of the American Chemical Society* **2020,** *142* (3), 1417-1423.
15. Wan, X.; Liu, X.; Li, Y.; Yu, R.; Zheng, L.; Yan, W.; Wang, H.; Xu, M.; Shui, J., Fe–N–C electrocatalyst with dense active sites and efficient mass transport for high-performance proton exchange membrane fuel cells. *Nature Catalysis* **2019,** *2* (3), 259-268.
16. Chung, H. T.; Higgins, D.; Zelenay, P.; Cullen, D. A.; Sneed, B. T.; More, K. L.; Holby, E. F., Direct atomic-level insight into the active sites of a high-performance PGM-free ORR catalyst. *Science* **2017,** *357* (6350), 479-484.
17. Fu, X.; Li, N.; Ren, B.; Jiang, G.; Liu, Y.; Hassan, F. M.; Su, D.; Zhu, J.; Yang, L.; Bai, Z.; Cano, Z. P.; Yu, A.; Chen, Z., Tailoring FeN 4 Sites with Edge Enrichment for Boosted Oxygen Reduction Performance in Proton Exchange Membrane Fuel Cell. *Advanced Energy Materials* **2019,** *9* (11), 1803737.
18. Zhang, N.; Zhou, T.; Chen, M.; Feng, H.; Yuan, R.; Zhong, C. A.; Yan, W.; Tian, Y.; Wu, X.; Chu, W.; Wu, C.; Xie, Y., High-purity pyrrole-type FeN4 sites as a superior oxygen reduction electrocatalyst. *Energy & Environmental Science* **2020,** *13* (1), 111-118.
19. Mun, Y.; Lee, S.; Kim, K.; Kim, S.; Lee, S.; Han, J. W.; Lee, J., Versatile Strategy for Tuning ORR Activity of a Single Fe-N4 Site by Controlling Electron-Withdrawing/Donating Properties of a Carbon Plane. *Journal of the American Chemical Society* **2019,** *141* (15), 6254-6262.

20. Jiao, L.; Wan, G.; Zhang, R.; Zhou, H.; Yu, S.-H.; Jiang, H.-L., From Metal-Organic Frameworks to Single-Atom Fe Implanted N-doped Porous Carbons: Efficient Oxygen Reduction in Both Alkaline and Acidic Media. *Angewandte Chemie International Edition* **2018,** *57* (28), 8525-8529.
21. Miao, Z.; Wang, X.; Tsai, M.-C.; Jin, Q.; Liang, J.; Ma, F.; Wang, T.; Zheng, S.; Hwang, B.-J.; Huang, Y.; Guo, S.; Li, Q., Atomically Dispersed Fe-N x /C Electrocatalyst Boosts Oxygen Catalysis via a New Metal-Organic Polymer Supramolecule Strategy. *Advanced Energy Materials* **2018,** *8* (24), 1801226.
22. Yuan, S.; Shui, J.-L.; Grabstanowicz, L.; Chen, C.; Commet, S.; Reprogle, B.; Xu, T.; Yu, L.; Liu, D.-J., A Highly Active and Support-Free Oxygen Reduction Catalyst Prepared from Ultrahigh-Surface-Area Porous Polyporphyrin. *Angewandte Chemie International Edition* **2013,** *52* (32), 8349-8353.
23. Zelenay, P, ElectroCat, 2020 Hydrogen and Fuel Cells Program Annual Merit Review.

3.2 Intrinsic activity evaluation

As discussed in section 1.4, the determination of SD and TOF for Fe-N-Cs has been elusive for many years. This section presents a new facile method for the evaluation of these values for M-N-Cs, with the example of ORR in acidic and alkaline environment. Being independent from probe molecules, this method based on the extraction of the active metal from the N_4 pocket presents several advantages. Moreover, the activity comparison of isomorphic catalysts containing different metals and in different amounts, allows for the elucidation of the ORR mechanism.

3.2.1 Evaluation of the Specific Activity of M-N-Cs and the Intrinsic Activity of Tetrapyrrolic Fe-N4 Sites for the Oxygen Reduction Reaction

The article "Evaluation of the Specific Activity of M-N-Cs and the Intrinsic Activity of Tetrapyrrolic Fe-N_4 Sites for the Oxygen Reduction Reaction" was submitted in May 2022 and published in September 2022 in the peer-reviewed journal *Angewandte Chemie International Edition* as very important paper (VIP). The permanent web-link to the article is https://onlinelibrary.wiley.com/doi/10.1002/anie.202207089.

In this work, a new method for the determination of the TOF of M-N_4 sites is presented. Due to the difficulties in assigning the nature of the active sites combined with the synthetic limitations in obtaining phase pure Fe-N-C catalysts, parameters such as SD and TOF have been elusive for many years for this class of materials. Current methods for their evaluation have been presented in section 1.4.

Firstly, the versatility of the newly developed synthetic method is shown by the synthesis of a new catalyst obtained from the carbonization of 1-Ethyl-3-methylimidazolium dicyanamide (Emim-dca) in a $ZnCl_2$/NaCl eutectic mixture. After low- and high-temperature Zn-to-Fe ion-exchange reaction, the final Fe-N-C is obtained. Cryo-Mössbauer spectroscopy measurements show a homogeneity of the active Fe-N_4 sites not observed in current Fe-N-C materials, which is pointed out by the sharpness of the two quadrupole doublets, namely a line width of 0.90 mm s^{-1} and 0.55 mm s^{-1} for D1 and D2 respectively. This values are unusual in Fe-N-C catalysts and more common in molecules.[118]

Exploiting the possibility to exchange the atomically dispersed Fe with protons, three isomorphic Fe-N-Cs with different Fe amount are synthetized. Moreover, as previously reported,[106] the use of Zn as active-site imprinter results into obtaining apparently exclusively tetrapyrrolic sites, which is further confirmed via EXAFS experiments. Comparing the activity of the isomorphic Fe-N-Cs with different Fe amount allows for the calculations of TOF values specifically for tetrapyrrolic sites as well as the utilization factor, which is close to 100 %. Not being linked to probe molecules, this newly developed method for the evaluation of intrinsic activity values is more robust and can be applied to the entire pH range, different temperatures and different reactions, as long as a M-to-H^+ ion exchange is possible.

Author contributions

D.M. and T.-P.F. planned and designed the experiments. D.M. synthesized and characterized the catalyst and performed the electrochemical testing. A.G.B. performed and analyzed the XAS measurements. F.E.W. performed and analyzed the Mössbauer spectroscopy measurements. D.M. and T.-P.F. wrote the manuscript. All authors discussed the results and commented on the manuscript.

A Journal of the Gesellschaft Deutscher Chemiker

Angewandte International Edition GDCh Chemie

www.angewandte.org

Accepted Article

Title: Evaluation of the Specific Activity of M-N-Cs and the Intrinsic Activity of Tetrapyrrolic Fe-N4 Sites for the Oxygen Reduction Reaction

Authors: Tim-Patrick Fellinger, Davide Menga, Ana Guilherme Buzanich, and Friedrich Wagner

To be cited as: *Angew. Chem. Int. Ed.* **2022**, e202207089

Link to VoR: https://doi.org/10.1002/anie.202207089

WILEY-VCH

10.1002/anie.202207089

WILEY-VCH

COMMUNICATION

Evaluation of the Specific Activity of M-N-Cs and the Intrinsic Activity of Tetrapyrrolic Fe-N_4 Sites for the Oxygen Reduction Reaction

Davide Menga, Ana Guilherme Buzanich, Friedrich Wagner and Tim-Patrick Fellinger*

[*] Dr. T.-P. Fellinger
Bundesanstalt für Materialforschung und -prüfung (BAM), 12203 Berlin, Germany
E-mail: tim-patrick.fellinger@bam.de
D.Menga
Chair of Technical Electrochemistry, Department of Chemistry and Catalysis Research Center
Technische Universität München (TUM), 85748 Garching, Germany
Prof. F. E. Wagner
Department of Physics
Technische Universität München (TUM), 85748 Garching, Germany
Dr. A. Guilherme Buzanich
Bundesanstalt für Materialforschung und -prüfung (BAM), 12203 Berlin, Germany

Supporting information for this article is given via a link at the end of the document.

Abstract: M-N-C electrocatalysts are considered pivotal to replace expensive precious group metal-based materials in electrocatalytic conversions. However, their development is hampered by the limited availability of methods for the evaluation of the intrinsic activity of different active sites, like pyrrolic Fe-N_4 sites within Fe-N-Cs. Currently, new synthetic procedures based on active-site imprinting followed by an ion exchange reaction, e.g. Zn-to-Fe, are producing single-site M-N-Cs with outstanding activity. Based on the same replacement principle, we employed a conservative iron extraction to partially remove the Fe ions from the N_4 cavities in Fe-N-Cs. Having catalysts with the same morphological properties and Fe ligation that differ solely in Fe content allows for the facile determination of the reduced density of active site and their turn-over frequency. In this way, insight into the specific activity of M-N-Cs is obtained and for single-site catalysts the intrinsic activity of the site is accessible. This new approach surpasses limitations of methods that rely on probe molecules and, together with those techniques, offers a novel tool to unfold the complexity of Fe-N-C catalyst and M-N-Cs in general.

In the field of electrochemistry, metal and nitrogen co-doped carbons (M-N-C) have attracted the interest of the community due to their application in many relevant energy conversion processes, such as oxygen reduction reaction (ORR),[1] CO_2 reduction reaction (CO_2RR)[2] and ammonia electrosynthesis.[3] In order to replace expensive precious group metals (PGM) electrocatalysts, M-N-C need to meet their activity and stability, or at least compensate with their reduced cost. This seems to be the case especially for the ORR in proton exchange membrane fuel cells (PEMFCs) where Fe-N-C approaches the activity of expensive Pt-based electrocatalyst[4] and their stability improvement towards system-relevant levels is becoming the focus of the community.[5] The improved understanding of these materials is pushing their development forward and recently synthetic procedures have been optimized to produce exclusively the desired Fe-N_4 active site free from less active inorganic side phases.[6] In our previous work, we showed that via an active-site imprinting strategy followed by a transmetalation reaction, Mg-N-C and Zn-N-C containing Mg-N_4 and Zn-N_4 sites respectively, can be transformed into active Fe-N-C electrocatalysts, avoiding the formation of elemental iron, or iron carbide side phases.[7] Moreover, when Zn is employed, the nature of the metal-coordinating nitrogen atoms is pyrrolic and very active and highly selective tetrapyrrolic Fe-N-Cs can be prepared.[6b] This newly developed synthetic method has proven able to surpass previous limitations in metal loading and to elucidate structure-performance relations. In fact, the most active Fe-N-C ORR electrocatalysts reported to date are made via the transmetalation of Zn-N_4 sites of a zeolitic imidazolate framework (ZIF)-based Zn-N-C material into Fe-N_4 sites.[8]

Since the effective activity of catalysts is overlayed with morphological features,[9] rationally comparing the activity of morphologically different catalysts is complicated and not always meaningful. The quantification of specific activity values (which excludes morphological effects) like mass activity and turnover frequency (TOF) is therefore desirable. Due to the difficulties in assigning the nature of active phase/sites, for Fe-N-C these parameters have been elusive for many years. Since the community agrees on atomically dispersed Fe-N_4 sites as most active phase, lately two methods have been proposed and are mainly employed, namely nitrite stripping, firstly reported by Kucernak et al.,[10] and CO cryo-sorption, introduced by Strasser et al.[11] In order to overcome their limitation, these two methods have been used in a complementary way and this approach has proven fundamental in quantifying the SD and TOF of Fe-N_4 active-sites.[12] Even more recently, an in-situ electrochemical method based on Fourier-transform alternating current voltammetry has been introduced.[13] Herein, we report a facile and accessible method that surpasses current limitations in the determination of SD and TOF, which is also applicable to M-N-Cs in general, not only to Fe-N-Cs. Moreover, we employ the new method to a catalyst that can be approximated as single-site catalyst revealing the intrinsic catalytic activity of tetrapyrrolic Fe-N_4 sites.

The pristine catalyst presented in this study is prepared by carbonizing 1-ethyl-3-methylimidazolium dicyanamide (Emim-

10.1002/anie.202207089

dca) in a $ZnCl_2$/NaCl eutectic mixture (T_m = 250 °C) at 900 °C in Ar atmosphere (for details see SI). This salt templating strategy allows to achieve high yields and the final morphology of the catalyst can be finely tuned by simply adjusting the mixture composition.[14] Moreover, the presence of the Lewis-acidic Zn^{2+} ions facilitates the formation of N_4 moieties.[7b] The precursor to salt ratio was chosen based on previous work in order to obtain an aerogel-like structure, which allows for high surface area and efficient mass-transport.[15] After low- and high-temperature Zn-to-Fe ion-exchange reaction,[6b] the final catalyst is obtained. Two isomorphic partially Fe-extracted catalysts are then obtained after partial extraction of Fe from the Fe-N_4 sites of the pristine Fe-N-C catalyst using 2.4 M HCl, a non-oxidizing acid, and moderate temperatures of 100 °C for different times. Based on their elemental composition, samples are named with their approximate stoichiometry with emphasis on the active- and Fe-removed Fe-N_4 site, i.e. $[FeN_4]N_{32}C_{520}$ indicates the pristine sample and $[FeN_4]_x[N_4]_{1-x}N_{32}C_{520}$ the partially Fe-extracted ones (x = 0.23 and 0.17, respectively). The composition obtained from elemental combustion analysis is confirmed by scanning electron microscopy energy-dispersive X-ray spectroscopy (SEM/EDX) spectra (Figure S1) and small impurities of Al and Si, most likely due to the crucible and lid employed in the synthesis, are also found. The presence of Cl is attributed to the washing of the sample. Importantly, $[FeN_4]_x[N_4]_{1-x}N_{32}C_{520}$ samples do not present more Cl compared to the pristine sample, excluding functionalization of the carbon scaffold from the HCl treatment employed to remove the Fe. Moreover, the Fe content in the Fe-extracted samples is too little to be detected in the SEM/EDX analysis. SEM images show the aerogel-like structure of the catalysts before and after Fe extraction (Figure 1c). The small and connected particles create a hierarchical pore structure with a large surface area, which is confirmed by nitrogen-sorption porosimetry measurements. As depicted in Figure 1a, $[FeN_4]N_{32}C_{520}$ shows a large N_2 uptake at low relative pressure, indicating the microporous structure of the primary particles. The mixed type II-type IV isotherm is indication of the meso- and macroporosity of the material and its large interstitial porosity between the moderately aggregated particles,[16] resulting in a very high apparent surface area of 2067 $m^2\ g^{-1}$, perspective of very accessible active sites. A QSDFT model for slit and cylindrical pores was employed to calculate the pore size distribution from the adsorption branch of the isotherms (Figure 1b). Qualitatively, no substantial change in mesoscale pore size distribution is observed, pointing to the retained morphology of the material after Fe removal. Small deviations at around 1 nm point to local nanoscopic rearrangements connected to the decomplexation (Figure S2). However, no substantial morphological effect on the activity is expected to arise.[9] The slightly lower N_2 uptake at higher relative pressure and larger pore sizes is attributed to a reduction of the interstitial distance between the primary particles. This may be ascribed to partial collapse of the aerogel structure towards a xerogel which also explains the lower surface area of 1922 $m^2\ g^{-1}$ and 1878 $m^2\ g^{-1}$ for $[FeN_4]_{0.23}[N_4]_{0.77}N_{32}C_{520}$ and $[FeN_4]_{0.17}[N_4]_{0.83}N_{32}C_{520}$, respectively.

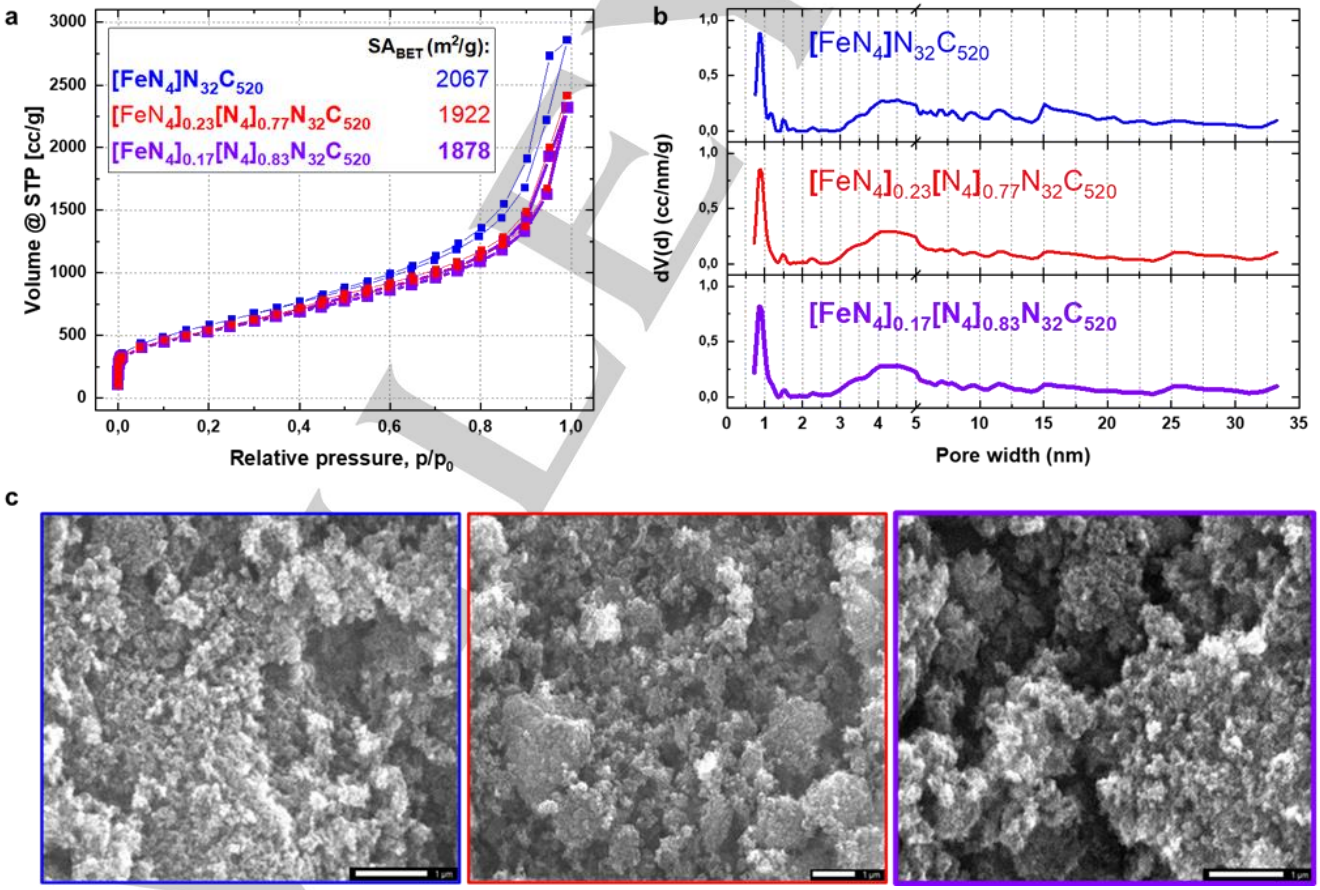

Figure 1. Morphological characterization of the sample in its pristine state and after partial Fe-extraction. a) Isotherms of the samples obtained from N_2 sorption measurement and b) the respective pore-size distribution from the adsorption branch employing the QSDFT model for slit and cylindrical pores. c) SEM images (scale bar: each 1 µm).

10.1002/anie.202207089

Cryo-Mössbauer spectroscopy measurements of $[FeN_4]N_{32}C_{520}$ at 4.2 K show the presence of two quadrupole doublets with a 3:1 intensity ratio. Such doublets are characteristic for atomically dispersed Fe-N_4 sites (Figure 2a). The first doublet with an IS of ≈0.25 mm s^{-1} and a QS of ≈1.5-1.7 mm s^{-1} (often referred to as D1)[11] may be explained by low-spin Fe^{2+} with covalent character or Fe^{3+} and therefore points to O_2 coordinated Fe^{+II}-N_4 sites. The second doublet (herein for the cryo-measurements referred to as D2) with an IS of ≈0.74 mm s^{-1} and a QS of ≈3.7-3.8 mm s^{-1} suggests high-spin Fe^{2+}, as in a bare tetrapyrrolic Fe^{+II}-N_4 structure. A magnetically split sextet component is an indication of only 8 % nanoscopic Fe(III) oxidic clusters. Due to the low relative area of this sextet, these clusters are herein neglected for clarity. Worth nothing is the sharpness of the two doublets, namely a line width of 0.90 mm s^{-1} and 0.55 mm s^{-1} for D1 and D2 respectively. These values are unusual in Fe-N-C catalysts and more common in molecules, likely pointing to a high homogeneity of the Fe-N_4 environment.[17] The Mössbauer spectrum of Fe in $[FeN_4]_{0.17}[N_4]_{0.83}N_{32}C_{520}$ (Figure 2c), despite its inferior statistical accuracy due to the low iron content of the sample, can be fitted with the same quadrupole doublets as that of $[FeN_4]N_{32}C_{520}$ (Figure 2a), showing that the iron species after extraction are still the same as before. Within the limits of accuracy there is no indication of the presence of a magnetically split pattern due to oxidic clusters. From the ratio of the spectral areas, and taking the slightly different absorber thicknesses into account, one estimates that after extraction the catalyst still contains about 13% of the iron in the original sample, which tallies well with the results of the ICP-MS determinations (Table S1). The atomic dispersion of the catalyst was further confirmed by extended X-ray absorption fine structure (EXAFS) measurements around Fe at the K-edge (7112 eV). Figure 2b shows the magnitude of the Fourier transformed spectrum of the sample, where one main peak at ~ 2 Å is found, typical for Fe-N/O scattering in Fe-N-Cs. A very good agreement with the model based on a 2D tetrapyrrolic Fe-N-C (inset of the figure) is found, allowing for the quantitative extraction of structural parameters. In agreement with expectations based on a general understanding the formation mechanism of Fe-N-Cs, Fe cations in the catalyst are coordinated to four pyrrolic N at 2.04 Å and ~ 1 O atoms (from axial OH ligands) at 1.83 Å. The Fe coordination is retained upon partial Fe-extraction as confirmed by the Fourier transformed EXAFS spectrum of the longest leached $[FeN_4]_{0.17}[N_4]_{0.83}N_{32}C_{520}$ (Figure 2d). The lower intensity of the Fe-N/O peak is attributed to the more facile extraction of FeN_4 sites, which previously contributed with Fe-O bonds due to the additional axial OH-ligand. The remaining sites are free from oxy coordination, as confirmed by the lack of Fe-O scattering path (Table S4).

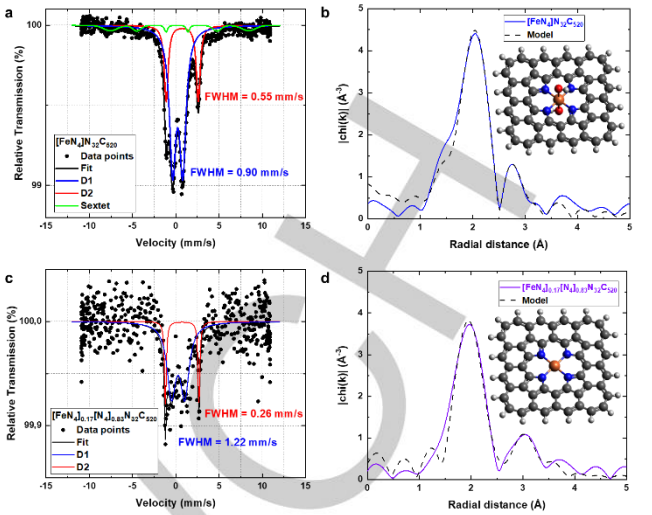

Figure 2. Characterization of the Fe environment of (a-b) $[FeN_4]N_{32}C_{520}$ and (c-d) $[FeN_4]_{0.17}[N_4]_{0.83}N_{32}C_{520}$. (a-c) Mössbauer spectrum measured at 4.2 K; FWHM indicates the line width of the corresponding quadrupole doublet. (b-d) Experimental Fourier transform of the Fe K-edge EXAFS spectra and best fit EXAFS model using the structure displayed in the corresponding inset (orange = Fe; blue = N; red = O; gray = C; white = H).

A rotating disc electrode (RDE) setup was employed to measure the activity and derive the TOF value of the catalysts in O_2-saturated 0.1 M $HClO_4$ electrolyte. Figure 3a shows the activity of the catalyst in its pristine state and after partial Fe extraction, with the identical catalyst loading of 0.145 mg cm^{-2}. Even with this relatively low loading, the catalyst has a good half-wave potential of 0.70 V_{RHE}, which shifts negatively about 140 mV after removing 0.55 wt. $\%_{Fe}$ of the initial 0.67 wt. $\%_{Fe}$. In terms of mass activity, the catalyst in its pristine state presents a very good value of 2.7 ± 0.3 A g^{-1} at 0.8 V_{RHE}. Figure 3b shows the Tafel plots for the pristine and Fe-extracted samples pointing to equal ORR mechanism before and after extraction. $[FeN_4]N_{32}C_{520}$ has a Tafel slope of ~60 mV dec^{-1}, quantifying the fast kinetics of the catalyst. The comparison of activity after the removal of active metal centres is comparable to the nitrite stripping method, where comparison of activity is carried out before and after active site poisoning. This allows for the TOF calculation of Fe-N_4 sites, according to equation 1.[10] For atomically dispersed Fe-N-Cs, the active site density difference (ΔSD) is calculated simply as the difference in Fe content between the samples (expressed in mol g^{-1}), which act as pristine and deactivated states (corresponding to the poisoned state in stripping techniques). This is possible because the extraction naturally targets accessible Fe sites. The gravimetric Fe content should not be used as SD metric due to the potential presence of different Fe phases or buried FeN_4 sites, although the herein used synthetic method based on active-site imprinting followed by Zn-to-Fe ion exchange promised potential for the exclusive presence of accessible Fe-N_4 sites.[6b]

$$TOF\ (s^{-1}) = \frac{\Delta i_k\ (A\ g^{-1})}{F\ (A\ s\ mol^{-1}) \times \Delta SD\ (mol\ g^{-1})} \qquad Equation\ (1)$$

Using equation 1 it is possible to calculate the TOF of the extracted Fe-N_4 sites under more realistic PEMFC conditions compared to the nitrite stripping method, i.e. pH = 1. For several extracted samples the kinetic current densities can be plotted over

10.1002/anie.202207089

the product of molar iron concentration and the Faraday constant. The linear fit reveals the TOF as the slope. At 0.8 V_{RHE}, Δi_{kin} and ΔSD have a value of 2.4 A g^{-1} and 9.85*10^{-5} mol g^{-1} when using the longest leached $[FeN_4]_{0.17}[N_4]_{0.83}N_{32}C_{520}$. This gives a TOF value of 0.25 s^{-1}. The more accurate graphical analysis results in a slope of 0.24 s^{-1} (Figure S3). The TOF value is in line with reported values for Fe-N-C catalyst at this potential, obtained via CO cryo-sorption and nitrite stripping methods,[12] supporting the validity of the described method. For lower potentials the error is increasing, likely due to contribution of the support material to the current. Assignment of the tetrapyrrolic motif to the active sites by means of EXAFS further allows for a more specific assignment of the average TOF of 0.24 s^{-1} at 0.8 V_{RHE} specifically to tetrapyrrolic Fe-N_4 sites. Since this intrinsic activity is below reported specific activity of Fe-N-Cs, the results suggest that more active FeN_x sites exist.[8b, 10] Moreover, and not less importantly, based on these results, further considerations about the utilization of the catalyst can be drawn. Keeping in mind that at higher potentials the carbon backbone does not contribute to the ORR activity (Figure 3a), equation 1 can be used to calculate the theoretical kinetic current obtained if all the active sites were available for the ORR (see SI). Using the gravimetric Fe content as theoretical SD at 100 % utilization in the pristine catalyst and the above-mentioned TOF of 0.25 s^{-1} obtained via extracting method, a theoretical value of 2.9 A g^{-1} at 0.8 V_{RHE} is calculated. This calculated value is close to the measured value of 2.7 ± 0.3 A g^{-1} obtained at the same potential, showing that the utilization factor corresponds to 93 ± 10 % in RDE measurements, confirming that active sites obtained via transmetalation reaction are highly accessible. Calculation based on the graphical analysis (with a TOF of 0.24 s^{-1}) results in a theoretical kinetic current density of 2.8 A g^{-1} and a utilization factor of 96 ± 11 %.

In conclusion, we introduce here a new methodology to derive the specific catalytic activity by means of TOF and utilization of active sites in atomically-dispersed M-N-C electrocatalysts. In contrast to the established methods like CO cryo-sorption and nitrite stripping, this method does not rely on probe molecules but solely on the possibility to replace the active-metal centre with protons. Since no selective binding is involved, the method can be used for any atomically-dispersed M-N-C catalyst if metal contents are known. The principle of the method is further eliminating questions regarding how many CO molecules bind the active site or how many electrons are transferred in the electrochemical stripping process of NO (i.e., if ammonia or hydroxylamine is formed[8a]). Being independent from probe molecules, this method presents several advantages. Compared to CO cryo-sorption, for example, no harsh pre-treatments are required and there is no risk of SD overestimation. This is ensured because, due to the conditions of the Fe-extraction process, all the removed Fe-N_4 sites are also accessible to the electrolyte and were hence ORR active.

Compared to the nitrite stripping method, there is no limitation to certain pH values (where the ORR mechanism, and hence the TOF, might be different) or in the concentration of the probe molecule. This allows for the application of this method at operating conditions, i.e. both in acidic and alkaline electrolytes and even at higher temperatures. As long as an extraction of the active metal sites is possible, this method can be extended to all kinds of M-N-Cs and other reactions, holding the potential to push the understanding of this type of materials further.

In the present work the catalyst can be approximated a single-site catalysts. Hence, the TOF value at 0.8 V_{RHE} is assigned specifically to the ORR activity of tetrapyrrolic Fe-N_4 sites (intrinsic activity). Since higher TOF values than 0.24 s^{-1} for Fe-N-Cs were previously reported it may be concluded that other active sites need to be targeted to approach Fe-N-C catalysts for the application in fuel cell electric vehicles.[5b]

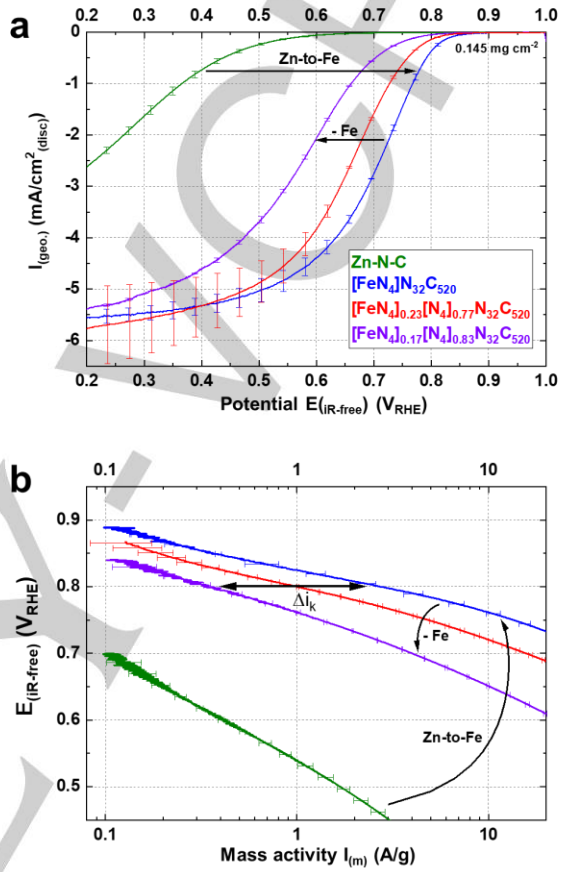

Figure 3. Electrochemical characterization of the sample in its pristine state and after partial Fe-extraction in comparison with the Zn-N-C material, i.e. the carbon scaffold without any Fe. a) Capacitance-corrected ORR curves recorded with an RDE setup at room temperature in O_2-saturated 0.1 M $HClO_4$ at 1600 rpm, 10 mV s^{-1} (anodic scans) and b) respective Tafel plots showing purely the kinetic mass activity corrected for mass-transport limitation; for Zn-N-C, since no limiting current is achieved, no correction has been applied. The plots clearly show that the carbon scaffold (Zn-N-C) does not contribute to the activity of the catalyst at 0.8 V_{RHE}.

Acknowledgements

We thank the Helmholtz-Zentrum Berlin for the allocation of synchrotron radiation beamtime. Jian Liang Low (FU Berlin) is acknowledged for providing chemical models used for the EXAFS fitting and illustration. Prof. Hubert Gasteiger is acknowledged for providing a supportive and educative working environment.

Keywords: M-N-C catalysts • Turnover Frequency • Tetrapyrrolic Fe-N4 Sites • Oxygen Reduction Reaction • Utilization

10.1002/anie.202207089

[1] F. Jaouen, D. Jones, N. Coutard, V. Artero, P. Strasser, A. Kucernak, *Johnson Matthey Technology Review* **2018**, *62*, 231-255.

[2] S. Paul, Y.-L. Kao, L. Ni, R. Ehnert, I. Herrmann-Geppert, R. van de Krol, R. W. Stark, W. Jaegermann, U. I. Kramm, P. Bogdanoff, *ACS Catalysis* **2021**, *11*, 5850-5864.

[3] P. Li, Z. Jin, Z. Fang, G. Yu, *Energy & Environmental Science* **2021**, *14*, 3522-3531.

[4] a) H. A. Gasteiger, S. S. Kocha, B. Sompalli, F. T. Wagner, *Applied Catalysis B* **2005**, *56*, 9-35; b) M. Lefèvre, E. Proietti, F. Jaouen, J.-P. Dodelet, *Science* **2009**, *324*, 71-74.

[5] a) D. Banham, T. Kishimoto, Y. Zhou, T. Sato, K. Bai, J.-i. Ozaki, Y. Imashiro, S. Ye, *Science Advances* **2018**, *4*; b) M.-M. Titirici, S. Baird, T. Sparks, S. M. Yang, A. Brandt-Talbot, O. Hosseinaei, D. P. Harper, R. Parker, S. Vignolini, L. Berglund, Y. Li, H.-L. Gao, L.-B. Mao, S. Yu, N. Díez, G. Alvarez.ferrero, M. Sevilla Solis, P. Szilagyi, C. Stubbs, J. Worch, Y. Huang, C. Luscombe, K.-y. Lee, H. Luo, J. Platts, D. Tiwari, D. Kovalevskiy, D. Fermin, H. Au, H. Alptekin, M. Crespo Ribadeneyra, V. Ting, T.-P. Fellinger, J. Barrio-hermida, O. Westhead, C. Roy, I. Stephens, S. A. Nicolae, S. Sarma, R. Oates, C. G. Wang, Z. Li, X. J. Loh, R. J. Myers, N. Heeren, A. Grégoire, C. Périssé, X. Zhao, Y. Vodovotz, B. Earley, G. Finnveden, A. Björklund, G. Harper, A. Walton, P. A. Anderson, *Journal of Physics: Materials* **2022**, *5*, 032001.

[6] a) A. Zitolo, V. Goellner, V. Armel, M.-T. Sougrati, T. Mineva, L. Stievano, E. Fonda, F. Jaouen, *Nat Mater* **2015**, *14*, 937-942; b) D. Menga, J. L. Low, Y.-S. Li, I. Arčon, B. Koyutürk, F. Wagner, F. Ruiz-Zepeda, M. Gaberšček, B. Paulus, T.-P. Fellinger, *Journal of the American Chemical Society* **2021**, *143*, 18010-18019.

[7] a) A. Mehmood, J. Pampel, G. Ali, H. Y. Ha, F. Ruiz-Zepeda, T.-P. Fellinger, *Advanced Energy Materials* **2018**, *8*, 1701771; b) D. Menga, F. Ruiz-Zepeda, L. Moriau, M. Šala, F. Wagner, B. Koyutürk, M. Bele, U. Petek, N. Hodnik, M. Gaberšček, T.-P. Fellinger, *Advanced Energy Materials* **2019**, *9*, 1902412.

[8] a) L. Jiao, J. Li, L. L. Richard, Q. Sun, T. Stracensky, E. Liu, M. T. Sougrati, Z. Zhao, F. Yang, S. Zhong, H. Xu, S. Mukerjee, Y. Huang, D. A. Cullen, J. H. Park, M. Ferrandon, D. J. Myers, F. Jaouen, Q. Jia, *Nature Materials* **2021**, *20*, 1385-1391; b) A. Mehmood, M. Gong, F. Jaouen, A. Roy, A. Zitolo, A. Khan, M.-T. Sougrati, M. Primbs, A. M. Bonastre, D. Fongalland, G. Drazic, P. Strasser, A. Kucernak, *Nature Catalysis* **2022**, *5*, 311-323.

[9] J. Pampel, T.-P. Fellinger, *Advanced Energy Materials* **2016**, *6*, 1502389.

[10] D. Malko, A. Kucernak, T. Lopes, *Nature Communications* **2016**, *7*, 13285.

[11] a) N. R. Sahraie, U. Kramm, J. Steinberg, Y. Zhang, A. Thomas, T. Reier, J.-P. Paraknowitsch, P. Strasser, *Nature Communications* **2015**, 6, 8618. b) F. Luo, C. H. Choi, M. J. M. Primbs, W. Ju, S. Li, N. D. Leonard, A. Thomas, F. Jaouen, P. Strasser, *ACS Catalysis* **2019**, *9*, 4841-4852.

[12] M. Primbs, Y. Sun, A. Roy, D. Malko, A. Mehmood, M.-T. Sougrati, P.-Y. Blanchard, G. Granozzi, T. Kosmala, G. Daniel, P. Atanassov, J. Sharman, C. Durante, A. Kucernak, D. Jones, F. Jaouen, P. Strasser, *Energy & Environmental Science* **2020**.

[13] R. Z. Snitkoff-Sol, A. Friedman, H. C. Honig, Y. Yurko, A. Kozhushner, M. J. Zachman, P. Zelenay, A. M. Bond, L. Elbaz, *Nature Catalysis* **2022**, *5*, 163-170.

[14] N. Fechler, T.-P. Fellinger, M. Antonietti, *Advanced Materials* **2013**, *25*, 75-79.

[15] K. Elumeeva, N. Fechler, T. P. Fellinger, M. Antonietti, *Materials Horizons* **2014**, *1*, 588-594.

[16] M. Thommes, K. Kaneko, A. V. Neimark, J. P. Olivier, F. Rodriguez-Reinose, J. Rouquerol, K. S. W. Sing, *Pure and Applied Chemistry* **2015**, *87*(9-10), 1051-1069.

[17] V. S. Kozlov, V. G. Semenov, K. G. Karateeva, V. Y. Bairamukov, *Physics of the Solid State* **2018**, *60*, 1035-1040.

10.1002/anie.202207089

WILEY-VCH

COMMUNICATION

Entry for the Table of Contents

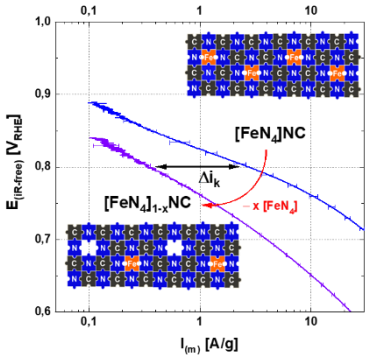

We herein used the equivalence of an active site extraction to the poisoning of active sites to develop a new method for the determination of site density, utilization factor and TOF. The method is reminiscent of stripping techniques but since there are no probe molecules involved it can be applied to different classes of M-N-C directly at the relevant pH. @BAMResearch; @TU_Muenchen; @TUMCatalysis

Supporting Information

Evaluation of the Specific Activity of M-N-Cs and the Intrinsic Activity of Tetrapyrrolic Fe-N_4 Sites for the Oxygen Reduction Reaction

Davide Menga, Ana Guilherme Buzanich, Friedrich Wagner and Tim-Patrick Fellinger*

Experimental Section

Preparation of $[FeN_4]N_{32}C_{520}$.

The catalyst was prepared adapting the synthetic procedure reported in previous work.[1] In a typical synthesis, 1 g of 1-ethyl-3-methylimidazolium dicyanamide (Emim-dca) were mixed with 8.26 g of ZnCl2 and 1.74 g of NaCl inside an Ar-filled glovebox. The resulting mixture was placed inside an alumina crucible covered with a quartz lid and heated up in a tube furnace under constant Ar flow. The heating rate was 2.5 K/min and the final temperature of 900 °C was held for 1 hour. Afterwards, the sample was allowed to cool down under Ar flow. The final material was ground and washed with 0.1 M HCl for several hours. After filtering and washing with deionized water until neutral pH was reached, the sample was dried at 80 °C overnight. As previously reported,[2] Zn-to-Fe ion exchange was carried out at low and high temperature. Firstly, the material was degassed at 250 °C under vacuum in a Buchi oven and mixed with a $FeCl_3$/LiCl eutectic mixture inside and Ar-filled flask. After heating the mixture at 170 °C for 5 hours, the sample was washed with deionized water to remove the salt mixture and stirred in 0.1 M HCl for several hours. The powder obtained after further water washing and drying (low temperature Zn-to-Fe exchange) was placed again in an alumina crucible and pushed inside a tube furnace pre-heated at 1000 °C under Ar atmosphere (flash pyrolysis). After 20 minutes the furnace was turned off and opened to achieve a quick cool down of the sample.

Preparation of $[FeN_4]_{0.23}[N_4]_{0.77}N_{32}C_{520}$.

For the partial Fe extraction, $[FeN_4]N_{32}C_{520}$ was placed inside a closed Carius tube and stirred for 16 hours in 2.4 M HCl at 100 °C. After filtering and thoroughly washing with deionized water until neutral pH was achieved, the final sample was obtained.

Preparation of $[FeN_4]_{0.17}[N_4]_{0.83}N_{32}C_{520}$.

For the partial Fe extraction, $[FeN_4]N_{32}C_{520}$ was placed inside a closed Carius tube and stirred for 6 days in 2.4 M HCl at 100 °C. After filtering and thoroughly washing with deionized water until neutral pH was achieved, the final sample was obtained.

Physical characterizations

SEM images were taken with a JEOL JSM-IT200 equipped with a EDX detector. N_2-sorption porosimetry measurements were performed on a Quantachrome Autosorb iQ2 after outgassing the samples at 250 °C under vacuum overnight prior to the measurements. Brunauer–Emmett–Teller (BET) theory was employed to determine the specific surface area using the Micropore BET Assistant supplied by Quantachrome ASiQwin software. Pore size distributions were calculated with the quenched-solid density functional theory (QSDFT) method (slit/cylindrical pores, adsorption branch). Mössbauer measurements at T = 4.2 K were performed on a standard transmission spectrometer using a sinusoidal velocity waveform with both the source of ^{57}Co in rhodium and the absorber in the liquid He bath of a cryostat. In order to refer the measured isomer shifts to α-Fe at ambient temperature, 0.245 mm s^{-1} was added to the measured values. Both X-ray absorption near edge structure (XANES) and extended X-ray absorption fine structure (EXAFS) measurements at the Fe K-edge (7112 eV) were carried out at the BAMline[3] located at BESSY-II (Berlin, Germany), operated by the Helmholtz-Zentrum Berlin für Materialien und Energie. Due to the low concentration of Fe (< 1 wt. %) the measurements were performed in fluorescence mode, with a 4-Element silicon drift detector, using backscattered geometry. For a good S/N ratio, the measurement time was optimized to have at least a total of 500 kcts at the Fe-Kα fluorescence peak. The scans were performed in 10 eV steps until 20 eV before the edge, followed by 0.5 eV steps until 50 eV above the edge, then in 1 eV steps until 200 eV, and from then on in 0.04 Å equidistant k-steps. XANES data evaluation and treatment was performed by using ATHENA program from Demeter package.[4] This includes background removal, energy calibration with Fe metal foil spectrum, and pre- and post-edge normalization. Further information on the local coordination environment was achieved by EXAFS. EXAFS curves were Fourier Transformed between 2-9 Å with a Hanning-type window, to obtain a radial distribution-like information. These were fitted with a model adapted from our previous publication[2] based on a $(OH)_2FeN_4C_{52}H_{20}$ cluster consisting of a Fe atom binding two OH groups in the axial positions and coordinated to four pyrrolic nitrogen atoms embedded in a planar carbon plane. The model was used to calculate the scattering paths by FEFF to be able to quantify the coordination number and bond-length. The goodness of the fit is determined by evaluating the reduced-chi2 test and R-factor. The fiting range was kept between 1-4 Å that includes all the scattering paths displayed in the tables S3 and S4. The degeneracy of the scattering path (which corresponds to the coordination number, N, in the case of single scattering paths) was varied until an amplitude reduction factor (S_0^2) of about 1 was achieved. The best results are displayed the tables S3 and S4. Following amplitude reduction factors were obtained for the two samples: $[FeN_4]N_{32}C_{520}$ ($S_0^2 = 1.0 \pm 0.1$); $[FeN_4]_{0.17}[N_4]_{0.83}N_{32}C_{520}$ ($S_0^2 = 1.0 \pm 0.2$).

Electrochemical measurements

Catalyst inks were prepared by dispersing 5 mg of catalyst in 1.68 mL of N,N-dimethylformamide and 50 µL of 5 wt% Nafion suspension, followed by sonication. To obtained a catalyst loading of 145 µg/cm^2, 10 µL of ink was drop-cast onto a well-polished glassy carbon electrode and dried under an infrared heater for 60 min. The obtained electrodes were measured in a three-electrode glass cell using 0.1 M $HClO_4$ as electrolyte, Au wire as the counter electrode and a freshly calibrated RHE as the reference electrode. The solution resistance was determined by electrochemical impedance spectroscopy. The ORR curves were corrected for capacitive contribution by subtracting from the curves recorded in O_2-saturated electrolyte the ones recorded in Ar-saturated electrolyte. For each curve at least two separate measurements were averaged to give the shown polarization curve, and the standard deviation is illustrated with error bars. Kinetic currents were calculated based on limiting current correction as in reference [5], but may also be evaluated based on Koutecký-Levich analysis.

Calculation of TOF values

For calculation of TOF values from the pristine Fe-N-C and the longest leached Fe-N-C, equation (1) from the manuscript was used. The pristine Fe-N-C contains 8 % of oxidic iron, which is considered in the calculation.

$$TOF\ (s^{-1}) = \frac{\Delta i_k\ (A\ g^{-1})}{F\ (A\ s\ mol^{-1}) \times \Delta SD\ (mol\ g^{-1})}$$ (equation 1´)

$$TOF\ (s^{-1}) = \frac{(2.7 - 0.3)\ A\ g^{-1}}{96480\ A\ s\ mol^{-1}\ \times \frac{(0.0067\ -0.0012)\ g}{55.8\ g\ mol^{-1}}} = 0.2524\ s^{-1} = 0.25\ s^{-1}$$

Graphical determination of the TOF value from linear interpolation of the pristine Zn-N-C, the pristine Fe-N-C and two extracted Fe-N-Cs reveals TOF = 0.24143 ± 0.01848 ≈ 0.24 s^{-1} (Figure S3).

Calculation of utilization factor

The utilization factor is defined as the fraction of accessible Fe active sites and the total amount of iron. For convenience both values are usually expressed as molar concentrations. If the catalyst has a homogeneous composition with a known specific activity (mass activity or TOF), it may also be defined as the fraction of the measured activity and the theoretical activity, e.g. the fraction of kinetic current density and the theoretical kinetic current density.

$$utilzation\ factor \equiv \frac{SD\ (mol\ g^{-1})}{molar\ iron\ concentration\ (mol\ g^{-1})} = \frac{i_k^{measured}\ (A\ g^{-1})}{i_k^{theoretical}\ (A\ g^{-1})}$$ (equation 2)

Herein the utilization factor can be derived from measured kinetic current density and the product of the Faraday constant, the molar iron concentration and the calculated TOF for tetrapyrrolic Fe-N_4 sites.

$$utilzation\ factor = \frac{\Delta i_k\ (A\ g^{-1})}{TOF \times F\ (A\ s\ mol^{-1}) \times molar\ iron\ concentration\ (mol\ g^{-1})}$$ (equation 3)

The theoretical kinetic current can be calculated as follows:

$$i_k^{theoretical} = TOF \cdot F \cdot SD$$ (equation 4)

$$i_k^{theoretical} = 0.25\ s^{-1} \cdot 96480\ A\ s\ mol^{-1} \cdot \frac{0.0067\ g}{55.8\ g\ mol^{-1}} = 2.896\ A\ g^{-1} \approx 2.9\ A\ g^{-1}$$

From the calculated kinetic current density, finally the utilization factor can be calculated:

$$utilzation\ factor = \frac{i_k^{measured}\ (A\ g^{-1})}{i_k^{theoretical}\ (A\ g^{-1})} = \frac{2.7 \pm 0.3\ A\ g^{-1}}{2.9\ A\ g^{-1}} = 93 \pm 10\ \%$$

Additional Figures and Tables

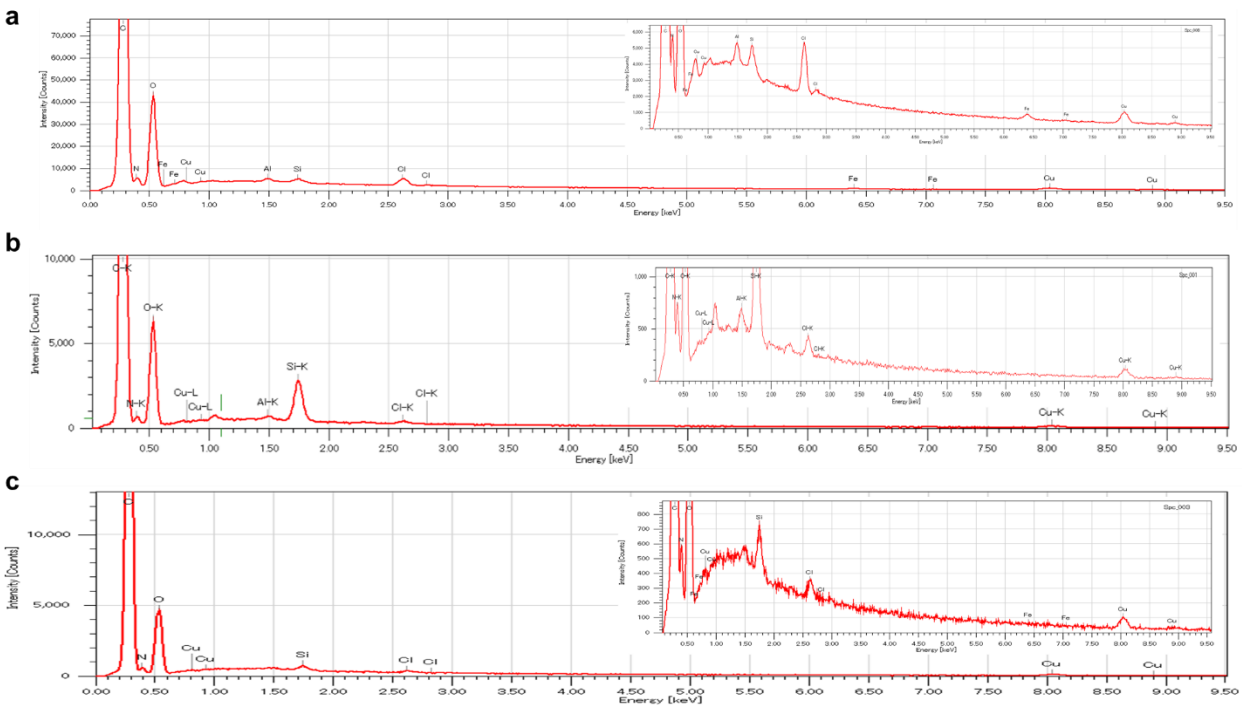

Figure S1. EDX spectra showing the elemental composition of the sample in its pristine state and after partial Fe-extraction. The Cu signal comes from the tape used as a backing for the measurement. a) $[FeN_4]N_{32}C_{520}$, (b) $[FeN_4]_{0.23}[N_4]_{0.77}N_{32}C_{520}$ and c) $[FeN_4]_{0.17}[N_4]_{0.83}N_{32}C_{520}$.

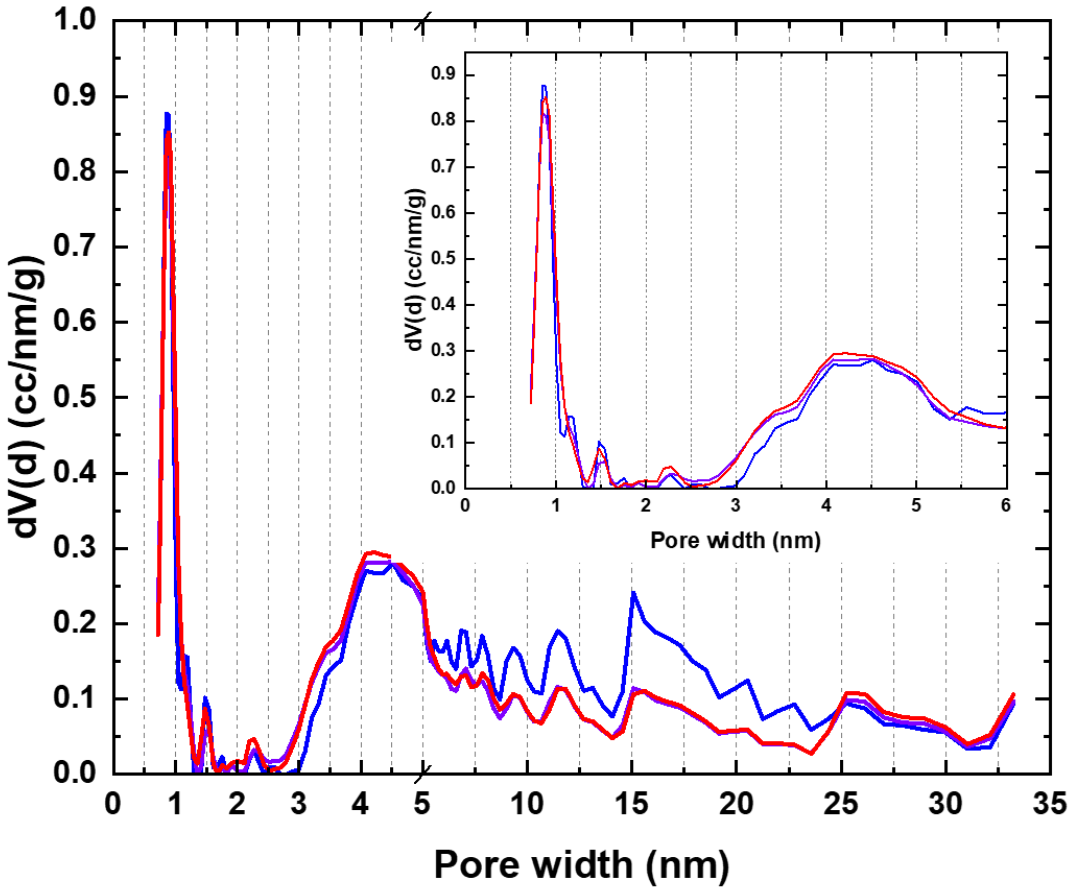

Figure S2. Overlap of the pore-size distribution of the sample in its pristine state and after partial Fe-extraction. The inset shows the region up to 6 nm.

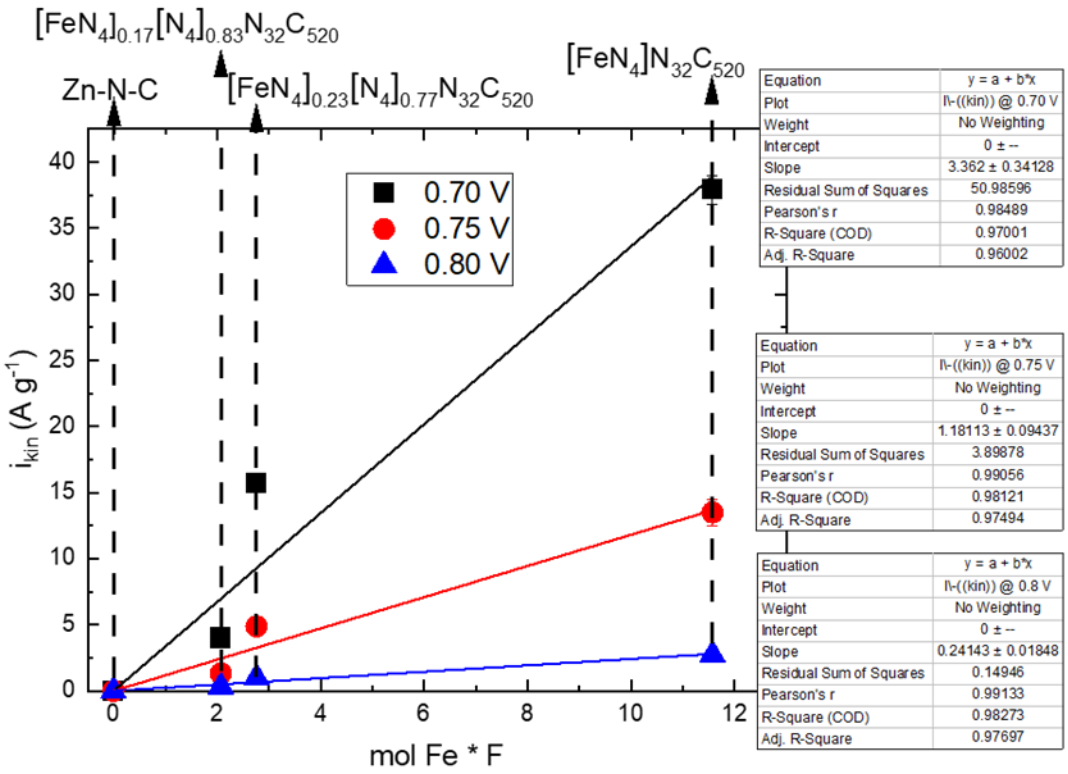

Figure S3. Plot for the TOF calculation. The mass activity at a specific potential is plotted in relation to the molar Fe content. The Zn-N-C sample is also included (0 A g-1 at the three potentials considered and no Fe present). Activity is measured with an RDE setup at room temperature in O_2-saturated 0.1 M $HClO_4$ at 1600 rpm, 10 mV s^{-1} (anodic scans) and the Fe content is measured via ICP-MS analysis. The SD is multiplied by the Faraday constant in order to obtain the TOF value directly from the slope of the line. Slope and R value are reported in the table in the inset.

Table S1. Iron content of the sample in its pristine state and after partial Fe-extraction obtained from ICP-MS analysis.

Sample	Fe (wt.%)
$\mathbf{[FeN_4]N_{32}C_{520}}$	0.67
$\mathbf{[FeN_4]_{0.23}[N_4]_{0.77}N_{32}C_{520}}$	0.16
$\mathbf{[FeN_4]_{0.17}[N_4]_{0.83}N_{32}C_{520}}$	0.12

Table S2. Fitting parameters of the different components obtained from the Mössbauer measurements of $[FeN_4]N_{32}C_{520}$ and $[FeN_4]_{0.17}[N_4]_{0.83}N_{32}C_{520}$ at 4.2 K; isomer shift (IS, mm s^{-1}) with respect to α-iron at 4.2 K, quadrupole splitting (QS, mm s^{-1}), magnetic hyperfine field (H, Tesla), percentage of the spectral area (%) and line width (FWHM, mm s^{-1}).

Sample	**D1** **(IS; QS; %; FWHM)**	**D2** **(IS; QS; %; FWHM)**	**Sextet** **(IS; H; %)**
$\mathbf{[FeN_4]N_{32}C_{520}}$	0.22; 1.17; 69; 0.90	0.74; 3.71; 23; 0.55	0.29; 49.6; 8
$\mathbf{[FeN_4]_{0.17}[N_4]_{0.83}N_{32}C_{520}}$	0.26; 1.55; 80; 1.22	0.73; 3.88; 20; 0.26	----------

Table S3. Structural information obtained from EXAFS by fitting the nearest coordination shells around Fe atoms in $[FeN_4]N_{32}C_{520}$ with model $(OH)_2FeN_4C_{52}H_{20}$: degeneracy of the scattering path (N), interatomic distance from the fit (R) and from the model (Reff), and Debye-Waller factor (σ^2). The goodness-of-fit parameter is indicated by the R-factor.

Scattering path	N	R (Å)	Reff (Å)	σ^2 (Å^2)	R-factor	
Fe-O	1.3	1.83	1.80	0.0036	0.014	Single-scattering
Fe-N	4	2.04	2.01	0.0036		Single-scattering
Fe-C	4	2.99	3.05	0.0116		Single-scattering
Fe-N-C	16	3.20	3.22	0.0181		Triangle scattering

Table S4. Structural information obtained from EXAFS by fitting the nearest coordination shells around Fe atoms in $[FeN_4]_{0.17}[N_4]_{0.83}N_{32}C_{520}$ with model $(OH)_2FeN_4C_{52}H_{20}$: degeneracy of the scattering path (N), interatomic distance from the fit (R) and from the model (Reff), and Debye-Waller factor (σ^2). The goodness-of-fit parameter is indicated by the R-factor.

Scattering path	N	R (Å)	Reff (Å)	σ^2 (Å^2)	R-factor	
Fe-N	4	2.00	2.01	0.0106	0.018	Single-scattering
Fe-C	4	3.02	3.04	0.0067		Single-scattering
Fe-N-C	16	3.22	3.22	0.013		Triangle scattering

Table S5. Surface area (SA) and pore volume (PV) of the sample in its pristine state and after partial Fe-extraction. For the SA, both the value obtained by applying the BET theory (SA_{BET}) and the one from QSDFT calculation with slyt and cylindrical pores (SA_{QSDFT}) are reported. For the PV, both the value from QSDFT (PV_{QSDFT}) and the one measured at $P/P_0 \sim 0.99$ (TPV) are reported. Micro indicates pores ≤ 2 nm and meso pores between 2 nm and 33 nm (upper value of the employed model).

Sample	SA_{BET} ($m^2 g^{-1}$)	TPV ($cc\ g^{-1}$)	SA_{QSDFT} ($m^2 g^{-1}$)			PV_{QSDFT} ($cc\ g^{-1}$)		
			micro	meso	total	micro	meso	total
$[FeN_4]N_{32}C_{520}$	2067	4.42	546	1367	1913	0.238	3.575	3.813
$[FeN_4]_{0.23}[N_4]_{0.77}N_{32}C_{520}$	1922	3.74	557	1184	1741	0.252	2.778	3.030
$[FeN_4]_{0.17}[N_4]_{0.83}N_{32}C_{520}$	1878	3.59	586	1142	1728	0.253	2.667	2.920

Table S6. Elemental composition of the sample in its pristine state. Values for carbon, hydrogen and nitrogen are obtained averaging two independent combustion measurements.

Sample	C (wt.%)	H (wt.%)	N (wt.%)	C/N
$[FeN_4]N_{32}C_{520}$	75.15	1.00	6.08	12.36

References

[1] K. Elumeeva, N. Fechler, T. P. Fellinger, M. Antonietti, *Materials Horizons* **2014**, *1*, 588-594.

[2] D. Menga, J. L. Low, Y.-S. Li, I. Arčon, B. Koyutürk, F. Wagner, F. Ruiz-Zepeda, M. Gaberšček, B. Paulus, T.-P. Fellinger, *Journal of the American Chemical Society* **2021**, *143*, 18010-18019.

[3] H. Riesemeier, K. Ecker, W. Görner, B. R. Müller, M. Radtke, M. Krumrey, *X-Ray Spectrometry* **2005**, *34*, 160-163.

[4] B. Ravel, M. Newville, *J Synchrotron Radiat* **2005**, *12*, 537-541.

[5] U. A. Paulus, T. J. Schmidt, H. A. Gasteiger, R. J. Behm, *J. Electroanal. Chem.*, 2001, *495*(2), 135-145.

3.2.2 Elucidating the Intrinsic Activity of Tetrapyrrolic Fe-N-C Electrocatalysts for the Oxygen Reduction Reaction in Alkaline Medium

The article "Elucidating the Intrinsic Activity of Tetrapyrrolic Fe-N-C Electrocatalysts for the Oxygen Reduction Reaction in Alkaline Medium" was submitted in October 2022 to the peer-reviewed journal *Materials Horizon*.

In this study, we exploit our newly developed method for the determination of the TOF of M-N_4 sites[119] to quantify intrinsic activity values for different M-N-Cs in alkaline medium.

Following the synthetic strategies presented in the previous publications,[105-106, 119] four isomorphic catalysts which differ only in the type/amount of M coordinated to the N_4 pocket are synthetised. These are a Zn-N-C, a metal-free N-doped carbon (NDC) and two Fe-N-Cs with different Fe content. As confirmed via EXAFS analysis, the type of N forming the M-coordinating (and M-free) N_4 moiety is pyrrolic. Moreover, the sharpness of the two quadrupole doublets of the Fe-N-C sample in cryo-Mössbauer spectroscopy measurements show a homogeneity of the active sites currently not observed in this class of materials.

The activity of the four catalysts is measured in alkaline electrolyte via RRDE experiments and their comparison allows for the calculations of TOF values for tetrapyrrolic Fe-N_4 sites as well as pyrrolic N sites. Zn, which is discovered to have a negative impact on the ORR in alkaline medium, is used to probe the TOF of $N_{pyrrolic}$ sites by comparing the difference in kinetic activity between Zn-N-C and NDC and values of 0.082 s^{-1} and 0.46 s^{-1} are reported at 0.80 V_{RHE} and 0.75 V_{RHE}, respectively. In the same way, the TOF is calculated for the isomorphic Fe-N-C material which has high values of 0.4 s^{-1} and 4 s^{-1} at 0.90 V_{RHE} and 0.85 V_{RHE}, respectively. The high TOF translates into high mass activity, i.e., 2.8 ± 0.8 A g^{-1} and 28 ± 10 A g^{-1} at 0.90 V_{RHE} and 0.85 V_{RHE}, respectively, making this catalyst one of the best reported so far in alkaline electrolyte.

The introduction of M in the tetrapyrrolic N_4 pocket reduces the peroxide formation, likely due to HO_2^- coordination to the M sites (which is stronger to Fe compared to Zn) and further reduction to OH^- (electrochemically, for a total of 4 e^-, or chemically), as confirmed via DFT calculations. Based on these results and

literature reports,[43, 45, 47, 49, 51] it is proposed that the ORR follows mainly an outer sphere mechanism on NDC, with a consecutive inner sphere mechanism on Zn-N-C and Fe-N-C. Because of the independency of the Tafel slope (TS) from the metal coordinated to the tetrapyrrolic N_4 pocket (including the metal free NDC), the rate determining step (RDS) is to be found in the first 2 e^- reduction. Moreover, by comparing the catalysts activity in alkaline and acidic electrolyte, it is found that in acidic electrolyte the M site plays a central role in the ORR activity, whereas in alkaline electrolyte it has a secondary function.

Employing DFT calculations, the density of states (DOS) and the energy of the Fermi level (E_f) of periodic models featuring different pyrrolic-type N_4 coordination sites is calculated. Mirroring the experimentally measured ORR activity, a correlation between the overpotential needed for the ORR and the E_f is found.

Author contributions

D.M. and T.-P.F. planned and designed the experiments. D.M. synthesized the catalyst and performed the electrochemical testing. A.G.B. performed and analyzed the XAS measurements. J.L.L. and B.P. provided the DFT calculations. D.M. and T.-P.F. wrote the manuscript. All authors discussed the results and commented on the manuscript.

Elucidating the intrinsic activity of tetrapyrrolic Fe-N-C electrocatalysts for the oxygen reduction reaction in alkaline medium

Davide Menga,[1] Jian Liang Low,[2] Ana Guilherme Buzanich,[3] Beate Paulus[2] and Tim-Patrick Fellinger[1,3]*

1) Chair of Technical Electrochemistry, Department of Chemistry and Catalysis Research Center, Technische Universität München (TUM), Lichtenbergstraße 4, 85748 Garching, Germany; 2) Chair for Theoretical Chemistry, Institut für Chemie und Biochemie, Freie Universität Berlin, Arnimallee 22, 14195 Berlin, Germany; 3) Bundesanstalt für Materialforschung und -prüfung (BAM), Unter den Eichen 44-46, 12203 Berlin, Germany

Abstract

Carbon-based precious-group metal-free electrocatalysts are gaining momentum in the scientific literature due to their application in many relevant energy conversion processes as well as low cost. However, their development and fundamental understanding are hampered by limitations in the quantification of the intrinsic activity of different catalytic sites as well as understanding the different reaction mechanisms. By complexation of tetrapyrrolic nitrogen doped carbons with iron ions and decomplexation of the corresponding Fe-N-C catalysts, we herein determine intrinsic activities of tetrapyrrolic active sites and gain insights into the reaction mechanism of the oxygen reduction reaction (ORR) in alkaline electrolyte. By comparison of the activity of isomorphic catalysts differing solely in type/amount of complexed metal, TOF values of 0.33 s^{-1} and 1.84 s^{-1} are found at 0.80 V_{RHE} and 0.75 V_{RHE}, respectively, for tetrapyrrolic N_4 sites and TOF values of 0.4 s^{-1} and 4 s^{-1} are reported for tetrapyrrolic Fe-N_4 sites at 0.90 V_{RHE} and 0.85 V_{RHE}, respectively.

Introduction

Carbon-based precious-group metal (PGM)-free electrocatalysts are materials that are intensively studied due to their low cost and application in a wide range of relevant electrochemical reactions.[1-3] Especially regarding the oxygen reduction reaction (ORR) in proton exchange membrane fuel cells (PEMFCs), they have reached promising initial activity, comparable to state-of-the-art Pt-based electrocatalysts.[4-6] Even though they are approaching system-relevant stability, they still lack the requirements to meet wide-spread practical application in the technologically more mature acid based PEMFCs.[7] On the other hand, they show exceptional activity and stability in anion exchange membrane fuel cells (AEMFCs), even better compared to Pt-based materials.[8] For this reason, the ORR activity of metal- and nitrogen- co-doped carbons (M-N-Cs) as well as the metal-free nitrogen-doped-carbons (NDCs) is widely studied in alkaline electrolyte. Generally, there are several differences in the ORR mechanism when the pH increases.[9-10] In acidic medium, an inner-sphere-mechanism model is generally employed to explain the reduction of O_2 to H_2O_2 or H_2O, with the initial oxidative addition of O_2 to the active metal centre (generally accompanied by a concerted H^+ transfer to the oxygen molecule) proposed as the rate determining step (RDS) for low polarizations.[11-13] In alkaline environment, in contrast, it has been proposed that both inner- and outer-sphere mechanisms can occur, both independently or in parallel.[10, 13-15] The RDS is generally attributed to the first electron transfer to O_2[16] or the first proton transfer to $*O_2^-$ to form *OOH (* indicates that the intermediate is adsorbed on the active site).[11, 17] Moreover, kinetic

isotope effect studies suggest the occurrence of two parallel pathways, one of which has a proton independent RDS.[13] When an inner-sphere mechanism is taken into account, the possible available adsorption sites in M-N-C are the metal centres, but the C atoms close to nitrogen dopants as well. This consideration arises from DFT calculations of the O_2 adsorption on metal-free NDCs (in the Japanese community also referred to as "carbon alloys") completely free from metal sites.[18-19] While NDCs often show high activity in alkaline medium, high activity in acid is less common for this materials class, sometimes rising concerns of metal impurities.[20] For Fe-N-Cs, Fe poisoning experiments suppress the activity in acidic but not under alkaline conditions, indicating a non-metal-centred active site in alkaline electrolyte, i.e., that Fe might not be directly involved in the ORR mechanism.[21] In alkaline electrolyte, the one e^- reduction of O_2 to superoxide ($O_2^{\bullet -}$) is generally reported as a long-range electron transfer happening in the outer Helmholtz plane (OHP) and in most cases promotes only a 2 e^- reduction,[14] unless adsorption of the reaction intermediates to the catalyst surface happens, in which case a further reduction can take place (for a total of 4 e^-).[22] In an outer-sphere mechanism, the key factor determining the catalytic activity would be the electronic band structure.[22] The relationship between density of state (DOS) at the Fermi level and electron transfer kinetics (i.e., catalytic activity) has been intensively studied.[23-27] However, the electron transfer is typically occurring at defect sites, which renders them as "apparent" active sites in outer sphere reactions.

In order to rationally compare the specific activity of different catalyst via the turnover frequency (TOF), quantifying catalytic parameters such as active-site density (SD) is desirable. For M-N-Cs, these parameters are hard to assess, and different methods have been proposed in the scientific literature. Except for new emerging techniques,[28-29] the most-established methods mostly rely on probe molecules.[30-32] The use of probe molecules can limit the applicability of the method to ex-situ measurements[31] or to a certain pH range[30] and usually requires pre-treatments of the catalytic surface and strict protocols in order to obtain reproducible results.[30-32] Moreover, so far no methods are available for NDCs for different N sites, due to the lack of a suitable probe molecule. When assessing SD and specific activity, a catalyst free from inactive side phases is desirable, since these could influence the obtained values by interacting with the probe molecule or by affecting the employed electrochemical method. In our previous work we showed that via an active-site imprinting strategy followed by a transmetalation reaction, Mg-N-C and Zn-N-C containing Mg-N_4 and Zn-N_4 sites respectively, but no iron carbide nor metallic iron, can be transformed into active Fe-N-C electrocatalyst.[33-34] Moreover, when Zn is employed, tetrapyrrolic metal-coordination sites and hence very active and selective tetrapyrrolic Fe-N_4 sites can be prepared.[35] This synthetic strategy gives the opportunity to obtain a platform to systematically investigate the specific activity of different catalytic sites as well as the reaction mechanism. Very recently, we exploit this methodology in order to assess SD and TOF of an Fe-N-C catalyst with state-of-the-art activity in acidic electrolyte.[36]

In this work, we employ the aforementioned catalyst both in its Zn-coordinating state and in the Fe-coordinating state. After performing a M-to-H^+ ion exchange reaction, different electrocatalysts that differ solely in the type of metal coordinated to the tetrapyrrolic N_4 sites as well as the amount (including the metal-free state) are obtained. The different materials are then measured in a rotating ring disc electrode (RRDE) setup in order to gain insights into the ORR mechanism and the specific activity of different catalytic sites in alkaline medium.

Results and discussion

The Zn-N-C electrocatalyst is prepared similarly to what previously reported.[36-37] Briefly, Zn-N-C is prepared by carbonizing 1-ethyl-3-methylimidazolium dicyanamide (Emim-dca) in a $ZnCl_2$/NaCl eutectic mixture (T_m = 250 °C) at 900 °C in Ar atmosphere. Besides having a control on the morphology by simply tuning the mixture composition,[38] the presence of the Lewis-acidic Zn^{2+} ions facilitates the formation of tetrapyrrolic N_4 moieties.[35] The Zn-N-C so obtained is employed in the low- and high-temperature Zn-to-Fe ion-exchange reaction as well as in the M-extraction (i.e., Zn-to-H^+ ion-exchange reaction) in order to obtain the Fe-N-C and the metal-free NDC, respectively. The partially Fe-extracted sample is obtained from the Fe-N-C after M-extraction. The M-extraction step is performed using HCl, a non-oxidizing acid, and elevated temperatures of 160 °C for three days. In order to completely remove the Zn from Zn-N-C, this procedure was repeated two times. The metal amount in the final catalysts was determined by inductively coupled plasma-mass spectrometry (ICP-MS).

Extended X-ray absorption fine structure (EXAFS) measurements are employed to confirm the tetrapyrrolic coordination of the M in the Zn-N-C as well as the Fe-N-C and the partially extracted Fe-N-C. No Zn signal was detected for NDC, further confirming the total extraction of Zn. Figure 1 a-c shows the magnitude of the Fourier transformed spectrum of the samples, where one main peak at ~ 2 Å is found, typical for M-N/O scattering in M-N-Cs. When comparing the experimental data with the model based on a 2D tetrapyrrolic Zn-N-C and hydroxy-coordinated Fe-N-C (inset of the figures), a very good agreement is found for Zn-N-C (Figure 1a), Fe-N-C (Figure 1b) and Fe-N-C-extr (Figure 1c), respectively, allowing for the quantitative extraction of structural parameters (Table S1). Zn cations in Zn-N-C are coordinated to four pyrrolic N at 2.04 Å. In Fe-N-C, Fe cations are coordinated to four pyrrolic N at 2.04 Å and ~ 1 O atoms (from OH groups) at 1.83 Å. Fe-N-C-extr shows similar Fe coordination, indicating the same Fe environment of the remaining Fe atoms after extraction (Table S1). Cryo-Mössbauer spectroscopy was employed on Fe-N-C to further confirm the environment around the Fe atoms.[39-40] The spectrum measured at T=4.2 K shows two quadrupole doublets, namely D1 and D2, assigned to atomically dispersed Fe-N_4 sites (Figure 1d), confirming the results obtained via EXAFS analysis. D1 and D2 have a line width of 0.90 mm s^{-1} and 0.55 mm s^{-1} respectively, which points to a high homogeneity of the Fe-N_4 environment.[36] The Fe content in Fe-N-C-extr is too little to allow for a meaningful deconvolution of the Mössbauer spectrum (Figure S1).

RRDE measurements were employed to measure the ORR activity of the four isomorphic catalysts in O_2-saturated 0.1 M NaOH electrolyte. For all the measured catalyst a relatively low loading of 0.145 mg cm^{-2} was employed. Figure 2 a and b show the Tafel plots and peroxide yield, respectively. Zn-N-C shows the lowest activity with an $E_{1/2}$ of 0.71 V_{RHE} and mass activity of 0.86 ± 0.2 A g^{-1} and 7.4 ± 1 A g^{-1} at 0.80 V_{RHE} and 0.75 V_{RHE}, respectively. The Tafel slope (TS) is ~ 50 mV dec^{-1}. When Zn is removed from the catalyst, the $E_{1/2}$ shifts to a more positive value of 0.73 V_{RHE} and the mass activity increases to 2.89 ± 0.3 A g^{-1} and 18.9 ± 1 A g^{-1} at 0.80 V_{RHE} and 0.75 V_{RHE}, respectively. This indicates a negative impact on the activity of Zn^{2+} coordinated to tetrapyrrolic N_4 sites and is in agreement with our previous study by Petek et al.[41] Interestingly, the NDC clearly shows an increased peroxide detection in the ring current (Figure 2b). The detected peroxide is more than doubled compared to Zn-N-C when comparing the same loading of 0.145 mg cm^{-2} i.e., ≈35 % vs ≈15 %, respectively.

The comparison of the kinetic current in the two samples, together with the Zn content in the Zn-N-C material, allows for the determination of the specific activity of tetrapyrrolic N_4 sites in alkaline electrolyte. Similarly to the nitrite stripping method[30] and our recent work,[36] it is possible to calculate the TOF using equation 1:

$$TOF\ (s^{-1}) = \frac{\Delta i_k\ (A\ g^{-1})}{F\ (A\ s\ mol^{-1}) \times \Delta SD\ (mol\ g^{-1})} \qquad Equation\ (1)$$

The ΔSD is calculated from the Zn content (Table S2), which is used as probe. The Δi_{kin} is calculated as difference in kinetic current. TOF values of 0.33 s^{-1} and 1.84 s^{-1} are herein reported for the ORR activity of tetrapyrrolic N_4 sites in alkaline media at 0.80 V_{RHE} and 0.75 V_{RHE}, respectively. Intriguingly, the TS is unchanged, pointing to the fact that the RDS of the reaction is similar for both catalysts. Fe-N-C presents an $E_{1/2}$ of 0.84 V_{RHE} and mass activity of 2.8 ± 0.8 A g^{-1} and 28 ± 10 A g^{-1} at 0.90 V_{RHE} and 0.85 V_{RHE}, respectively, which places this catalyst among the best ORR catalysts reported so far in alkaline electrolyte.[31, 42-46] After partial Fe extraction, the $E_{1/2}$ shifts to a more negative value of 0.82 V_{RHE} and the mass activity at 0.90 V_{RHE} and 0.85 V_{RHE} drops to 1.1 ± 0.7 A g^{-1} and 10 ± 5 A g^{-1}, respectively. Both catalysts produce a negligible amount of H_2O_2 (< 3 %) at this catalyst loading (Figure 2b), pointing to a 4 e^- reduction (either direct or apparent) of the O_2 for Fe-N-C, differently compared to Zn-N-C and NDC, for which the 2 e^- reduction has a strong contribution on the ORR activity.[16, 47] The good activity of Fe-N-C is a consequence of its high TOF value which is calculated using equation 1. The ΔSD is the difference in Fe content between Fe-N-C and Fe-N-C-extr and the Δi_{kin} is the difference in kinetic activity between the two catalysts. The catalyst has a TOF of 0.4 s^{-1} and 4 s^{-1} at 0.90 V_{RHE} and 0.85 V_{RHE}, respectively, which are amongst the highest values ever reported for Fe-N-C electrocatalysts in alkaline medium.[29, 31-32] These values are also in line with reported values obtained with well-established methods,[31] supporting the validity of the described procedure. Intriguingly, Fe-N-C and Fe-N-C-extr show the same TS of ~ 50 mV dec^{-1} like Zn-N-C and NDC, pointing to the fact that the RDS is similar for all the four isomorphic catalysts considered. This allows for further considerations about the reaction mechanism of these materials in alkaline electrolytes. Due to the high pH, it is expected a strong OH^- adsorption on the electrode surface, as well as on the M-N_4 sites, making a double layer effect dominant in the ORR mechanism and promoting the outer-sphere mechanism.[10] This picture matches very well with the activity of NDC, which produces high amounts of HO_2^-, since the outer-sphere mechanism will promote mostly the 2 e^- reduction.[14] When a metal is introduced in the N_4 pocket, a lower HO_2^- yield is observed. This effect is particularly pronounced in the Fe-based samples, where even a minute Fe amount is enough to bring the peroxide yield almost to zero. For Fe-N-Cs it has been reported that peroxide reduction in alkaline electrolyte is kinetically favoured and that any peroxide intermediate formed during ORR is immediately reduced further to OH^-.[14] The adsorption of the HO_2^- produced by the NDC on the M sites with further reduction to OH^- (for a total of 4 e^- involved) requires an inner sphere mechanism. Since the TS are unaffected by the M introduction, this means that the RDS is not affected, hence the RDS for all four catalysts is to be found in the first 2 e^- reduction. Like for poisoning experiments,[21] the majority of the current generated by Fe-N-C in alkaline environment does not originate from Fe-N_4 sites. This is evident when comparing the difference in activity between Fe-N-C and Fe-N-C-extr in acidic electrolyte (Figure S2), where a far larger loss in performance is observed after Fe extraction compared to alkaline electrolyte. The higher efficiency of Fe-N-C and Fe-N-C-extr towards the 4 e^- reduction does not explain the lower overpotential needed for the ORR. Moreover, Zn-N-C shows lower HO_2^-

yield compared to NDC but higher overpotential. To explain the difference in activity, we looked at the difference in electrode potential (i.e., energy of the Fermi level, E_f) of NDC, Zn-N-C and Fe-N-C, since it will affect the first electron transfer to O_2.[22] It has been shown that for outer-sphere electron transfer, the DOS around the Fermi level and the electronic structure relates to the catalytic activity.[25-27] In the case of NDCs, the nitrogen doping causes the material to behave as a semiconductor and samples with higher carrier concentration and flat band potential were shown to require lower overpotential to start the ORR.[25] We performed DFT calculation employing periodic models featuring different pyrrolic-type N_4 coordination sites, namely the metal free H_2N_4, the Zn- and Fe- coordinated M-N_4, resembling NDC, Zn-N-C and Fe-N-C respectively (Figure 3 d-f). When O_2 is in proximity of the NDC surface, no binding is found, further supporting the hypothesis of the outer-sphere mechanism. Due to the OH^- adsorption on the electrode surface, as well as on the M-N_4 sites, we considered the DOS of the OH-adsorbed models for Zn-N-C and Fe-N-C. A large difference in E_f is found, namely -2.93 eV and -2.67 eV for Zn-N-C and Fe-N-C, respectively. This result agrees with the difference in activity observed between the two materials. Due to its higher electrode potential and higher carrier concentration at the Fermi level (Figure 3), Fe-N-C requires a lower overpotential to start the ORR. For NDC, when an OH is in close vicinity of the H_2N_4 site, the relaxation of the system induces a proton transfer to form H_2O. This situation is not representative of NDC in the experimentally measured conditions since, due to their high pK_a value, pyrrolic-type nitrogen atoms will stay protonated even in very alkaline environment.[10] For this reason, for NDC we considered the H_2N_4 periodic model where H_2O molecules are in close proximity of the site. In contrast to Fe-N-C and Z-N-C, due to the absence of specific sites, H_2O adsorption does not happen in H_2N_4. Reflecting the experimental trend in ORR activity, the E_f = - 2.80 eV of NDC is located in between the one of Zn-N-C and Fe-N-C.

Conclusion

In conclusion, the specific activity of M-N-C electrocatalysts with tetrapyrrolic M-N_4 sites was evaluated in alkaline electrolyte using a RRDE setup. Zn, which has been discovered to have a negative impact on the ORR in alkaline medium, was used to probe the TOF of tetrapyrrolic N_4 sites by comparing the difference in kinetic activity between Zn-N-C and NDC and values of 0.33 s^{-1} and 1.84 s^{-1} are reported at 0.80 V_{RHE} and 0.75 V_{RHE}, respectively. Moreover, a clear increase in the 2 e^- reduction of O_2 to HO_2^- takes place when more $N_{pyrrolic}$ sites become available for the ORR. In the same way, the TOF is calculated for the isomorphic Fe-N-C material which has extremely high values of 0.4 s^{-1} and 4 s^{-1} at 0.90 V_{RHE} and 0.85 V_{RHE}, respectively. The high TOF translates into high mass activity, i.e., 2.8 ± 0.8 A g^{-1} and 28 ± 10 A g^{-1} at 0.90 V_{RHE} and 0.85 V_{RHE}, respectively, making this catalyst one of the best reported so far in alkaline electrolyte. It has been found that the introduction of M in the tetrapyrrolic N_4 pocket reduces the peroxide formation, likely due to HO_2^- coordination to the M sites and further reduction to OH^- (for a total of 4 e^-). Because of the independency of the TS from the metal coordinated to the tetrapyrrolic N_4 sites (including the metal free NDC), the RDS is to be found in the first 2 e^- reduction. Employing DFT, the DOS and E_f of periodic models featuring different pyrrolic-type N_4 coordination sites is calculated. Mirroring the experimentally measured ORR activity, a correlation between the overpotential needed for the ORR and the E_f is found. Proposing a new method for the determination of TOF values in alkaline electrolyte for different catalytic sites and elucidating the ORR mechanism of M-N-C

materials with tetrapyrrolic M-N_4 sites, we believe that this work will advance the further development and fundamental understanding of ORR electrocatalysts and, because of its general applicability, it will eventually shine light to other reactions.

References

1. Shi, Z.; Yang, W.; Gu, Y.; Liao, T.; Sun, Z., Metal-Nitrogen-Doped Carbon Materials as Highly Efficient Catalysts: Progress and Rational Design. *Advanced Science* **2020,** *7* (15), 2001069.
2. Asset, T.; Maillard, F.; Jaouen, F., Electrocatalysis with Single-Metal Atom Sites in Doped Carbon Matrices. In *Supported Metal Single Atom Catalysis*, 2022; pp 531-582.
3. Kumar, A.; Vashistha, V. K.; Das, D. K.; Ibraheem, S.; Yasin, G.; Iqbal, R.; Nguyen, T. A.; Gupta, R. K.; Rasidul Islam, M., M-N-C-based single-atom catalysts for H2, O2 & CO2 electrocatalysis: activity descriptors, active sites identification, challenges and prospects. *Fuel* **2021,** *304*, 121420.
4. Liu, S.; Li, C.; Zachman, M. J.; Zeng, Y.; Yu, H.; Li, B.; Wang, M.; Braaten, J.; Liu, J.; Meyer, H. M.; Lucero, M.; Kropf, A. J.; Alp, E. E.; Gong, Q.; Shi, Q.; Feng, Z.; Xu, H.; Wang, G.; Myers, D. J.; Xie, J.; Cullen, D. A.; Litster, S.; Wu, G., Atomically dispersed iron sites with a nitrogen–carbon coating as highly active and durable oxygen reduction catalysts for fuel cells. *Nature Energy* **2022**.
5. Mehmood, A.; Gong, M.; Jaouen, F.; Roy, A.; Zitolo, A.; Khan, A.; Sougrati, M.-T.; Primbs, M.; Bonastre, A. M.; Fongalland, D.; Drazic, G.; Strasser, P.; Kucernak, A., High loading of single atomic iron sites in Fe–NC oxygen reduction catalysts for proton exchange membrane fuel cells. *Nature Catalysis* **2022,** *5* (4), 311-323.
6. Jiao, L.; Li, J.; Richard, L. L.; Sun, Q.; Stracensky, T.; Liu, E.; Sougrati, M. T.; Zhao, Z.; Yang, F.; Zhong, S.; Xu, H.; Mukerjee, S.; Huang, Y.; Cullen, D. A.; Park, J. H.; Ferrandon, M.; Myers, D. J.; Jaouen, F.; Jia, Q., Chemical vapour deposition of Fe–N–C oxygen reduction catalysts with full utilization of dense Fe–N4 sites. *Nature Materials* **2021,** *20* (10), 1385-1391.
7. Banham, D.; Kishimoto, T.; Zhou, Y.; Sato, T.; Bai, K.; Ozaki, J.-i.; Imashiro, Y.; Ye, S., Critical advancements in achieving high power and stable nonprecious metal catalyst-based MEAs for real-world proton exchange membrane fuel cell applications. *Sci. Adv.* **2018,** *4* (3).
8. Hossen, M. M.; Hasan, M. S.; Sardar, M. R. I.; Haider, J. b.; Mottakin; Tammeveski, K.; Atanassov, P., State-of-the-art and developmental trends in platinum group metal-free cathode catalyst for anion exchange membrane fuel cell (AEMFC). *Applied Catalysis B: Environmental* **2022**, 121733.
9. Sgarbi, R.; Kumar, K.; Jaouen, F.; Zitolo, A.; Ticianelli, E. A.; Maillard, F., Oxygen reduction reaction mechanism and kinetics on M-NxCy and M@N-C active sites present in model M-N-C catalysts under alkaline and acidic conditions. *Journal of Solid State Electrochemistry* **2021,** *25* (1), 45-56.
10. Rojas-Carbonell, S.; Artyushkova, K.; Serov, A.; Santoro, C.; Matanovic, I.; Atanassov, P., Effect of pH on the Activity of Platinum Group Metal-Free Catalysts in Oxygen Reduction Reaction. *ACS Catalysis* **2018,** *8* (4), 3041-3053.
11. Wei, J.; Xia, D.; Wei, Y.; Zhu, X.; Li, J.; Gan, L., Probing the Oxygen Reduction Reaction Intermediates and Dynamic Active Site Structures of Molecular and Pyrolyzed Fe–N–C Electrocatalysts by In Situ Raman Spectroscopy. *ACS Catalysis* **2022,** *12* (13), 7811-7820.
12. Zagal, J. H.; Koper, M. T. M., Reactivity Descriptors for the Activity of Molecular MN4 Catalysts for the Oxygen Reduction Reaction. *Angewandte Chemie International Edition* **2016,** *55* (47), 14510-14521.
13. Malko, D.; Kucernak, A., Kinetic isotope effect in the oxygen reduction reaction (ORR) over Fe-N/C catalysts under acidic and alkaline conditions. *Electrochemistry Communications* **2017,** *83*, 67-71.
14. Ramaswamy, N.; Mukerjee, S., Influence of Inner- and Outer-Sphere Electron Transfer Mechanisms during Electrocatalysis of Oxygen Reduction in Alkaline Media. *The Journal of Physical Chemistry C* **2011,** *115* (36), 18015-18026.
15. Ramaswamy, N.; Tylus, U.; Jia, Q.; Mukerjee, S., Activity Descriptor Identification for Oxygen Reduction on Nonprecious Electrocatalysts: Linking Surface Science to Coordination Chemistry. *Journal of the American Chemical Society* **2013,** *135* (41), 15443-15449.

16. Wu, Y.; Nagata, S.; Nabae, Y., Genuine four-electron oxygen reduction over precious-metal-free catalyst in alkaline media. *Electrochimica Acta* **2019,** *319*, 382-389.
17. Li, X.; Cao, C.-S.; Hung, S.-F.; Lu, Y.-R.; Cai, W.; Rykov, A. I.; Miao, S.; Xi, S.; Yang, H.; Hu, Z.; Wang, J.; Zhao, J.; Alp, E. E.; Xu, W.; Chan, T.-S.; Chen, H.; Xiong, Q.; Xiao, H.; Huang, Y.; Li, J.; Zhang, T.; Liu, B., Identification of the Electronic and Structural Dynamics of Catalytic Centers in Single-Fe-Atom Material. *Chem* **2020,** *6* (12), 3440-3454.
18. Yang, W.; Fellinger, T.-P.; Antonietti, M., Efficient metal-free oxygen reduction in alkaline medium on high-surface-area mesoporous nitrogen-doped carbons made from ionic liquids and nucleobases. *J. Am. Chem. Soc.* **2011,** *133* (2), 206-209.
19. Ikeda, T.; Boero, M.; Huang, S.-F.; Terakura, K.; Oshima, M.; Ozaki, J.-i., Carbon Alloy Catalysts: Active Sites for Oxygen Reduction Reaction. *The Journal of Physical Chemistry C* **2008,** *112* (38), 14706-14709.
20. Masa, J.; Xia, W.; Muhler, M.; Schuhmann, W., On the Role of Metals in Nitrogen-Doped Carbon Electrocatalysts for Oxygen Reduction. *Angewandte Chemie International Edition* **2015,** *54* (35), 10102-10120.
21. Malko, D.; Kucernak, A.; Lopes, T., Performance of Fe–N/C Oxygen Reduction Electrocatalysts toward NO₂[–], NO, and NH₂OH Electroreduction: From Fundamental Insights into the Active Center to a New Method for Environmental Nitrite Destruction. *Journal of the American Chemical Society* **2016,** *138* (49), 16056-16068.
22. Choi, C. H.; Lim, H.-K.; Chung, M. W.; Park, J. C.; Shin, H.; Kim, H.; Woo, S. I., Long-Range Electron Transfer over Graphene-Based Catalyst for High-Performing Oxygen Reduction Reactions: Importance of Size, N-doping, and Metallic Impurities. *Journal of the American Chemical Society* **2014,** *136* (25), 9070-9077.
23. Gerischer, H.; McIntyre, R.; Scherson, D.; Storck, W., Density of the electronic states of graphite: derivation from differential capacitance measurements. *The Journal of Physical Chemistry* **1987,** *91* (7), 1930-1935.
24. Gerischer, H., An interpretation of the double layer capacity of graphite electrodes in relation to the density of states at the Fermi level. *The Journal of Physical Chemistry* **1985,** *89* (20), 4249-4251.
25. Bera, B.; Chakraborty, A.; Kar, T.; Leuaa, P.; Neergat, M., Density of States, Carrier Concentration, and Flat Band Potential Derived from Electrochemical Impedance Measurements of N-Doped Carbon and Their Influence on Electrocatalysis of Oxygen Reduction Reaction. *The Journal of Physical Chemistry C* **2017,** *121* (38), 20850-20856.
26. Szroeder, P.; Górska, A.; Tsierkezos, N.; Ritter, U.; Strupiński, W., The role of band structure in electron transfer kinetics in low-dimensional carbon. *Materialwissenschaft und Werkstofftechnik* **2013,** *44* (2-3), 226-230.
27. Cline, K. K.; McDermott, M. T.; McCreery, R. L., Anomalously Slow Electron Transfer at Ordered Graphite Electrodes: Influence of Electronic Factors and Reactive Sites. *The Journal of Physical Chemistry* **1994,** *98* (20), 5314-5319.
28. Snitkoff-Sol, R. Z.; Friedman, A.; Honig, H. C.; Yurko, Y.; Kozhushner, A.; Zachman, M. J.; Zelenay, P.; Bond, A. M.; Elbaz, L., Quantifying the electrochemical active site density of precious metal-free catalysts in situ in fuel cells. *Nature Catalysis* **2022,** *5* (2), 163-170.
29. Jin, Z.; Li, P.; Meng, Y.; Fang, Z.; Xiao, D.; Yu, G., Understanding the inter-site distance effect in single-atom catalysts for oxygen electroreduction. *Nature Catalysis* **2021,** *4* (7), 615-622.
30. Malko, D.; Kucernak, A.; Lopes, T., In situ electrochemical quantification of active sites in Fe–N/C non-precious metal catalysts. *Nature Communications* **2016,** *7* (1), 13285.
31. Luo, F.; Choi, C. H.; Primbs, M. J. M.; Ju, W.; Li, S.; Leonard, N. D.; Thomas, A.; Jaouen, F.; Strasser, P., Accurate Evaluation of Active-Site Density (SD) and Turnover Frequency (TOF) of PGM-Free Metal–Nitrogen-Doped Carbon (MNC) Electrocatalysts using CO Cryo Adsorption. *ACS Catalysis* **2019,** *9* (6), 4841-4852.
32. Bae, G.; Kim, H.; Choi, H.; Jeong, P.; Kim, D. H.; Kwon, H. C.; Lee, K.-S.; Choi, M.; Oh, H.-S.; Jaouen, F.; Choi, C. H., Quantification of Active Site Density and Turnover Frequency: From Single-Atom Metal to Nanoparticle Electrocatalysts. *JACS Au* **2021,** *1* (5), 586-597.

33. Mehmood, A.; Pampel, J.; Ali, G.; Ha, H. Y.; Ruiz-Zepeda, F.; Fellinger, T.-P., Facile Metal Coordination of Active Site Imprinted Nitrogen Doped Carbons for the Conservative Preparation of Non-Noble Metal Oxygen Reduction Electrocatalysts. *Adv. Energy Mater.* **2018,** *8* (9), n/a.
34. Menga, D.; Ruiz-Zepeda, F.; Moriau, L.; Šala, M.; Wagner, F.; Koyutürk, B.; Bele, M.; Petek, U.; Hodnik, N.; Gaberšček, M.; Fellinger, T.-P., Active-Site Imprinting: Preparation of Fe–N–C Catalysts from Zinc Ion–Templated Ionothermal Nitrogen-Doped Carbons. *Advanced Energy Materials* **2019,** *9* (43), 1902412.
35. Menga, D.; Low, J. L.; Li, Y.-S.; Arčon, I.; Koyutürk, B.; Wagner, F.; Ruiz-Zepeda, F.; Gaberšček, M.; Paulus, B.; Fellinger, T.-P., Resolving the Dilemma of Fe–N–C Catalysts by the Selective Synthesis of Tetrapyrrolic Active Sites via an Imprinting Strategy. *Journal of the American Chemical Society* **2021,** *143* (43), 18010-18019.
36. Menga, D.; Buzanich, A. G.; Wagner, F.; Fellinger, T.-P., Evaluation of the Specific Activity of M-N-Cs and the Intrinsic Activity of Tetrapyrrolic Fe-N4 Sites for the Oxygen Reduction Reaction. *Angewandte Chemie International Edition* **2022**.
37. Elumeeva, K.; Fechler, N.; Fellinger, T. P.; Antonietti, M., Metal-free ionic liquid-derived electrocatalyst for high-performance oxygen reduction in acidic and alkaline electrolytes. *Materials Horizons* **2014,** *1* (6), 588-594.
38. Fechler, N.; Fellinger, T.-P.; Antonietti, M., "Salt Templating": A Simple and Sustainable Pathway toward Highly Porous Functional Carbons from Ionic Liquids. *Advanced Materials* **2013,** *25* (1), 75-79.
39. Wagner, S.; Auerbach, H.; Tait, C. E.; Martinaiou, I.; Kumar, S. C. N.; Kübel, C.; Sergeev, I.; Wille, H.-C.; Behrends, J.; Wolny, J. A.; Schünemann, V.; Kramm, U. I., Elucidating the Structural Composition of an Fe–N–C Catalyst by Nuclear- and Electron-Resonance Techniques. *Angewandte Chemie International Edition* **2019,** *58* (31), 10486-10492.
40. Sougrati, M. T.; Goellner, V.; Schuppert, A. K.; Stievano, L.; Jaouen, F., Probing active sites in iron-based catalysts for oxygen electro-reduction: A temperature-dependent 57Fe Mössbauer spectroscopy study. *Catalysis Today* **2016,** *262*, 110-120.
41. Petek, U.; Ruiz-Zepeda, F.; Arcon, I.; Sala, M.; Kopac Lautar, A.; Kovac, J.; Mozetic, M.; Menga, D.; Bele, M.; Fellinger, T. P.; Gaberšček, M., Imprinted N4 Sites in Nitrogen Doped Carbon with Improved Oxygen Reduction Activity. *Submitted* **2022**.
42. Santori, P. G.; Speck, F. D.; Cherevko, S.; Firouzjaie, H. A.; Peng, X.; Mustain, W. E.; Jaouen, F., High Performance FeNC and Mn-oxide/FeNC Layers for AEMFC Cathodes. *Journal of The Electrochemical Society* **2020,** *167* (13), 134505.
43. Huo, L.; Liu, B.; Zhang, G.; Si, R.; Liu, J.; Zhang, J., 2D Layered non-precious metal mesoporous electrocatalysts for enhanced oxygen reduction reaction. *Journal of Materials Chemistry A* **2017,** *5* (10), 4868-4878.
44. Adabi, H.; Shakouri, A.; Ul Hassan, N.; Varcoe, J. R.; Zulevi, B.; Serov, A.; Regalbuto, J. R.; Mustain, W. E., High-performing commercial Fe–N–C cathode electrocatalyst for anion-exchange membrane fuel cells. *Nature Energy* **2021,** *6* (8), 834-843.
45. Yuan, K.; Lützenkirchen-Hecht, D.; Li, L.; Shuai, L.; Li, Y.; Cao, R.; Qiu, M.; Zhuang, X.; Leung, M. K. H.; Chen, Y.; Scherf, U., Boosting Oxygen Reduction of Single Iron Active Sites via Geometric and Electronic Engineering: Nitrogen and Phosphorus Dual Coordination. *Journal of the American Chemical Society* **2020,** *142* (5), 2404-2412.
46. Jiang, Z.; Sun, W.; Shang, H.; Chen, W.; Sun, T.; Li, H.; Dong, J.; Zhou, J.; Li, Z.; Wang, Y.; Cao, R.; Sarangi, R.; Yang, Z.; Wang, D.; Zhang, J.; Li, Y., Atomic interface effect of a single atom copper catalyst for enhanced oxygen reduction reactions. *Energy & Environmental Science* **2019,** *12* (12), 3508-3514.
47. Wu, Y.; Nabae, Y., Rotating ring-disk electrode theory and method to correct quasi-four-electron oxygen reduction over Fe/N/C and N/C cathode catalysts. *Current Opinion in Electrochemistry* **2021,** *25*, 100633.

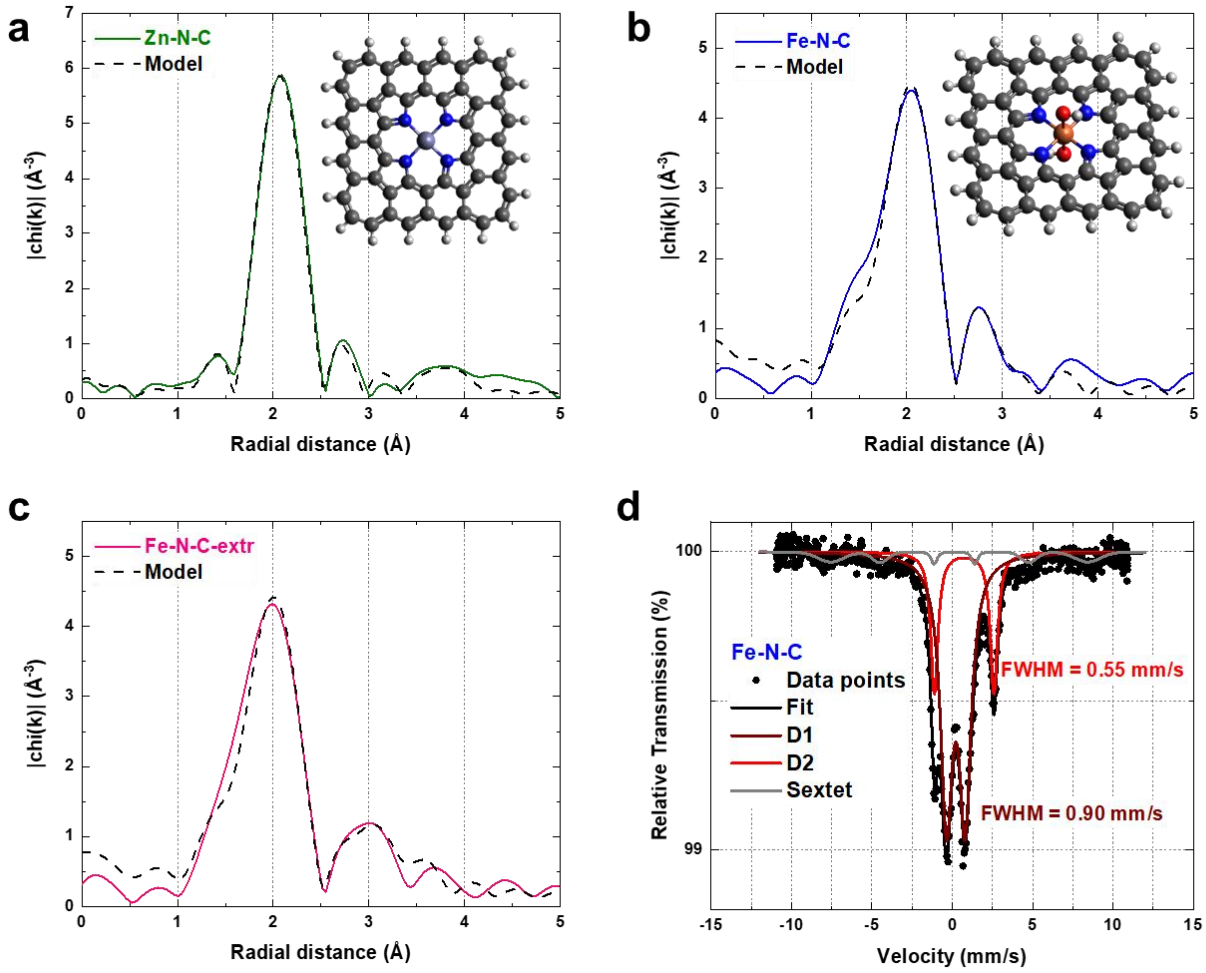

Figure 1. Experimental Fourier transform and best fit EXAFS model of the Zn K-edge EXAFS spectra of Zn-N-C (a) and Fe K-edge EXAFS spectra of Fe-N-C (b) and Fe-N-C-extr (c). The model used for Zn-N-C is displayed in the inset of (a) and the one used for the two Fe-containing samples is shown in the inset of (b) (Light blue = Zn; orange = Fe; blue = N; red = O; gray = C; white = H). Mössbauer spectrum of Fe-N-C measured at 4.2 K (d); FWHM refers to the line width of the indicated quadrupole doublet.

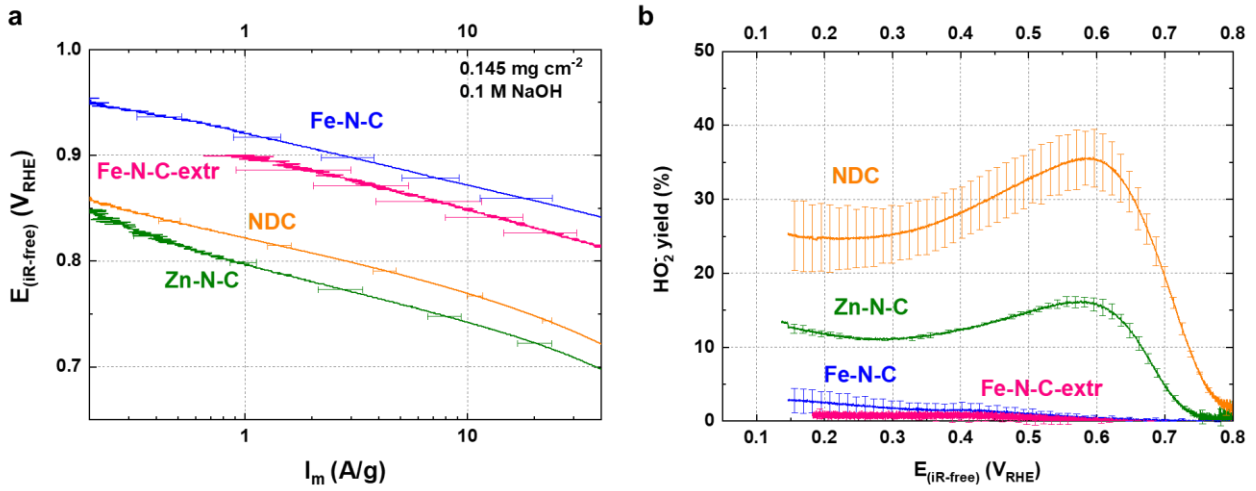

Figure 2. Tafel plots displaying the kinetic mass activity corrected for mass-transport limitation (a). HO_2^- yield obtained via RRDE experiments for the four isomorphic catalysts. Measurements were performed at room temperature in O_2-saturated 0.1 M NaOH at 1600 rpm, 10 mV s^{-1} (anodic scans).

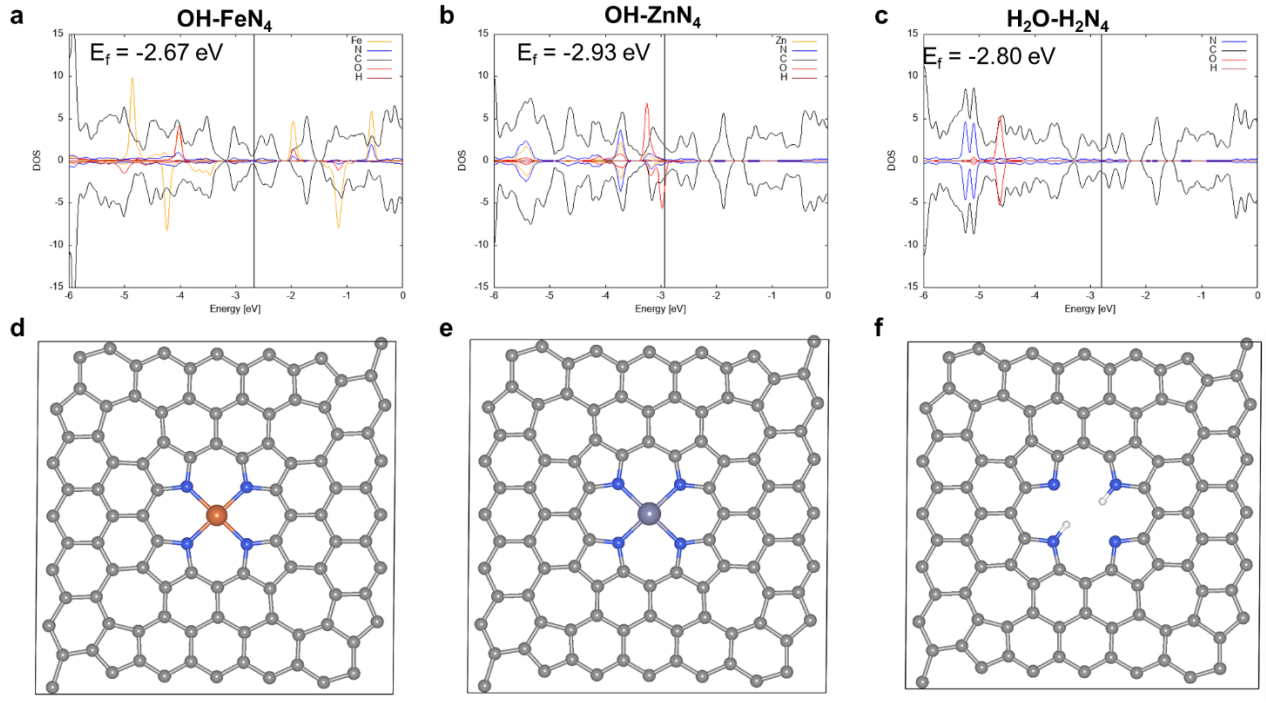

Figure 3. Density of states (DOS) and energy of the Fermi level (E_f) of the OH-adsorbed models for FeN_4 sites (a) ZnN_4 sites (b) and H_2N_4 with additional water molecule (c) calculated with the periodic models (displayed without OH^- or H_2O) shown in d-f.

Supporting Information

Experimental Section

Preparation of Zn-N-C

The catalyst was prepared similarly to what previously reported.[1] 1 g of 1-ethyl-3-methylimidazolium dicyanamide (Emim-dca) were thoroughly mixed with 8.26 g of $ZnCl_2$ and 1.74 g of NaCl inside an Ar-filled glovebox. The mixture was then transferred inside a crucible made of alumina and covered with a quartz lid. This was placed inside a tube furnace under constant Ar flow and heated up to a temperature of 900 °C for 1 hour, employing a heating rate of 2.5 °C/min. The final powder was ground in an agate mortar and washed with 0.1 M HCl overnight. After filtering and washing with deionized water in order to reach neutral pH, the sample was dried at 80 °C.

Preparation of Fe-N-C

As previously reported,[1, 2] the Zn-to-Fe ion exchange was carried out at low and high temperature. Firstly, Zn-N-C was degassed at 250 °C under vacuum and transferred inside an Ar-filled glovebox. Here, it was mixed with a $FeCl_3$/LiCl eutectic mixture and placed inside a closed Ar-filled flask. After heating the mixture at 170 °C for 5 hours, the sample was let to cool down to room temperature, opened to air and washed with deionized water to remove the salt mixture. Afterwards, it was stirred in 0.1 M HCl for several hours, filtered, washed with deionized water until neutral pH was reached and dried at 80 °C. The obtained powder was placed again in an alumina crucible and pushed inside a tube furnace pre-heated at 1000 °C under Ar atmosphere. After 15 minutes the furnace was turned off and opened to achieve a quick cool down of the sample.

Preparation of NDC

The metal free sample (NDC) was obtained from Zn-N-C after Zn removal (Zn-to-H^+ ion-exchange reaction). Zn-N-C was placed inside a closed Carius tube and stirred for 3 days in 2.4 M HCl at 160 °C. After filtering, thoroughly washing with deionized water and drying, the powder obtained was placed again inside the Carius tube and the entire procedure was repeated a second time in order to achieve the complete extraction of Zn.

Preparation of Fe-N-C-extr

For the partial Fe extraction, Fe-N-C was placed inside a closed Carius tube and stirred for 3 days in 2.4 M HCl at 160 °C. After filtering, washing with deionized water and drying, the final sample was obtained.

Physical characterizations

X-ray absorption near edge structure (XANES) and extended X-ray absorption fine structure (EXAFS) measurements at the Zn K-edge and at the Fe K-edge were carried out at the BAMline[3] located at BESSY-II (Berlin, Germany), operated by the Helmholtz-Zentrum Berlin für Materialien und Energie. Due to the low metal concentration (< 1 wt. %) the measurements were performed in fluorescence mode. XANES data evaluation and treatment was performed by using ATHENA program from Demeter package.[4] EXAFS curves were Fourier Transformed and fitted with a model adapted from our previous publication[1, 2] based on a $MN_4C_{52}H_{20}$ cluster (M = Zn or Fe). The model was used to calculate the scattering paths by FEFF to be able to quantify the coordination number and bond-length. Mössbauer measurements at T = 4.2 K were performed on a standard transmission spectrometer using a sinusoidal velocity waveform with both the source of ^{57}Co in rhodium and the absorber in the liquid He bath of a cryostat. In order to refer the measured isomer shifts to α-Fe at ambient temperature, 0.245 mm s^{-1} was added to the measured values.

Electrochemical measurements

Rotating ring disk electrode (RRDE) measurements in alkaline electrolyte were performed in a Teflon® cell in order to avoid glass dissolution. 0.1 M NaOH was prepared from monohydrate NaOH pellets and deionized ultrapure water. Saturated Ag/AgCl was employed as reference electrode and a Pt wire as counter. Measurements in acidic electrolyte were performed in a three-electrode glass cell using 0.1 M $HClO_4$ as electrolyte, Au wire as the counter electrode and a freshly calibrated RHE as the reference electrode The solution resistance was determined by electrochemical impedance spectroscopy and the reported potentials were corrected accordingly. The ORR polarization curves were corrected for capacitive contributions by subtracting the curves recorded in Ar-saturated electrolyte from the ones recorded in O_2-saturated electrolyte. Catalyst inks were prepared by dispersing 5 mg of catalyst in 1.68 mL of N,N-dimethylformamide and 50 µL of 5 wt% Nafion suspension, followed by sonication. To obtained a catalyst loading of 145 µg cm^{-2}, 10 µL of ink was drop-cast onto a well-polished glassy carbon electrode and dried under an infrared heater for 60 min. For each curve at least two separate measurements were averaged to give the shown polarization curve, and the standard deviation is illustrated with error bars. Kinetic currents were calculated based on limiting current correction as in reference [5].

Density functional theory (DFT) calculations

Spin-polarized DFT calculations were performed with the Vienna *ab initio* Simulation Package (VASP) in the framework of the projector-augmented wave (PAW) method.[6-9] The PBE functional was used with Grimme D3(BJ) dispersion correction with Becke-Johnson damping.[10-12] Hubbard correction for Fe was applied to account for delocalization error associated with the d-electrons (U = 4 eV, J = 1 eV).[13-15] The RMM-DIIS algorithm was applied for electronic relaxation with a convergence criterion of 10^{-5} eV. The Gaussian smearing approach with smearing width σ = 0.05 eV was applied. Ionic relaxation steps were performed with the conjugate gradient algorithm with force convergence of 10^{-2} eV/Å. K-points were sampled using a 3x3x1 *Γ*-centered mesh grid during optimization, and a 6x6x1 grid for single point calculations. The pyrrolic model used in the calculation was constructed based on the pyrrolic-D_{4h} model introduced by Menga et al. whereby the carbon lattice is extended to form a periodic 2D lattice with an interlayer vacuum of 15 Å.[2]

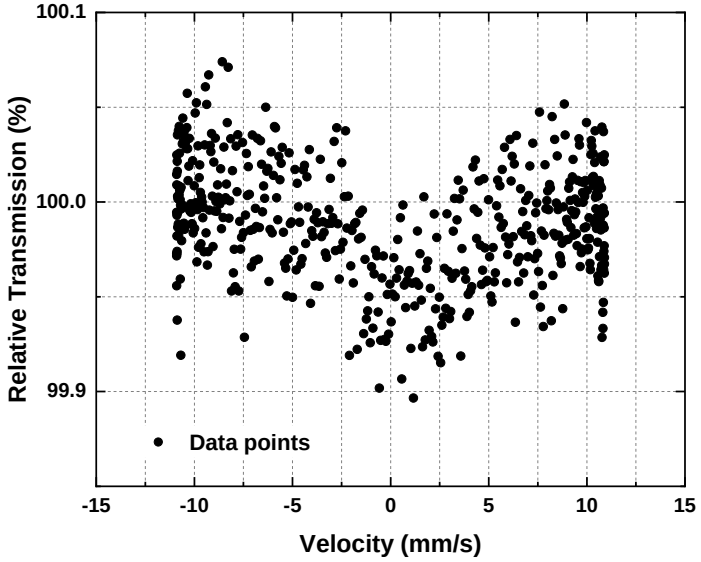

Figure S1. Mössbauer spectrum of Fe-N-C-extr measured at 4.2 K.

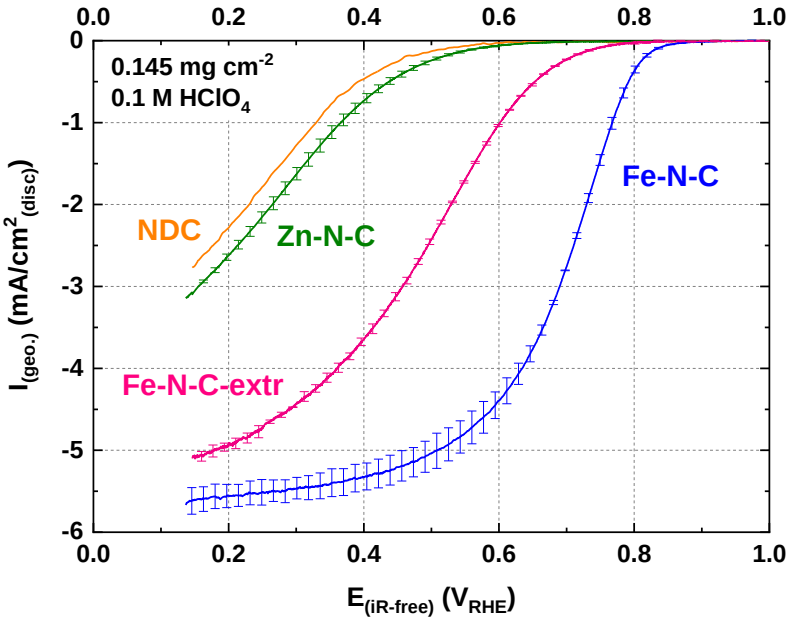

Figure S2. Capacitance-corrected ORR curves recorded with an RDE setup at room temperature in O_2-saturated 0.1 M $HClO_4$ at 1600 rpm, 10 mV s^{-1} (anodic scans).

Table S1. Structural information obtained from EXAFS by fitting the nearest coordination shells around Fe or Zn atoms in the samples with model $ZnN_4C_{52}H_{20}$ or $(OH)_2FeN_4C_{52}H_{20}$: degeneracy of the scattering path (N), interatomic distance from the fit (R) and from the model (Reff), and Debye-Waller factor (σ^2). The goodness-of-fit parameter is indicated by the R-factor.

Fe-N-C						
Scattering path	N	R (Å)	Reff (Å)	σ^2 (Å^2)	R-factor	
Fe-O	1.3	1.83	1.80	0.0036	0.014	Single-scattering
Fe-N	4	2.04	2.01	0.0036		Single-scattering
Fe-C	4	2.99	3.05	0.0116		Single-scattering
Fe-N-C	16	3.20	3.22	0.0181		Triangle scattering
Fe-N-C-extr						
Scattering path	N	R (Å)	Reff (Å)	σ^2 (Å^2)	R-factor	
Fe-O	1.5	1.80	1.80	0.0031	0.019	Single-scattering
Fe-N	4	2.01	2.01	0.0031		Single-scattering
Fe-C	4	3.03	3.05	0.0038		Single-scattering
Fe-N-C	16	3.21	3.22	0.0037		Triangle scattering
Zn-N-C						
Scattering path	N	R (Å)	Reff (Å)	σ^2 (Å^2)	R-factor	
Zn-N	4	2.04	2.01	0.0052	0.001	Single-scattering
Zn-C	8	3.07	3.04	0.0420		Single-scattering
Zn-N-C	16	3.24	3.21	0.0420		Triangle scattering

Table S2. Elemental composition of the four isomorphic samples. The metal content (M) is obtained from ICP-MS analysis and refers to Zn for Zn-N-C and Fe for Fe-N-C and Fe-N-C-extr. All values are expressed as wt.%.

Sample	C (%)	H (%)	N (%)	M (%)	C/N
Zn-N-C	68.17	1.94	5.89	0.42	11.57
Fe-N-C	75.15	1.00	6.08	0.67	12.36
NDC	72.64	1.09	6.24	-	11.64
Fe-N-C-extr	68.25	1.57	5.16	0.16	13.23

References

[1] D. Menga, A.G. Buzanich, F. Wagner, T.-P. Fellinger, Evaluation of the Specific Activity of M-N-Cs and the Intrinsic Activity of Tetrapyrrolic Fe-N4 Sites for the Oxygen Reduction Reaction, Angewandte Chemie International Edition, (2022).
[2] D. Menga, J.L. Low, Y.-S. Li, I. Arčon, B. Koyutürk, F. Wagner, F. Ruiz-Zepeda, M. Gaberšček, B. Paulus, T.-P. Fellinger, Resolving the Dilemma of Fe–N–C Catalysts by the Selective Synthesis of Tetrapyrrolic Active Sites via an Imprinting Strategy, Journal of the American Chemical Society, 143 (2021) 18010-18019.
[3] H. Riesemeier, K. Ecker, W. Görner, B.R. Müller, M. Radtke, M. Krumrey, Layout and first XRF applications of the BAMline at BESSY II, X-Ray Spectrometry, 34 (2005) 160-163.
[4] B. Ravel, M. Newville, ATHENA, ARTEMIS, HEPHAESTUS: data analysis for X-ray absorption spectroscopy using IFEFFIT, J Synchrotron Radiat, 12 (2005) 537-541.
[5] U.A. Paulus, T.J. Schmidt, H.A. Gasteiger, R.J. Behm, Oxygen reduction on a high-surface area Pt/Vulcan carbon catalyst: a thin-film rotating ring-disk electrode study, Journal of Electroanalytical Chemistry, 495 (2001) 134-145.
[6] G. Kresse, J. Hafner, Ab initiomolecular dynamics for liquid metals, Physical Review B, 47 (1993) 558-561.
[7] G. Kresse, D. Joubert, From ultrasoft pseudopotentials to the projector augmented-wave method, Physical Review B, 59 (1999) 1758-1775.
[8] G. Kresse, J. Furthmüller, Efficiency of ab-initio total energy calculations for metals and semiconductors using a plane-wave basis set, Computational Materials Science, 6 (1996) 15-50.
[9] G. Kresse, J. Furthmüller, Efficient iterative schemes forab initiototal-energy calculations using a plane-wave basis set, Physical Review B, 54 (1996) 11169-11186.
[10] J.P. Perdew, K. Burke, M. Ernzerhof, Generalized Gradient Approximation Made Simple, Physical Review Letters, 77 (1996) 3865-3868.
[11] S. Grimme, J. Antony, S. Ehrlich, H. Krieg, A consistent and accurate ab initio parametrization of density functional dispersion correction (DFT-D) for the 94 elements H-Pu, The Journal of Chemical Physics, 132 (2010) 154104.
[12] S. Grimme, S. Ehrlich, L. Goerigk, Effect of the damping function in dispersion corrected density functional theory, Journal of Computational Chemistry, 32 (2011) 1456-1465.
[13] S.L. Dudarev, G.A. Botton, S.Y. Savrasov, C.J. Humphreys, A.P. Sutton, Electron-energy-loss spectra and the structural stability of nickel oxide: An LSDA+U study, Physical Review B, 57 (1998) 1505-1509.
[14] A. Allerdt, H. Hafiz, B. Barbiellini, A. Bansil, A.E. Feiguin, Many-Body Effects in FeN4 Center Embedded in Graphene, Applied Sciences, 10 (2020) 2542.
[15] H. Wende, M. Bernien, J. Luo, C. Sorg, N. Ponpandian, J. Kurde, J. Miguel, M. Piantek, X. Xu, P. Eckhold, W. Kuch, K. Baberschke, P.M. Panchmatia, B. Sanyal, P.M. Oppeneer, O. Eriksson, Substrate-induced magnetic ordering and switching of iron porphyrin molecules, Nature Materials, 6 (2007) 516-520.

3.3 Stability assessment

As discussed in Section 1.3, the stability of Fe-N-Cs remains a critical challenge for their practical use as cathode catalysts in PEMFCs. This section focuses on this issue investigating both the shelf life of the material and its electrochemical stability under realistic PEMFC conditions.

3.3.1 Shelf Life of Single Atom Catalysts - Powder Degradation of Tetrapyrrolic Fe-N-C Electrocatalysts

This section presents the article "Shelf Life of Single Atom Catalysts - Powder Degradation of Tetrapyrrolic Fe-N-C Electrocatalysts" which was submitted in October 2022 to the peer-reviewed journal *Advanced Energy Materials*.

In the literature, the quadrupole doublet D1 observed in Mössbauer spectroscopy is usually assigned to a tetrapyrrolic Fe-N_4 moiety, whereas D2 is assigned to a tetrapyridinic one.[30, 36, 40] Moreover, even though one recent study has tackled the storage stability of Fe-N-Cs, it focused on its effect on the carbon surface rather than the active site.[92] Hence, the evolution of the active site over time due to the catalyst storage has not yet being investigated.

The purpose of this study is to employed Mössbauer spectroscopy to track how the exposure to air effects the active sites in a tetrapyrrolic Fe-N-C material from the moment of their formation to ~ one year of air exposure. After high temperature Zn-to-Fe transmetalation, the Fe-N-C was transferred as quickly as possible to an Ar-filled glovebox in order to reduce its exposure to air (air-free state). Cryo-Mössbauer spectra of the sample were recorded in the air-free state and after 2, 9, 30, 125 and 320 days. Simply upon air exposure, hence in non-pyrolytic conditions, D2 turns into D1, clearly showing that the different quadrupole doublets are both related to the same Fe-N_4 site and are a characteristic of the oxidation state or, more specifically, the coordination of an axial O_2/OH ligand. Over time, D1 turns into a sextet, indicating the chemical decomposition of Fe-N_4 sites into Fe(III) oxide that also results in electrocatalytic activity loss.

Similarly to the high-temperature Zn-to-Fe transmetalation, a thermal treatment is proposed in order to convert back the Fe(III) oxide into active Fe-N_4 sites. Since Fe-N_4 sites may decompose at high temperature, TGA-MS experiments of the aimed

thermal recovery process are carried out to search for a balance of recovery of oxidic iron and the degradation of functional Fe-N_4 sites. Thermal treatment below 850 °C has the potential for a thermal recovery in which Fe(III) oxide is reconverted into active Fe-N_4 sites, which remain stable at this temperature. We present an increase higher than 400 % of the mass activity at 0.8 V_{RHE} after almost one year of aging when performing the thermal recovery step. Considering that the discovered aging process presents the opposite process of the commonly used thermal catalyst post-treatment, this step is recommended to be done directly before use. Alternatively, is suggested that Fe-N-Cs should be stored under inert atmosphere. Because of the equivalent structure and chemistry of their active sites, we assume a closely related aging and recovery option for other atomically dispersed M-N-C materials or SACs.

Author contributions

D.M. and T.-P.F. planned and designed the experiments. D.M. synthesized and characterized the catalyst. D.M. performed the electrochemical testing and TGA-MS analysis. F.E.W. performed and analyzed the Mössbauer spectroscopy measurements. D.M. and T.-P.F. wrote the manuscript. All authors discussed the results and commented on the manuscript.

Shelf Life of Single Atom Catalysts: Powder Degradation of Tetrapyrrolic Fe-N-C Electrocatalysts

Davide Menga,[1] Friedrich E. Wagner[2] and Tim-Patrick Fellinger[, 1, 3]*

1) Chair of Technical Electrochemistry, Department of Chemistry and Catalysis Research Center, Technische Universität München (TUM), 85748 Garching, Germany; 2) Department of Physics, Technische Universität München (TUM), 85748 Garching, Germany; 3) Bundesanstalt für Materialforschung und -prüfung (BAM), 12203 Berlin, Germany

Abstract

M-N-C electrocatalyst are attracting the interest of the scientific community due to their possible application in many energy-related technologies as well as low fabrication cost and sustainability. This class of electrocatalysts is set to replace expensive critical raw materials in some applications and may allow the technically viable introduction of others. Before this can become reality, their current limitations need to be overcome. For example, Fe-N-Cs have reached sufficient activity to replace platinum in the electrochemical oxygen reduction reaction, but they still lack the required stability for widespread utilization. The activity loss during operation is reported in degradation or durability studies, but the shelf life of the typically powdered catalysts is largely unnoted. The understanding of the degradation of the active sites is needed to be able to stabilize catalysts to allow for long-time storage and suitable processing required for industrial production and application. In this work, we employ Mössbauer spectroscopy to follow structural changes of Fe-N-Cs originally mainly composed of tetrapyrrolic Fe-N_4 sites upon air exposure over about one year of shelf life. It is found that, in presence of O_2 and water, the active site responsible for the quadrupole doublet D1 decomposes forming Fe(III) oxide with concomitant loss in activity. Structural changes over time are related with changes in activity and as a result a procedure is proposed that can substantially recover aged catalyst even after about one year of shelf storage. The proposed recovery procedure is able to increase the mass activity at 0.8 V_{RHE} of the catalyst after about one year of shelf storage by more than 400 %.

Introduction

Electrochemical devices able to convert chemical energy into electricity and vice versa are a key technology compatible with the aims to push the decarbonization of the energy sector further. Reactions such as oxygen reduction and evolution (ORR and OER, respectively) and CO_2 reduction (CO_2RR) are fundamental in order to reduce our carbon footprint and a great scientific effort is being made to improve our knowledge and understanding about these complicated processes. State-of-the-art catalysts possess good activity but rely on expensive critical raw materials such as platinum-group metals (PGMs). For economic viability, these technologies should employ more inexpensive materials with competitive activity and stability, or at least level off at increased loadings due to reduced cost. Especially metal and nitrogen co-doped carbons (M-N-Cs, with M being usually first-row transition metals) have been intensively studied due to the low cost and availability of their constituents combined with promising activity towards a wide range of relevant electrochemical reactions.[1] The recent focus of those scientific efforts is on atomically dispersed M-N-Cs, also

referred to as single-atom-catalysts (SACs) which call for a complete metal utilization and hence optimal atom efficiency.[2] So far, the most studied M-N-Cs are those employing Fe as metal center. Fe-N-Cs find applications in different reactions, from the ORR[3] and CO_2RR[4] to, possibly, tumor therapy.[5] Synthetic methods have been optimized in order to yield materials containing entirely Fe-N_4 surface complexes, which are desirable active sites, being free from less active and often harmful inorganic side phases of metallic iron or iron carbide.[6-7] Moreover, we reported that the formation can be avoided and a high metal loading could be achieved using a different metal (e.g. Mg or Zn) to imprint the desired N_4 chelate coordination site (pyrolytic template-ion reaction), and coordinating the Fe in a later step via a transmetalation (ion-exchange) reaction.[7-8] This method has been recently employed to reach record high site density and activity.[9-10] Since Fe is a Mössbauer-active element, the very sensitive Mössbauer spectroscopy is widely employed to characterize Fe-N-Cs. At cryogenic conditions (T=4.2 K), Fe-N_4 sites apparently have a specific fingerprint signal that can be distinguished from side-phases.[11] The sites produce quadrupole doublet signals with isomer shifts (IS) usually in the range 0.2-0.7 mm s^{-1} and quadrupole splitting (QS) usually between 1-4 mm s^{-1}, depending on their exact coordination environment, which affects the spin of the Fe atoms and consequentially the Mössbauer spectrum. Atomically dispersed Fe-N-Cs with the desired Fe-N_x coordination show usually one to three of those quadrupole doublet signals.[6-7, 12-14] In the scientific literature, there has been the long-standing question whether these quadrupole doublets arise from different active sites or from the same one with and without an additional O_2 ligand.[15] Employing theoretical calculations, Mineva and co-workers recently attributed the doublet with mean QS value at 0.94 mm s^{-1}, here from now on referred to as D1, mostly to a Fe(III)N_4C_{12} surface site with an additional O_2 ligand and the doublet with mean QS value at 2.25 mm s^{-1}, referred from now on as D2, to a different Fe(II)N_4C_{10} moiety free from additional ligands.[16] Moreover, employing in-situ Mössbauer spectroscopy, Li and co-workers identified the site related to D1 as the most active but unstable one and the site related to D2 as the less active but very stable site.[17] Another important difference between the two sites is the local carbon structure. The site responsible for D1 is attributed to a defect-rich site with a pyrrolic-type nitrogen coordinating the Fe, whereas the site responsible for D2 has pyridinic nitrogen to chelate the Fe and is perfectly matching the graphene structure.[16-18]

In the present work, we employ a catalyst that can be assumed phase-pure with tetrapyrrolic Fe-N_4 sites that would refer to a Fe(III)N_4C_{12} structure. While the aging of multiphase catalysts may show an overlay of different aging mechanisms, the aging of such single-site catalyst should reveal a distinct degradation mechanism. We herein show by cryo-Mössbauer spectroscopy that D2 turns into D1 upon air exposure, indicating the presence of a single site as the origin of two distinct doublets, depending on the exposure of air. Moreover, we follow the degradation of the catalyst in its powder form over time and find that the air-exposed sites degrade into nanoscopic Fe(III) oxide, with concomitant transformation of D1 into a sextet signal accompanied by loss in activity. Some sites remain unchanged upon air-exposure, with D2 being unchanged for almost a year. The kinetic performance of the catalyst that was aged und air exposure can almost entirely be recovered by a thermal treatment. Therein the nanoscopic Fe(III) oxide is successfully converted back into active Fe-N_4 sites.

Results and discussion

NDC-Fe-HT was prepared similarly to what we previously reported.[7] Briefly, a Zn-N-C material was firstly synthetized carbonizing phthalonitrile in a $ZnCl_2$/LiCl eutectic salt melt at 800 °C in Ar atmosphere. The Lewis-acidic Zn^{2+} ions ensure the formation of a high density of N_4 moieties.[19] The material obtained after acidic workup was employed as solid-state ligand in the low- and high-temperature Zn-to-Fe transmetalation.[7] After high-temperature ion exchange, the material was transferred into an Ar-filled glovebox, trying to minimize its air exposure as much as possible. The material obtained is named NDC-Fe-HT-X where X indicates the duration of air exposure in days. Mössbauer spectra were recorded after zero (air free), 2, 9, 30, 125 and 320 days of air exposure, on the same catalyst sample, i.e., by keeping the catalyst inside the absorber for the entire time in order to exclude effects arising from different absorber thicknesses. Based on our previous work the structure of the surface complexes is a square-planar tetrapyrrolic Fe-N_4 motif, perfectly embedded into the planar graphitic backbone via compensation of pyrrolic 5-membered rings with 7-membered ring defects as in Stone-Wales defects.[7] Our reported structure presents a FeN_4C_{12} stoichiometry in the first coordination shell, however it is homogeneously embedded into carbon. Previously reported structural models were introducing pores close to the pyrrolic site and therefore had no isotropic second coordination shell.[6, 16] Despite the apparent single-site nature of the catalyst, the NDC-Fe-HT-0 spectrum (Figure 1a) is composed of two quadrupole doublets, of which 58% of the total area accounts for D1 (IS = 0.27 mm s^{-1}, QS = 1.54 mm s^{-1}) and 42% accounts for D2 (IS = 0.63 mm s^{-1}, QS = 2.89 mm s^{-1}), respectively. According to literature reports,[16-17] D1 is assigned to a Fe(III)-N_4 site with an axial O_2 ligand, while D2 is assigned to the square-planar Fe(II)-N_4 moiety, free from any additional oxy ligand, due to its high QS value.[7, 16-17] Up to now it remains unclear, if those are structurally different Fe-N_4 sites (refs. [16-18] assign D1 to a pyrrolic and D2 to a pyridinic structure), or if the different IS and QS may be caused by the effect of axial ligands. For square-planar tetrapyrrolic Fe-N_4 surface complexes an oxidation state of +2 for iron is expected, which could theoretically turn into +3 by oxidative addition, e.g., axial coordination with O_2, as observed for the respective molecular analogues. Indeed, after two days of air exposure (Figure 1b), the ratio between D1 and D2 changes drastically, with D1 contributing 73 % of the area and D2 accounting for the remaining 27 %. NDC-Fe-HT-9 (Figure 1c) shows only minor changes (74 % for D1 and 26 % for D2), indicating that the changes happening in the first two days do not continue at the same rate. The fact that D2 turns into D1 upon ambient conditions, clearly shows that the different quadrupole doublets are both related to the same Fe-N_4 site, since structural transformation of the FeN_4-surrounding carbon backbone would require temperatures above ≈1500 °C. Therefore, the D1 and D2 signals are either a characteristic of the oxidation state of iron, or more specifically a signature of the state of axial coordination. Moreover, the fact that D2 is still present in NDC-Fe-HT-9 indicates that 26 % of the Fe-N_4 sites are not accessible or not sensitive to the gas phase. After 30 days of air exposure (Figure 1d), D2 is unchanged whereas the D1 signal reduces by 8 % on the costs of the formation of two sextet components, each accounting for 4 % of the total area. This result indicates that after 30 days of ambient storage, a fraction of oxygen coordinated Fe(III)-N_4 sites are converted into nanosized Fe(III) oxide, while the square-planar Fe(II)-N_4 sites remain stable. The conversion of D1 into the two sextet components continues over time (Figure 1 e-f), with NDC-Fe-HT-125 showing an additional ≈20 % conversion of Fe-N_4 sites into Fe(III) oxide. The parameters for NDC-Fe-HT-320, on the other hand, hardly changed compared to NDC-Fe-HT-125. Similarly to what is reported for the electrochemical degradation of Fe-N-C catalysts,[17] also upon air exposure the

sites responsible for D1 are converted into Fe(III) oxide, whereas the sites responsible for D2 are stable. The contradiction that D2 has previously been assigned to less active sites compared to D1, while we herein show that the Fe-N_4 structure related to D1 and D2 hitherto is identical, can be reasonably explained by inaccessibility of remaining D2 sites to air. This is in line with previous assignments to surface-accessible sites (D1) versus buried sites (D2), however it is now evident that those can be isostructural.

We conducted rotating disc electrode (RDE) experiments to assess the effect of air exposure on the ORR activity of the catalyst. Figure 2a shows the activity of the pristine catalyst, after 200 and after 320 days of air exposure measured in O_2-saturated 0.1 M $HClO_4$ electrolyte with identical catalyst loadings of 0.29 mg cm^{-2}. The activity clearly decreases for the air exposed catalysts with NDC-Fe-HT-200 losing ≈ 70 mV in half-wave potential ($E_{1/2}$) and having a mass activity of ≈ 1.2 A g^{-1} at 0.8 V_{RHE}, lower compared to the pristine mass activity of ≈ 3.8 A g^{-1} at the same potential. Even though Mössbauer spectra indicate an unchanged relative abundance of Fe phases between day 125 and day 320, NDC-Fe-HT-320 shows further decreased activity in comparison to NDC-Fe-HT-200. More specifically, an additional loss of ≈ 70 mV in $E_{1/2}$ and ≈ 0.81 A g^{-1} @ 0.8 V_{RHE} is measured. Additionally, reduced slopes of the polarization curve of the aged catalysts become apparent in the kinetic region (at low currents). In the Tafel plot (Figure 2b) the corresponding increase in Tafel slope (TS) is observed only for potentials below 0.75 $V_{RHE,}$ indicating a regime of a mixed reaction mechanism due to the activity contribution of the carbon support. This is further supported by measuring the ORR activity of the catalyst without Fe in it, i.e. as Zn-N-C, which starts indeed around 0.75 V_{RHE} (Figure 2a). The pristine catalyst presents a TS of ≈ 75 mV dec^{-1}, indicative of predominant contribution of Fe-N_4 sites with their fast kinetics. NDC-Fe-HT-200 and NDC-Fe-HT-320 have a TS of ≈ 95 mV dec^{-1} and ≈ 120 mV dec^{-1}, respectively, suggesting that the kinetics increasingly dominated by the support material due to a reduced Fe-N_4 active site density. Consequently, the measured TS represents the convoluted activity of the remaining active Fe-N_4 sites and the arising electrocatalytic activity of the support in the lower potential range. The reduced contribution of Fe-N_4 sites to the electrocatalytic conversion is further confirmed via rotating ring disc electrode (RRDE) experiments. A clear increase in H_2O_2 production is observed, pointing to the increased contribution of the support activity and its lower selectivity.

The loss of ≈ 3.42 A g^{-1} @ 0.8 V_{RHE} after 320 days corresponds to a loss of about 90 % of the initial activity. This cannot be explained solely by a reduced intrinsic activity caused by the transformation of Fe-N_4 sites into Fe(III) oxide, since only about 25 % of D1 turn into the sextet component. Hence, other effects, possibly related to the morphology of the sample, reduce the effective activity and further compromise the catalyst efficiency after air exposure. Figure 3a shows the N_2-sorption porosimetry measurements of the pristine sample and after 320 days in air. At the beginning, the sample presents high micro- and mesoporosity and possess a Brunauer–Emmett–Teller (BET) surface area of 1247 m^2 g^{-1}. After 320 days in air a clear downshift of the isotherm is observed and the BET surface area drops to 922 m^2 g^{-1}. Quenched solid density functional theory (QSDFT) model with slit and cylindrical pores was employed to extract the pore size distribution (PSD) from the adsorption branch of the isotherms (Figure 3b). The results show that the PSD of the catalyst remains qualitatively unchanged, but the overall gas uptake is decreased, indicating that a fraction of the pore system is blocked, reasonably by the Fe(III) oxide particles, and hence not utilized for electrocatalysis. Even though the percentage of lost surface area is lower than the percentage of lost activity, the pore blocking may account for the remaining activity loss, since the

PSD displays no information on the pore connectivity, which is directly related to kinetics. In fact, the total pore volume loss is ≈ 50 % (Table 2). This could explain why the catalyst efficiency is even lower than expected from Mössbauer spectroscopy.

Short shelf life of Fe-N-C catalysts may complicate reproducibility of experimental results and can explain challenges in benchmarking experiments. Therefore, our results strongly suggest the storage of atomically dispersed catalysts in inert atmosphere. Moreover, on commercial scale an inappropriate storage may result in severe loss of the material value. Heat treatments are commonly used to activate catalysts and also the conversion of metal oxides on carbon supports into atomically dispersed catalysts has been reported.[18, 20-21] Additionally, Boldrin *et al.* reported a decreased ORR activity due to atmospheric storage and attributed this affect to the adsorption of H_2O and O_2 to the carbon surface.[22] The authors could also show a recovery *via* a thermal or electrochemical treatment.[22] Can the aged Fe-N-C catalyst be recycled by an additional heat treatment?

Fe(III) oxide is thermally stable, but sensitive to the carbothermal reduction in presence of carbon at high temperatures. The reaction is not conservative to the carbon support, which may be disadvantageous. However, controlled support degradation may also have advantageous effects on the catalyst efficiency.[23-24] Therefore, we conducted thermogravimetric analysis coupled with mass spectrometry (TGA-MS) of the aimed thermal recovery process to search for a balance of recovery of oxidic iron and the degradation of functional Fe-N_4 sites. Figure 5a shows the thermogram in Ar atmosphere for an Fe-N-C composed of 1.34 wt.% atomically dispersed Fe and 1.78 wt.% of oxidic Fe (Fe_2O_3@Fe-N-C). Two degassing steps, one at 150 °C and one at 250 °C, are performed in order to remove air and adsorbed water, before the temperature is raised to 1000 °C with a heating rate of 10 K min^{-1}. During the degassing steps signals related to CO_2, H_2O, NO and N_2 are detected (Figure 4b-e). At around 800 °C - the preparation temperature of the catalyst support - pyrolytic support reorganization is observed, indicated by evolution of CO_2, H_2O and NO (Figure 4b-e). At ≈ 950 °C (with onset at ≈ 850 °C) N_2 evolution is observed, which may go in hand with the decomposition of Fe-N_4 sites. The metastability of Fe-N_4 sites at the temperature of their pyrolytic formation has previously been considered the dilemma of Fe-N-C syntheses.[7] Here, the preformed nature of the catalyst support (having N_4 coordination sites) opens a temperature range below 850 °C in which Fe-N_4 sites can be formed, as recently elegantly deployed by Myers, Jaouen and Jia et al.[9] Consequently, the thermal recovery step on NDC-Fe-HT-320 was carried out at 800 °C for 15 min, in order to convert the Fe(III) oxide into active Fe-N_4 sites without reaching their decomposition temperature. Figure 2a shows the ORR activity measured with RDE setup in O_2-saturated 0.1 M $HClO_4$ electrolyte with the same catalyst loading of 0.29 mg cm^{-2}. After the recovery step, the catalyst shows an $E_{1/2}$ only 20 mV lower compared to the pristine catalyst and a mass activity of 1.93 A g^{-1} at 0.8 V_{RHE}. This reflects a high degree of recovery (only a factor of 2 less when comparing the mass activity at 0.8 V_{RHE}) or an improvement compared to the aged NDC-Fe-HT-320 of 120 mV in $E_{1/2}$ and 1.56 A g^{-1} at 0.8 V_{RHE}, which correspond to an increase of more than 400 % of its mass activity at 0.8 V_{RHE}. Even though the H_2O_2 production remains slightly higher compared to the pristine state (Figure 2c), it is 8 % less compared to NDC-Fe-HT-320, where the H_2O_2 production reaches its maximum (at 0.45 V_{RHE}). The recovery of the good catalytic kinetics of the material is further confirmed by the TS of ≈ 75 mV dec^{-1}, which equals the pristine state (Figure 2b). Mössbauer spectroscopy further confirms the conversion of Fe(III) oxide formed during almost one year of aging under air exposure into active Fe-N_4 sites (Figure 5). After recovery, D1 is responsible for 69 % of the spectral area (vs 52 % in NDC-Fe-HT-320), explaining the increased ORR activity, whereas D2

decreases to 15 %. As shown from TGA-MS analysis, the conversion of Fe(III) oxide into Fe-N_4 sites can be accompanied by carbon oxidation to CO_2. It is reasonable to assume that some previously buried D2 sites, are now accessible to air, hence contributing to D1. The sextet component, on the other hand, decreases from a total area of 24 % to 16 %. This indicates that some Fe(III) oxide is still present and explains why the catalyst does not recover entirely its activity. Further work should target the optimization of the recovery step in terms of time, temperature and gas atmosphere employed. The fact that the Fe-N-Cs obtained after low temperature transmetalation (NDC-Fe) are composed of atomically-dispersed Fe-N_4 sites and Fe(III) oxide, makes the material a reasonable precursor which can be stored and activated just before use, ultimately saving one energy-consuming thermal step.[19]

Conclusions

In conclusion, we showed experimentally that the D1 and D2 Mössbauer signals observed for atomically dispersed Fe-N-C catalysts are not characteristics of different Fe-N_4 sites, but the state of axial coordination of Fe-N_4 sites. Different IS and QS may be related to different axial ligands in general. Specifically, for tetrapyrrolic Fe(II)-N_4 sites, the quadrupole doublet D2 with IS and QS of ≈ 0.60 mm s^{-1} and ≈ 2.90 mm s^{-1}, can be turned into D1 (IS and QS ≈ 0.24 mm s^{-1} and ≈ 1.13 mm s^{-1}) by air exposure and assigned to O_2-coordinated Fe(III)-N_4 sites. Moreover, it supports literature reports that assign D1 to Fe-N_4 sites located on the catalyst surface, hence accessible to the gas phase and ORR active, whereas D2 is assigned to a site which is not accessible to the gas phase, although the coordination chemistry may vary for different Fe-N_4 sites. Mössbauer spectroscopy analysis of the calendar aging of tetrapyrrolic Fe-N-Cs over almost a year reveals the chemical decomposition mechanism that also results in electrocatalytic activity loss. Analogous to the well-known iron cycle in nature, the Fe(II) species is oxidized in presence of oxygen to Fe(III), which in the presence of moisture results in the precipitation of Fe(III) oxide. The powder degradation mirrors the reported electrochemical degradation of this class of materials and strongly suggests the storage of freshly prepared catalysts under inert atmosphere.[17] Thermal treatment below 850 °C has the potential for a thermal recovery in which Fe(III) oxide is reconverted into active Fe-N_4 sites, which remain stable at this temperature. We present an increase higher than 400 % of the mass activity at 0.8 V_{RHE} after almost one year of aging when performing the thermal recovery step. Considering that the discovered aging process presents the opposite process of the commonly used thermal catalyst post-treatment, this step is recommended to be done directly before use. Because of the equivalent structure and chemistry of their active sites, we assume a closely related aging and recovery option for other atomically dispersed M-N-C materials or SACs, depending on the stability of the metal inside the active sites versus its oxidic form.

References

1. Shi, Z.; Yang, W.; Gu, Y.; Liao, T.; Sun, Z., Metal-Nitrogen-Doped Carbon Materials as Highly Efficient Catalysts: Progress and Rational Design. *Advanced Science* **2020,** *7* (15), 2001069.
2. Single atom catalysts push the boundaries of heterogeneous catalysis. *Nature Communications* **2021,** *12* (1), 5884.
3. Jaouen, F.; Jones, D.; Coutard, N.; Artero, V.; Strasser, P.; Kucernak, A., Toward Platinum Group Metal-Free Catalysts for Hydrogen/Air Proton-Exchange Membrane Fuel Cells. *Johnson Matthey Technology Review* **2018,** *62* (2), 231-255.
4. Paul, S.; Kao, Y.-L.; Ni, L.; Ehnert, R.; Herrmann-Geppert, I.; van de Krol, R.; Stark, R. W.; Jaegermann, W.; Kramm, U. I.; Bogdanoff, P., Influence of the Metal Center in M–N–C Catalysts on the CO2 Reduction Reaction on Gas Diffusion Electrodes. *ACS Catalysis* **2021,** *11* (9), 5850-5864.
5. Huo, M.; Wang, L.; Wang, Y.; Chen, Y.; Shi, J., Nanocatalytic Tumor Therapy by Single-Atom Catalysts. *ACS Nano* **2019,** *13* (2), 2643-2653.
6. Zitolo, A.; Goellner, V.; Armel, V.; Sougrati, M.-T.; Mineva, T.; Stievano, L.; Fonda, E.; Jaouen, F., Identification of catalytic sites for oxygen reduction in iron- and nitrogen-doped graphene materials. *Nat Mater* **2015,** *14* (9), 937-942.
7. Menga, D.; Low, J. L.; Li, Y.-S.; Arčon, I.; Koyutürk, B.; Wagner, F.; Ruiz-Zepeda, F.; Gaberšček, M.; Paulus, B.; Fellinger, T.-P., Resolving the Dilemma of Fe–N–C Catalysts by the Selective Synthesis of Tetrapyrrolic Active Sites via an Imprinting Strategy. *Journal of the American Chemical Society* **2021,** *143* (43), 18010-18019.
8. Mehmood, A.; Pampel, J.; Ali, G.; Ha, H. Y.; Ruiz-Zepeda, F.; Fellinger, T.-P., Facile Metal Coordination of Active Site Imprinted Nitrogen Doped Carbons for the Conservative Preparation of Non-Noble Metal Oxygen Reduction Electrocatalysts. *Advanced Energy Materials* **2018,** *8* (9), 1701771.
9. Jiao, L.; Li, J.; Richard, L. L.; Sun, Q.; Stracensky, T.; Liu, E.; Sougrati, M. T.; Zhao, Z.; Yang, F.; Zhong, S.; Xu, H.; Mukerjee, S.; Huang, Y.; Cullen, D. A.; Park, J. H.; Ferrandon, M.; Myers, D. J.; Jaouen, F.; Jia, Q., Chemical vapour deposition of Fe–N–C oxygen reduction catalysts with full utilization of dense Fe–N4 sites. *Nature Materials* **2021,** *20* (10), 1385-1391.
10. Mehmood, A.; Gong, M.; Jaouen, F.; Roy, A.; Zitolo, A.; Khan, A.; Sougrati, M.-T.; Primbs, M.; Bonastre, A. M.; Fongalland, D.; Drazic, G.; Strasser, P.; Kucernak, A., High loading of single atomic iron sites in Fe–NC oxygen reduction catalysts for proton exchange membrane fuel cells. *Nature Catalysis* **2022,** *5* (4), 311-323.
11. Kramm, U. I.; Ni, L.; Wagner, S., 57Fe Mössbauer Spectroscopy Characterization of Electrocatalysts. *Advanced Materials* **2019,** *31* (31), 1805623.
12. Kramm, U. I.; Herrmann-Geppert, I.; Behrends, J.; Lips, K.; Fiechter, S.; Bogdanoff, P., On an Easy Way To Prepare Metal–Nitrogen Doped Carbon with Exclusive Presence of MeN4-type Sites Active for the ORR. *Journal of the American Chemical Society* **2016,** *138* (2), 635-640.
13. Koslowski, U. I.; Abs-Wurmbach, I.; Fiechter, S.; Bogdanoff, P., Nature of the Catalytic Centers of Porphyrin-Based Electrocatalysts for the ORR: A Correlation of Kinetic Current Density with the Site Density of Fe−N4 Centers. *The Journal of Physical Chemistry C* **2008,** *112* (39), 15356-15366.
14. Kramm, U. I.; Abs-Wurmbach, I.; Herrmann-Geppert, I.; Radnik, J.; Fiechter, S.; Bogdanoff, P., Influence of the Electron-Density of FeN[sub 4]-Centers Towards the Catalytic Activity of Pyrolyzed FeTMPPCl-Based ORR-Electrocatalysts. *Journal of The Electrochemical Society* **2011,** *158* (1), B69.
15. Jia, Q.; Liu, E.; Jiao, L.; Pann, S.; Mukerjee, S., X-Ray Absorption Spectroscopy Characterizations on PGM-Free Electrocatalysts: Justification, Advantages, and Limitations. *Advanced Materials* **2019,** *31* (31), 1805157.
16. Mineva, T.; Matanovic, I.; Atanassov, P.; Sougrati, M.-T.; Stievano, L.; Clémancey, M.; Kochem, A.; Latour, J.-M.; Jaouen, F., Understanding Active Sites in Pyrolyzed Fe–N–C Catalysts for Fuel Cell Cathodes by Bridging Density Functional Theory Calculations and 57Fe Mössbauer Spectroscopy. *ACS Catalysis* **2019,** *9* (10), 9359-9371.
17. Li, J.; Sougrati, M. T.; Zitolo, A.; Ablett, J. M.; Oğuz, I. C.; Mineva, T.; Matanovic, I.; Atanassov, P.; Huang, Y.; Zenyuk, I.; Di Cicco, A.; Kumar, K.; Dubau, L.; Maillard, F.; Dražić, G.; Jaouen, F., Identification of durable and non-durable FeNx sites in Fe–N–C materials for proton exchange membrane fuel cells. *Nature Catalysis* **2021,** *4* (1), 10-19.

18. Liu, S.; Li, C.; Zachman, M. J.; Zeng, Y.; Yu, H.; Li, B.; Wang, M.; Braaten, J.; Liu, J.; Meyer, H. M.; Lucero, M.; Kropf, A. J.; Alp, E. E.; Gong, Q.; Shi, Q.; Feng, Z.; Xu, H.; Wang, G.; Myers, D. J.; Xie, J.; Cullen, D. A.; Litster, S.; Wu, G., Atomically dispersed iron sites with a nitrogen–carbon coating as highly active and durable oxygen reduction catalysts for fuel cells. *Nature Energy* **2022**.
19. Menga, D.; Ruiz-Zepeda, F.; Moriau, L.; Šala, M.; Wagner, F.; Koyutürk, B.; Bele, M.; Petek, U.; Hodnik, N.; Gaberšček, M.; Fellinger, T.-P., Active-Site Imprinting: Preparation of Fe–N–C Catalysts from Zinc Ion–Templated Ionothermal Nitrogen-Doped Carbons. *Advanced Energy Materials* **2019,** *9* (43), 1902412.
20. Kramm, U. I.; Herrmann-Geppert, I.; Bogdanoff, P.; Fiechter, S., Effect of an Ammonia Treatment on Structure, Composition, and Oxygen Reduction Reaction Activity of Fe–N–C Catalysts. *The Journal of Physical Chemistry C* **2011,** *115* (47), 23417-23427.
21. Sahraie, N. R.; Kramm, U. I.; Steinberg, J.; Zhang, Y.; Thomas, A.; Reier, T.; Paraknowitsch, J.-P.; Strasser, P., Quantifying the density and utilization of active sites in non-precious metal oxygen electroreduction catalysts. *Nature Communications* **2015,** *6* (1), 8618.
22. Boldrin, P.; Malko, D.; Mehmood, A.; Kramm, U. I.; Wagner, S.; Paul, S.; Weidler, N.; Kucernak, A., Deactivation, reactivation and super-activation of Fe-N/C oxygen reduction electrocatalysts: Gas sorption, physical and electrochemical investigation using NO and O2. *Applied Catalysis B: Environmental* **2021,** *292*, 120169.
23. Lazaridis, T.; Gasteiger, H. A., Pt-Catalyzed Oxidation of PEMFC Carbon Supports: A Path to Highly Accessible Carbon Morphologies and Implications for Start-Up/Shut-Down Degradation. *Journal of The Electrochemical Society* **2021,** *168* (11), 114517.
24. Kongkanand, A.; Carpenter, M. K. US Patent Application US 9,947,935 B1, filed Sep. 30, 2016 and published Apr. 17, 2018.

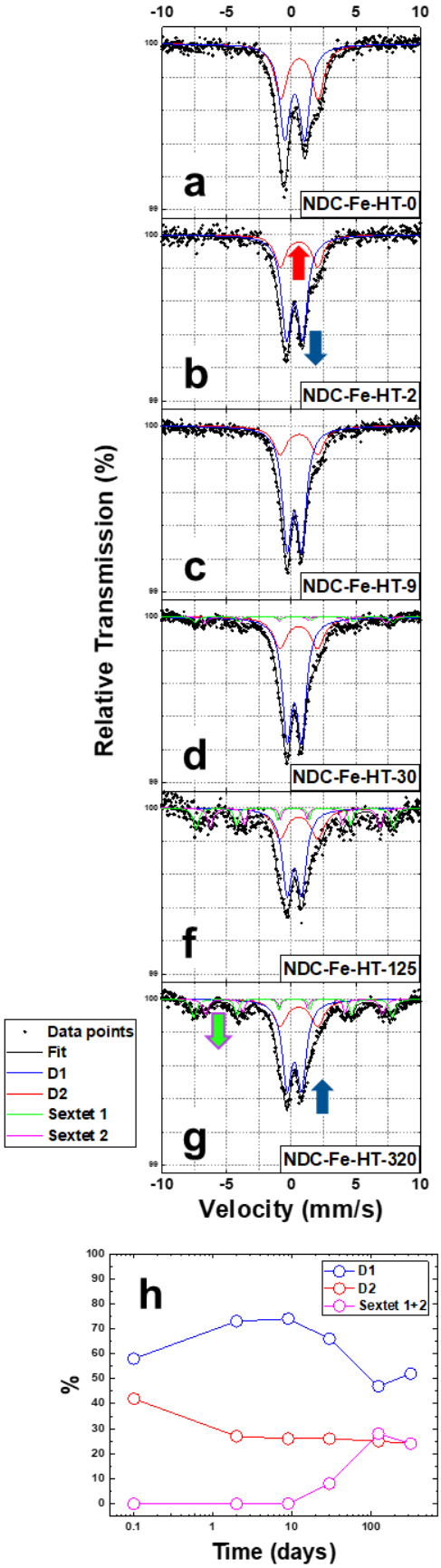

Figure 1. (a-g) Mössbauer spectra of NDC-Fe-HT-X in the 320 days of air exposure. (h) Summary of the percentage of the different components in the Mössbauer spectra over time. Spectra are measured at T = 4.2 K.

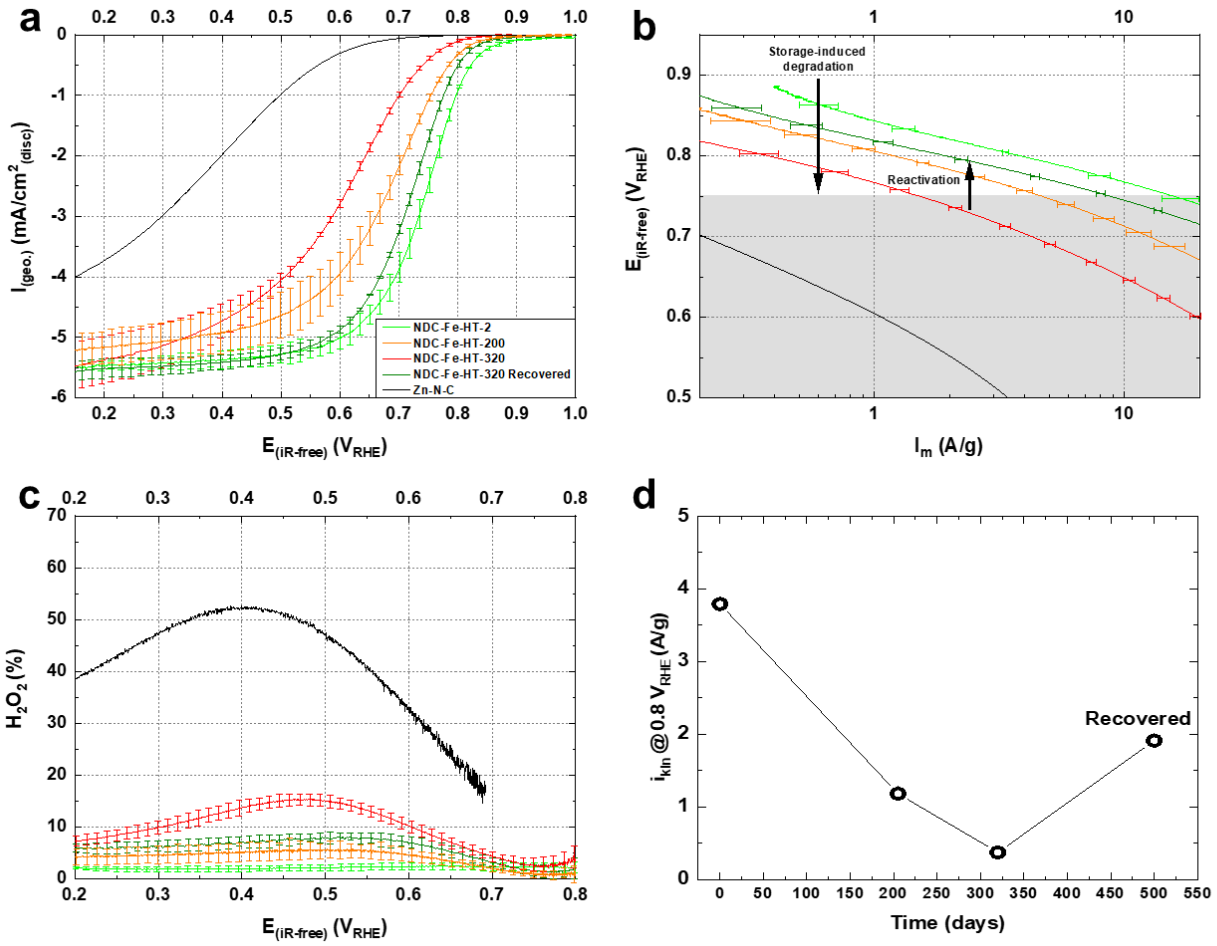

Figure 2. (a) Capacitance-corrected ORR curves recorded with an RDE setup at room temperature in O_2-saturated 0.1 M $HClO_4$ at 1600 rpm, 10 mV s^{-1} (anodic scans) for NDC-Fe-HT-X and the sample after thermal recovery. The Zn-N-C starting material is plotted to show that the activity of the carbon support starts around 0.75 V_{RHE}. (b) Respective Tafel plots showing purely the kinetic mass activity corrected for mass-transport limitation. The shaded gray area marks the potential region where the support activity takes over. (c) Respective H_2O_2 yield obtained via RRDE experiments. (d) Mass activity at 0.80 V_{RHE} of NDC-Fe-HT-X and the sample after thermal recovery.

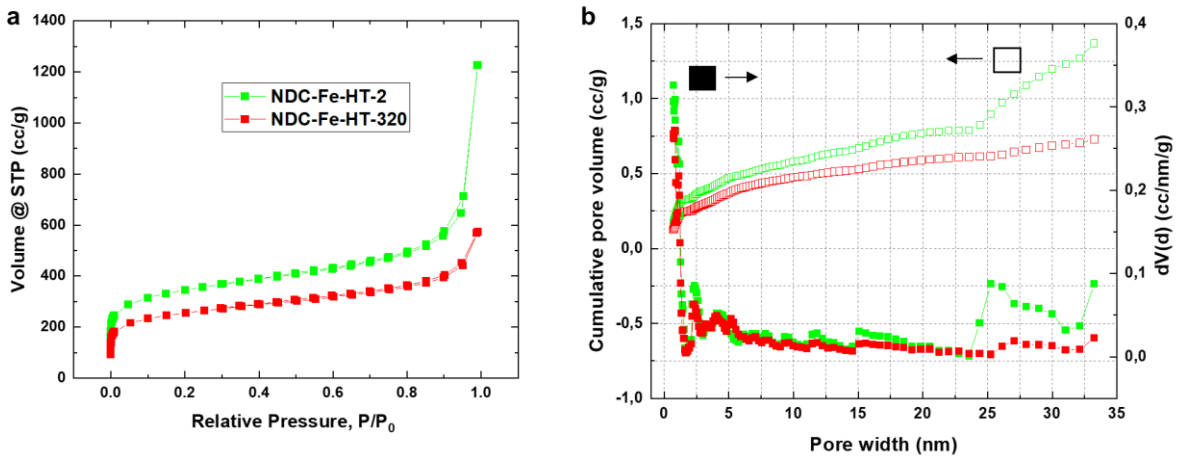

Figure 3. (a) Isotherms of NDC-Fe-HT-X obtained from N_2 sorption measurement. (b) The respective pore-size distribution from the adsorption branch employing the QSDFT model for slit and cylindrical pores.

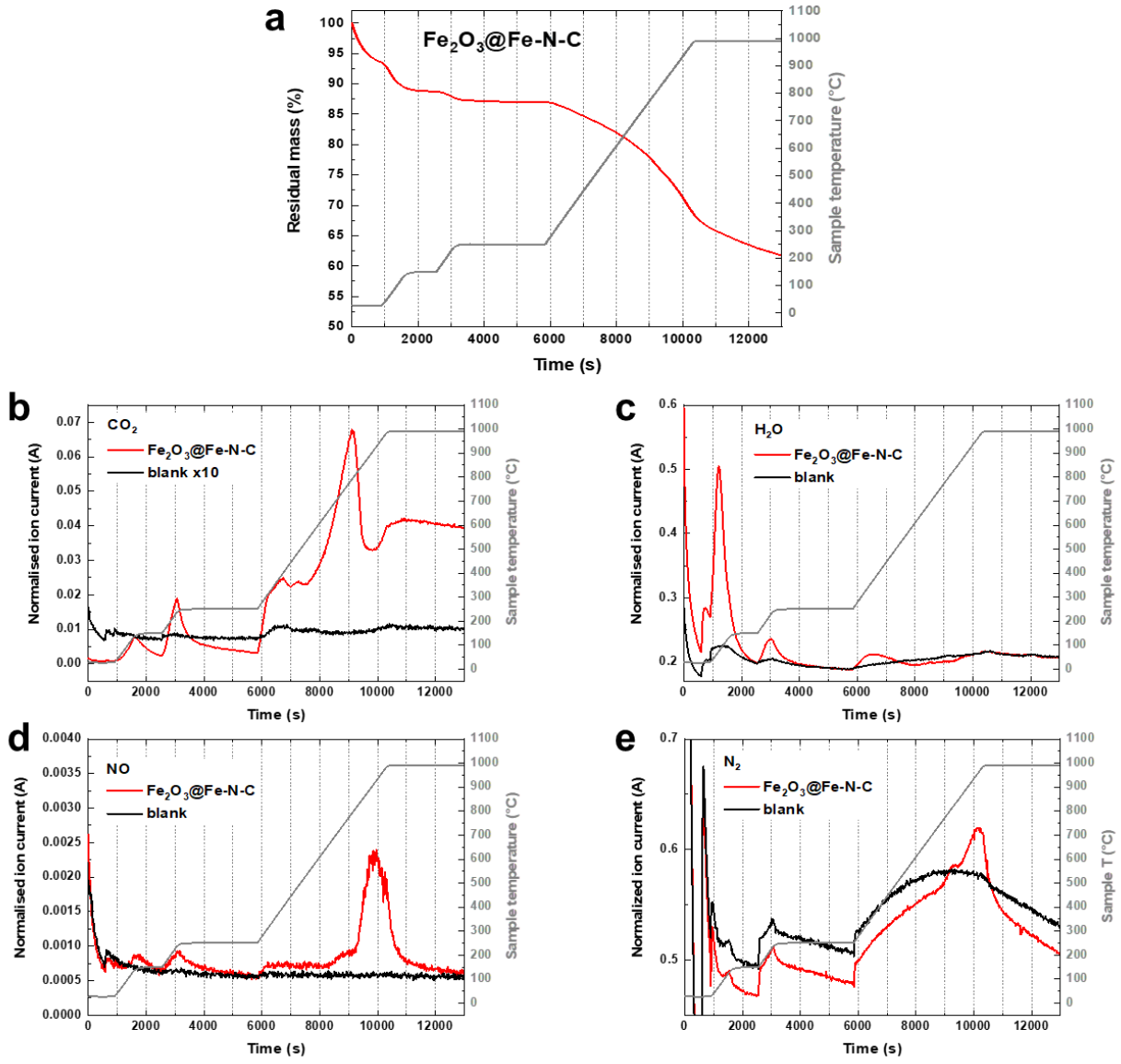

Figure 4. (a) Results of the TGA-MS investigation of Fe_2O_3@Fe-N-C upon heating to 1000 °C under Ar atmosphere. TGA curve displaying the sample mass in percentage (red) and sample temperature (gray). (b) CO_2, (c) H_2O, (d) NO and (e) N_2 MS signals for the sample (red) in comparison with a blank measurement where only the crucible without sample is employed (black). The sample temperature is displayed in gray.

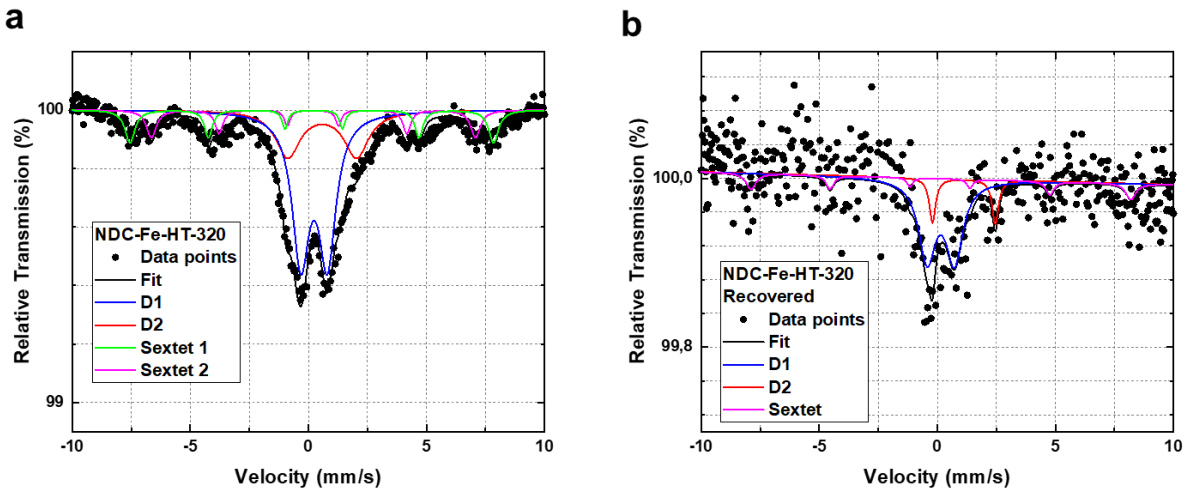

Figure 5. Mössbauer spectra of NDC-Fe-HT-320 measured at 4.2 K (a) before and (b) after thermal recovery.

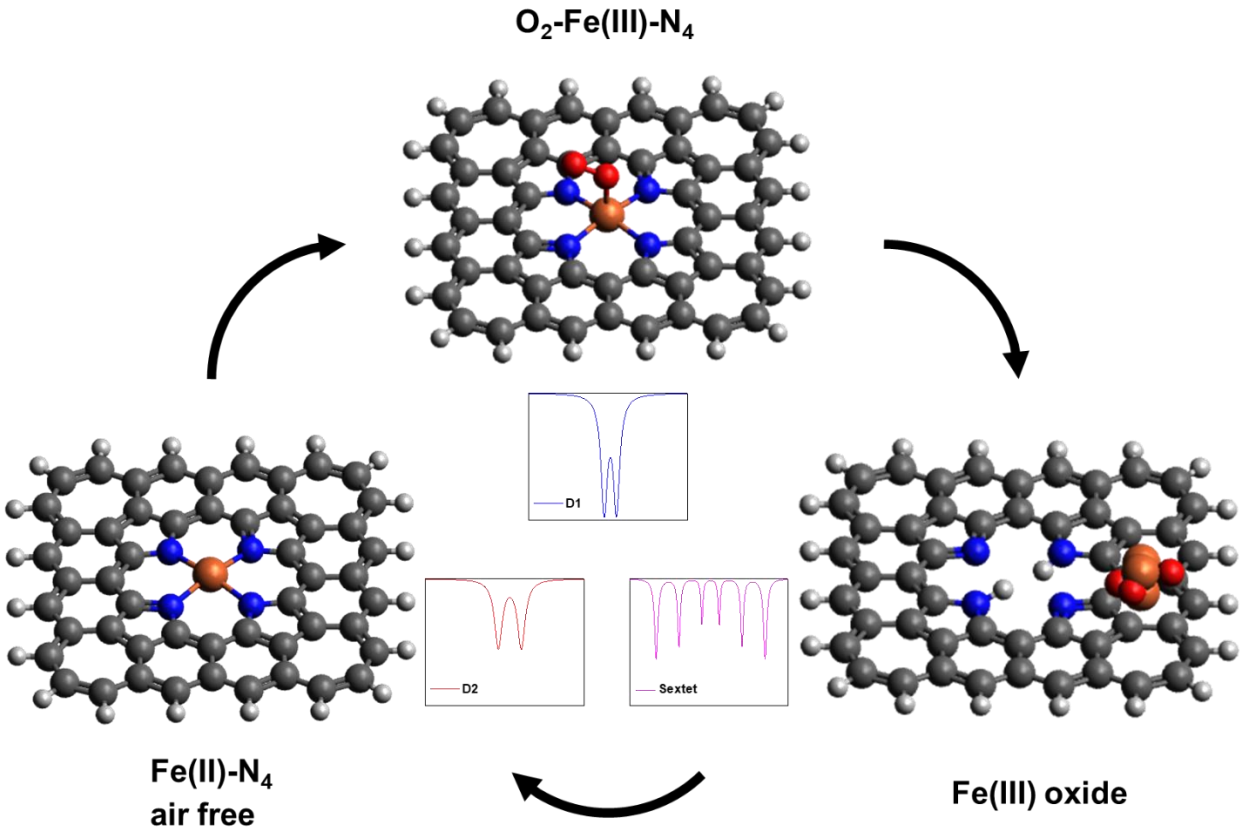

Figure 6. Schematic representation of the proposed shelf-life cycle. Tetrapyrrolic air-free Fe(II)-N_4 sites (D2 in Mössbauer spectroscopy) are oxidized to O_2 coordinating Fe(III)-N_4 sites upon air exposure (D1 in Mössbauer spectroscopy). Over time, O_2-Fe(III)-N_4 sites decompose to Fe(III) oxide (Sextet in Mössbauer spectroscopy) due to contact to air and moisture. Fe(III) oxide can finally be converted back into Fe-N_4 sites following a thermal recovery step.

Table 1. Fitting parameters of the different components obtained from the Mössbauer measurements of NDC-Fe-HT-X at 4.2 K; isomer shift (IS, mm s^{-1}) with respect to α-iron at 4.2 K, quadrupole splitting (QS, mm s^{-1}), magnetic hyperfine field (H, Tesla) and percentage of the spectral area (%).

Sample	D1 (IS; QS; %)	D2 (IS; QS; %)	Sextet (IS; H; %)	Sextet (IS; H; %)
NDC-Fe-HT-0	0.27; 1.54; 58	0.63; 2.89; 42	-	-
NDC-Fe-HT-2	0.25; 1.24; 73	0.60; 2.90; 27	-	-
NDC-Fe-HT-9	0.24; 1.13; 74	0.58; 2.91; 26	-	-
NDC-Fe-HT-30	0.24; 1.13; 66	0.58; 2.91; 26	0.3; 47.5; 4	0.28; 43.6; 4
NDC-Fe-HT-125	0.24; 1.13; 47	0.58; 2.91; 25	0.22; 47.4;14	0.25; 40.8; 14
NDC-Fe-HT-320	0.24; 1.13; 52	0.58; 2.90; 24	0.22; 47.7; 13	0.20; 42.5; 11
NDC-Fe-HT-320 Reactivated	0.15; 1.16; 69	1.12; 2.66; 15	0.13; 49.8; 16	

Table 2. Structural values obtained from N_2-sorption porosimetry measurements for NDC-Fe-HT. For the surface area (SA), both the value obtained by applying the Brunauer–Emmett–Teller theory (SA_{BET}) and the one from quenched solid density functional theory calculation with slyt and cylindrical pores (SA_{QSDFT}) are reported. For the pore volume (PV), both the value from QSDFT (PV_{QSDFT}) and the one measured at $P/P_0 \approx 0.99$ (TPV) are reported. Micro indicates pores ≤ 2 nm and meso pores between 2 nm and 33 nm (upper value of the employed model).

Sample	SA_{BET} (m^2/g)	TPV (cc/g)	SA_{QSDFT} (m^2/g)			PV_{QSDFT} (cc/g)		
			micro	meso	total	micro	meso	total
NDC-Fe-HT-2	1247	1.90	954	368	1322	0.331	1.037	1.368
NDC-Fe-HT-320	922	0.89	716	251	967	0.250	0.479	0.729

Experimental Section

Preparation of Zn-N-C, Fe_2O_3@Fe-N-C and NDC-Fe-HT-X

The samples were prepared similarly to what previously reported.[7] In a typical synthesis, 0.7 g of 1,2-dicyanobenzene were mixed with 7 g of LiCl/$ZnCl_2$ mixture (60 mol% LiCl) in a Ar-filled glovebox. The resulting powder was heated with a heating rate of 10 K/min to 800 °C in a tube furnace with a constant Ar flow and let at this temperature for 1 h. The obtain material was ground, washed with 0.1 M HCl for several hours and dried (Zn-N-C). Zn-N-C was degassed at 250 °C under vacuum, transferred inside an Ar-filled glovebox and mixed with a eutectic mixture of LiCl/$FeCl_3$ in a Schlenk tube. The closed tube was heated up to 170 °C for 5 hours in order to melt the salt mixture and exchange Zn with Fe. Afterwards, the sample was let to cool down to room temperature and washed with deionized water to remove the salt mixture. Finally, it was washed with 0.1 M HCl for several hours and dried (Fe_2O_3@Fe-N-C). NDC-Fe-HT-0 (air free state) was prepared from Fe_2O_3@Fe-N-C after further washing it with 1 M HCl at 80 °C. The dried sample was placed in an alumina crucible and pushed inside a tube furnace pre-heated at 1000 °C under Ar atmosphere. After 10 minutes the furnace was turned off and opened to quickly cool down the sample to room temperature. The sample was then transferred as quick as possible to an Ar-filled glovebox. NDC-Fe-HT-X were obtained after exposing NDC-Fe-HT-0 to air for X days.

Characterizations

Mössbauer measurements were performed at T = 4.2 K on a transmission spectrometer using a sinusoidal velocity waveform with both the source of ^{57}Co in rhodium and the absorber in the liquid He bath of a cryostat. In order to refer the measured isomer shifts to α-Fe at ambient temperature, 0.245 mm s^{-1} was added to the measured values. The spectra were fitted with Lorentzian lines grouped into electric quadrupole doublets and sextets arising from magnetic hyperfine splitting.

N_2-sorption measurements were carried out on a Quantachrome Autosorb iQ2. Prior to the measurements, the samples were outgassed at 250 °C under vacuum overnight. Brunauer–Emmett–Teller (BET) theory was employed to determine the specific surface area using the Micropore BET Assistant supplied by the instrument software. Pore size distributions were calculated with the quenched-solid density functional theory (QSDFT) method (slit/cylindrical pores, adsorption branch).

TGA-MS was performed on a Mettler Toledo TGA/DSC 1 instrument connected to a Pfeiffer Vacuum Thermostar mass spectrometer in Ar atmosphere. The employed heating rate was 10 K/min. Two isothermal steps (150 °C and 250 °C for 20 and 45 minutes, respectively) were performed in order to ensure the complete outgas of the samples.

Electrochemical measurements

Electrochemical measurements were performed in a three-electrode glass cell using 0.1 M $HClO_4$ as electrolyte, an Au wire as counter electrode and a freshly calibrated RHE as reference electrode. Catalyst inks were prepared by dispersing 5 mg of catalyst in 840 µL of N,N-dimethylformamide and 50 µL of 5 wt% Nafion suspension, followed by sonication. To obtained a catalyst loading of 290 µg/cm^2, 10 µL of ink was drop-cast onto a well-polished glassy carbon electrode and dried. An Autolab PGSTAT302N (Metrohm) potentiostat was employed for the measurements. The solution resistance was determined by electrochemical impedance spectroscopy. The ORR curves were

corrected for capacitive currents by subtracting the curves recorded in Ar-saturated electrolyte from the curves recorded in O_2-saturated electrolyte.

3.3.2 On the stability of an atomically dispersed Fe-N-C ORR catalyst: an in-situ XAS study in a PEMFC

This section presents the article "On the stability of an atomically dispersed Fe-N-C ORR catalyst: an in-situ XAS study in a PEMFC" which will be submitted to a peer-reviewed journal in the near future.

Fe-N-C materials are considered the best alternative to replace expensive Pt catalysts for the ORR at the cathode side of PEMFC but they still lack the required stability.[60-63] The most active Fe-N-Cs reported to date are made via the transmetalation of Zn-N_4 sites in ZIF-based Zn-N-C material into Fe-N_4 sites.[55-56] For this reason, the investigation of the degradation mechanisms of Zn imprinted Fe-N-Cs is of particular interest. The possible degradation mechanisms have been presented in section 1.3. So far, there is no clear evidence on the potential dependency of one specific degradation mechanism.

In this work, we employ in-situ XAS measurements to investigated the stability of a home-made Fe-N-Cs electrocatalyst obtained via Zn active-site imprinting method under realistic PEMFC conditions, i.e. the electrochemical stability of the material upon operation. The catalyst is synthetized at the gram scale forming the active site directly onto a Ketjenblack®-type carbon, further proving the versatility of the active-site imprinting method employing Zn as imprinting metal.

Potential cycling in either inert or reactive (i.e., O_2) gas is a very common technique employed to assess the stability of various electrocatalysts. In the case of Fe-N-C, the Fe sites electrochemically active will undergo a redox transition and switch between 3^+ and 2^+ depending on the potential window employed. In order to disentangle different degradation pathways and to correlate them with the oxidation state of the Fe, we performed two different protocols specifically designed to tackle the stability of both states independently, namely voltage hold at high and low cell potential (0.8 V and 0.4 V, respectively) and two different mechanisms are identified depending on the oxidation state of the Fe.

Author contributions

D.M. synthesized and characterized the catalyst. D.M., Y.-S.L. and A.M.D. performed the in-situ XAS PEMFC measurements with the help of O.P., who also provided the

XANES calculations. D.M. treated the XAS data. Y.-S.L. treated the PEMFC data. F.E.W. performed and analyzed the Mössbauer spectroscopy measurements. O.P., M.P., T.-P.F. and H.G. contributed on the interpretation of the data. D.M. and Y.-S.L. wrote the manuscript. All authors discussed the results.

On the stability of an atomically dispersed Fe-N-C ORR catalyst: an *in-situ* XAS study in a PEMFC

Davide Menga[= 1], Yan-Sheng Li[= 1], Ana Marija Damjanovic[1], Olivier Proux[2], Frederich E. Wagner[3], Hubert A. Gasteiger[1], Michele Piana[1], Tim-Patrick Fellinger[4]

1) Chair of Technical Electrochemistry, Department of Chemistry and Catalysis Research Center, Technische Universität München (TUM), 85748 Garching, Germany; 2) Observatoire des Sciences de l'Univers de Grenoble (OSUG) UMS 832 CNRS, Univ. Grenoble Alpes, F-38041 Grenoble, France; 3) Department of Physics, Technische Universität München (TUM), 85748 Garching, Germany; 4) Bundesanstalt für Materialforschung und -prüfung (BAM), 12203 Berlin, Germany

[=] these authors contributed equally to the manuscript

Abstract

The stability of Fe-N-C oxygen reduction reaction (ORR) electrocatalysts has been considered as a primary challenge for their application in proton exchange membrane fuel cells (PEMFCs). While several studies have attempted to reveal the possible degradation mechanism of Fe-N-C ORR catalyst, there are still no general conclusions on their stability against different operational voltage in real PEMFC testing. In this work, we employ *in-situ* X-ray absorption spectroscopy (XAS) to monitor the active-site degradation of an atomically dispersed Fe-N-C ORR catalyst under a H_2/O_2-operating PEMFC at 80 °C. For this, a stability test based on constant voltage was carried out at two cell voltages, namely 0.4 and 0.8 V. Despite the ORR activity of the Fe-N-C catalyst decreased significantly and was almost identical at the end of test for the two voltages employed, the analysis of the XAS spectra suggested that two different degradation mechanisms occur, i.e., attack from reactive oxygen species (ROS) at 0.4 V and Fe demetalation at 0.8 V.

Introduction

Proton exchange membrane fuel cells (PEMFCs) represent a central technology in order to produce clean energy and reduce CO_2 emissions.[1] The key component of a PEMFC is the membrane electrode assembly (MEA), which consists of a cathode and an anode electrode divided by the PEM. In the cathode electrode, a high loading of precious metal catalyst (such as Pt) is generally required in order to catalyse the sluggish kinetics of the oxygen reduction reaction (ORR).

According to the cost analysis of PEMFC systems for lightweight duty vehicles (LDVs), the major cost of a fuel cell stack is largely contributed from the platinum-group-metals (PGM) catalyst, especially when further increasing the manufacture volume of stacks.[2] Consequently, in order to reduce the cost of PEMFC systems, finding an alternative ORR catalyst to reduce/replace PGM loadings has become one of the major research interests. In the family of PGM-free ORR catalyst, transition metal- and nitrogen- co-doped carbon materials (M-N-C, M = Fe, Co, Mn) are undoubtedly the most promising candidates. In particular, many years of research effort led Fe-N-C catalysts to achieve beginning-of-life (BoL) activity comparable to that of Pt in PEMFC testing.[3-5]

Despite their promising performance at BoL in PEMFC testing, Fe-N-C ORR catalysts suffer from poor stability during operation.[6] For example, a typical PEMFC using Pt/C ORR catalyst can be operated at least ~5000 hours with reasonable end-of-life (EoT) performance.[7] However, this would be extremly challenging for most PEMFC based on PGM-free ORR catalysts. Their fuel cell performance drops significantly in the initial few hours and the majority of the activity is lost after ~100 hours operation.[8, 9] Studies have attributed the poor stability of Fe-N-C ORR catalysts in PEMFC to four possible degradation mechanisms. These are (i) demetalation,[10, 11] (ii) carbon oxidation (chemical and/or electrochemical),[12, 13] (iii) micropore flooding[14] and (iv) N-protonation followed by anion adsorption.[15] Out of these four, the first two are generally believed to be more probable, according to several theoretical and experimental findings. Regarding micropore flooding and N-protonation, contradictory results have been reported, therefore no consensus has been achieved for these two mechanisms.[16]

The demetalation of Fe from the active-site centre has been widely reported in the literature[10-12, 17] and different intermediates have been proposed to play a key role in the demetalation mechanism.[17, 18] This process suggests that the atomic Fe in the active-site centre loses the coordination with nitrogen and carbon, resulting in loss of ORR activity. Many groups proposed that after demetalation the Fe cations will contaminate the perfluorinated acid (PFSA)

ionomer and/or possibly precipitate as iron oxide depending on the specific conditions according to the Pourbaix diagram (i.e., concentration of Fe cations, pH, and the potential during the operation).[4, 19] On the other hand, carbon oxidation is believed to reduce the specific activity of the Fe-N_4 sites by introducing oxygen functionalities on the carbon surface that change the electron density around the Fe active centre.[13] Other studies also suggested that a strong oxidation may lead to the demetalation of the Fe due to the destruction of the carbon support itself.[12, 20, 21] This oxidation can be either electrochemical (i.e., when the cathode potential is higher than ~ 1.3 V)[12] or chemical (i.e., triggered by H_2O_2 and/or radicals attack).[13] The latter one is mainly attributed to the poor selectivity of Fe-N-C catalysts toward the ORR (i.e., 2 e^- reduction and/or 2+2 e^- mechanism instead of direct 4 e^- pathway), which leads to a Fenton-like reaction with further production of the highly reactive and detrimental radical species.[22] While the above studies attempted to investigate the structural change of the catalyst, there is no clear evidence on the potential dependency of one specific degradation mechanism.

The general understanding on structure-performance relations of Fe-N-C catalysts has been pushed forward by spectroscopic techniques able to identify the active-site environment at the atomic level. Mössbauer spectroscopy, for example, has proven fundamental in the development of Fe-N-C catalysts due to its ability to discern different Fe phases as well as different Fe coordination. [19, 23, 24] On the other hand, the low amount of Fe present (usually < 3 wt.%) makes the data acquisition especially long. For this reason, X-ray absorption spectroscopy (XAS) is also considered as a useful technique allowing to probe the low amount of Fe in the catalyst with reasonable time and providing a high sensitivity for data acquisition. Therefore, XAS is often used together with *in-situ* or *operando* electrochemical measurement of Fe-N-C catalysts.[25-27] Nevertheless, Mössbauer spectroscopy and XAS are bulk techniques which probes all the Fe phases in the system, therefore a Fe-N-C catalyst that is free from side phases is desirable in order to obtain meaningful data on the change of the Fe active sites. One major challenge in order to understand the degradation mechanism of Fe-N-C ORR catalysts is to have a material containing exclusively well-defined atomically dispersed Fe-N_4 active

sites. Typically, it is difficult to prepare a Fe-N-C catalysts that are free from any Fe-based side phases and with a high density of catalytic sites. Lately, new synthetic approaches have proven to be able to synthetized only the desired active site free from side phases, pushing the understanding of these materials forward. [3, 4, 28-30]

In this study, we investigated the potential dependency on the degradation of an atomic dispersed Fe-N-C ORR catalyst in the operating PEMFC (in a 5 cm^2 active area with differential flow operation). For this, we first synthetized a novel Fe-N-C catalyst employing an active-site imprinting method based on Zn^{2+} ions followed by low- and high-temperature Zn-to-Fe transmetalation. This method has proven to yield catalysts with well-defined tetrapyrrolic active sites and free from side-phases.[29, 31] *In-situ* X-ray absorption spectroscopy is employed to monitor the degradation of the aforementioned catalyst in an O_2-fed cathode of a PEMFC at 80 °C. Potential cycling in either inert or reactive (i.e., O_2) gas is a very common technique employed to assess the stability of various electrocatalysts. In the case of Fe-N-C, the Fe sites electrochemically active will undergo a redox transition and switch between 3^+ and 2^+ depending on the potential window employed. Moreover, it has been shown that the gas employed has a major impact on the stability.[32] In order to disentangle different degradation pathways and to correlate them with the oxidation state of the Fe (i.e., 2^+ or 3^+), we performed two different protocols specifically designed to tackle the stability of both states independently, namely voltage hold at high and low cell potential (0.8 V and 0.4 V, respectively) and two different mechanisms are identified depending on the oxidation state of the Fe.

Experimental

Catalyst synthesis. In a typical synthesis, 1 g of Ketjenblack was mixed with 1.3 g of $ZnCl_2$ and 1.3 g of 1-ethyl-3-methylimidazolium dicyanamide (Emim-dca) in an Ar-filled glovebox. The resulting mixture was placed inside an alumina crucible covered with a quartz lid and heated up to 850 °C for 1 h in a tube furnace under a constant Ar flow of 2 L min^{-1} and with a heating rate of 2.5 °C min^{-1}. After letting the sample naturally cool down to room temperature, it was ground and washed with 0.1 M HCl for several hours. The sample was then filtered and washed with deionized water until neutral pH was reached and dried at 80 °C overnight. The material was subsequentially degassed at 250 °C under vacuum in a Büchi oven and mixed with a $FeCl_3$/LiCl eutectic mixture inside and Ar-filled flask in order to perform the low temperature Zn-to-Fe ion exchange.[29] After stirring the sample at 170 °C for 5 hours in the molten salt mixture, it was first washed with deionized water to remove the salt and stirred in 0.1 M HCl for several hours. The powder obtained after further water washing and drying was placed again in an alumina crucible and pushed inside a tube furnace pre-heated at 800 °C under Ar atmosphere (flash pyrolysis). After 20 minutes the furnace was turned off and opened to achieve a quick cool down of the sample.

N_2-sorption porosymetry. Measurements were performed on a Quantachrome Autosorb iQ2 after outgassing the samples at 250 °C under vacuum overnight prior to the measurements. Brunauer–Emmett–Teller (BET) theory was employed to determine the specific surface area using the Micropore BET Assistant supplied by Quantachrome ASiQwin software.

Mössbauer spectroscopy. Mössbauer measurements at T = 4.2 K were performed on a standard transmission spectrometer using a sinusoidal velocity waveform with both the source of ^{57}Co in rhodium and the absorber in the liquid He bath of a cryostat. In order to refer the measured isomer shifts to α-Fe at ambient temperature, 0.245 mm s^{-1} was added to the measured values.

Rotating ring disk electrode measurements (RRDE). Catalyst inks were prepared by dispersing 5 mg of catalyst in 0.84 mL of Q-POD water, 1.68 mL of isopropanol and 50 µL of 5 wt.%

Nafion suspension, followed by sonication. To obtained a catalyst loading of 0.1 mg cm^{-2}, 10 μL of ink was drop-cast onto a well-polished glassy carbon electrode and dried under an infrared heater for 60 min. The obtained electrodes were measured in a three-electrode glass cell using 0.1 M $HClO_4$ as electrolyte, Au wire as the counter electrode and a freshly calibrated RHE as the reference electrode. The solution resistance was determined by electrochemical impedance spectroscopy. The ORR curves were corrected for capacitive contribution by subtracting from the curves recorded in O_2-saturated electrolyte the ones recorded in Ar-saturated electrolyte. H_2O_2 production was quantified with RRDE technique where the platinum ring was held at 1.2 V_{RHE}, while the potential of the disk was swept between 1.0–0.1 V_{RHE}. The collection efficiency of the ring (N) was taken to be −0.255 and the percentage of H_2O_2 was calculated using equation 1.

$$H_2O_2\% = \frac{2\ {i_R}/{N}}{i_D + {i_R}/{N}} \qquad (1)$$

Where i_R and i_D represent the current measured at the ring and at the disc, respectively.

Membrane electrode assembly (MEA) preparation and single-cell PEMFC assembly. The PGM-free cathode catalyst ink is prepared by suing a plantary mixer. In brief, prior to the PGM-free catalyst ink preparation, the PGM-free catalyst powder is dry ball mill at 200 rpm for 90 minutes. The PGM-free cathode catalyst ink is then prepared by mixing ball-milled powder, ionomer (700 EW, Asahi Kasel, Japan), solvent mixture of 1-PA/H_2O (27 wt% of H_2O), and ZrO_2 beads of 10 mm diameter in planertary mixer at 500 rpm for 10 min. The catalyst ink has a carbon content 0.065 g/ml_{ink} and the ionomer to carbon ratio (I/C) in the ink is 0.5/1. The catalyst ink is then coated on PTFE substrate (50 μm) using 500 μm wet-film thickness, and is dried under ambient condition. The anode electrode is prepared using the method reported in reference x, using a Pt/C catalyst (19.6 wt% Pt on Vulcan carbon support, Tanaka, Japan). The ink is prepared by using same ionomer (I/C = 0.65) with 1-PA/H_2O mixture (10 wt% of H_2O content). The MEA (with active area 5 cm^2) is then prepared by the method of catalyst coated membrane (CCM), using a decal transfer method. In brief, the hot-

press procedure is applied to sandwich between membrane (Nafion 212, Fuel Cell Store, Japan), anode and cathode decals at 130 and 4 KN for 10 minutes. The PTFE substrates are subsequently peeled off from anode and cathode decals, yielding the final CCMs.

The 5 cm^2 single-cell PEMFC tested in beamline were performed by using an in-house designed graphite flow field and modified fuel cell hardware, which was previously used in reference [33]. The fuel cell hardware (Fuel Cell Technology, INC, USA) is modified with an X-ray window machined in conical shape with lowest part inside the middle of hardware (1.5 x 2 mm^2, see Figure 1a). The flow field is designed in a single channels and single serpentine (0.5/0.5 mm land/channel widths; manufactured by Poco Graphite, USA) with a rectangular x-ray window in the center that is only 0.5 mm thin of graphite material to allow the x-ray go thorough in the meantime to prevent any gas permeation. The gas diffusion lays (GDLs) are using Freudenberg H14C10 with a quasi-compression strain of 13 $\pm$ 1% of thickness reduction during the cell assembly. This GDL compression is controlled by adjusting the thickness of PTFE-coated glassfiber subgasket and by assembling at a torque 12 Nm, detail see Simon et al.

PEMFC measurements. The configuration of fuel cell testing with *in-situ* XAS spectra measurements is shown in Figure 1c. The gas flow, cell temperature, gas humidification and pressure parameters were controlled by a customized portable fuel cell test system (Fuel Cell Technologies, Inc., see right hand side of Figure 1c). All electrochemical measurements were performed with a VSP-300 multi-channel potentiostat equipped with a 20 A booster board (Biologic SAS, see left hand side of Figure 1c).

The sequence of stability testing, diagnostic and XAS spectra is refer to the explanation in Figure 3. Here we describe the detail of fuel cell testing condition and method. Prior to any fuel cell testing, the cell is warm up under a H_2/N_2 configuration at 90% relative humidity (RH) and 80℃ (anode and cathode flow are 400 nccm) for 15 minutes. The stability is conducted under a H_2/O_2 configuration at 90% RH, 80℃, and 150 $kPa_{abs,inlet}$ (anode and cathode flow are 400 nccm). The cell

potential is then controlled at either 0.4 V or 0.8 V. The linear scan voltammatric is recorded at a scan rate of 2 mV s^{-1} from OCV to 0.4 V. The high frequency resistance (HFR) is subsequently recorded at 0.6 V (in H_2/O_2 configuration) using electrochemical impedance spectroscopy (EIS) acquired from 200K to 1 HZ with 10 mV perturbation. The HFR is then determined at the x-axis = 0 (real part) from Nyquist plot. The Cyclic voltammetrics (CV) is recorded under a H_2/N_2 configuration at 90% RH, 80℃, and 150 $kPa_{abs,inlet}$ using scan rate 100 mV s^{-1}.

XAS measurements. XAS spectra at Fe K-edge were collected on BM30 beamline at the European Synchrotron Radiation Facility (Grenoble, France). Beamline description can be found in [33], in which the same operando cell was used. Beam size was measured around 210µm X 100µm (Full Width Half Maximum values). *In situ* spectra were recorded in fluorescence mode with a 45-degree angle between sample surface and beam (see Figure 1d). The beam damage was minimized by moving between four different spots while collecting consecutive spectra. Moreover, the possibility of MEA failure due to beam damage was tested collecting consecutive spectra on the same spot for 2 hours. No membrane collapse was detected electrochemically and no spectroscopic change was visible during this time. Analysis was focused on the X-ray Absorption Near Edge Structure (XANES), the edge region, sensitive both to the valence/oxidation state and to the site geometry (nature and number of the neighbors, distance, etc.) of the probed element.

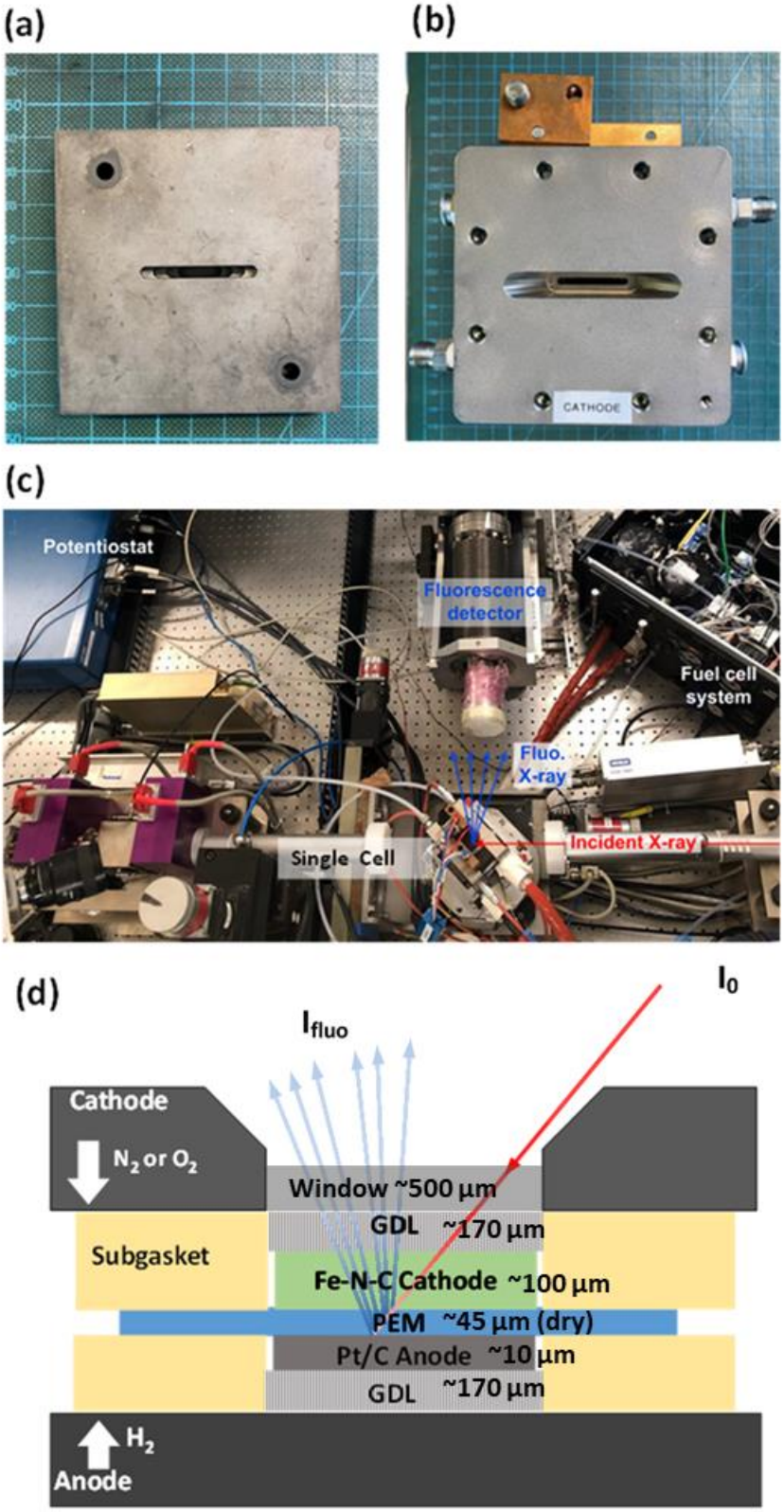

Figure 1. Photo of the flow field (a) and cell hardware (b) employed for the PEMFC testing showing the window for XAS measurements. (c) Top view of the experimental setup employed at the BM30 beamline at the European Synchrotron Radiation Facility. (d) Schematic representation of the PEMFC cell setup indicating the components and their respective thickness.

Results

Catalyst synthesis and characterization

The catalyst presented in this study was synthetized employing the active-site imprinting method.[28, 29, 31] Ketjen black E-type (KB) was used as conductive carbon support, 1-Ethyl-3-methylimidazolium dicyanamide (emim-dca) was employed as C and N source and $ZnCl_2$ as Zn source in order to build Zn-N_4 sites. The best performing catalyst was obtained with a KB:emim-dca:$ZnCl_2$ ratio of 1:1.3:1.3 in mass and with a synthetic temperature of 850 °C. After thoroughly mixing the precursors in an Ar-filled glovebox, the mixture was placed in an alumina crucible and pyrolized for one hour in a tube furnace under Ar flow. The obtained Zn-N-C material was stirred in 0.1 M HCl to dissolve the $ZnCl_2$ eventually still present. After filtering and washing with water until neutral pH was reached, the material was first dried at 80 °C overnight and then degassed under vacuum at 250 °C in a Büchi oven. As previously reported, Zn is able to coordinate N atoms to form Zn-N_4 sites, which can undergo a low- and high-temperature ion exchange reaction with Fe to form Fe-N4 sites.[29] In the same way, the Zn-N-C was first stirred in a $FeCl_3$/LiCl eutectic mixture at 170 °C and, after acidic work-up, subjected to a second heat treatment in Ar atmosphere at 800 °C. The final catalyst was obtained and used without further treatments.

The surface area and porosity of the catalyst was evaluated with N_2-sorption porosimetry. The catalyst has a surface area of 446 m^2/g and presents a typical type-I isotherm, indication of its micropore structure, with a high gas uptake at high relative pressure, indicating the interstitial porosity between the catalyst particles (Figure S1).

Before MEA preparation and *in-situ* XAS characterization, the catalyst powder was subjected to Mössbauer spectroscopy measurements at 4.2 K. The spectrum (Figure S2) consists of two quadrupole doublets, namely D1 and D2, assigned to atomically dispersed Fe-N_4 sites, and a sextet component (~ 10 %) attributed to nanoscopic oxidic Fe(III). Due to the low relative area of the sextet component, the oxidic clusters are neglected for clarity. Moreover, as shown in the corresponding

session, this small amount does not have an impact on the XAS data, therefore only atomically dispersed Fe-N_4 sites are considered. Based on literature reports and previous work,[19, 29, 34] D1 is assigned to a Fe(III)-N_4 site with an axial oxy ligand, while D2 is assigned to the square-planar Fe(II)-N_4 moiety without oxy ligand. In addition, D1 is assigned to the site which is more active but less stable whereas D2 is attributed to the site which is more stable but less active.[19]

Development of Stability Testing in single-cell PEMFC

In general, it is common to conduct a diagnostic polarization curve or linear scan voltammetry (LSV) in between aging procedures for a given PEMFC testing, which allows to track the ORR activity change of the catalyst over the course of the degradation. Nevertheless, Fe-N-C ORR catalysts typically exhibit extremely poor stability and are prone to degradation during fuel-cell operations. Thus, prior to the investigation of the potential-dependent stability and degradation of the catalyst, we first evaluated the catalyst stability upon the diagnostic of ORR activity by measuring consecutive LSVs.

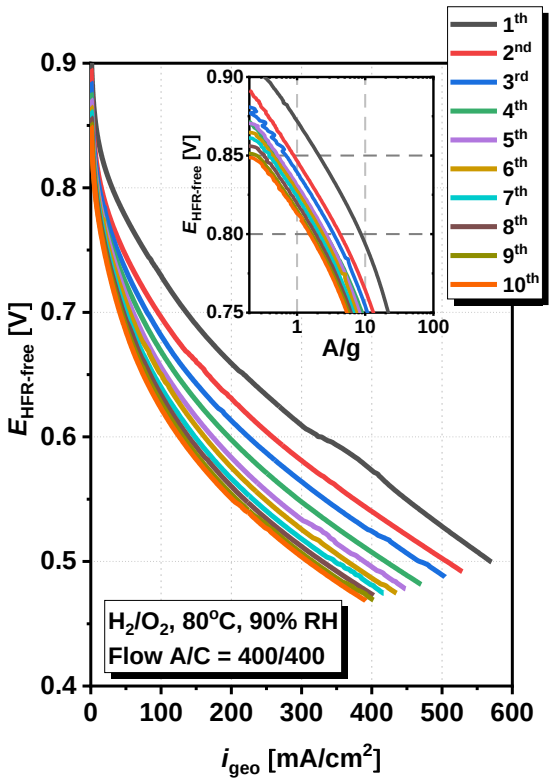

Figure 2. Ten consecutive LSVs measured in H_2/O_2 configuration using the portable Fuel Cell Technologies test station for operando measurements. Catalyst loading on the cathode is ≈ 3.5 mg_{cat}/cm^2_{MEA}.

Figure 2 shows the result of measuring 10 consecutive LSVs from OCV to 0.4 V cell potential in H_2/O_2 configuration at a slow scan rate of 2 mV s^{-1}. The cell voltages in Figure 2 are corrected by HFRs ($E_{\mathrm{HFR-free}}$) determined at 0.6 V cell voltage in O_2-feed cathode right after each LSV (method see Experimental). From the results, it is clear that the H_2/O_2 performances of the MEA drops significantly when recording LSVs. The current density at $E_{\mathrm{HFR-free}}$ = 0.6 V decreases ~ 60% after 10 consecutive LSVs, i.e., from ~340 mA cm^{-2} at BoT (in black) to ~130 mA cm^{-2} for the 10th LSV (in orange). To further obtain the kinetic information of the catalyst for each LSV, the inset in Figure 2 shows the Tafel representations obtained by using the current densities normalized by the catalyst loading (≈3.5 mg cm^{-2}). The initial ORR mass activity determined at $E_{\mathrm{HFR-free}}$ = 0.8 V is ~ 10 A g^{-1}, whereas that of the 2nd LSV is 5 A g^{-1}, corresponding to a ≈ 50% loss. It should be noted that the time scale of performing a LSV is indeed very short, only ~5 min per LSV, however, a significant ORR activity loss was observed.

Similar experiments were conducted by Osmiri *et al*. and Chenitz *et al.* where the authors observed negligible performance losses when measuring polarization curves in H_2/Air.[9, 10] Comparing with their results, the catalyst tested here is less stable against diagnostic of LSV. This can be attributed to the intrinsically poor stability of the catalyst or the impact of O_2 partial pressure on the catalyst degradation. For the latter one, it has been shown that the O_2 partial pressure (i.e., concentration of O_2) impacts the degradations of Fe-N-C ORR catalysts.[9] Additionally, in the case of LSV or polarization curve, the potential sweep could possible accelerate the degradation of the catalyst. Despite the actual reason for the poor stability of the catalyst investigated is not clear, the result shown here highlights the difficulty of conducting a diagnostic to determine the ORR activity prior or in between the stability test.

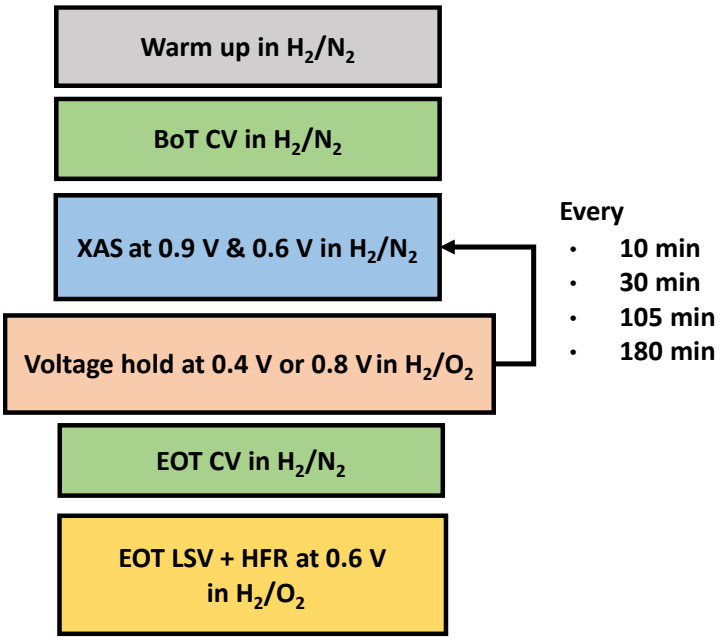

Figure 3. Schematic representation of the protocol employed for testing the stability of the catalyst and record the XAS data.

According to the testing result shown in Figure 2, to avoid any degradation due to the diagnostic of LSV in H_2/O_2, we particularly conducted a protocol that only measures the LSV (in H_2/O_2 configuration) at the EoT as shown in Figure 3. In brief, the stability tests were performed by using a potential controlled method at a high (E_{cell} = 0.8 V_{RHE}) and low (E_{cell} = 0.4 V_{RHE}) cell potential in O_2-feed cathode for a total of 3 hours testing time. For simplicity, we labelled those stability testing protocol as 0.8 V hold and 0.4 V hold, respectively. In order to track the evolution of the Fe structure of the tested catalyst, the XAS spectra were recorded under N_2-feed cathode after every 10, 30, 105, and 180 minutes of the O_2-feed cathode stability tests. At the EoT, a LSV is then recorded to obtain the ORR kinetics of the catalyst. Detail methods are described in the experimental part. It has to be noted that the catalyst activity was also tested by measuring a LSV after 20 consecutive XAS spectra for a total time of ~ 8.5 hours (data not shown) and the results indicated that the ORR activity is not affected by recording the XAS spectra in N_2-feed cathode.

Potential-dependent Stability in PEMFC

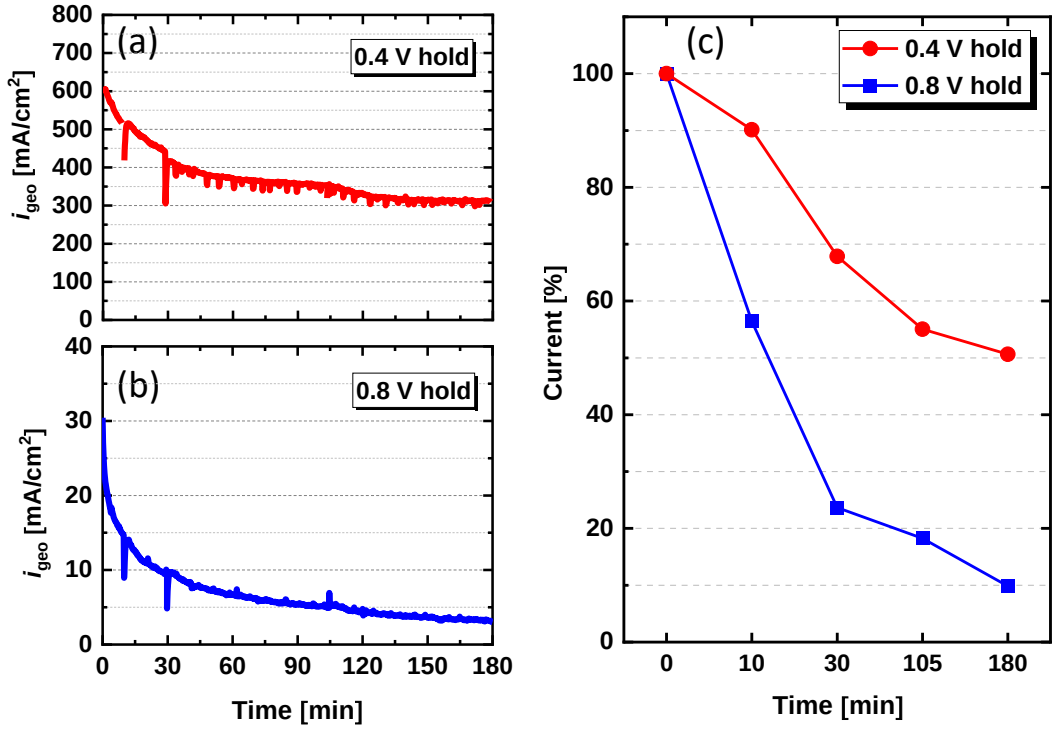

Figure 4. Current profile in H_2/O_2 configuration of the 0.4 V hold (a) and 0.8 V hold (b). (c) Current profile percentage normalized to their respective initial value**.**

Figures 4a and 4b show the current density profile within 3 hours of the employed 0.8 V hold and 0.4 V hold, respectively. Note that the data were collected together with the XAS spectra shown later. From those two current profiles, both cases show a similar behavior. Specifically, a fast current loss is observed in the initial 30 minutes, and a much slower one occurs afterwards. To further compare the current loss of the two testing protocols, the current densities at a given time were normalized to the initial current density (i.e., at t = 0) and the results are plotted in Figure 4c. The normalized current density profiles indicate that a much stronger loss occurs when holding the potential at 0.8 V (blue curve) compared to 0.4 V (red curve). In the first 30 minutes, ~ 80 % of the current is lost for the 0.8 V hold, but only a 30 % loss is observed for the 0.4 V hold. After 3 hours (EoT), the majority of the current is lost for the 0.8 V hold, whereas 50 % of the current still remains for the 0.4 V hold.

Compared to the literature, our results show a similar trend. In fact, Chenitz *et al*. reported an initial fast decay of the current profiles followed by a slow decay when holding various cell potentials in single-cell experiment.[10] Similar observations were also reported by Zhang *et al.*, using a constant cell potential of 0.6 V in both H_2/Air and H_2/O_2 configurations.[35] Both publications attributed the current decay profile to the demetalation of Fe from the active site. This conclusion is based on numerical fitting of the resulting current decay profile. Nevertheless, recently Yin *et al.* argued that it is not desired to use the current profile obtained from non-kinetic region (i.e., lower cell voltage, < 0.7 V).[36] According to results from Yin *et al.*, the current profile obtained from holding the cell voltage at 0.84 V fits well when considering a logistic decay of an autocatalytic model, which describes the OH radical attack to the catalyst due to the presence of H_2O_2.[37]

To further discuss the possible reason for the current loss in our case, we performed a rotating ring disk electrode (RRDE) experiment to quantify the H_2O_2 production (H_2O_2%) of the presented catalyst (Figure S3). The results indicate that our catalyst exhibits a higher H_2O_2 at 0.4 V (~6%), whereas the H_2O_2% at 0.8 V is negligible (close to 0%). Accordingly, the impact of H_2O_2 should be more significant on the catalyst stability when holding the potential at 0.4 V instead of holding it at 0.8 V, despite a much higher current loss for the 0.8 V hold case. Nevertheless, we would like to emphasize the statement from Yin *et al.*, that when holding the cell potential at relatively low potential, the current loss may not represent the kinetic information due to other transport losses dominating in this potential window, i.e., the case of the 0.4 V hold in this study. Consequently, to compare the activity change due to the given stability test, we performed a LSV at the EoT.

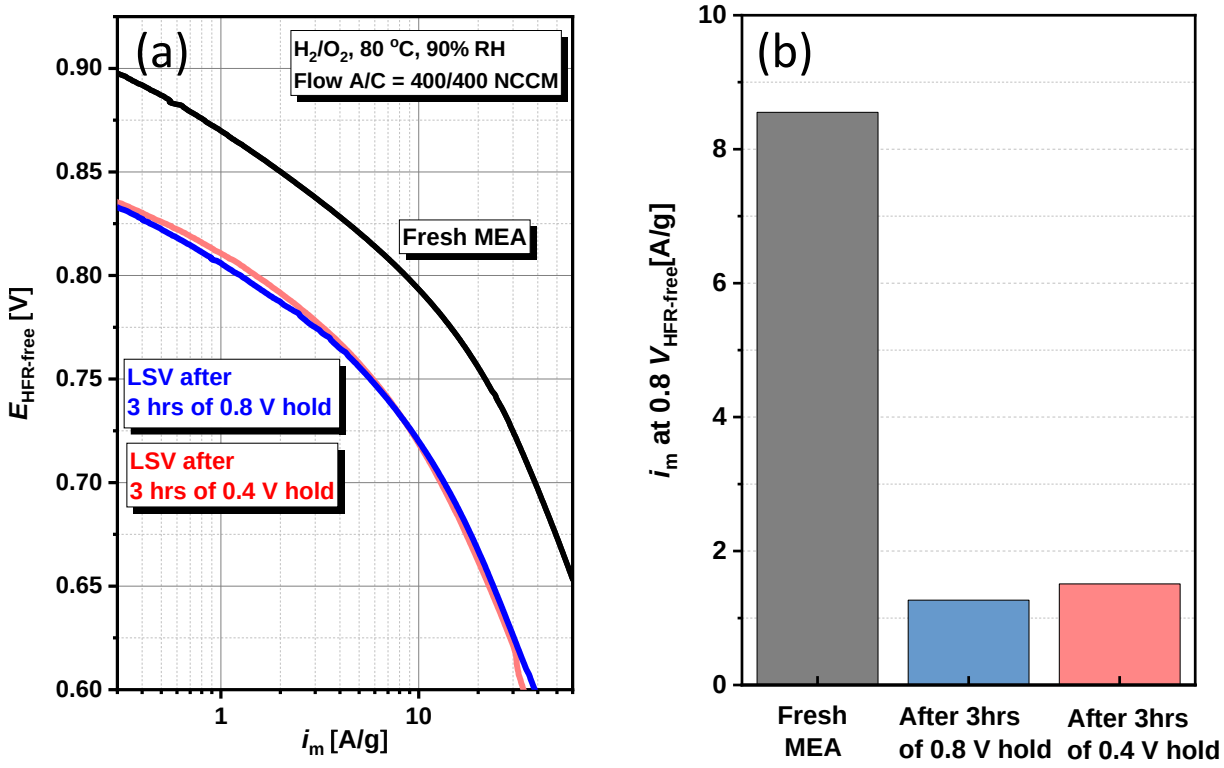

Figure 5. (a) Tafel representation of the mass activity derived from the LSVs measured in H_2/O_2 configuration at BoT (black) and after the 0.8 V hold (blue) and 0.4 V hold (pink). Catalyst loading on the cathode is ≈ 3.5 mg_{cat}/cm^2_{MEA}. (b) Summary of the mass activity at 0.8 $V_{HFR\text{-}free}$.

In order to compare the ORR activity of the catalyst after holding the cell voltage at 0.4 and 0.8 V for 3 hours, the EoT LSVs are measured in H_2/O_2 configuration after each stability testing. As mentioned earlier, the testing protocol applied here does not proceed with any diagnostic of polarization curves or LSVs in between or before the stability test (see Figure 3). Therefore, we consider the LSV at EoT the state of the catalytic activity (i.e., active site density or turn over frequency) that is solely degraded by the constant voltage test (either at 0.4 or 0.8 V).

Figure 5a shows the Tafel representations of the EoT LSV after holding the cell voltage at 0.4 V (in red) and 0.8 V (in blue) for 3 hours. For comparison, a LSV of a fresh MEA measured without any aging is plotted together (in black). The cell voltages in Figure 5a are corrected by HFR and the current is normalized to the respective loading of cathode electrode ≈3.5 mg cm^{-2} for all cases. Surprisingly, the EoT Tafel representations of both cases overlap and show a significant performance

loss compared to the fresh MEA. Additionally, when compared with the Tafel representation of the non-degraded catalyst, we notice that both aged MEAs show a clear voltage drop of ~ 75 mV at the same current. By considering a simple Tafel kinetic, this 75 mV drop indicates an increased ORR overpotential for the aged MEAs.

To further quantify the ORR activity after the stability testing, the mass activity is determined using the current at 0.8 V HFR-free (i_m at 0.8 $V_{\mathrm{HFR-free}}$) from Figure 5a. Those results are summarized in Figure 5b. The determination of i_m should ideally apply a linear regression covering at least a decade of current change. However, as the Tafel representations in Figure 5a exhibit two Tafel slopes, this may lead to a misinterpretation. While it is believed that the second Tafel slope originates from the utilization of Fe-N_4 (fully utilized when in a Fe^{2+} state, i.e., below 0.75 V), one cannot exclude the unassigned voltage losses at high current for typical thick cathode electrodes of PGM-free catalyst (≈100 µm here). In agree with the Tafel representations, it is clear the i_m of both cases are almost identical (see red for 0.4 V and blue for 0.8 V), and degraded ca. 80% compared to that of the fresh MEA (in grey).

Since there is no difference for the EoT i_m regardless of using 0.4 or 0.8 V during the constant-voltage stability test, we further valid those results by conducting a similar testing using a Greenlight custom-made fuel cell test station (result shown in Figure S4). In fact, we obtained the same results from those repetitions showing that i_m at 0.8 $V_{\mathrm{HFR-free}}$ is almost identical for 0.4 V hold and 0.8 V hold. In order to accelerate the degradation during the beamline experiment, the stability tests were performed in 100 % O_2-feed environment. It is therefore possible that most of the catalytic sites (or at least the utilized ones) are degraded at EoT in both cases.

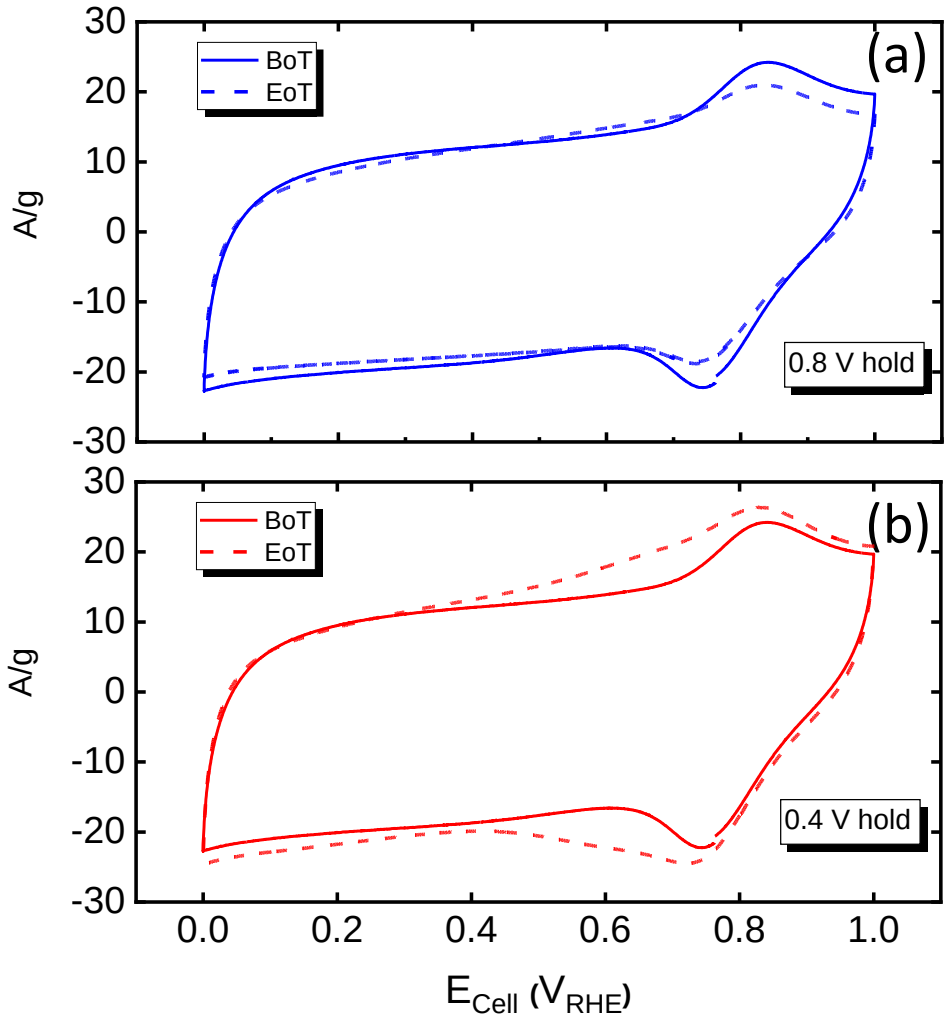

Figure 6. Cyclic voltammetry recorded in H_2/N_2 configuration of the cathode electrode measured at BoT and EoT of the 0.8 (blue) and 0.4 V hold (red).

Cyclic voltammetry (CV) at BoT and EoT− To further provide additional information on the catalyst before/after the stability test, Figure 6a and 6b present the cyclic voltammetry (CVs) recorded in N_2 of the cathode electrode measured at BoT and EoT of the 0.8 and 0.4 V hold, respectively. The y-axis in the CVs represent the mass normalized current (expressed in A g^{-1}, i.e., the current divided by the loading of the cathode electrode, ≈3.5 mg cm^{-2} for all the cases here). For the BoT CVs (see solid line in Figure 6a and 6b), two redox features were observed at ~0.8 and ~0.77 V_{RHE}, typically attributed to the $Fe^{3+/}Fe^{2+}$ redox feature of Fe-N-C catalysts. After the stability testing, there are only minor changes for both cases. For the 0.8 V hold, the $Fe^{3+/}Fe^{2+}$ redox feature slightly decreases, but

we consider this change to be negligible. On the other hand, a more obvious change is observed for the 0.4 V hold where in the EoT CV a broad feature is overlaying the $Fe^{3+/}Fe^{2+}$ redox. Similar observations were reported by Bamhan *et al.* and Osmari *et al.*[8, 9] It is suggested that this increase in capacitance corresponds to the quinone/hydroquinone redox. The presence of these functional groups on the carbon surface is ascribed to the chemical oxidation of the carbon support due to the chemical attack of reactive OH· or other oxy radicals. It is believed that these radicals are produced through a Fenton-like reaction due to the presence of H_2O_2 and Fe in the Fe-N-C cathode electrode. In fact, when considering the H_2O_2% from RRDE experiments (Figure S3), we hypothesize that the major degradation mechanism happening during the 0.4 V hold may be related to the radical attack on the carbon support, since a higher H_2O_2% is found in this potential region. According to Choi et al., these oxygen functional groups near the Fe-N_4 sites weaken the binding energy of oxygen on the active sites, thereby decreasing the ORR activity.[13] However, it is difficult to provide a conclusion based only on minor changes in the CVs. Therefore, the investigation of the degradation mechanism is discussed in detail in the following sections, through the *in-situ* XAS experiments.

In-situ XAS

Before discussing the XAS results, it is paramount to understand the area being probed by the X-rays in terms of penetration depth of the incident beam and attenuation of the fluorescence beam. For PGM-free-based cathodes a high layer thickness is usually obtained due to the higher loadings employed.[38]. For this reason, if only a certain portion of the MEA is probed during the experiments, e.g., only the cathode side or even only a part of it, and this is not taken into account, misleading results might be drawn. This appears especially important in the case of degradation via demetalation, in which case the Fe might leave the cathode side and equilibrate in the entire MEA throughout the ionomer phase.

To understand the area being probed and the corresponding attenuation, the online X-ray attenuation length software provided by the Center for X-ray optics at Lawrence Berkley National Laboratory

was employed.[39] By using the density of the different materials constituting the cell setup and their thickness, a total transmission of 55 % has been calculated at the Fe K-edge (7.112 keV), indicating that the entire MEA is probed, even though the Fe amount is not high enough to allow a proper data evaluation using the transmitted signal. The total transmission at the Fe Kα fluorescence line energy (6.4 keV) has been calculated to ~47%, indicating that the signal measured in fluorescence is also characteristic of the entire MEA probed volume.

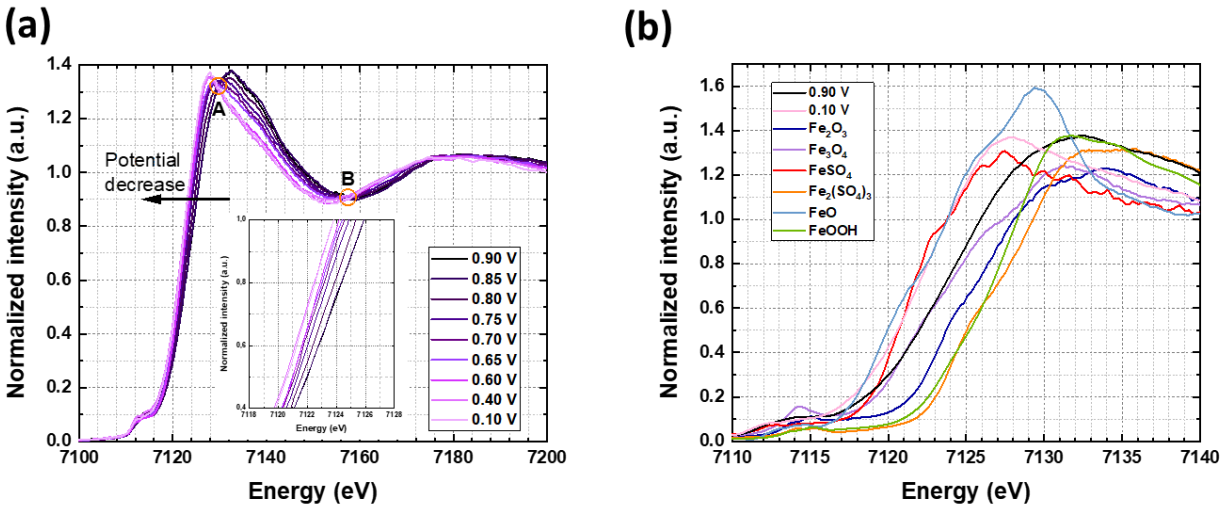

Figure 7. (a) Fe K-edge XANES spectra of the cathode catalyst recorder at different potentials under N_2. The two orange circles A and B represent the two isosbestic points at 7130 eV and 7155 eV, respectively. (b) Fe K-edge XANES spectra of the cathode catalyst recorder under N_2 at 0.90 V (black) and 0.10 V (pink) in comparison with standard compounds.

Figure 7a shows the XANES spectra of the catalyst recorder at different potential under N_2. As reported in previous literature about *in-situ* PEMFC XAS measurements,[25] the edge position shifts to lower energy when the potential is decreased. It is worth noting the two isosbestic points at 7130 eV (A on figure 7a) and 7155 eV (B on figure 7a). These features indicate that only two species contribute to the XANES spectra and that they transform one into the other depending on the potential. Based on the results from Mössbauer spectroscopy and previous literature,[26] these are assigned to the hydroxy-poisoned (OH)-Fe(III)-N_4 site, present at high potential, and the Fe(II)-N_4 site, which is the active site at low potential upon OH desorption. The corresponding XANES

spectrum of the active site has been calculated using the FDMNES software,[40] with a self-consistent calculation of the electronic structure before the final-state calculation performed using the Finite Difference Method with a 5 Å radius for both calculations and applying an energy shift of 7112 eV with respect to the photo-electron energy value (Figure S5a) using the $[(OH)FeN_4]C_{52}H_{20}$ cluster displayed in the inset of the figure. The same procedure is employed for all the displayed calculated XANES spectra. A good agreement between the calculated and experimental data is obtained. The presence of the two isosbestic points allows for the linear combination fitting (LCF) of the spectra obtained at different potentials using the spectra obtained at 0.9 V and 0.1 V as the two limit cases. The results are summarized in Table 1. The pre-edge position further confirms the observed and calculated data, shifting from ~7113.7 eV, typical for Fe^{3+} compounds, to ~7112.5 eV, typical for Fe^{2+} compounds.[41]

Table 1. Summary of the results obtained from the linear combination fitting of the Fe K-edge XANES spectra of the cathode catalyst recorder at different potentials under N_2 shown in figure 7a. The fitting is performed using the spectra recorded at 0.90 V and 0.10 V as standards.

Spectrum	**0.90 V (%)**	**0.10 V (%)**	**R-factor (x 10^{-4})**
0.90 V	100	0	-
0.85 V	100	0	3.4
0.80 V	78.6	21.4	2.9
0.75 V	56.9	43.1	7.5
0.70 V	42.4	57.6	3.4
0.65 V	33.2	66.8	3.5
0.60 V	15.5	84.5	10.5
0.40 V	0	100	5.5
0.10 V	0	100	-

Because Fe-N-C catalyst are not stable for long time under O_2 gas,[32] all the XAS spectra were recorded under N_2 to avoid degradation while recording them, since this would resolve in a time averaged spectrum (typically 40 minutes) of the degradation process which would be hard to deconvolute. In this study, we recorded the fresh and degraded spectra of the catalyst always at high and low potential (i.e., 0.9 V and 0.6 V) in order to gain a better understanding of the degradation mechanisms by looking at both states of the Fe, namely the OH-poisoned Fe(III)-N_4 site (high potential) and the active Fe(II)-N_4 site (low potential) nominally free from OH adsorbates.[26]

It has been showed that the stability of Fe-N-C is critical in the first hours of operation, with the current decaying extremely fast at first and more steadily afterwards.[8, 9, 42] For this reason, in an attempt to catch the degradation processes at their very beginning, XAS spectra were collected after 10, 30, 105 and 180 minutes (EoT). In order to disentangle different degradation mechanisms, we investigated the stability of the Fe under different conditions, namely at high and low potential (0.8 V and 0.4 V, respectively). At 0.8 V the majority of the Fe sites are in a 3^+ state and poisoned by OH groups, whereas at 0.4 V they are in a 2^+ state, with the Fe-N_4 sites free to perform the ORR.[26]

Degradation at 0.8 V

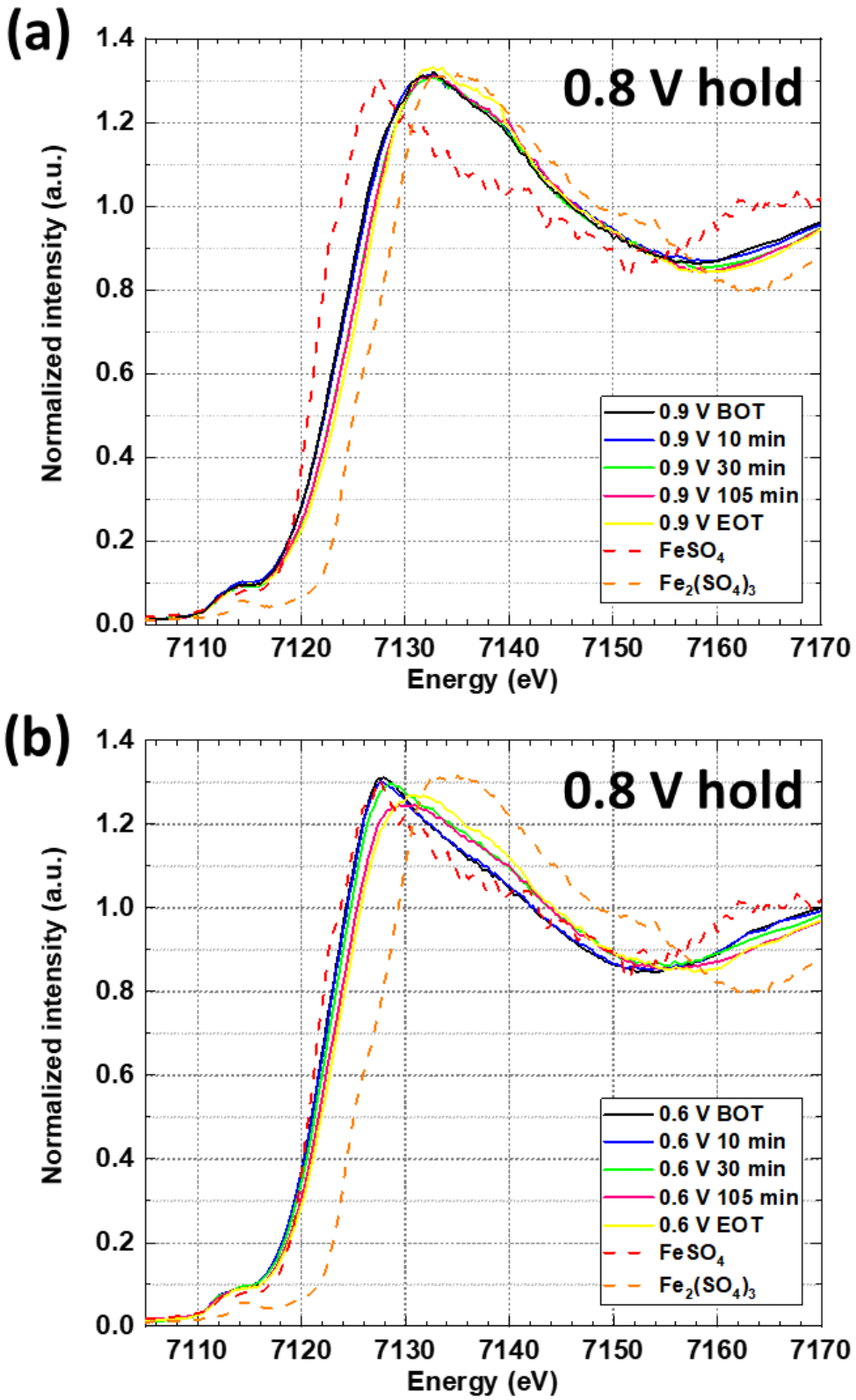

Figure 7. Evolution of the XANES spectra with time recorded during the 0.8 V hold degradation. Spectra were recorded under N_2 at 0.9 V (a) and 0.6 V (b). The spectra of $FeSO_4$ (red dotted line) and $Fe_2(SO_4)_3$ (orange dotted line) are shown for comparison.

When looking at the development of the spectra recorder at high and low potential (i.e., 0.9 and 0.6 V) during the 0.8 V hold (Figure 7), the edge position shifts towards higher energy. A change in edge position, when holding a certain potential, indicates a potential-independent change in oxidation state and/or coordination around the Fe atoms. A similar trend was also observed by Nabae et al. and the authors indeed attributed this effect to the demetalation of the Fe-N-C catalyst.[27] It is important to note that when the demetalation of Fe occurs, the leached cations can be flushed out by the water produced during fuel cell operations. This would result in a decrease of raw intensity in the fluorescence XAS spectra (for a constant sample-to-detector distance, which was the case for a given measurement set), i.e., in a lower amount of Fe probed. In our case, since no change in raw μ(E) is observed (Figure S6), we suggest that those leached Fe cations stay inside the MEA (i.e., the probing area of the X-rays).

Given the smaller size of Fe^{3+} cations compared to Fe^{2+}, degradation via demetalation is not surprising during the 0.8 V hold testing (since the Fe oxidation state is 3^+ at this potential). On the other hand, Holby et al calculated with DFT the Pourbaix diagram of Fe embedded in N-doped graphene and showed that OH-Fe(III)-N_4 sites are stable at low pH and high potential.[43] Nevertheless, the stability of Fe-N_4 sites can be likely different upon fuel cell operations. In fact, Xu et al. reported that hydroxy-coordinated Fe-N_4 sites are indeed the first stage of the demetalation process,[17] and Li et al reported the formation of Fe_2O_3 upon demetalation of Fe-N_4 sites.[19] The mechanism proposed by the authors involves firstly the demetalation of the Fe, which further coordinates to the ionomer and then the formation of Fe oxide upon air exposure. In our case, since the degradation happens already in O_2 atmosphere, the direct formation of Fe oxide would be expected, assuming that the conditions for the precipitation are met (i.e., pH and Fe concentration).

When considering the mechanism of Fe dematellation, it is important to consider the operational history of the fuel cell since Fe cations will move within the entire MEA depending on the operational conditions. During the 0.8 V hold in O_2-feed cathode, if demetalation occurs, a certain

amount of Fe would go into the PFSA ionomer, coordinating with the sulfuric acid group (SO_3^-) due to their stronger affinity compared to that of H^+. Under this condition (0.8 V hold in O_2), these Fe cations would remain in the cathode electrode due to a migration-controlled process, hence the leached Fe has an oxidation state of 3^+. When switching to a N_2-feed cathode in order to record the XAS data, those leached Fe cations would diffuse back into the ionomer of membrane and anode electrode due to a concentration gradient (a diffusion-controlled process) and the fast diffusion coefficient of Fe at high temperature and humidity. In this case, the Fe cations are equilibrating everywhere in the ionomer of the entire MEA. Accordingly, when recording the spectrum at 0.9 V in N_2-feed cathode, the leached Fe cation in the cathode electrode would be in a 3^+ state, whereas those diffused into membrane and anode electrode would be in a 2^+ state due to their contact with H_2, i.e., a potential ≈ 0 V. In this case, if a considerable amount of Fe cation is coordinated to the SO_3^- groups of the ionomer upon demetalation, a shift of the edge position towards lower energy in the XAS recorded at 0.9 V compared to that of BoT would be expected, since there is a mixture of 2^+ (anode electrode and membrane) and 3^+ (cathode electrode) Fe cations in the entire MEA.

When comparing the 0.9 V XAS spectra at BoT and 10 minutes (black and blue line, respectively), no appreciable shift in edge position is visible. This could point to the fact that the amount of Fe lost in the ionomer phase is not high enough to have an impact on the XAS spectra, which are an average of the entire Fe in the bulk. Nevertheless, when looking at 30 (green line), 105 (pink line) and 180 minutes (yellow line, EoT) a notable shift in edge position towards higher energy is visible. This is the case also for the evolution of the 0.6 V spectra (Figure 7b) and it is not consistent with the Fe being coordinated to the ionomer phase. In fact, if that was the case, a shift towards lower energy would be expected for the 0.9 V spectra and, when measuring the 0.6 V spectra, the Fe would be completely in a 2^+ state, which does not agree with the edge shifting to higher energy (characteristic of 3^+ compounds). In addition, the 0.6 V spectra show a clear change in the shape of the white line. In accord with previous literature,[19] these results are consistent with the Fe being precipitated as Fe(III) oxide, since it would remain in a 3^+ state independently of the applied potential.

We performed LCF of the spectra at different degradation time using as reference the BoT spectra and two different Fe(III) oxide, namely FeOOH and Fe_2O_3. Better results are obtained when using the FeOOH spectrum. A good agreement between the LCF and the experimental EoT spectra is obtained both at 0.9 and 0.6 V (Figure 8). Even though approximative, this analysis gives a percentage of demetallation and Fe(III) oxide precipitation between 31 and 37 % (Table S2).

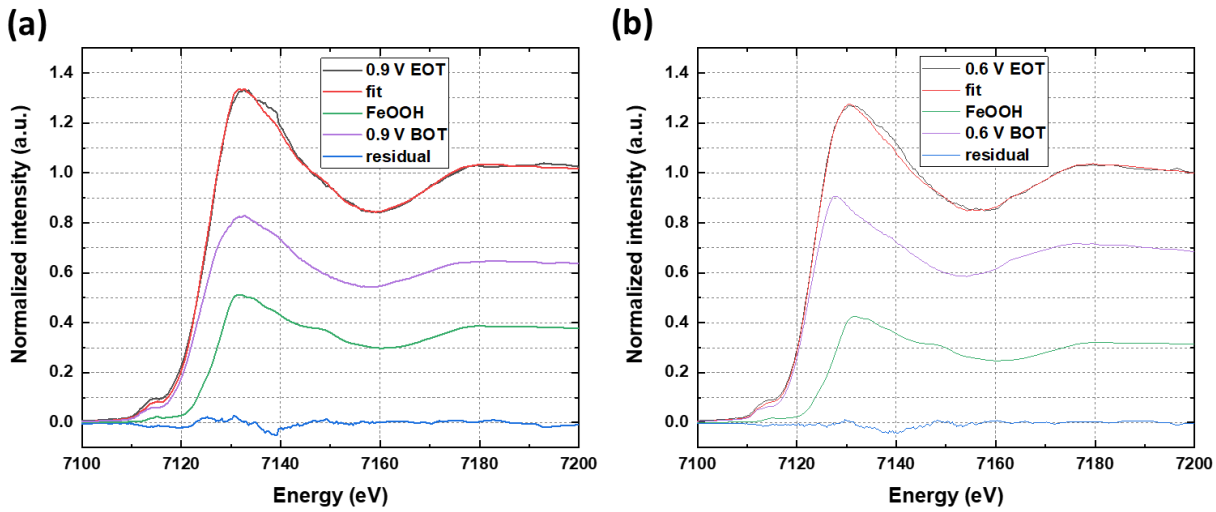

Figure 8. Comparison of the EoT spectra (black line) with the LCF (red line) at 0.9 V (a) and 0.6 V (b). The LFC is performed employing as standards the XANES spectrum of FeOOH (green line) and the respective spectrum at BoT (purple line).

Thermodynamic considerations of Fe oxide formation−While the LCF analysis of the XAS spectra indicates that Fe demetalation occurs with further precipitation as Fe oxide towards the EoT, it is important to consider whether this is thermodynamically possible. According to the Pourbaix diagram of Fe,[44] three factors govern the possibility of Fe cations to precipitate into Fe oxide species: 1) pH, 2) Fe concentration, and 3) potential. As mentioned earlier, when operating a Fe-containing cathode electrode in a fuel cell, the demetalated Fe cations will coordinate with the SO_3^- groups of the ionomer. Therefore, one would expect the pH of the cathode electrode or of the MEA to increase due to a reduced availability of SO_3^- sites for hosting H^+. When the demetalation of Fe continues and the right pH and Fe cations concentration in the ionomer phase are met, there is a chance for Fe oxide formation when operating the fuel cell (or cathode electrode) at high potential.

Additionally, as described earlier, since the applied testing protocol is a dynamic process, i.e., we are exchanging between N_2-feed and O_2-feed cathode, the leached Fe cation will diffuse/migrate into different compartment of the MEA, leading to changing in the local pH and Fe concentration.

Consequently, to analyse the possibility of Fe oxide formation, we further estimate the pH and Fe cations concentration (demetalated Fe) in the ionomer of the cathode electrode and in the entire MEA under a given % of Fe demetalation. These estimations were developed under three assumptions, and details of the calculation are described in the Appendix.

1) We assume that Fe demetalation is the only degradation occurring during the 0.8 V hold test. Therefore, we use 3^+ as oxidation state of Fe for the entire calculation. This would lead to three SO_3^- sites occupied by one Fe^{3+} cation.
2) The estimation is separated in two cases where Fe cations stay in the ionomer of the cathode electrode only or in that of the entire MEA. As mentioned earlier, this is due to the fact that during the 0.8 V hold in O_2-feed cathode, the Fe stays in the cathode electrode (a migration-controlled process), whereas when recording the XAS spectra in a N_2-feed cathode, the Fe cation equilibrates within the entire MEA (a diffusion-controlled process).
3) To calculate the Fe concentration and pH (i.e., H+ concentration) in the ionomer phase, it is necessary to consider the volume of the water in the system. For this, we simply assume that the water is only carried by the ionomer only due to water uptake (λ, in unit of $nH_2O/n\,SO_3^-$). In our case, since all the measurement were carried under 90 % RH, a λ = 9.34 is applied for all the cases.

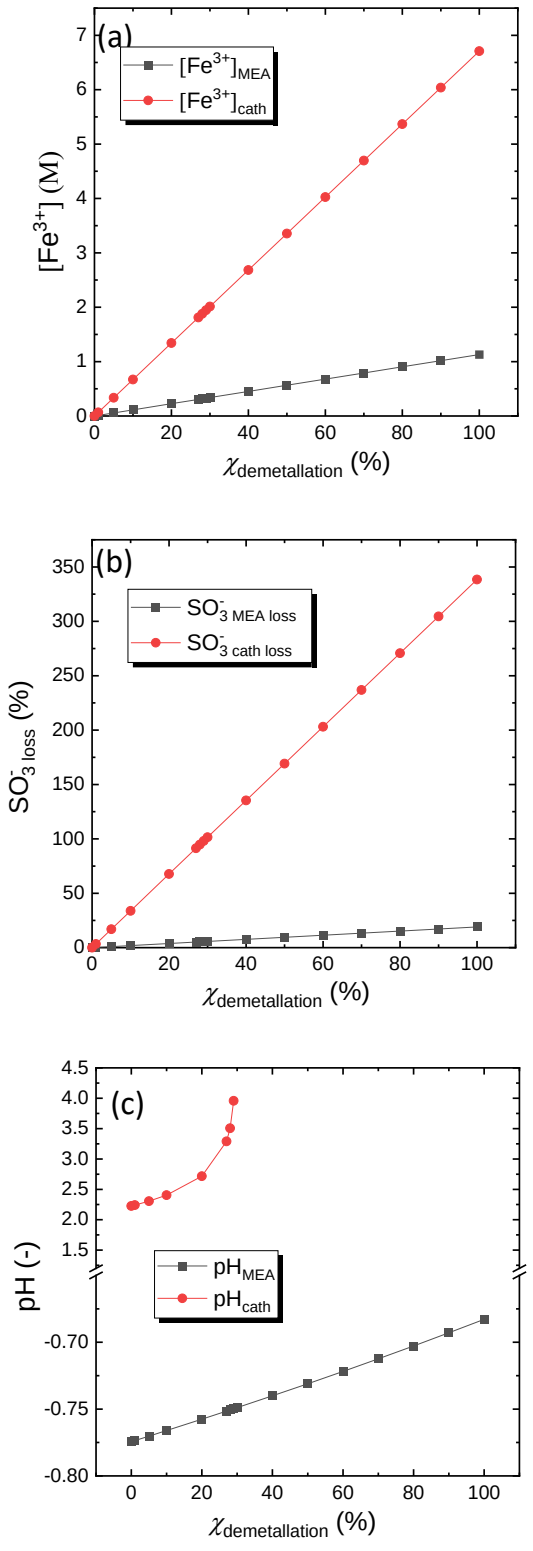

Figure 9. (a) Fe^{3+} concentration considering the ionomer of the cathode electrode only ($[Fe^{3+}]_{cath}$, in red) or of the entire MEA ($[Fe^{3+}]_{MEA}$, in black) under different fraction of Fe demetalation from the cathode electrode ($x_{demetalation}$). (b) Loss of H^+-available SO_3^- sites of the ionomer considering only the cathode electrode ($SO_{3,cath,loss}^-$, in red) and the entire MEA ($SO_{3,MEA,loss}^-$, in black) under different $x_{demetalation}$. (c) Estimated pH of the system considering only the cathode electrode (pH_{cath}, in red) and the entire MEA (pH_{MEA}, in black). The above results are calculated according to the assumption made in the text and detail of the calculation described in the Appendix.

Figure 9a shows the concentration of Fe^{3+} cations in the ionomer calculated considering the cathode electrode only ($[Fe^{3+}]_{cath}$, in red) or the entire MEA ($[Fe^{3+}]_{MEA}$, in black) for a given fraction of Fe demetalated from the cathode electrode ($x_{\mathrm{demetalation}}$).

ICP-MS analysis of the catalyst powder revealed a Fe content of 2.7 wt. %, with a residual Zn amount of 0.74 wt. % and Si impurities of 0.12 wt. %, originating most likely from the synthesis of the sample. It is important to note that Zn and Si could also demetalate during FC operation, further decreasing the H^+ availability when coordinating to the ionomer, with consequent pH increase.

From the estimation in Figure 9a, it is straightforward that when the demetalation of Fe from the catalyst continues, the Fe^{3+} concentration in the ionomer increases for both cases. Nevertheless, when only considering the Fe^{3+} migrating into the ionomer of cathode electrode (i.e., under 0.8 V hold in O_2-feed cathode), the local $[Fe^{3+}]$ becomes very high compared to the one obtained considering the entire MEA (i.e., when recording the XAS in a N_2-feed cathode). This difference is simply due to a much higher ionomer content in the membrane, leading to more H^+-available SO_3^- and higher water uptake from the ionomer. Therefore, a much lower Fe concentration is obtained in this case.

Similarly, the loss of SO_3^- sites available for H^+ ($SO_{3,\mathrm{loss}}^-$) in the ionomer of the cathode electrode only ($SO_{3,\mathrm{cath,loss}}^-$, in red) and entire MEA ($SO_{3,\mathrm{MEA,loss}}^-$, in black) are plotted in Figure 9b. The results follow the same trend as in Figure 9a. The $SO_{3,\mathrm{loss}}^-$ of the ionomer in the cathode electrode is much higher compared to the one of the entire MEA. In our estimation when considering, for example, $x_{\mathrm{demetalation}} \approx 30\%$, almost ~100% of SO_3^- sites in the ionomer of the cathode electrode will be occupied by Fe^{3+}, leading to a significant failure in fuel cell performance due to the unavailability of SO_3^- sites to host H^+. Nevertheless, it is important to mention that the precipitation of Fe oxide is a dynamic process. When the Fe concentration and pH are met, the Fe cation starts precipitating as Fe oxide. In this case, the SO_3^- in the ionomer is no longer coordinated with Fe cations,

resulting in an increased SO_3^- availability for H^+. In other words, the ~30 % of demetalation obtained from the LCF is not to be confused with $x_{demetallaion} \approx 30$ % in Figure 9b.

The pH of the system considering the cathode electrode only (pH_{cath}) or the entire MEA (pH_{MEA}) are further calculated in Figure 9c. It should be noted again that the pH estimated here is only based on the assumption that water is only carried by the ionomer for the calculation of the H^+ concentration change. Although the actual volume of water in the MEA might change due to fuel cell operation during the 0.8 V hold, it is very difficult to estimate the production or management of water in the cathode electrode. From this estimation, it is found that when a small amount of Fe is leached from the active site, the pH increases significantly when considering the Fe cations staying in the cathode electrode compared to considering the entire MEA. For example, when assuming a $x_{\mathrm{demetallaion}}$ = 15%, the $\mathrm{pH_{cath}}$ is ~2.3 and $[Fe^{3+}]_{\mathrm{cath}}$ is ~0.8 M. Whereas at the same $x_{\mathrm{demetallaion}}$, the Fe concentration and pH remain low when considering the entire MEA due to an overall higher ionomer content (i.e., $\mathrm{pH_{MEA}} \approx$ -0.77 and $[Fe^{3+}]_{\mathrm{MEA}} \approx 0.1$). This suggests that Fe oxide precipitation may occur when holding the potential at 0.8 V under O_2 due to a high local pH and Fe concentration in the cathode electrode.

Combining the results in Figure 9, it is noted that when considering that the demetaleted Fe cations stay in the entire MEA, the Fe concentration and pH remain very low, i.e., it is hard to form Fe oxide. In fact, in our testing measurement, the degradation (in O_2-feed cathode) and spectra (in N_2-feed cathode) are switched in between each other. In other words, while it is possible to form the Fe oxide species during the O_2-feed cathode degradation (a much higher local pH and Fe concentration) in the cathode electrode, those Fe oxide species should be dissolved again when switching back to the N_2-feed cathode to record the XAS spectra. Such dynamic process is in contrast with the observed trend in the XAS spectra showing that a significant amount of Fe(III) oxide is formed at EoT. We hypothesize that this could be due a kinetic hindrance of the dissolution process, since the time under N_2-feed is rather short, therefore, the formed Fe oxide may not be redissolved

under these conditions. It is crucial to point out that the above estimation is not for quantification purposes but it is rather a simple analysis on the possibility of Fe oxide formation in the case of the 0.8 V hold. The precipitation of Fe oxide is a dynamic process, which is strongly affected by the fuel cell operations. The precipitation of Fe oxide will lead to a decrease of the Fe concentration in the ionomer phase, leading to an increased availability of SO_3^- sites, hence decreasing the local pH. Additionally, the kinetics of the formation/dissolution of Fe oxide might change according to different Fe oxide species. It is therefore hard to provide an exact analysis of the time scale of the process.

Degradation at 0.4 V

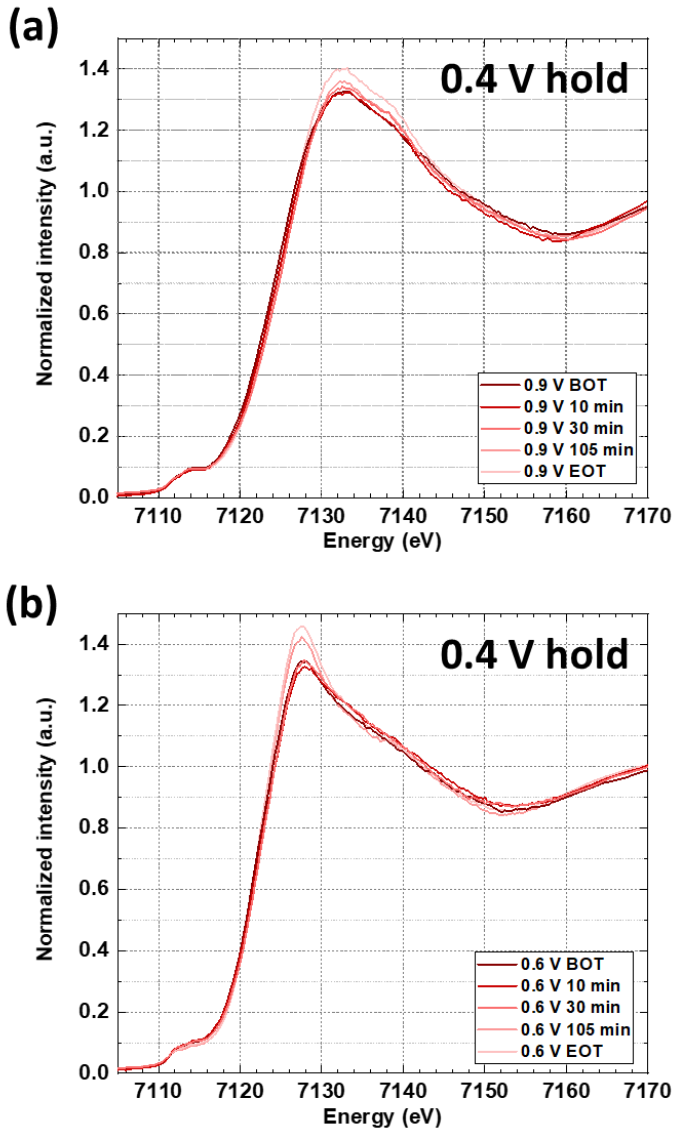

Figure 10. Evolution of the XANES spectra with time recorded during the 0.4 V hold degradation. Spectra were recorded under N_2 at 0.9 V (a) and 0.6 V (b).

During the 0.4 V hold degradation, the development of the spectra recorder at low and high potential (i.e., 0.6 V and 0.9 V, respectively) is consistently different compared to the 0.8 V hold degradation, pointing to the fact that the mechanism involved is different (Figure 10). Both at low and high potential, no appreciable change in edge position is observed, meaning that the oxidation state of the Fe stays the same depending on the applied potential, whereas the intensity of white line increases notably over time.

The white line is attributed to the Fe(1s) → Fe(4p) transition. An increase in white line intensity would mean that less electrons are present in the Fe(4p) band. This could be the case if the number of ligands around the Fe atom increases, due to exchange of electrons with the ligands' orbitals, or if the electron density is being pulled away from the Fe centre. As already showed for the 0.8 V hold, in case of demetalation the edge position would shift towards higher energy, moreover, no LCF could be obtained with any of the reference compounds employed. For these reasons, demetalation is excluded in this case. Moreover, the transition between 3^+ and 2^+ remains reversible during the entire curse of the experiment, pointing to the fact the Fe cations are always electrochemically active, hence in contact to the electrode.

Another probable degradation mechanism is the attack from reactive oxygen species (ROS)[13] which would result in a chemical carbon oxidation (for the electrochemical oxidation higher potential is required). This hypothesis is consistent with the EoT CV, where an increase in area at ~0.6 V (quinone/hydroquinone redox) is observed (Figure 6b). Moreover, this degradation mechanism seems reasonable at low potential due to the higher reaction rate and higher H_2O_2 produced (Figure S3). It could eventually also result in demetalation once the carbon scaffold starts being destroyed, but we did not observe this in the 3 hours of the experiment.

How can the attack by ROS be linked to the observed XAS trend? In case of carbon oxidation only, no change in the Fe K-edge would be expected. This suggests that the Fe atoms are also interested by the ROS attack. Xie et al showed that OH and OOH radicals would preferentially attack

the Fe-N_4 sites and that the durability of Fe-N-C catalysts can be improved when Ta-TiO_x nanoparticles are employed due to their ability to scavenge radicals.[45] As already mentioned, the increase in white line could be attributed to an increase of ligands around the Fe, for example with further ligation by oxygen atoms.

A first hypothesis to explain the increase in white line is the ligation by Fe atoms of oxy radicals which are not removed anymore even at low potential. Choi et al. showed that the oxidation of the carbon scaffold (regarded as functionalization by oxy groups) would result in a depletion of electrons from the Fe sites, with the d_z orbital of the Fe being pulled closer to the Fe, further increase in work function and decreased TOF.[13] This could suggest that the Fe-N_4 sites are being poisoned by oxy radicals and that their absorption energy is too high for them to be removed even at low potential, consistently with the XAS results. Moreover, the ligation of OH radicals to the Fe could hypothetically be accompanied by the breaking of one or more Fe-N bond, possibly resulting in a lower reactivity of the Fe-N_x sites ($x < 4$) and representing the first step of the demetalation process at this potential. This hypothesis is supported by comparing the calculated XANES spectra (Figure 11) of the $[FeN_4]C_{52}H_{20}$ cluster (black line) with the one of the $[(OH)FeN_3]NC_{52}H_{20}$ where the Fe atom binds only three N atoms and one OH (green line). In agreement with the experimental results, the two XANES spectra show same energy position but different white line intensity.

A second hypothesis for the degradation mechanism by ROS attack finds its rational in molecular chemistry. The first steps of OH radical attack to a porphyrin ring could result in the opening of one five-membered ring, with loss of one N atom as NH_3 and coordination of two O atoms. The calculated XANES spectrum of the hydrolysed $[O_2FeN_3]C_{52}H_{20}$ structure where the Fe binds 3 N and 2 O atoms (blue line) shows the same edge position of the $[FeN_4]C_{52}H_{20}$ one (black line) but with higher with line intensity, consistently with the experimental results (Figure 11).

In order to gain more insight into the Fe structure after ROS attack and discern between the different proposed hypothesis, we conducted a simple experiment where we stirred the catalyst in

0.05 M H_2SO_4 in the presence of a Fenton reagent (H_2O_2 + $FeSO_4$) at 80 °C in order to simulate the conditions in a PEMFC. After 24 h we checked the presence of NH_4^+ ions in solution using a qualitative stripes test which gave a positive result (Figure S7). Moreover, the sample was collected after filtering and washing and the elemental analysis showed a decrease of ~ 4 wt.% in N content, clearly showing the loss of N due to the ROS attack. This degradation mechanism further supports what has been recently reported for the degradation of Fe phthalocyanine during the ORR in acidic electrolyte, where OH· radicals attack followed by NH_3 loss was proposed.[46]

The EoT ORR activity after the 0.4 V hold degradation is overlapped to the one after 0.8 V hold (Figure 5). This result can be explained if the majority of the sites responsible for D1 in Mössbauer spectroscopy have degraded in the 3 hours of test in O_2 and, after this time, only the stable sites responsible for D2 are contributing to the activity of the catalyst.

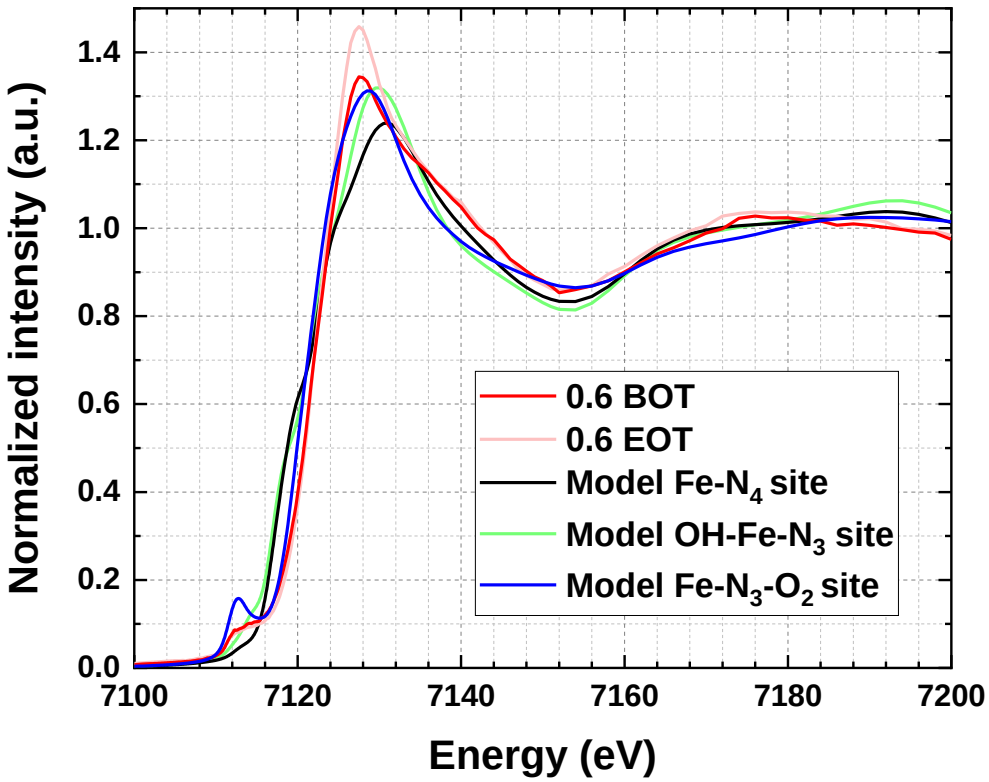

Figure 11. Calculated XANES spectra of the $[FeN_4]C_{52}H_{20}$ (black), $[(OH)FeN_3]NC_{52}H_{20}$ (green) and hydrolysed $[O_2FeN_3]C_{52}H_{20}$ structure (blue) in comparison with the spectra of the catalyst measured at 0.6 V at BoT (red) and EoT (pink) during the 0.4 V hold.

Conclusions

We studied the potential-dependent degradation mechanisms of an active-site imprinted catalyst consisting of atomically dispersed Fe-N_4 sites employing *in-situ* XAS measurements in a PEMFC setup. Two different degradation protocols were evaluated under operating conditions, i.e., with O_2-feed cathode, namely potentiostatic hold at 0.8 V and 0.4 V for 3 hours. The fuel cell results showed that the two cases exhibit a similar current loss profile, with a fast decay within the first 30 min followed by a slow one. When holding the cell potential at 0.8 V, an 80 % current loss is observed after 3 hours, whereas there was only a 50% current loss when holding at 0.4 V. Nevertheless, the EoT ORR activity is similar for both cases, degrading ca. 90 % of the initial activity determined at 0.8 $V_{HFR\text{-}free}$. These results suggest that, independently of the protocol employed, the majority of the active sites have degraded in the 3 hours of testing in O_2 and, after this time, only the most stable sites are contributing to the activity of the catalyst.

To elucidate the degradation mechanism, the XAS spectra were recorded and analysed. At high potential, the majority of the Fe sites are in a 3^+ state and undergo demetalation during the measured time. We found that at EoT ~ 35 % of the Fe is precipitated as Fe(III) oxide. At low potential, where the majority of the Fe sites is in a 2^+ state, no demetalation could be detected and the observed XAS results can be linked to the attack by ROS. This is also supported by the increased EoT CV area at ~ 0.6 V where quinone/hydroquinone features are located. Moreover, based on molecular chemistry, we proposed a mechanism for the ROS attack to the Fe-N_4 sites, which could be proved by detecting NH_4^+ after degradation by ROS.

By employing constant potential measurements instead of cycling and probing different oxidation state of Fe, we were able to disentangle different degradation mechanisms happening in a Fe-N-C electrocatalyst upon realistic operating conditions. We believe that this work will help future research effort designed to improve the understanding and stability of this class of materials.

Appendix

In this section, we describe the calculation for the result shown in Figure 9. The following calculations are based on the three assumptions made in the main text.

The amount of dematelated Fe from the cathode electrode (nFe^{3+}, expressed in moles) is calculated with equation A1:

$$n\mathrm{Fe}^{3+} = \frac{L_{\mathrm{cat,cath}} \cdot A_{\mathrm{MEA}} \cdot X_{\mathrm{Fe,cat}}}{M_{\mathrm{Fe}}} \cdot x_{\mathrm{demetalation}} \quad \text{(A1)}$$

Where $L_{\mathrm{cat,cathode}}$ is the loading of the PGM-free catalyst in the cathode electrode (in unit of mg cm^{-2}, 3.5 mg cm^{-2} is used in our case). A_{MEA} is the active area (5 cm^2). $X_{\mathrm{Fe,cat}}$ is the fraction of Fe in the catalyst (expressed as wt.%), ~2.7 wt.% is obtained from ICP-MS. M_{Fe} is the molecular weight of Fe, 56 g mole^{-1}. $x_{demetallaion}$ is the % of Fe demetalation from the catalyst, we assume $x_{\mathrm{demetallaion}}$ = 0, 10, 20, 30, 40, 50, 60, 70, 80, 90, and 100 % for calculating the plot in Figure 9 (i.e., x-axis of the plots).

To calculate the Fe concentration, the water uptake from the ionomer is considered. For this, the number of moles of SO_3^- sites in the ionomer of the electrodes (cathode: $n\mathrm{SO}_{3,\mathrm{cath}}^-$ and anode: $n\mathrm{SO}_{3,\mathrm{an}}^-$) and membrane ($n\mathrm{SO}_{3,\mathrm{memb}}^-$) at beginning state (i.e., without any demetalation) are calculated according to equation A2, A3, and A4 respectively:

$$n\mathrm{SO}_{3,\mathrm{cath}}^- = \left(\frac{I}{C}\right) \cdot \left(\frac{L_{\mathrm{c,cath}} \cdot A_{\mathrm{MEA}}}{EW}\right) \quad \text{(A2)}$$

$$n\mathrm{SO}_{3,\mathrm{an}}^- = \left(\frac{I}{C}\right) \cdot \left(\frac{L_{\mathrm{c,an}} \cdot A_{\mathrm{MEA}}}{EW}\right) \quad \text{(A3)}$$

$$n\mathrm{SO}_{3,\mathrm{memb}}^- = \left(\frac{t_{\mathrm{dry,thickness}} \cdot A_{\mathrm{MEA}}}{EW}\right) \quad \text{(A4)}$$

Subsequently, the SO_3^- sites in the ionomer of the entire MEA at the initial state is:

$$nSO_{3,\mathrm{MEA}}^{-} = nSO_{3,\mathrm{cath}}^{-} + nSO_{3,\mathrm{an}}^{-} + nSO_{3,\mathrm{memb}}^{-} \quad \text{(A5)}$$

Where *I/C* is the ionomer to carbon ratio in the electrode (in unit of $g_{ionomer}/g_{carbon}$), which is 0.65 and 0.5 for anode and cathode electrode, respectively. $L_{\mathrm{c,cath}}$ and $L_{\mathrm{c,an}}$ (in unit of g cm^{-2}) are the carbon loading of the cathode and anode electrode, respectively. In our case, the $L_{\mathrm{c,cath}} \approx L_{\mathrm{cat,cath}}$, since the majority of the catalyst is carbon, whereas $L_{\mathrm{c,an}}$= 0.4 g cm^{-2}. *EW* is the equivalent weight of the ionomer (in unit of $g_{ionomer}$/mole SO_3^-). The *EW* of electrodes and membrane is 700 and 1100, respectively. $t_{\mathrm{dry,thickness}}$ is the dry thickness of the membrane (~45 µm for Nafion 212 here). Consequently, the volume of water due to water uptake of the ionomer in the electrodes, membrane, and entire MEA are calculated with equation A6, A7, A8, and A9:

$$V_{\mathrm{H_2O,cath}} = \lambda \cdot nSO_{3,\mathrm{cath}}^{-} \cdot M_{H_2O} \cdot \rho_{H_2O} \quad \text{(A6)}$$

$$V_{\mathrm{H_2O,an}} = \lambda \cdot nSO_{3,an}^{-} \cdot M_{H_2O} \cdot \rho_{H_2O} \quad \text{(A7)}$$

$$V_{\mathrm{H_2O,memb}} = \lambda \cdot nSO_{3,\mathrm{memb}}^{-} \cdot M_{H_2O} \cdot \rho_{H_2O} \quad \text{(A8)}$$

$$V_{\mathrm{H_2O,MEA}} = V_{\mathrm{H_2O,cath}} + V_{\mathrm{H_2O,an}} + V_{\mathrm{H_2O,memb}} \quad \text{(A9)}$$

Where λ is the water uptake of the ionomer (in unit of $\mathrm{n}H_2O/\mathrm{n}\,SO_3^-$), a λ = 9.34 is used here (at RH = 90 %). M_{H_2O} is the molar weight of water (18 g $mole^{-1}$). ρ_{H_2O} is the density of the water (0.97 $cm^3\,g^{-1}$). Therefore, the result of the Fe^{3+} concentration in Figure 7a are calculated according to equation A11 and A12 for the cathode electrode and the entire MEA, respectively:

$$[\mathrm{Fe}^{3+}]_{\mathrm{cath}} = \frac{nFe^{3+}}{V_{\mathrm{H_2O,cath}}}$$

$$[\mathrm{Fe}^{3+}]_{\mathrm{MEA}} = \frac{nFe^{3+}}{V_{\mathrm{H_2O,MEA}}}$$

As mentioned earlier, when operating the fuel cell in N_2-feed cathode to record the XAS spectra, the Fe cations will diffuse into the ionomer and coordinate with the SO_3^- groups of the entire MEA. Whereas when operating in an O_2-feed cathode during the 0.8 V hold, the Fe cations will migrate into the cathode electrode, occupying the SO_3^- groups of the ionomer in the cathode electrode only. Consequently, based on these two scenarios, the losses of available SO_3^- for H^+ are calculated according to equation A12 and A13:

$$SO_{3,cath,loss}^- = \frac{(nSO_{3.cath}^- - 3 \cdot nFe^{3+})}{nSO_{3,cath}^-} \times 100\ \% \quad \text{(A12)}$$

$$SO_{3,MEA,loss}^- = \frac{(nSO_{3,MEA}^- - 3 \cdot nFe^{3+})}{nSO_{3,MEA}^-} \times 100\ \% \quad \text{(A13)}$$

Where the conversion factor of 3 in both equation A12 and A13 represents the valence of Fe^{3+}.

Similarly, the pH (i.e., -log [H+]) of the cathode electrode and MEA are defined as the available SO_3^- for H^+ in the entire MEA or cathode electrode after a given $x_{demetallaion}$, which are calculated with equation A14 and A15; respectively:

$$pH_{cath} = -\log [H+]_{cath} = \frac{nSO_{3.cath}^- - 3 \cdot nFe^{3+}}{V_{H_2O,cath}}$$

$$pH_{MEA} = -\log [H+]_{MEA} = \frac{nSO_{3.MEA}^- - 3 \cdot nFe^{3+}}{V_{H_2O,MEA}}$$

References

[1] F. Jaouen, D. Jones, N. Coutard, V. Artero, P. Strasser, A. Kucernak, Toward Platinum Group Metal-Free Catalysts for Hydrogen/Air Proton-Exchange Membrane Fuel Cells, Johnson Matthey Technology Review, 62 (2018) 231-255.
[2] S.T. Thompson, D. Papageorgopoulos, Platinum group metal-free catalysts boost cost competitiveness of fuel cell vehicles, Nature Catalysis, 2 (2019) 558-561.
[3] L. Jiao, J. Li, L.L. Richard, Q. Sun, T. Stracensky, E. Liu, M.T. Sougrati, Z. Zhao, F. Yang, S. Zhong, H. Xu, S. Mukerjee, Y. Huang, D.A. Cullen, J.H. Park, M. Ferrandon, D.J. Myers, F. Jaouen, Q. Jia, Chemical vapour deposition of Fe–N–C oxygen reduction catalysts with full utilization of dense Fe–N4 sites, Nature Materials, 20 (2021) 1385-1391.
[4] A. Mehmood, M. Gong, F. Jaouen, A. Roy, A. Zitolo, A. Khan, M.-T. Sougrati, M. Primbs, A.M. Bonastre, D. Fongalland, G. Drazic, P. Strasser, A. Kucernak, High loading of single atomic iron sites in Fe–NC oxygen reduction catalysts for proton exchange membrane fuel cells, Nature Catalysis, 5 (2022) 311-323.
[5] X. Wan, X. Liu, Y. Li, R. Yu, L. Zheng, W. Yan, H. Wang, M. Xu, J. Shui, Fe–N–C electrocatalyst with dense active sites and efficient mass transport for high-performance proton exchange membrane fuel cells, Nature Catalysis, 2 (2019) 259-268.
[6] J. Weiss, H. Zhang, P. Zelenay, Recent progress in the durability of Fe-N-C oxygen reduction electrocatalysts for polymer electrolyte fuel cells, Journal of Electroanalytical Chemistry, 875 (2020) 114696.
[7] R.K.F. Della Bella, B.M. Stühmeier, H.A. Gasteiger, Universal Correlation between Cathode Roughness Factor and H₂/Air Performance Losses in Voltage Cycling-Based Accelerated Stress Tests, Journal of The Electrochemical Society, 169 (2022) 044528.
[8] D. Banham, T. Kishimoto, Y. Zhou, T. Sato, K. Bai, J.-i. Ozaki, Y. Imashiro, S. Ye, Critical advancements in achieving high power and stable nonprecious metal catalyst-based MEAs for real-world proton exchange membrane fuel cell applications, Sci. Adv., 4 (2018).
[9] L. Osmieri, D.A. Cullen, H.T. Chung, R.K. Ahluwalia, K.C. Neyerlin, Durability evaluation of a Fe–N–C catalyst in polymer electrolyte fuel cell environment via accelerated stress tests, Nano Energy, 78 (2020) 105209.
[10] R. Chenitz, U.I. Kramm, M. Lefèvre, V. Glibin, G. Zhang, S. Sun, J.-P. Dodelet, A specific demetalation of Fe–N4 catalytic sites in the micropores of NC_Ar + NH3 is at the origin of the initial activity loss of the highly active Fe/N/C catalyst used for the reduction of oxygen in PEM fuel cells, Energy & Environmental Science, 11 (2018) 365-382.
[11] M. Ferrandon, X. Wang, A.J. Kropf, D.J. Myers, G. Wu, C.M. Johnston, P. Zelenay, Stability of iron species in heat-treated polyaniline–iron–carbon polymer electrolyte fuel cell cathode catalysts, Electrochimica Acta, 110 (2013) 282-291.
[12] C.H. Choi, C. Baldizzone, J.-P. Grote, K.J.J. Mayrhofer, A.K. Schuppert, F. Jaouen, Stability of Fe-N-C Catalysts in Acidic Medium Studied by Operando Spectroscopy, Angew Chem Int Ed Engl, 54 (2015) 12753-12757.
[13] C.H. Choi, H.-K. Lim, M.W. Chung, G. Chon, N. Ranjbar Sahraie, A. Altin, M.-T. Sougrati, L. Stievano, H.S. Oh, E.S. Park, F. Luo, P. Strasser, G. Dražić, K.J.J. Mayrhofer, H. Kim, F. Jaouen, The Achilles' heel of iron-based catalysts during oxygen reduction in an acidic medium, Energy & Environmental Science, 11 (2018) 3176-3182.
[14] G. Zhang, R. Chenitz, M. Lefèvre, S. Sun, J.-P. Dodelet, Is iron involved in the lack of stability of Fe/N/C electrocatalysts used to reduce oxygen at the cathode of PEM fuel cells?, Nano Energy, 29 (2016) 111-125.
[15] G. Liu, X. Li, J.-W. Lee, B.N. Popov, A review of the development of nitrogen-modified carbon-based catalysts for oxygen reduction at USC, Catalysis Science & Technology, 1 (2011) 207-217.
[16] Y. Shao, J.-P. Dodelet, G. Wu, P. Zelenay, PGM-Free Cathode Catalysts for PEM Fuel Cells: A Mini-Review on Stability Challenges, Advanced Materials, 31 (2019) 1807615.
[17] X. Xu, X. Zhang, Z. Kuang, Z. Xia, A.I. Rykov, S. Yu, J. Wang, S. Wang, G. Sun, Investigation on the demetallation of Fe-N-C for oxygen reduction reaction: The influence of structure and structural evolution of active site, Applied Catalysis B: Environmental, 309 (2022) 121290.

[18] S. Liu, C. Li, M.J. Zachman, Y. Zeng, H. Yu, B. Li, M. Wang, J. Braaten, J. Liu, H.M. Meyer, M. Lucero, A.J. Kropf, E.E. Alp, Q. Gong, Q. Shi, Z. Feng, H. Xu, G. Wang, D.J. Myers, J. Xie, D.A. Cullen, S. Litster, G. Wu, Atomically dispersed iron sites with a nitrogen–carbon coating as highly active and durable oxygen reduction catalysts for fuel cells, Nature Energy, (2022).
[19] J. Li, M.T. Sougrati, A. Zitolo, J.M. Ablett, I.C. Oğuz, T. Mineva, I. Matanovic, P. Atanassov, Y. Huang, I. Zenyuk, A. Di Cicco, K. Kumar, L. Dubau, F. Maillard, G. Dražić, F. Jaouen, Identification of durable and non-durable FeNx sites in Fe–N–C materials for proton exchange membrane fuel cells, Nature Catalysis, 4 (2021) 10-19.
[20] U.I. Kramm, M. Lefèvre, P. Bogdanoff, D. Schmeißer, J.-P. Dodelet, Analyzing Structural Changes of Fe–N–C Cathode Catalysts in PEM Fuel Cell by Mößbauer Spectroscopy of Complete Membrane Electrode Assemblies, The Journal of Physical Chemistry Letters, 5 (2014) 3750-3756.
[21] V. Goellner, C. Baldizzone, A. Schuppert, M.T. Sougrati, K. Mayrhofer, F. Jaouen, Degradation of Fe/N/C catalysts upon high polarization in acid medium, Phys. Chem. Chem. Phys., 16 (2014) 18454-18462.
[22] M. Lefèvre, J.-P. Dodelet, Fe-based catalysts for the reduction of oxygen in polymer electrolyte membrane fuel cell conditions: determination of the amount of peroxide released during electroreduction and its influence on the stability of the catalysts, Electrochimica Acta, 48 (2003) 2749-2760.
[23] U.I. Kramm, L. Ni, S. Wagner, 57Fe Mössbauer Spectroscopy Characterization of Electrocatalysts, Advanced Materials, 31 (2019) 1805623.
[24] L. Ni, C. Gallenkamp, S. Wagner, E. Bill, V. Krewald, U.I. Kramm, Identification of the Catalytically Dominant Iron Environment in Iron- and Nitrogen-Doped Carbon Catalysts for the Oxygen Reduction Reaction, Journal of the American Chemical Society, 144 (2022) 16827-16840.
[25] L. Osmieri, R.K. Ahluwalia, X. Wang, H.T. Chung, X. Yin, A.J. Kropf, J. Park, D.A. Cullen, K.L. More, P. Zelenay, D.J. Myers, K.C. Neyerlin, Elucidation of Fe-N-C electrocatalyst active site functionality via in-situ X-ray absorption and operando determination of oxygen reduction reaction kinetics in a PEFC, Applied Catalysis B: Environmental, 257 (2019) 117929.
[26] Q. Jia, N. Ramaswamy, H. Hafiz, U. Tylus, K. Strickland, G. Wu, B. Barbiellini, A. Bansil, E.F. Holby, P. Zelenay, S. Mukerjee, Experimental Observation of Redox-Induced Fe-N Switching Behavior as a Determinant Role for Oxygen Reduction Activity, ACS Nano, 9 (2015) 12496-12505.
[27] Y. Nabae, Q. Yuan, S. Nagata, K. Kusaba, T. Aoki, N. Takao, T. Itoh, M. Arao, H. Imai, K. Higashi, T. Sakata, T. Uruga, Y. Iwasawa, In Situ X-ray Absorption Spectroscopy to Monitor the Degradation of Fe/N/C Cathode Catalyst in Proton Exchange Membrane Fuel Cells, Journal of The Electrochemical Society, 168 (2021) 014513.
[28] D. Menga, F. Ruiz-Zepeda, L. Moriau, M. Šala, F. Wagner, B. Koyutürk, M. Bele, U. Petek, N. Hodnik, M. Gaberšček, T.-P. Fellinger, Active-Site Imprinting: Preparation of Fe–N–C Catalysts from Zinc Ion–Templated Ionothermal Nitrogen-Doped Carbons, Advanced Energy Materials, 9 (2019) 1902412.
[29] D. Menga, J.L. Low, Y.-S. Li, I. Arčon, B. Koyutürk, F. Wagner, F. Ruiz-Zepeda, M. Gaberšček, B. Paulus, T.-P. Fellinger, Resolving the Dilemma of Fe–N–C Catalysts by the Selective Synthesis of Tetrapyrrolic Active Sites via an Imprinting Strategy, Journal of the American Chemical Society, 143 (2021) 18010-18019.
[30] A. Mehmood, J. Pampel, G. Ali, H.Y. Ha, F. Ruiz-Zepeda, T.-P. Fellinger, Facile Metal Coordination of Active Site Imprinted Nitrogen Doped Carbons for the Conservative Preparation of Non-Noble Metal Oxygen Reduction Electrocatalysts, Advanced Energy Materials, 8 (2018) 1701771.
[31] D. Menga, A.G. Buzanich, F. Wagner, T.-P. Fellinger, Evaluation of the Specific Activity of M-N-Cs and the Intrinsic Activity of Tetrapyrrolic Fe-N4 Sites for the Oxygen Reduction Reaction, Angewandte Chemie International Edition, (2022).
[32] K. Kumar, L. Dubau, M. Mermoux, J. Li, A. Zitolo, J. Nelayah, F. Jaouen, F. Maillard, On the Influence of Oxygen on the Degradation of Fe-N-C Catalysts, Angewandte Chemie International Edition, 59 (2020) 3235-3243.
[33] A. Siebel, Y. Gorlin, J. Durst, O. Proux, F. Hasché, M. Tromp, H.A. Gasteiger, Identification of Catalyst Structure during the Hydrogen Oxidation Reaction in an Operating PEM Fuel Cell, ACS Catalysis, 6 (2016) 7326-7334.
[34] T. Mineva, I. Matanovic, P. Atanassov, M.-T. Sougrati, L. Stievano, M. Clémancey, A. Kochem, J.-M. Latour, F. Jaouen, Understanding Active Sites in Pyrolyzed Fe–N–C Catalysts for Fuel Cell Cathodes by

Bridging Density Functional Theory Calculations and 57Fe Mössbauer Spectroscopy, ACS Catalysis, 9 (2019) 9359-9371.
[35] G. Zhang, X. Yang, M. Dubois, M. Herraiz, R. Chenitz, M. Lefèvre, M. Cherif, F. Vidal, V.P. Glibin, S. Sun, J.-P. Dodelet, Non-PGM electrocatalysts for PEM fuel cells: effect of fluorination on the activity and stability of a highly active NC_Ar + NH₃ catalyst, Energy & Environmental Science, 12 (2019) 3015-3037.
[36] X. Yin, E.F. Holby, P. Zelenay, Comment on “Non-PGM electrocatalysts for PEM fuel cells: effect of fluorination on the activity and stability of a highly active NC_Ar + NH₃ catalyst” by Gaixia Zhang, Xiaohua Yang, Marc Dubois, Michael Herraiz, Régis Chenitz, Michel Lefèvre, M, Energy & Environmental Science, 14 (2021) 1029-1033.
[37] X. Yin, P. Zelenay, (Invited)Kinetic Models for the Degradation Mechanisms of PGM-Free ORR Catalysts, ECS Transactions, 85 (2018) 1239-1250.
[38] A.M. Damjanović, B. Koyutürk, Y.-S. Li, D. Menga, C. Eickes, H.A. El-Sayed, H.A. Gasteiger, T.-P. Fellinger, M. Piana, Loading Impact of a PGM-Free Catalyst on the Mass Activity in Proton Exchange Membrane Fuel Cells, Journal of The Electrochemical Society, 168 (2021) 114518.
[39] B.L. Henke, E.M. Gullikson, J.C.David, X-ray interactions: photoabsorption, scattering, transmission, and reflection at E=50-30000 eV, Z=1-92, Atomic Data and Nuclear Data Tables, 54 (2) (1993) 182-342.
[40] S.A. Guda, A.A. Guda, M.A. Soldatov, K.A. Lomachenko, A.L. Bugaev, C. Lamberti, W. Gawelda, C. Bressler, G. Smolentsev, A.V. Soldatov, Y. Joly, Optimized Finite Difference Method for the Full-Potential XANES Simulations: Application to Molecular Adsorption Geometries in MOFs and Metal–Ligand Intersystem Crossing Transients, Journal of Chemical Theory and Computation, 11 (2015) 4512-4521.
[41] M. Wilke, F. Farges, P.-E. Petit, G.E. Brown, F. Martin, Oxidation state and coordination of Fe in minerals: An Fe K-XANES spectroscopic study, American Mineralogist, 86 (2001) 714-730.
[42] E. Proietti, F. Jaouen, M. Lefèvre, N. Larouche, J. Tian, J. Herranz, J.-P. Dodelet, Iron-based cathode catalyst with enhanced power density in polymer electrolyte membrane fuel cells, Nature Communications, 2 (2011) 416.
[43] E.F. Holby, G. Wang, P. Zelenay, Acid Stability and Demetalation of PGM-Free ORR Electrocatalyst Structures from Density Functional Theory: A Model for “Single-Atom Catalyst” Dissolution, ACS Catalysis, 10 (2020) 14527-14539.
[44] L.L. Pesterfield, J.B. Maddox, M.S. Crocker, G.K. Schweitzer, Pourbaix (E–pH-M) Diagrams in Three Dimensions, Journal of Chemical Education, 89 (2012) 891-899.
[45] H. Xie, X. Xie, G. Hu, V. Prabhakaran, S. Saha, L. Gonzalez-Lopez, A.H. Phakatkar, M. Hong, M. Wu, R. Shahbazian-Yassar, V. Ramani, M.I. Al-Sheikhly, D.-e. Jiang, Y. Shao, L. Hu, Ta–TiOx nanoparticles as radical scavengers to improve the durability of Fe–N–C oxygen reduction catalysts, Nature Energy, 7 (2022) 281-289.
[46] L. Wan, K. Zhao, Y.-C. Wang, N. Wei, P. Zhang, J. Yuan, Z. Zhou, S.-G. Sun, Molecular Degradation of Iron Phthalocyanine during the Oxygen Reduction Reaction in Acidic Media, ACS Catalysis, (2022) 11097-11107.

Supporting Information

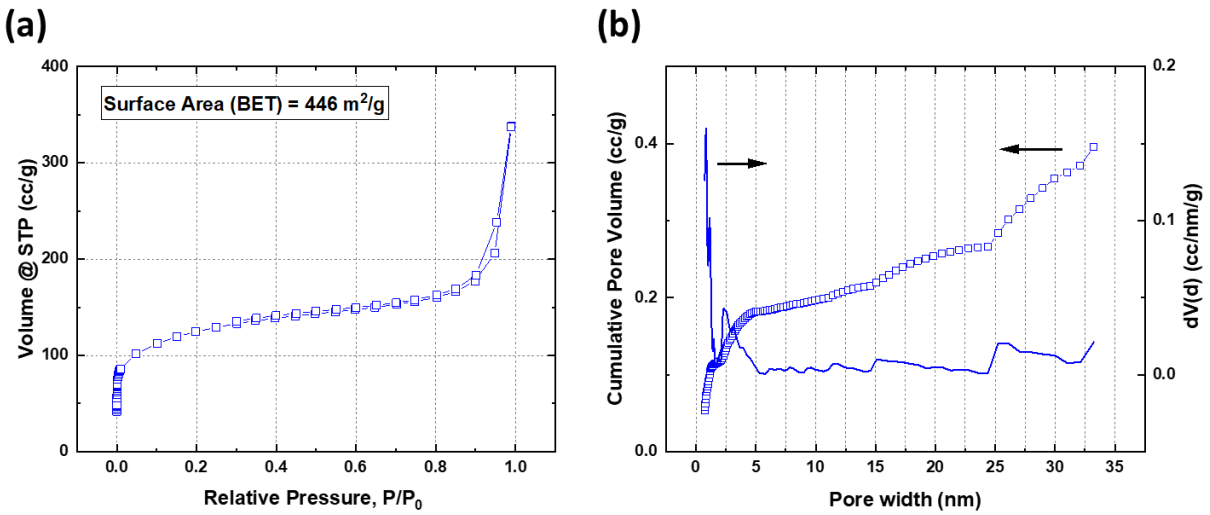

Figure S1. (a) N_2-sorption porosimetry isotherm of the catalyst. (b) Pore-size distribution from the adsorption branch of the isotherm employing the QSDFT model (slit and cylindrical pores).

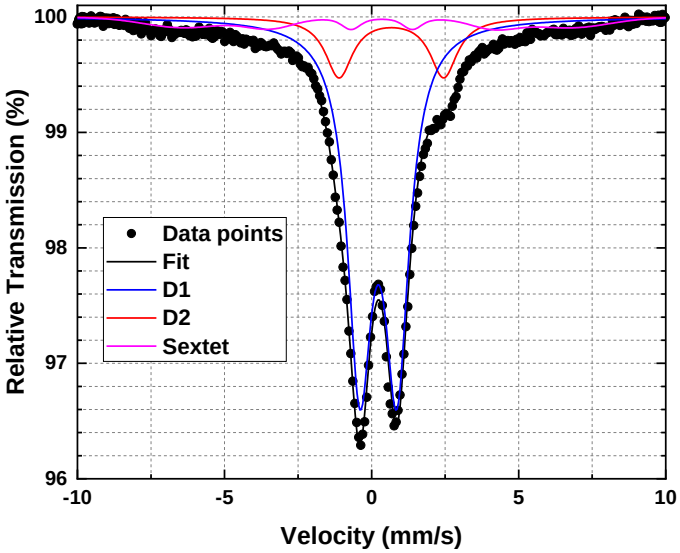

Figure S2. Mössbauer spectrum of the catalyst measured at 4.2 K.

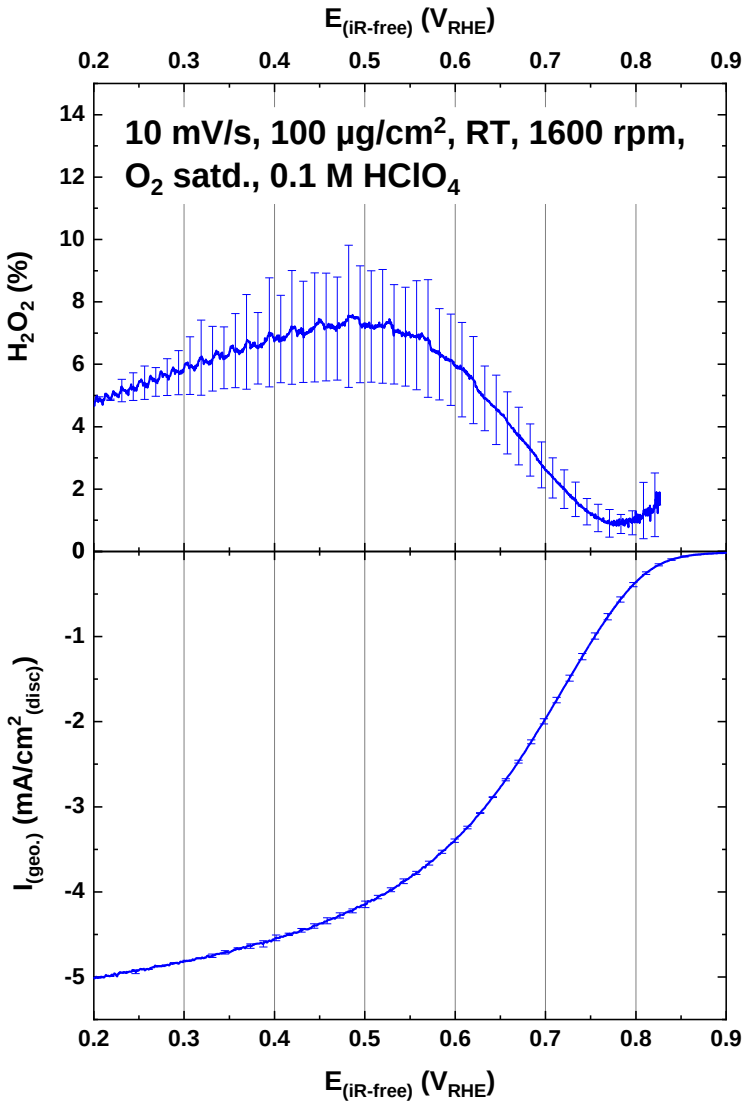

Figure S3. ORR curve of the catalyst (bottom) and corresponding H_2O_2 yield obtained via RRDE experiments (top). Measurements were performed at room temperature in O_2-saturated 0.1 M $HClO_4$ at 1600 rpm, 10 mV s^{-1} (anodic scans).

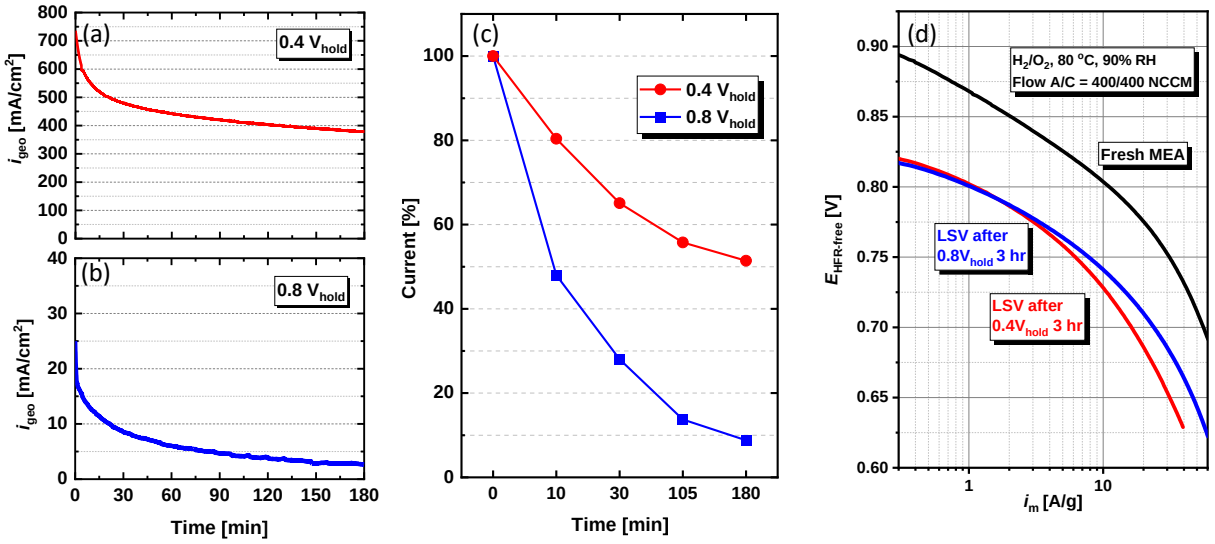

Figure S4. Current profile in H_2/O_2 configuration of the 0.4 V hold (a) and 0.8 V hold (b) measured in the Greenlight test station. (c) Current profile percentage normalized to their respective initial value**.** (d) Tafel representation of the mass activity derived from the LSVs measured in H_2/O_2 configuration at BoT (black) and after the 0.8 V hold (blue) and 0.4 V hold (red) in the Greenlight test station. Catalyst loading on the cathode is ≈ 3.5 mg_{cat}/cm^2_{MEA}.

The validation measurements of the two stability tests were conducted using a Greenlight fuel cell station (G60, Greenlight Innovation, Canada) equipped with a load-bank and an additional potentiostat (Reference3000, Gamry, USA). A flow field with 1 channel / 7 serpentine (0.8 mm deep/width) was employed. The MEA designs and GDL (including compression strain) are the same as the MEAs tested during the XAS measurements. The testing procedure is similar to that performed in the portable fuel cell test system (Figure 3) but without XAS measurements in between the stability testing.

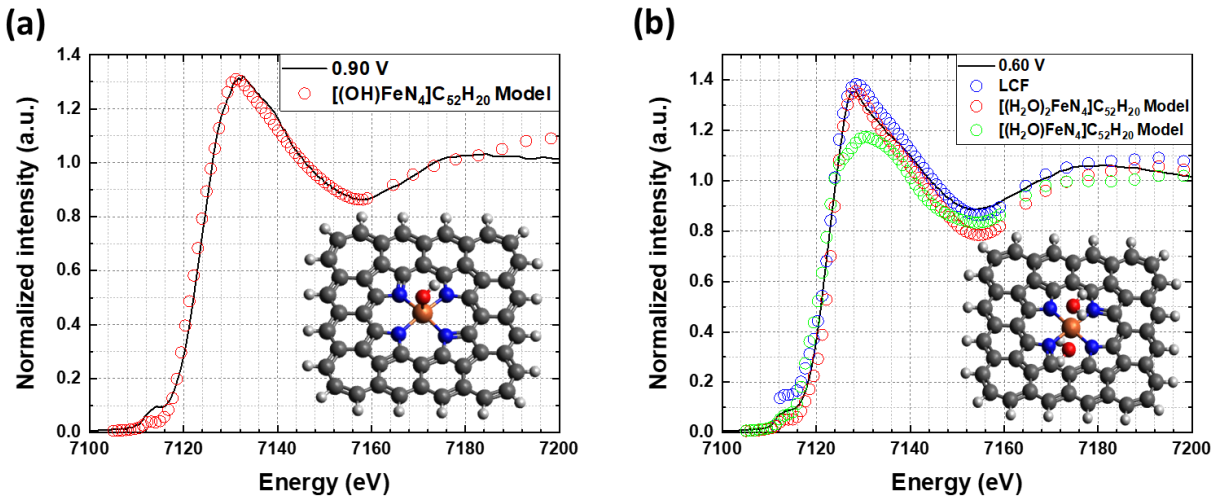

Figure S5. (a) Calculated XANES spectrum of the $[(OH)FeN_4]C_{52}H_{20}$ cluster (red empty circles) in comparison with the experimentally measured spectrum at 0.9 V (black line). (b) Calculated XANES spectra of the $[FeN_4]C_{52}H_{20}$ cluster with 1 (green empty circles) and 2 (red empty circles) H_2O molecules close by the FeN_4 site and their LCF (blue empty circles) in comparison with the experimentally measured spectrum at 0.6 V (black line).

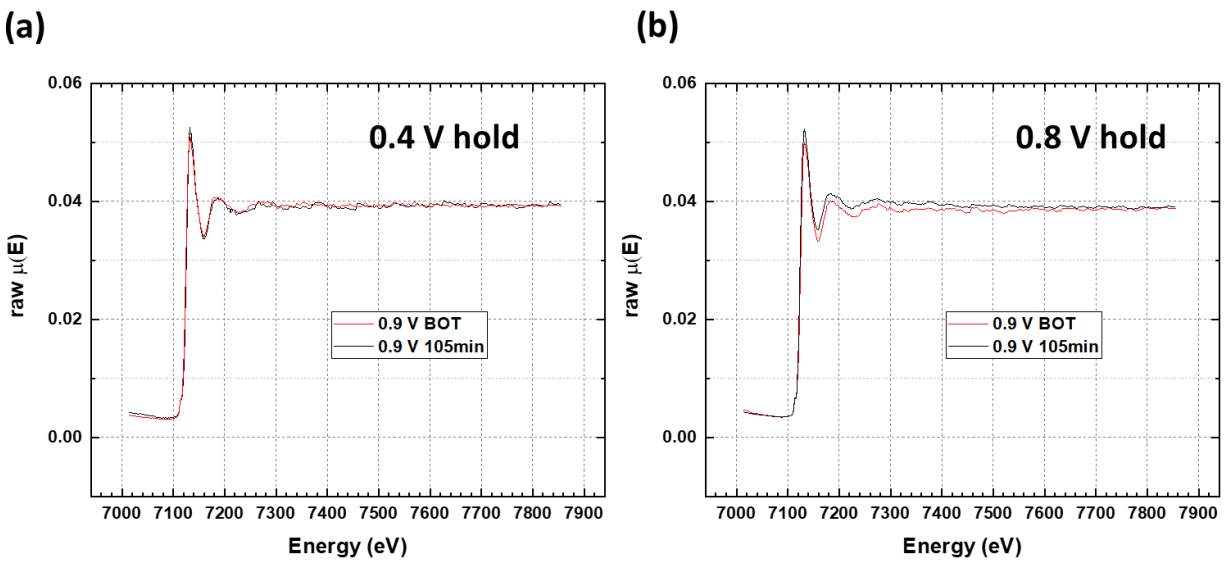

Figure S6. Raw intensity of the fluorescence XAS spectra measured on the same spot at BoT and after 105 minutes during the 0.4 V hold (ab) and the 0.8 V hold (b).

Figure S7. Photograph of the qualitative stripe test for the detection of NH_4^+ ions in solution.

Table S1. Isomer shift (IS), quadrupole splitting (QS), magnetic field (H) and percentage (%) values extracted from the Mössbauer measurement of the sample at T = 4.2 K.

Sample	D1 (IS; QS; %)	D2 (IS; QS; %)	Sextet (IS; H; %)
Fe-N-C	0.23; 1.26; 75	0.67; 3.56; 14	0.26; 40.8; 11

Table S2. Results obtained from the LCF of the spectra at different degradation time using as reference the BoT spectrum of the catalyst and FeOOH.

0.9 V Spectrum (fit with BoT)	**FeOOH %; R-factor ($x10^{-3}$)**
EoT	37; 1.1
105 min	25; 0.7
0.6 V Spectrum (fit w/ BoT)	**FeOOH %; R-factor ($x10^{-3}$)**
EoT	31; 1.2
105min	23; 0.6

4 Conclusions

The aim of this thesis work was to develop a new method for the synthesis of Fe-N-C materials based on active-site imprinting with Zn as imprinting metal. In the first part, the new synthetic method was elaborated and validated and it effectively allowed to decouple the pyrolytic formation of the conductive carbon scaffold from the low-temperature formation of the active site, obtaining well-defined tetrapyrrolic Fe-N_4 single sites. In the second part of this thesis work, the single-site nature of Zn-imprinted catalysts combined with the possibility to exchange/remove the central M atom in a morphologically-conservative fashion allows for the facile quantification of SD and TOF both in acidic and alkaline electrolyte and for the elucidation of the ORR reaction mechanism. The third part of this thesis work deals with the stability of the well-defined tetrapyrrolic Fe-N_4 single site both as storage stability as well as stability under realistic PEMFC conditions.

In the first research project (section 3.1.1), we investigated the active-site imprinting method with Zn^{2+} as metal imprinter. The focus of the work was to show that Zn^{2+} is able to create N_4 coordination sites and that a Zn-to-Fe transmetalation reaction is possible. By employing IL-TEM we were able to visualize the same portion of the catalyst before and after the ion exchange and this clearly showed the presence of atomically dispersed Fe atoms, at the cost of Zn ones, after the transmetalation reaction. The fact that a pre-formed N_4 coordination is needed for the coordination of Fe cations was proven via EFC-ICP-MS experiments by comparing the degradation of an N_4-containing (i.e. Zn-imprinted) NDC with an NDC with a random distribution of N dopants (i.e. without the use of an imprinting metal during its synthesis) both subjected to Fe-coordination experiments in situ in the same cell. With the aid of Mössbauer spectroscopy, it has been proven that the coordination of Fe cations via a wet-chemical ion-exchange reaction employing Fe^{2+} and a salt-melt based one employing Fe^{3+} lead to the same Fe-N_4 sites. Moreover, in both cases the presence of nanoscopic Fe(III) oxide has been detected. Elemental analysis revealed a higher Fe content when using the Fe^{3+}-based salt melt which

subsequently translated into higher activity compared to the Fe^{2+}-coordinated sample. By measuring ORR activities with an RDE setup, we showed that the Zn-to-Fe transmetalation is able to convert ORR inactive Zn-N_4 sites into active Fe-N_4 sites, effectively decoupling the pyrolytic formation of the carbon scaffold from the formation of the active site. The second research project (section 3.1.2) deals with obtaining a catalyst containing exclusively the desired active phase free from the presence of the Fe(III) oxide nanoclusters and with understanding fundamental principles for the synthesis of M-N-C materials. Aided by DFT calculations, it is proposed that, throughout heating of metal, nitrogen and carbon precursors, tetrapyrrolic M-N_4 sites are formed within defective carbon scaffolds. At ~ 750 °C pyrolytic reactions happen and generate the critical conductivity required for electrocatalysis. Finally, if catalytic graphitization takes place, pyridinic M-N_4 sites are formed. EXAFS analysis in combination with extraction experiments and XPS proved that the Zn-N_4 sites in the material are tetrapyrrolic and these are retained after Zn-to-Fe transmetalation. TGA-MS experiments and previous literature[120] showed that the nanoscopic Fe(III) oxide can be thermally decomposed with subsequent Fe coordination to empty N_4-pocket. Consequently, subjecting the catalyst to a second heat treatment allows for the synthesis of an Fe-N-C electrocatalyst containing apparently exclusively tetrapyrrolic Fe-N_4 sites with Fe content > 3 wt.% which shows remarkable activity and stability both in RDE and single cell PEMFC measurements.

In the second part of this thesis work, the possibility to extract the metal from the tetrapyrrolic N_4-pocket has been exploit to measure TOF values in a facile fashion in acidic (section 3.2.1) and alkaline electrolyte (section 3.2.2) and to elucidate the ORR mechanism. By comparing the ORR activity of isomorphic catalysts containing different Fe amounts a TOF value of 0.24 s^{-1} at 0.8 V_{RHE} is found for tetrapyrrolic Fe-N_4 sites in acidic electrolyte, whereas values of 0.4 s^{-1} and 4 s^{-1} are found at 0.90 V_{RHE} and 0.85 V_{RHE}, respectively, in alkaline electrolyte for the same sites. By comparing the catalysts activity and TS in alkaline and acidic electrolyte, it is found that in acidic electrolyte the M site plays a central role in the ORR activity, likely due to an inner sphere mechanism, whereas in alkaline electrolyte it has a secondary function, due to the occurrence of the ORR mostly via an outer sphere mechanism and with the RDS being part of the first $2e^-$ reduction. Employing DFT calculations,

the DOS and the E_f of periodic models featuring different pyrrolic-type N_4 coordination sites is calculated and a correlation between the overpotential needed for the ORR and the E_f is found, which tallies with the activity trends observed in alkaline electrolyte.

In the last section of the thesis, we investigated the stability of tetrapyrrolic Fe-N_4 sites. This has been done by monitoring the storage stability of the catalyst powder over time (section 3.3.1) and by probing the electrochemical stability under realistic PEMFC operating conditions (section 3.3.2). By monitoring the evolution of the active site in the first moments of its formation employing Mössbauer spectroscopy, it is found that simply upon air exposure, hence in non-pyrolytic conditions, the quadrupole doublet D2 turns into D1, showing that they are both related to the same Fe-N_4 site and are a characteristic of the presence/absence of an axial O_2/OH ligand. Over time, D1 turns into a sextet, indicating the chemical decomposition of Fe-N_4 sites into Fe(III) oxide that also results in electrocatalytic activity loss and blocked porosity. After TGA-MS studies, we successfully developed a thermal recovery step which is able to increase the mass activity of the catalyst of more than 400 % (related to the ORR, measured with RDE setup and at 0.8 V_{RHE}) after ~ one year of aging, almost entirely recovering its initial activity. Finally, we employed in-situ XAS measurements to investigated the electrochemical stability of Zn-imprinted Fe-N_4 sites under realistic PEMFC conditions. We tackled the stability of the material in two different oxidation states (+III and +II) in order to possibly correlate different degradation pathways with the oxidation state of the Fe. It is found that at 0.8 V_{RHE} and under O_2, the Fe leaches out of the N_4 pocket and precipitates in the form of Fe(III) oxide, resulting in loss of activity. When performing the degradation protocol again under O_2 but at a constant potential of 0.4 V_{RHE}, the activity loss is the same as for the 0.8 V_{RHE} protocol but XAS reveals a different mechanism at play, which can be related to ROS attack to the active sites, without any demetallation observed in the 3 hours of the degradation.

In summary, this PhD thesis has contributed in several ways to a better understanding of the synthesis, activity and stability of M-N-C materials, more specifically the ones containing tetrapyrrolic sites. The most active Fe-N-C ORR electrocatalysts to date are synthetized based on this newly developed method.[55-56]

The active-site imprinting effectively decouples the formation of the active site from the high temperature pyrolysis and the use of Zn as imprinting metal gives the possibility to synthetize exclusively tetrapyrrolic sites. The tailor-made synthetic procedure developed allowed for the formation of a single-site catalyst, which could be used to deconvolute intrinsic properties of tetrapyrrolic Fe-N_4 sites from the complexity of the material. The evaluation of the intrinsic activity via metal extraction provides not only a new method for the quantification of TOF and utilization factor in different reactions, but also specifically provides TOF values for tetrapyrrolic sites both in acidic and alkaline environment. Finally, the investigation of the powder degradation over time provides guidelines on how to properly store and activate these materials and the finding of two different degradation pathways depending on the oxidation state of the Fe will allow researchers to better tackle stability issues of Fe-N-C ORR electrocatalysts in PEMFCs.

References

1. Titirici, M.-M.; Baird, S.; Sparks, T.; Yang, S. M.; Brandt-Talbot, A.; Hosseinaei, O.; Harper, D. P.; Parker, R.; Vignolini, S.; Berglund, L.; Li, Y.; Gao, H.-L.; Mao, L.-B.; Yu, S.; Díez, N.; Alvarez.ferrero, G.; Sevilla Solis, M.; Szilagyi, P.; Stubbs, C.; Worch, J.; Huang, Y.; Luscombe, C.; Lee, K.-y.; Luo, H.; Platts, J.; Tiwari, D.; Kovalevskiy, D.; Fermin, D.; Au, H.; Alptekin, H.; Crespo Ribadeneyra, M.; Ting, V.; Fellinger, T.-P.; Barrio-hermida, J.; Westhead, O.; Roy, C.; Stephens, I.; Nicolae, S. A.; Sarma, S.; Oates, R.; Wang, C. G.; Li, Z.; Loh, X. J.; Myers, R. J.; Heeren, N.; Grégoire, A.; Périssé, C.; Zhao, X.; Vodovotz, Y.; Earley, B.; Finnveden, G.; Björklund, A.; Harper, G.; Walton, A.; Anderson, P. A., The Sustainable Materials Roadmap. *Journal of Physics: Materials* **2022**.
2. Qiao, S.; Liu, J.; Kawi, S., Editorial: Electrocatalysis - From Batteries to Clean Energy Conversion. *ChemCatChem* **2019,** *11* (24), 5835-5837.
3. Ritchie, H.; Roser, M.; Rosado, P., CO_2 and Greenhouse Gas Emissions. *Our World in Data* **2020**.
4. Jaouen, F.; Jones, D.; Coutard, N.; Artero, V.; Strasser, P.; Kucernak, A., Toward Platinum Group Metal-Free Catalysts for Hydrogen/Air Proton-Exchange Membrane Fuel Cells. *Johnson Matthey Technology Review* **2018,** *62* (2), 231-255.
5. Pollet, B. G.; Kocha, S. S.; Staffell, I., Current status of automotive fuel cells for sustainable transport. *Current Opinion in Electrochemistry* **2019,** *16*, 90-95.
6. Gasteiger, H. A.; Panels, J. E.; Yan, S. G., Dependence of PEM fuel cell performance on catalyst loading. *Journal of Power Sources* **2004,** *127* (1), 162-171.
7. Neyerlin, K. C.; Gu, W.; Jorne, J.; Clark, A.; Gasteiger, H. A., Cathode Catalyst Utilization for the ORR in a PEMFC. *Journal of The Electrochemical Society* **2007,** *154* (2), B279.
8. Thompson, S. T.; Papageorgopoulos, D., Platinum group metal-free catalysts boost cost competitiveness of fuel cell vehicles. *Nature Catalysis* **2019,** *2* (7), 558-561.
9. Paul, S.; Kao, Y.-L.; Ni, L.; Ehnert, R.; Herrmann-Geppert, I.; van de Krol, R.; Stark, R. W.; Jaegermann, W.; Kramm, U. I.; Bogdanoff, P., Influence of the Metal Center in M–N–C Catalysts on the CO2 Reduction Reaction on Gas Diffusion Electrodes. *ACS Catalysis* **2021,** *11* (9), 5850-5864.
10. Koshy, D. M.; Chen, S.; Lee, D. U.; Stevens, M. B.; Abdellah, A. M.; Dull, S. M.; Chen, G.; Nordlund, D.; Gallo, A.; Hahn, C.; Higgins, D. C.; Bao, Z.; Jaramillo, T. F., Understanding the Origin of Highly Selective CO2 Electroreduction to CO on Ni,N-doped Carbon Catalysts. *Angewandte Chemie International Edition* **2020,** *59* (10), 4043-4050.
11. Karapinar, D.; Tran, N.-H.; Giaume, D.; Ranjbar, N.; Jaouen, F.; Mougel, V.; Fontecave, M., FeNC catalysts for CO2 electroreduction to CO: effect of nanostructured carbon supports. *Sustainable Energy & Fuels* **2019,** *3* (7), 1833-1840.
12. Karapinar, D.; Huan, N. T.; Ranjbar Sahraie, N.; Li, J.; Wakerley, D.; Touati, N.; Zanna, S.; Taverna, D.; Galvão Tizei, L. H.; Zitolo, A.; Jaouen, F.; Mougel, V.; Fontecave, M., Electroreduction of CO_2 on Single-Site Copper-Nitrogen-Doped

Carbon Material: Selective Formation of Ethanol and Reversible Restructuration of the Metal Sites. *Angewandte Chemie International Edition* **2019,** *58* (42), 15098-15103.
13. Du, L.; Xing, L.; Zhang, G.; Dubois, M.; Sun, S., Strategies for Engineering High-Performance PGM-Free Catalysts toward Oxygen Reduction and Evolution Reactions. *Small Methods* **2020,** *4* (6), 2000016.
14. Gong, M.; Dai, H., A mini review of NiFe-based materials as highly active oxygen evolution reaction electrocatalysts. *Nano Research* **2015,** *8* (1), 23-39.
15. Moschkowitsch, W.; Lori, O.; Elbaz, L., Recent Progress and Viability of PGM-Free Catalysts for Hydrogen Evolution Reaction and Hydrogen Oxidation Reaction. *ACS Catalysis* **2022,** *12* (2), 1082-1089.
16. Yang, F.; Bao, X.; Zhao, Y.; Wang, X.; Cheng, G.; Luo, W., Enhanced HOR catalytic activity of PGM-free catalysts in alkaline media: the electronic effect induced by different heteroatom doped carbon supports. *Journal of Materials Chemistry A* **2019,** *7* (18), 10936-10941.
17. Mittermeier, T.; Madkikar, P.; Wang, X.; Gasteiger, H.; Piana, M., Probing Transition-Metal Silicides as PGM-Free Catalysts for Hydrogen Oxidation and Evolution in Acidic Medium. *Materials* **2017,** *10* (6), 661.
18. Ni, W.; Krammer, A.; Hsu, C. S.; Chen, H. M.; Schüler, A.; Hu, X., Ni_3N as an Active Hydrogen Oxidation Reaction Catalyst in Alkaline Medium. *Angewandte Chemie International Edition* **2019,** *58* (22), 7445-7449.
19. Asset, T.; Maillard, F.; Jaouen, F., Electrocatalysis with Single-Metal Atom Sites in Doped Carbon Matrices. *Supported Metal Single Atom Catalysis* **2022**, 531-582.
20. Kumar, A.; Vashistha, V. K.; Das, D. K.; Ibraheem, S.; Yasin, G.; Iqbal, R.; Nguyen, T. A.; Gupta, R. K.; Rasidul Islam, M., M-N-C-based single-atom catalysts for H_2, O_2 & CO_2 electrocatalysis: activity descriptors, active sites identification, challenges and prospects. *Fuel* **2021,** *304*, 121420.
21. Wang, A.; Li, J.; Zhang, T., Heterogeneous single-atom catalysis. *Nature Reviews Chemistry* **2018,** *2* (6), 65-81.
22. Cheng, N.; Zhang, L.; Doyle-Davis, K.; Sun, X., Single-Atom Catalysts: From Design to Application. *Electrochemical Energy Reviews* **2019,** *2* (4), 539-573.
23. Jasinski, R., A New Fuel Cell Cathode Catalyst. *Nature* **1964,** *201* (4925), 1212-1213.
24. Jahnke, H.; Schönborn, M.; Zimmermann, G. Organic dyestuffs as catalysts for fuel cells, *Physical and Chemical Applications of Dyestuffs* **1976**, 133-181.
25. Gasteiger, H. A.; Kocha, S. S.; Sompalli, B.; Wagner, F. T., Activity benchmarks and requirements for Pt, Pt-alloy, and non-Pt oxygen reduction catalysts for PEMFCs. *Appl. Catal., B* **2005,** *56* (1-2), 9-35.
26. Lefèvre, M.; Proietti, E.; Jaouen, F.; Dodelet, J.-P., Iron-Based Catalysts with Improved Oxygen Reduction Activity in Polymer Electrolyte Fuel Cells. *Science* **2009,** *324* (5923), 71-74.
27. Zitolo, A.; Goellner, V.; Armel, V.; Sougrati, M.-T.; Mineva, T.; Stievano, L.; Fonda, E.; Jaouen, F., Identification of catalytic sites for oxygen reduction in iron- and nitrogen-doped graphene materials. *Nat Mater* **2015,** *14* (9), 937-942.
28. Asset, T.; Atanassov, P., Iron-Nitrogen-Carbon Catalysts for Proton Exchange Membrane Fuel Cells. *Joule* **2020,** *4* (1), 33-44.
29. Kramm, U. I.; Ni, L.; Wagner, S., 57Fe Mössbauer Spectroscopy Characterization of Electrocatalysts. *Advanced Materials* **2019,** *31* (31), 1805623.

30. Li, J.; Sougrati, M. T.; Zitolo, A.; Ablett, J. M.; Oğuz, I. C.; Mineva, T.; Matanovic, I.; Atanassov, P.; Huang, Y.; Zenyuk, I.; Di Cicco, A.; Kumar, K.; Dubau, L.; Maillard, F.; Dražić, G.; Jaouen, F., Identification of durable and non-durable FeNx sites in Fe–N–C materials for proton exchange membrane fuel cells. *Nature Catalysis* **2021,** *4* (1), 10-19.
31. Kramm, U. I.; Herranz, J.; Larouche, N.; Arruda, T. M.; Lefevre, M.; Jaouen, F.; Bogdanoff, P.; Fiechter, S.; Abs-Wurmbach, I.; Mukerjee, S.; Dodelet, J.-P., Structure of the catalytic sites in Fe/N/C-catalysts for O2-reduction in PEM fuel cells. *Physical Chemistry Chemical Physics* **2012,** *14* (33), 11673-11688.
32. Ferrandon, M.; Kropf, A. J.; Myers, D. J.; Artyushkova, K.; Kramm, U.; Bogdanoff, P.; Wu, G.; Johnston, C. M.; Zelenay, P., Multitechnique Characterization of a Polyaniline-Iron-Carbon Oxygen Reduction Catalyst. *J. Phys. Chem. C* **2012,** *116* (30), 16001-16013.
33. Ni, L.; Gallenkamp, C.; Wagner, S.; Bill, E.; Krewald, V.; Kramm, U. I., Identification of the Catalytically Dominant Iron Environment in Iron- and Nitrogen-Doped Carbon Catalysts for the Oxygen Reduction Reaction. *Journal of the American Chemical Society* **2022,** *144* (37), 16827-16840.
34. Osmieri, L.; Ahluwalia, R. K.; Wang, X.; Chung, H. T.; Yin, X.; Kropf, A. J.; Park, J.; Cullen, D. A.; More, K. L.; Zelenay, P.; Myers, D. J.; Neyerlin, K. C., Elucidation of Fe-N-C electrocatalyst active site functionality via in-situ X-ray absorption and operando determination of oxygen reduction reaction kinetics in a PEFC. *Applied Catalysis B: Environmental* **2019,** *257*, 117929.
35. Jia, Q.; Ramaswamy, N.; Hafiz, H.; Tylus, U.; Strickland, K.; Wu, G.; Barbiellini, B.; Bansil, A.; Holby, E. F.; Zelenay, P.; Mukerjee, S., Experimental Observation of Redox-Induced Fe-N Switching Behavior as a Determinant Role for Oxygen Reduction Activity. *ACS Nano* **2015,** *9* (12), 12496-12505.
36. Mineva, T.; Matanovic, I.; Atanassov, P.; Sougrati, M.-T.; Stievano, L.; Clémancey, M.; Kochem, A.; Latour, J.-M.; Jaouen, F., Understanding Active Sites in Pyrolyzed Fe–N–C Catalysts for Fuel Cell Cathodes by Bridging Density Functional Theory Calculations and 57Fe Mössbauer Spectroscopy. *ACS Catalysis* **2019,** *9* (10), 9359-9371.
37. Chung, H. T.; Cullen, D. A.; Higgins, D.; Sneed, B. T.; Holby, E. F.; More, K. L.; Zelenay, P., Direct atomic-level insight into the active sites of a high-performance PGM-free ORR catalyst. *Science* **2017,** *357* (6350), 479-484.
38. Marshall-Roth, T.; Libretto, N. J.; Wrobel, A. T.; Anderton, K. J.; Pegis, M. L.; Ricke, N. D.; Voorhis, T. V.; Miller, J. T.; Surendranath, Y., A pyridinic Fe-N4 macrocycle models the active sites in Fe/N-doped carbon electrocatalysts. *Nature Communications* **2020,** *11* (1).
39. Zhang, N.; Zhou, T.; Chen, M.; Feng, H.; Yuan, R.; Zhong, C. A.; Yan, W.; Tian, Y.; Wu, X.; Chu, W.; Wu, C.; Xie, Y., High-purity pyrrole-type FeN4 sites as a superior oxygen reduction electrocatalyst. *Energy & Environmental Science* **2020,** *13* (1), 111-118.
40. Liu, S.; Li, C.; Zachman, M. J.; Zeng, Y.; Yu, H.; Li, B.; Wang, M.; Braaten, J.; Liu, J.; Meyer, H. M.; Lucero, M.; Kropf, A. J.; Alp, E. E.; Gong, Q.; Shi, Q.; Feng, Z.; Xu, H.; Wang, G.; Myers, D. J.; Xie, J.; Cullen, D. A.; Litster, S.; Wu, G., Atomically dispersed iron sites with a nitrogen–carbon coating as highly active and durable oxygen reduction catalysts for fuel cells. *Nature Energy* **2022**.
41. Wei, J.; Xia, D.; Wei, Y.; Zhu, X.; Li, J.; Gan, L., Probing the Oxygen Reduction Reaction Intermediates and Dynamic Active Site Structures of Molecular and

Pyrolyzed Fe–N–C Electrocatalysts by In Situ Raman Spectroscopy. *ACS Catalysis* **2022,** *12* (13), 7811-7820.
42. Zagal, J. H.; Koper, M. T. M., Reactivity Descriptors for the Activity of Molecular MN4 Catalysts for the Oxygen Reduction Reaction. *Angewandte Chemie International Edition* **2016,** *55* (47), 14510-14521.
43. Malko, D.; Kucernak, A., Kinetic isotope effect in the oxygen reduction reaction (ORR) over Fe-N/C catalysts under acidic and alkaline conditions. *Electrochemistry Communications* **2017,** *83*, 67-71.
44. Malko, D.; Kucernak, A.; Lopes, T., In situ electrochemical quantification of active sites in Fe–N/C non-precious metal catalysts. *Nature Communications* **2016,** *7* (1), 13285.
45. Malko, D.; Kucernak, A.; Lopes, T., Performance of Fe–N/C Oxygen Reduction Electrocatalysts toward NO2–, NO, and NH2OH Electroreduction: From Fundamental Insights into the Active Center to a New Method for Environmental Nitrite Destruction. *Journal of the American Chemical Society* **2016,** *138* (49), 16056-16068.
46. Ramaswamy, N.; Tylus, U.; Jia, Q.; Mukerjee, S., Activity Descriptor Identification for Oxygen Reduction on Nonprecious Electrocatalysts: Linking Surface Science to Coordination Chemistry. *Journal of the American Chemical Society* **2013,** *135* (41), 15443-15449.
47. Rojas-Carbonell, S.; Artyushkova, K.; Serov, A.; Santoro, C.; Matanovic, I.; Atanassov, P., Effect of pH on the Activity of Platinum Group Metal-Free Catalysts in Oxygen Reduction Reaction. *ACS Catalysis* **2018,** *8* (4), 3041-3053.
48. Artyushkova, K.; Rojas-Carbonell, S.; Santoro, C.; Weiler, E.; Serov, A.; Awais, R.; Gokhale, R. R.; Atanassov, P., Correlations between Synthesis and Performance of Fe-Based PGM-Free Catalysts in Acidic and Alkaline Media: Evolution of Surface Chemistry and Morphology. *ACS Applied Energy Materials* **2019,** *2* (8), 5406-5418.
49. Ramaswamy, N.; Mukerjee, S., Influence of Inner- and Outer-Sphere Electron Transfer Mechanisms during Electrocatalysis of Oxygen Reduction in Alkaline Media. *The Journal of Physical Chemistry C* **2011,** *115* (36), 18015-18026.
50. Blizanac, B. B.; Ross, P. N.; Markovic, N. M., Oxygen electroreduction on Ag(111): The pH effect. *Electrochimica Acta* **2007,** *52* (6), 2264-2271.
51. Choi, C. H.; Lim, H.-K.; Chung, M. W.; Park, J. C.; Shin, H.; Kim, H.; Woo, S. I., Long-Range Electron Transfer over Graphene-Based Catalyst for High-Performing Oxygen Reduction Reactions: Importance of Size, N-doping, and Metallic Impurities. *Journal of the American Chemical Society* **2014,** *136* (25), 9070-9077.
52. Wu, Y.; Nagata, S.; Nabae, Y., Genuine four-electron oxygen reduction over precious-metal-free catalyst in alkaline media. *Electrochimica Acta* **2019,** *319*, 382-389.
53. Li, X.; Cao, C.-S.; Hung, S.-F.; Lu, Y.-R.; Cai, W.; Rykov, A. I.; Miao, S.; Xi, S.; Yang, H.; Hu, Z.; Wang, J.; Zhao, J.; Alp, E. E.; Xu, W.; Chan, T.-S.; Chen, H.; Xiong, Q.; Xiao, H.; Huang, Y.; Li, J.; Zhang, T.; Liu, B., Identification of the Electronic and Structural Dynamics of Catalytic Centers in Single-Fe-Atom Material. *Chem* **2020,** *6* (12), 3440-3454.
54. Yang, W.; Fellinger, T.-P.; Antonietti, M., Efficient metal-free oxygen reduction in alkaline medium on high-surface-area mesoporous nitrogen-doped carbons made from ionic liquids and nucleobases. *J. Am. Chem. Soc.* **2011,** *133* (2), 206-209.
55. Mehmood, A.; Gong, M.; Jaouen, F.; Roy, A.; Zitolo, A.; Khan, A.; Sougrati, M.-T.; Primbs, M.; Bonastre, A. M.; Fongalland, D.; Drazic, G.; Strasser, P.; Kucernak, A.,

High loading of single atomic iron sites in Fe–NC oxygen reduction catalysts for proton exchange membrane fuel cells. *Nature Catalysis* **2022,** *5* (4), 311-323.
56. Jiao, L.; Li, J.; Richard, L. L.; Sun, Q.; Stracensky, T.; Liu, E.; Sougrati, M. T.; Zhao, Z.; Yang, F.; Zhong, S.; Xu, H.; Mukerjee, S.; Huang, Y.; Cullen, D. A.; Park, J. H.; Ferrandon, M.; Myers, D. J.; Jaouen, F.; Jia, Q., Chemical vapour deposition of Fe–N–C oxygen reduction catalysts with full utilization of dense Fe–N4 sites. *Nature Materials* **2021,** *20* (10), 1385-1391.
57. Wan, X.; Liu, X.; Li, Y.; Yu, R.; Zheng, L.; Yan, W.; Wang, H.; Xu, M.; Shui, J., Fe–N–C electrocatalyst with dense active sites and efficient mass transport for high-performance proton exchange membrane fuel cells. *Nature Catalysis* **2019,** *2* (3), 259-268.
58. Hossen, M. M.; Hasan, M. S.; Sardar, M. R. I.; Haider, J. b.; Mottakin; Tammeveski, K.; Atanassov, P., State-of-the-art and developmental trends in platinum group metal-free cathode catalyst for anion exchange membrane fuel cell (AEMFC). *Applied Catalysis B: Environmental* **2022**, 121733.
59. Hossen, M. M.; Artyushkova, K.; Atanassov, P.; Serov, A., Synthesis and characterization of high performing Fe-N-C catalyst for oxygen reduction reaction (ORR) in Alkaline Exchange Membrane Fuel Cells. *Journal of Power Sources* **2018,** *375*, 214-221.
60. Weiss, J.; Zhang, H.; Zelenay, P., Recent progress in the durability of Fe-N-C oxygen reduction electrocatalysts for polymer electrolyte fuel cells. *Journal of Electroanalytical Chemistry* **2020,** *875*, 114696.
61. Banham, D.; Kishimoto, T.; Zhou, Y.; Sato, T.; Bai, K.; Ozaki, J.-i.; Imashiro, Y.; Ye, S., Critical advancements in achieving high power and stable nonprecious metal catalyst-based MEAs for real-world proton exchange membrane fuel cell applications. *Sci. Adv.* **2018,** *4* (3).
62. Osmieri, L.; Cullen, D. A.; Chung, H. T.; Ahluwalia, R. K.; Neyerlin, K. C., Durability evaluation of a Fe–N–C catalyst in polymer electrolyte fuel cell environment via accelerated stress tests. *Nano Energy* **2020,** *78*, 105209.
63. Proietti, E.; Jaouen, F.; Lefèvre, M.; Larouche, N.; Tian, J.; Herranz, J.; Dodelet, J.-P., Iron-based cathode catalyst with enhanced power density in polymer electrolyte membrane fuel cells. *Nature Communications* **2011,** *2* (1), 416.
64. Banham, D.; Choi, J.-Y.; Kishimoto, T.; Ye, S., Integrating PGM-Free Catalysts into Catalyst Layers and Proton Exchange Membrane Fuel Cell Devices. *Adv. Mater.* **2019**, 31, 1804846.
65. Banham, D.; Ye, S.; Pei, K.; Ozaki, J.-i.; Kishimoto, T.; Imashiro, Y., A review of the stability and durability of non-precious metal catalysts for the oxygen reduction reaction in proton exchange membrane fuel cells. *J. Power Sources* **2015,** *285*, 334-348.
66. Banham, D.; Ye, S., Current Status and Future Development of Catalyst Materials and Catalyst Layers for Proton Exchange Membrane Fuel Cells: An Industrial Perspective. *ACS Energy Lett.* **2017,** *2* (3), 629-638.
67. Martinez, U.; Komini Babu, S.; Holby, E. F.; Zelenay, P., Durability challenges and perspective in the development of PGM-free electrocatalysts for the oxygen reduction reaction. *Curr. Opin. Electrochem.* **2018,** *9*, 224-232.
68. Chen, Z.; Higgins, D.; Yu, A.; Zhang, L.; Zhang, J., A review on non-precious metal electrocatalysts for PEM fuel cells. *Energy & Environmental Science* **2011,** *4* (9), 3167.

69. Jaouen, F.; Proietti, E.; Lefevre, M.; Chenitz, R.; Dodelet, J.-P.; Wu, G.; Chung, H. T.; Johnston, C. M.; Zelenay, P., Recent advances in non-precious metal catalysis for oxygen-reduction reaction in polymer electrolyte fuel cells. *Energy Environ. Sci.* **2011,** *4* (1), 114-130.
70. Shao, M.; Chang, Q.; Dodelet, J.-P.; Chenitz, R., Recent Advances in Electrocatalysts for Oxygen Reduction Reaction. *Chemical Reviews* **2016,** *116* (6), 3594-3657.
71. Speck, F. D.; Kim, J. H.; Bae, G.; Joo, S. H.; Mayrhofer, K. J. J.; Choi, C. H.; Cherevko, S., Single-Atom Catalysts: A Perspective toward Application in Electrochemical Energy Conversion. *JACS Au* **2021,** *1* (8), 1086-1100.
72. Chenitz, R.; Kramm, U. I.; Lefèvre, M.; Glibin, V.; Zhang, G.; Sun, S.; Dodelet, J.-P., A specific demetalation of Fe–N4 catalytic sites in the micropores of NC_Ar + NH3 is at the origin of the initial activity loss of the highly active Fe/N/C catalyst used for the reduction of oxygen in PEM fuel cells. *Energy & Environmental Science* **2018,** *11* (2), 365-382.
73. Ferrandon, M.; Wang, X.; Kropf, A. J.; Myers, D. J.; Wu, G.; Johnston, C. M.; Zelenay, P., Stability of iron species in heat-treated polyaniline–iron–carbon polymer electrolyte fuel cell cathode catalysts. *Electrochimica Acta* **2013,** *110*, 282-291.
74. Choi, C. H.; Baldizzone, C.; Grote, J.-P.; Mayrhofer, K. J. J.; Schuppert, A. K.; Jaouen, F., Stability of Fe-N-C Catalysts in Acidic Medium Studied by Operando Spectroscopy. *Angew Chem Int Ed Engl* **2015,** *54* (43), 12753-7.
75. Choi, C. H.; Lim, H.-K.; Chung, M. W.; Chon, G.; Ranjbar Sahraie, N.; Altin, A.; Sougrati, M.-T.; Stievano, L.; Oh, H. S.; Park, E. S.; Luo, F.; Strasser, P.; Dražić, G.; Mayrhofer, K. J. J.; Kim, H.; Jaouen, F., The Achilles' heel of iron-based catalysts during oxygen reduction in an acidic medium. *Energy & Environmental Science* **2018,** *11* (11), 3176-3182.
76. Shao, Y.; Dodelet, J.-P.; Wu, G.; Zelenay, P., PGM-Free Cathode Catalysts for PEM Fuel Cells: A Mini-Review on Stability Challenges. *Advanced Materials* **2019,** *31* (31), 1807615.
77. Choi, J.-Y.; Yang, L.; Kishimoto, T.; Fu, X.; Ye, S.; Chen, Z.; Banham, D., Is the rapid initial performance loss of Fe/N/C non precious metal catalysts due to micropore flooding? *Energy Environ. Sci.* **2017,** *10* (1), 296-305.
78. Xu, X.; Zhang, X.; Kuang, Z.; Xia, Z.; Rykov, A. I.; Yu, S.; Wang, J.; Wang, S.; Sun, G., Investigation on the demetallation of Fe-N-C for oxygen reduction reaction: The influence of structure and structural evolution of active site. *Applied Catalysis B: Environmental* **2022,** *309*, 121290.
79. Nabae, Y.; Yuan, Q.; Nagata, S.; Kusaba, K.; Aoki, T.; Takao, N.; Itoh, T.; Arao, M.; Imai, H.; Higashi, K.; Sakata, T.; Uruga, T.; Iwasawa, Y., In Situ X-ray Absorption Spectroscopy to Monitor the Degradation of Fe/N/C Cathode Catalyst in Proton Exchange Membrane Fuel Cells. *Journal of The Electrochemical Society* **2021,** *168* (1), 014513.
80. Kumar, K.; Dubau, L.; Mermoux, M.; Li, J.; Zitolo, A.; Nelayah, J.; Jaouen, F.; Maillard, F., On the Influence of Oxygen on the Degradation of Fe-N-C Catalysts. *Angewandte Chemie International Edition* **2020,** *59* (8), 3235-3243.
81. Sgarbi, R.; Kumar, K.; Saveleva, V. A.; Dubau, L.; Chattot, R.; Martin, V.; Mermoux, M.; Bordet, P.; Glatzel, P.; Ticianelli, E. A.; Jaouen, F.; Maillard, F., Electrochemical transformation of Fe-N-C catalysts into iron oxides in alkaline

medium and its impact on the oxygen reduction reaction activity. *Applied Catalysis B: Environmental* **2022,** *311*, 121366.
82. Yang, N.; Peng, L.; Li, L.; Li, J.; Liao, Q.; Shao, M.; Wei, Z., Theoretically probing the possible degradation mechanisms of an FeNC catalyst during the oxygen reduction reaction. *Chemical Science* **2021,** *12* (37), 12476-12484.
83. Ku, Y.-P.; Ehelebe, K.; Hutzler, A.; Bierling, M.; Böhm, T.; Zitolo, A.; Vorokhta, M.; Bibent, N.; Speck, F. D.; Seeberger, D.; Khalakhan, I.; Mayrhofer, K. J. J.; Thiele, S.; Jaouen, F.; Cherevko, S., Oxygen Reduction Reaction in Alkaline Media Causes Iron Leaching from Fe–N–C Electrocatalysts. *Journal of the American Chemical Society* **2022,** *144* (22), 9753-9763.
84. Goellner, V.; Baldizzone, C.; Schuppert, A.; Sougrati, M. T.; Mayrhofer, K.; Jaouen, F., Degradation of Fe/N/C catalysts upon high polarization in acid medium. *Phys. Chem. Chem. Phys.* **2014,** *16* (34), 18454-18462.
85. Kramm, U. I.; Lefèvre, M.; Bogdanoff, P.; Schmeißer, D.; Dodelet, J.-P., Analyzing Structural Changes of Fe–N–C Cathode Catalysts in PEM Fuel Cell by Mößbauer Spectroscopy of Complete Membrane Electrode Assemblies. *The Journal of Physical Chemistry Letters* **2014,** *5* (21), 3750-3756.
86. Goellner, V.; Armel, V.; Zitolo, A.; Fonda, E.; Jaouen, F., Degradation by Hydrogen Peroxide of Metal-Nitrogen-Carbon Catalysts for Oxygen Reduction. *Journal of The Electrochemical Society* **2015,** *162* (6), H403-H414.
87. Wan, L.; Zhao, K.; Wang, Y.-C.; Wei, N.; Zhang, P.; Yuan, J.; Zhou, Z.; Sun, S.-G., Molecular Degradation of Iron Phthalocyanine during the Oxygen Reduction Reaction in Acidic Media. *ACS Catalysis* **2022**, 11097-11107.
88. Pampel, J.; Fellinger, T.-P., Opening of Bottleneck Pores for the Improvementof Nitrogen Doped Carbon Electrocatalysts. *Adv. Energy Mater.* **2016,** *6* (8), 1502389.
89. Snitkoff-Sol, R. Z.; Elbaz, L., Assessing and measuring the active site density of PGM-free ORR catalysts. *Journal of Solid State Electrochemistry* **2022,** *26* (9), 1839-1850.
90. Primbs, M.; Sun, Y.; Roy, A.; Malko, D.; Mehmood, A.; Sougrati, M.-T.; Blanchard, P.-Y.; Granozzi, G.; Kosmala, T.; Daniel, G.; Atanassov, P.; Sharman, J.; Durante, C.; Kucernak, A.; Jones, D.; Jaouen, F.; Strasser, P., Establishing reactivity descriptors for platinum group metal (PGM)-free Fe–N–C catalysts for PEM fuel cells. *Energy & Environmental Science* **2020**.
91. Kim, D. H.; Ringe, S.; Kim, H.; Kim, S.; Kim, B.; Bae, G.; Oh, H.-S.; Jaouen, F.; Kim, W.; Kim, H.; Choi, C. H., Selective electrochemical reduction of nitric oxide to hydroxylamine by atomically dispersed iron catalyst. *Nature Communications* **2021,** *12* (1).
92. Boldrin, P.; Malko, D.; Mehmood, A.; Kramm, U. I.; Wagner, S.; Paul, S.; Weidler, N.; Kucernak, A., Deactivation, reactivation and super-activation of Fe-N/C oxygen reduction electrocatalysts: Gas sorption, physical and electrochemical investigation using NO and O2. *Applied Catalysis B: Environmental* **2021,** *292*, 120169.
93. Sahraie, N. R.; Kramm, U. I.; Steinberg, J.; Zhang, Y.; Thomas, A.; Reier, T.; Paraknowitsch, J.-P.; Strasser, P., Quantifying the density and utilization of active sites in non-precious metal oxygen electroreduction catalysts. *Nat. Commun.* **2015,** *6*, 8618.
94. Luo, F.; Choi, C. H.; Primbs, M. J. M.; Ju, W.; Li, S.; Leonard, N. D.; Thomas, A.; Jaouen, F.; Strasser, P., Accurate Evaluation of Active-Site Density (SD) and

Turnover Frequency (TOF) of PGM-Free Metal–Nitrogen-Doped Carbon (MNC) Electrocatalysts using CO Cryo Adsorption. *ACS Catalysis* **2019,** *9* (6), 4841-4852.
95. Bae, G.; Kim, H.; Choi, H.; Jeong, P.; Kim, D. H.; Kwon, H. C.; Lee, K.-S.; Choi, M.; Oh, H.-S.; Jaouen, F.; Choi, C. H., Quantification of Active Site Density and Turnover Frequency: From Single-Atom Metal to Nanoparticle Electrocatalysts. *JACS Au* **2021,** *1* (5), 586-597.
96. Snitkoff-Sol, R. Z.; Friedman, A.; Honig, H. C.; Yurko, Y.; Kozhushner, A.; Zachman, M. J.; Zelenay, P.; Bond, A. M.; Elbaz, L., Quantifying the electrochemical active site density of precious metal-free catalysts in situ in fuel cells. *Nature Catalysis* **2022,** *5* (2), 163-170.
97. Liu, Q.; Liu, X.; Zheng, L.; Shui, J., The Solid-Phase Synthesis of an Fe-N-C Electrocatalyst for High-Power Proton-Exchange Membrane Fuel Cells. *Angewandte Chemie International Edition* **2018,** *57* (5), 1204-1208.
98. Wan, X.; Chen, W.; Yang, J.; Liu, M.; Liu, X.; Shui, J., Synthesis and Active Site Identification of Fe–N–C Single-Atom Catalysts for the Oxygen Reduction Reaction. *ChemElectroChem* **2019,** *6* (2), 304-315.
99. Ellingham, H. J. T., Transactions and Communications. *Journal of the Society of Chemical Industry* **1944,** *63* (5), 125-160.
100. Gokhale, R.; Chen, Y.; Serov, A.; Artyushkova, K.; Atanassov, P., Novel dual templating approach for preparation of highly active Fe-N-C electrocatalyst for oxygen reduction. *Electrochimica Acta* **2017,** *224*, 49-55.
101. Janarthanan, R.; Serov, A.; Pilli, S. K.; Gamarra, D. A.; Atanassov, P.; Hibbs, M. R.; Herring, A. M., Direct Methanol Anion Exchange Membrane Fuel Cell with a Non-Platinum Group Metal Cathode based on Iron-Aminoantipyrine Catalyst. *Electrochim. Acta* **2015,** *175*, 202-208.
102. Sebastián, D.; Baglio, V.; Aricò, A. S.; Serov, A.; Atanassov, P., Performance analysis of a non-platinum group metal catalyst based on iron-aminoantipyrine for direct methanol fuel cells. *Applied Catalysis B: Environmental* **2016,** *182*, 297-305.
103. Serov, A.; Artyushkova, K.; Atanassov, P., Fe-N-C Oxygen Reduction Fuel Cell Catalyst Derived from Carbendazim: Synthesis, Structure, and Reactivity. *Advanced Energy Materials* **2014,** *4* (10), 1301735.
104. Mehmood, A.; Pampel, J.; Ali, G.; Ha, H. Y.; Ruiz-Zepeda, F.; Fellinger, T.-P., Facile Metal Coordination of Active Site Imprinted Nitrogen Doped Carbons for the Conservative Preparation of Non-Noble Metal Oxygen Reduction Electrocatalysts. *Advanced Energy Materials* **2018,** *8* (9), 1701771.
105. Menga, D.; Ruiz-Zepeda, F.; Moriau, L.; Šala, M.; Wagner, F.; Koyutürk, B.; Bele, M.; Petek, U.; Hodnik, N.; Gaberšček, M.; Fellinger, T.-P., Active-Site Imprinting: Preparation of Fe–N–C Catalysts from Zinc Ion–Templated Ionothermal Nitrogen-Doped Carbons. *Advanced Energy Materials* **2019,** *9* (43), 1902412.
106. Menga, D.; Low, J. L.; Li, Y.-S.; Arčon, I.; Koyutürk, B.; Wagner, F.; Ruiz-Zepeda, F.; Gaberšček, M.; Paulus, B.; Fellinger, T.-P., Resolving the Dilemma of Fe–N–C Catalysts by the Selective Synthesis of Tetrapyrrolic Active Sites via an Imprinting Strategy. *Journal of the American Chemical Society* **2021,** *143* (43), 18010-18019.
107. Caturla, F.; Molina-Sabio, M.; Rodríguez-Reinoso, F., Preparation of activated carbon by chemical activation with ZnCl2. *Carbon* **1991,** *29* (7), 999-1007.

108. Heidarinejad, Z.; Dehghani, M. H.; Heidari, M.; Javedan, G.; Ali, I.; Sillanpää, M., Methods for preparation and activation of activated carbon: a review. *Environmental Chemistry Letters* **2020,** *18* (2), 393-415.
109. Wang, Q.; Ina, T.; Chen, W.-T.; Shang, L.; Sun, F.; Wei, S.; Sun-Waterhouse, D.; Telfer, S. G.; Zhang, T.; Waterhouse, G. I. N., Evolution of Zn(II) single atom catalyst sites during the pyrolysis-induced transformation of ZIF-8 to N-doped carbons. *Science Bulletin* **2020**.
110. Su, T.-Y.; Lu, G.-P.; Sun, K.-K.; Zhang, M.; Cai, C., ZIF-derived metal/N-doped porous carbon nanocomposites: efficient catalysts for organic transformations. *Catalysis Science & Technology* **2022,** *12* (7), 2106-2121.
111. Cheng, N.; Ren, L.; Xu, X.; Du, Y.; Dou, S. X., Recent Development of Zeolitic Imidazolate Frameworks (ZIFs) Derived Porous Carbon Based Materials as Electrocatalysts. *Advanced Energy Materials* **2018,** *8* (25), 1801257.
112. Fechler, N.; Fellinger, T.-P.; Antonietti, M., "Salt Templating": A Simple and Sustainable Pathway toward Highly Porous Functional Carbons from Ionic Liquids. *Adv. Mater. (Weinheim, Ger.)* **2013,** *25* (1), 75-79.
113. Fellinger, T.-P.; Thomas, A.; Yuan, J.; Antonietti, M., 25th Anniversary Article: "Cooking Carbon with Salt": Carbon Materials and Carbonaceous Frameworks from Ionic Liquids and Poly(ionic liquid)s. *Adv. Mater. (Weinheim, Ger.)* **2013,** *25* (41), 5838-5855.
114. Anastas, P.; Eghbali, N., Green Chemistry: Principles and Practice. *Chem. Soc. Rev.* **2010,** *39* (1), 301-312.
115. Siebel, A.; Gorlin, Y.; Durst, J.; Proux, O.; Hasché, F.; Tromp, M.; Gasteiger, H. A., Identification of Catalyst Structure during the Hydrogen Oxidation Reaction in an Operating PEM Fuel Cell. *ACS Catalysis* **2016,** *6* (11), 7326-7334.
116. Jovanovič, P.; Pavlišič, A.; Šelih, V. S.; Šala, M.; Hodnik, N.; Bele, M.; Hočevar, S.; Gaberščček, M., New Insight into Platinum Dissolution from Nanoparticulate Platinum-Based Electrocatalysts Using Highly Sensitive In Situ Concentration Measurements. *ChemCatChem* **2014,** *6* (2), 449-453.
117. Pavlišič, A.; Jovanovič, P.; Šelih, V. S.; Šala, M.; Hodnik, N.; Hočevar, S.; Gaberščček, M., The influence of chloride impurities on Pt/C fuel cell catalyst corrosion. *Chemical Communications* **2014,** *50* (28), 3732-3734.
118. Kozlov, V. S.; Semenov, V. G.; Karateeva, K. G.; Bairamukov, V. Y., A Study of Iron Phthalocyanine Pyrolyzate with Mössbauer Spectroscopy and Transmission Electron Microscopy. *Physics of the Solid State* **2018,** *60* (5), 1035-1040.
119. Menga, D.; Buzanich, A. G.; Wagner, F.; Fellinger, T.-P., Evaluation of the Specific Activity of M-N-Cs and the Intrinsic Activity of Tetrapyrrolic Fe-N4 Sites for the Oxygen Reduction Reaction. *Angewandte Chemie International Edition* **2022**.
120. Li, J.; Jiao, L.; Wegener, E.; Richard, L. L.; Liu, E.; Zitolo, A.; Sougrati, M. T.; Mukerjee, S.; Zhao, Z.; Huang, Y.; Yang, F.; Zhong, S.; Xu, H.; Kropf, A. J.; Jaouen, F.; Myers, D. J.; Jia, Q., Evolution Pathway from Iron Compounds to Fe1(II)–N4 Sites through Gas-Phase Iron during Pyrolysis. *Journal of the American Chemical Society* **2020,** *142* (3), 1417-1423.

Acknowledgements

I could have never imagined that this would have been the hardest part to write of the entire thesis. Not because I have no one to thank, far from it, but because it is very hard to put into words how grateful I am to the people I have had around during this journey.

First of all, I would like to express my deepest gratitude to Tim Fellinger and Hubert Gasteiger for being such amazing role models. Looking up to both of you during these years made me grow both as a scientist and as a person. Tim, thank you for giving me this chance and being the best teacher I could have wished for, inside and outside the lab. Hubert, your inspiring ways taught me what it takes to be a true leader, this is something I will never forget.

During these years I had the great pleasure to collaborate with amazing people from a lot of different places. What they all have in common is an immense kindness. Thank you all for your patience in taking me a bit closer to your fields. A special thanks goes to professor Fritz Wagner of course. Not only for the amount of work he has put into this but also for being so helpful and kind-hearted. Another special mention goes to the people at the National Institute of Chemistry in Ljubljana, during those few months you have been great colleagues and good friends, above all.

I want to thank the current members and the alumni of the Chair of Technical Electrochemistry. Coming to work to the great environment you create every day has been amazing, even on the toughest days. I want to especially thank Ana, Ceren, Paulette, Anna, Alexandra, Franzi, Vroni, Mohammad, Burak and Yan-Sheng. We started off as colleagues but I am happy to call you friends now. Thank you for being there for me, for the laughs and these wonderful years we've spent together, I will cherish them in my heart forever.

I want to thank my Italian friends here in Munich, who made me feel less homesick and have been a true second family during these years.

Speaking of second families, the warmest "thank you" goes to my long-life friends: Riccardo, Angelo, Giovanni, Elena, Annapaola, Annalisa, Desirè, Andrea, Giulia and Emanuela. All the distance of this world could never make me feel less loved from each one of you.

Last, but definitely not least, I want to express my deepest love and gratitude to my family, especially my parents, Ivana and Francesco, my sister Alessandra, and my grandmothers, Anna and Agata. I would have not made it this far without your love and support.

Scientific Contributions

Articles

- **D. Menga**, F. Wagner, T.-P. Fellinger*, Shelf Life of Single Atom Catalysts - Powder Degradation of Tetrapyrrolic Fe-N-C Electrocatalysts, *submitted*
- **D. Menga**, J.L. Low, A. Guilherme Buzanich, B. Paulus, T.-P. Fellinger*, Elucidating the Intrinsic Activity of Tetrapyrrolic Fe-N-C Electrocatalysts for the Oxygen Reduction Reaction in Alkaline Medium, *submitted*
- U. Petek, F. Ruiz-Zepeda, I. Arčon, M. Šala, A. Kopač Lautar, J. Kovač, M. Mozetič, **D. Menga**, M. Piana, M. Bele, T.-P. Fellinger*, M. Gaberšček*, Imprinted N_4 Sites in Nitrogen Doped Carbon with Improved Oxygen Reduction Activity, *submitted*
- **D. Menga**, A. Guilherme Buzanich, F. Wagner, T.-P. Fellinger*, Evaluation of the Specific Activity of M-N-Cs and the Intrinsic Activity of Tetrapyrrolic Fe-N_4 Sites for the Oxygen Reduction Reaction, **Angewandte Chemie International Edition**, e202207089 (2022)
- A.M. Damjanović=, B. Koyutürk=, Y.-S. Li, **D. Menga**, C. Eickes, H.A. El-Sayed, H.A. Gasteiger, T.-P. Fellinger, M. Piana*, Loading Impact of a PGM-Free Catalyst on the Mass Activity in Proton Exchange Membrane Fuel Cells, **Journal of The Electrochemical Society**, 168 (2021) 114518
- **D. Menga**, J.L. Low, Y.-S. Li, I. Arčon, B. Koyutürk, F. Wagner, F. Ruiz-Zepeda, M. Gaberšček, B. Paulus, T.-P. Fellinger*, Resolving the Dilemma of Fe–N–C Catalysts by the Selective Synthesis of Tetrapyrrolic Active Sites via an Imprinting Strategy, **Journal of the American Chemical Society**, 143 (2021) 18010-18019
- T. Greese*, P.A. Loichet Torres, **D. Menga**, P. Dotzauer, M. Wiener, G. Reichenauer, Impact of Plasma and Thermal Treatment on the Long-term Performance of Vanadium Redox Flow Electrodes – Significance of Surface Structure vs Oxygen Functionalities, **Journal of The Electrochemical Society**, 168 (2021) 070554
- **D. Menga**, F. Ruiz-Zepeda, L. Moriau, M. Šala, F. Wagner, B. Koyutürk, M. Bele, U. Petek, N. Hodnik, M. Gaberšček, T.-P. Fellinger*, Active-Site Imprinting: Preparation of Fe–N–C Catalysts from Zinc Ion–Templated Ionothermal Nitrogen-Doped Carbons, **Advanced Energy Materials**, 9 (2019) 1902412
- P. Madkikar*, **D. Menga**, G.S. Harzer, T. Mittermeier, A. Siebel, F.E. Wagner, M. Merz, S. Schuppler, P. Nagel, A.B. Muñoz-García, M. Pavone, H.A. Gasteiger, M.

Piana, Nanometric Fe-Substituted ZrO_2 on Carbon Black as PGM-Free ORR Catalyst for PEMFCs, **Journal of The Electrochemical Society**, 166 (2019) F3032-F3043

* corresponding author
[=] these authors contributed equally to this work

Articles in preparation

- **D. Menga**[=], Y.-S. Li[=], A.M. Damjanović, O. Proux, F. Wagner, H.A. Gasteiger, M. Piana, T.-P. Fellinger, On the stability of atomically dispersed Fe-N-C ORR catalyst: an in-situ XAS study in PEMFC
- A.M. Damjanović, A.T.S. Freiberg, A.Siebel, B. Koyutürk, **D. Menga**, K. Krempl, P. Madkikar, O. Proux, H.A. Gasteiger, M. Piana[*], XAS Operando Degradation Analysis on PGM-free ORR catalysts for PEMFCs: Fe-N-C vs. $Fe_{0.07}Zr_{0.93}O_{2-\delta}$/C
- Y.-S. Li, **D. Menga**, H.A. Gasteiger, B. Suthar[*], Design of PGM-free Cathode Catalyst Layer for PEMFC Application: The Impact of Electronic Conductivity
- B. Koyutürk, F. Ruiz-Zepeda, J.L. Low, A. Manzo, **D. Menga**, B. Paulus, M. Gaberšček, T.-P. Fellinger[*], Atomically dispersed P-N-C Electrocatalysts by Sol-Gel Carbonization
- Y.-S. Li[=*], L. Reinschlüssel[=], N.L.T. Pham, **D. Menga**, H.A. Gasteiger, Performance and Stability of PGM-free ORR cathode catalyst in PEMFC: the impact of radical scavenger

* corresponding author
[=] these authors contributed equally to this work

Oral and poster presentations

- 2022 Materials for Sustainable Development Conference (invited oral presentation)
- 2022 Gordon Research Conference/Seminar (poster presentation)
- 2021 Bundesanstalt für Materialforschung und -prüfung seminar (invited oral presentation)
- 2021 Italian Virtual Workshop on Fuel Cells 2021 (invited oral presentation)
- 2020 ECS Prime 2020 (oral presentation)
- 2020 Electrochemistry Undercover (poster presentation)
- 2019 Munich School of Engineering Kolloquium 2019 (poster presentation)

- 2019 Young and Experienced Investigators' Exchange Workshop (oral presentation)
- 2019 Deutsche Zeolith-Tagung (poster presentation)
- 2018 Gordon Research Conference/Seminar (poster presentation)
- 2018 Munich School of Engineering Kolloquium 2018 (poster presentation)
- 2017 Munich School of Engineering Kolloquium 2017 (poster presentation)